
Radio-frequency adiabatic potentials for guided atom-clock interferometry

PHYSICS DEPARTMENT, UNIVERSITY OF CRETE

By:
Hector MAS

Advisor:
Dr. Wolf VON KLITZING
Supervisors:
Dr. Peter RAKITZIS
Dr. Pavlos SAVVIDIS



Abstract:

Trapped and guided matterwave interferometry holds the promise of a step-change in the sensitivity of measurements such as gravity or rotation. This thesis studies the proposal of a Sagnac clock-type trapped-atom interferometer based on the independent manipulation of two hyperfine spin sub-states of Rubidium 87 (^{87}Rb) in a coherent matter-wave guide. I demonstrate the loading of a Radio-Frequency (RF) dressed Bose Einstein Condensate (BEC) in the Time Averaged Adiabatic Potential (TAAP) ring waveguide and the state-dependent transport of atomic clouds in such trap. These beam-splitters in a clock-type atom interferometer are multi-photon Microwave (MW) transitions between RF-dressed states. This thesis studies these transitions in two trapping schemes. Firstly, it explores the dressed atom MW spectrum and the sources of dephasing in the clock transition with atoms trapped in a crossed-dipole optical potential. Secondly, it expands this work to magnetically trapped atoms in adiabatic potentials. In this case, we propose and test a novel bi-chromatic RF-dressed potential with which the line-width of the clock transition can be reduced by one order of magnitude, reaching coherence times of $\tau \approx 20$ ms.

This thesis is based on the following manuscripts and publications:

- **Matter-wave interferometers using TAAP rings**
P. Navez, S. Pandey, H. Mas, K. Poulios, T. Fernholz and W. von Klitzing
New Journal of Physics **18**, 075014 (2016)
- **Antireflection coated semiconductor laser amplifier for Bose-Einstein condensation experiments**
S. Pandey*, H. Mas*, G. Drougakis, K. Mavrakis, M. Mylonakis, G. Vasilakis, V. Bolpasi, W. von Klitzing
AIP Adv., **8**, 95020 (2018)
*Equal contribution
- **Hypersonic Bose-Einstein Condensates in Accelerator Rings**
S. Pandey, H. Mas, G. Drougakis, P. Thekkepatt, V. Bolpasi, G. Vasilakis, K. Poulios and W. von Klitzing
Nature **570** 205-209 (2019).
- **Microwave Spectroscopy of Radio Frequency Dressed ^{87}Rb**
G. Sinuco, B. Garraway, H. Mas, S. Pandey, G. Vasilakis, V. Bolpasi, W. von Klitzing, B. Foxon, S. Jammi, K. Poulios and T. Fernholz
(pre-print: arXiv:1904.12073, 2019)
- **A bi-chromatic adiabatic potential for atom interferometry**
H. Mas, S. Pandey, G. Vasilakis and W. von Klitzing
(In preparation, 2019)
- **Protected states in RF-dressed atoms**
H. Mas, G. Sinuco, W. von Klitzing B. Garraway et al. (author list and author order undecided)
(In preparation, 2019)

Per a Carmina, Jordi i Lluís†

Acknowledgements

El públic lector de la secció d'agraïments té tres poblacions típiques: 1) voyeurs, 2) acadèmics o estudiants profundament avorrits i 3) la gent agraïda. Als primers, els done la benvinguda. D'entre totes les perversions del món, n'heu triat una de les poques que només tenen text. Als segons, els demane que m'envien un mail amb la seua opinió de la tesi, idependentment de quan arriben ací. Als tercers supose que els he dit que llegiren este text, així que poc més a dir-los. Però, clar, este text és per a ells.

I would never hire somebody like me. Initially, I interpreted the fact that Wolf let me work at his lab as either a very optimistic gamble from his side, or the ultimate imposture from mine. But he designed a plan and I suppose I followed it, as well as I could, until finishing this thesis. The privileges and perks at the Cretan Matter Waves lab have been too many, and I won't list them here, and I have to show my deepest gratitude to Wolf for being a mentor.

When I came to Crete, Saurabh (Pandey) had been an intern student for some months. He found me a room, and, during the first days, he taught me some english and some soldering. Afterwards, we've spent about 5 years alongside in the experiment. I can't thank him enough for tolerating my absurd ego, and for the uncountable hours he spent to get the experiment going. Cheers, Saurabh.

There have been two post-docs over these years at the experiment: Giorgos Vasilakis and Konstantinos (Kostas) Poullos. Little to say: I really admire them in and out of the lab. Two MSc students that made the lab a very appealing place to work were Panagiotis Christodoulou -with his insatiable search for Q!- and Premjith Thekkepatt -with his unrivalled AMO experimentalist skillset and quiet sarcasm. I want to thank the BEC2 people for occasional technical support and constant moral support: cheers to Vasiliki Bolpasi -thanks for many good advices!- and Ivan Alonso. And, last but not least: thanks to Giannis Drougakis -who is now taking on BEC1, and good luck with the experiment!

I want to thank Germán Sinuco for the incalculable hours we spent discussing and drafting ideas, but even more so, for his kindness in explaining some math and sending out very useful notes on several topics. I wouldn't have learnt so much without him, so cheers too, Germán. In this same category, I have to include Barry Garraway and Thomas Fernholz. Barry's many works, together with direct advice and suggestions, particularly in this thesis, have shaped my view of this little bit of physics. When Thomas came to Crete for the first time, and told me to prepare this dressed cloud and shine these frequencies, and you'll see this or that transition, I

was overwhelmed. At least two chapters of this thesis can be traced back to that week, and his influence in this work is clear.

I want to thank my co-supervisors Peter Rakitzis and Pavlos Savvidis. They, together with Ioannis Komminis, Dimitrios Charalambidis, Dimitris Papazoglou, Barry Garraway and Wolf von Klitzing, formed the thesis defense committee. I am thankful for their feedback and corrections on the thesis manuscript.

Agraïments llatins

Volia començar esta part recordant i agraint mon pare. No vaig poder contar-li res durant l'últim any i tinc la sensació que s'ha perdut molta informació, que moltes coses no s'han enregistrat completament. Però també volia començar agraint ma mare i el meu germà. Així que comence amb els tres. I com a bon habitant de la Mediterrània, cal afegir ací tota la família, perquè res no funciona sense una família.

També tinc amics que han contribuït a mantindre un centre psicològic i moral. La meua correspondència amb Omar, lligada i deslligada de la música en Étoimoi, ha sigut indispensable per sobreviure l'*ennui* absolut d'Heraklion. Genís, Pablo, Guillem i Míriam no ho saben, però ací estan els seus noms. Nico, Marc i Gabi no han fet res, no han dit res i no són ningú (de fet, estes lletres són transparents). A Martina ja li vam dedicar el LP.

He conegut a gent molt més heraklionana que jo, que han fet la vida un poc més fàcil: Luca, Pilar, Ruth, Carlos, Silvia, Petra, Carmen... I bé, Alberto, però amb Alberto la qüestió és política. Menys heraklionia, però igualment visible: graciñas Miguel.

A Heraklion també vaig conèixer Greta, que m'ha fet canviar opinions i repensar idees.

Contents

Table of contents	iii
1 Introduction	1
1.1 Context	1
1.2 Content of this thesis	4
2 Fundamentals of ultracold atoms	1
2.1 Laser cooling and trapping of neutral atoms	1
2.1.1 Doppler and sub-Doppler cooling	2
2.1.2 The Molasses and the Magneto Optical Trap	5
2.1.3 Optical dipole traps	6
2.1.4 Magnetic trapping: the quadrupole trap	10
2.2 Bose-Einstein Condensates	12
2.2.1 Collisions in ultra-cold gases	14
3 Hyperfine Theory of ^{87}Rb	19
3.1 Atoms in the presence of a static field B_{DC}	21
3.2 Hyperfine theory with Radio-frequency fields $B_{\text{DC}} + B_{\text{RF}}$	24
3.2.1 Intra-manifold transitions between RF-dressed states	29
3.3 Hyperfine theory of Radio-frequency dressed atoms in the presence of a microwave field $B_{\text{DC}} + B_{\text{RF}} + B_{\text{MW}}$	32
3.3.1 Example case: $B_{\text{MW}} \perp B_{\text{RF}} \perp B_{\text{DC}}$	34
3.3.2 Other examples	35
3.4 Protected transitions	39
3.4.1 Bi-chromatic protected transitions	41
3.5 Summary and concluding remarks	42
4 Radio-Frequency Dressed Potentials	45
4.1 The adiabatic Shell trap	45

4.1.1	RF coupling in the quadrupole	46
4.1.2	Trap characteristics	48
4.2	The Bi-chromatic Shell Trap	51
4.3	Time Averaged Adiabatic Potentials	55
4.3.1	The TAAP ring trap	56
5	Experiment Setup	63
5.1	Cretan BEC1 experiment	64
5.2	780nm lasers system	65
5.3	Imaging system	71
5.4	Dipole trap laser system	74
5.5	Magnetic fields	77
5.5.1	DC magnetic fields	77
5.5.2	Audio-frequency magnetic fields	80
5.5.3	Radio-frequency magnetic fields	80
5.5.4	Microwave-frequency magnetic fields	83
5.6	Experiment control	84
6	BEC in a TAAP	87
6.1	BEC Production	87
6.1.1	MOT-CMOT	87
6.1.2	Magnetic Trap	88
6.1.3	Hybrid trap and crossed dipole	89
6.2	The TAAP ring	94
7	Spectroscopy with Radio-Frequency Dressed ^{87}Rb ultra-cold atoms	101
7.1	RF-spectroscopy in Adiabatic Potentials	101
7.1.1	RF-spectroscopy in the shell trap	102
7.1.2	RF-spectroscopy in a TAAP ring	103
7.2	MW-spectroscopy in a dipole trap	105
7.2.1	Spectrum	106
7.2.2	Spectrum characteristics	108
7.2.3	Coherent driving	111
7.3	MW-spectroscopy in a shell trap	117
7.4	The bi-chromatic shell	120
7.5	Spectroscopy in the Bi-chromatic Shell Trap	123
7.5.1	Multi-photon spectrum	124
7.5.2	Line-shift with a bias field	127

7.5.3	Line-shift with $\Delta\Omega_{\text{RF}}$	128
7.5.4	Line-shift at low gradients	129
7.5.5	Tuning $\Delta\omega_{\text{F}}$	130
8	Conclusions	133
	Appendices	139
A	Angular Momentum Algebra	141
B	Decay curves in Coherent Driving	143
C	Two-states imaging processing	147
D	Quadrupole-field line-shifts in the bi-chromatic shell.	149
	Bibliography	153

1

Introduction

In this thesis, we explore the use of RF-dressed magnetically trapped atoms for guided Sagnac interferometry using a Ramsey scheme. We ask two questions. First: is it possible to guide two spin-states adiabatically along opposite¹ paths in a closed loop? Second: is it possible to reduce the dephasing of the superposition state after a first beam splitter for a time span of the order of the guiding time? This thesis takes these ideas as its building blocks, and explores one particular set of trapping potentials for atomic interferometry called TAAP (time-averaged adiabatic potentials), based on RF-dressing. With the goal of measuring the Sagnac phase in a trapped atom interferometer, this work introduces an atom ring waveguide and shows its experimental realisation and then delves into the topic of microwave transitions between RF-dressed states. The interest in the latter lies in that these transitions are necessary for atom-clock interferometry in adiabatic potentials. We will show that the transition between the commonly referred to as clock states of ⁸⁷Rb is broadened in a RF-dressed trap and propose a method to overcome this broadening.

1.1 Context

The atom hypothesis was closer to a leap into the dark than to a conjecture in classical times. Some philosophers substituted the ancient mythology of the unreachable with a newer mythology of the immeasurable. However, they were

¹Here we are thinking of a Sagnac interferometer. But this same idea applies to other types of interferometer.

proven to be *wrong*². Atoms can be measured, seen and manipulated. Since the 19th century atoms (and atomic spectra) became the test of Thomson, Rutherford, and Bohr's theories of the composition of matter [Baily, 2013]. One could safely state that atomic spectra have been in fact the experimental proving ground for much of quantum theory's predictions, including one of the key components of this thesis: the quantisation of angular momentum [Kleppner, 1999]. But this intertwinement runs on an almost fundamental level. Browsing through the 1910s-1920s literature one realises that the first developments towards quantum mechanics were aimed at explaining transition frequencies and transition strengths of already-measured atomic spectra [van der Waerden, 2007].

In the past decades, the quest for cold neutral atoms [Gordon and Ashkin, 1980; Phillips and Metcalf, 1982], either trapped or freely propagating expanded the interest and scientific production in this field [Phillips, 1998]. The deep connection and ceaseless feedback between cold atoms and atomic spectroscopy has led to some of the most notable advances in what today we call quantum technologies. With Bose Einstein Condensation of neutral atoms being one of its hallmarks, this experimental revolution has produced the most precise clock [Bloom *et al.*, 2014], some of the most precise gravimeters [Peters *et al.*, 1999; Abend *et al.*, 2016] atom rotation sensors [Lenef *et al.*, 1997; Barrett *et al.*, 2014; Dutta *et al.*, 2016], a new approach to measure G [Rosi *et al.*, 2014], the most accurate measurement of the fine structure constant [Parker *et al.*, 2018], or quantum simulators [Gross and Bloch, 2017]. Advances³ in atom interferometry are reported regularly (e.g. [Kuhn *et al.*, 2014; Hamilton *et al.*, 2015], a review in [de Angelis *et al.*, 2009]) and a number of mega-projects for detecting gravitational waves on Earth [Canuel *et al.*, 2018] or testing the equivalence principle in the International Space Station [Williams *et al.*, 2016], for example, have been proposed.

²See [Robert, 2011] for an account of Medieval Atomism. Popular literature tends to oversimplify and disregard medieval thought as that of a Dark Age: both backward and reactionary. This stream presents two problems: 1) it overlooks non Western-European sources, and 2) it mythologises the classical greek societies, thus mystifying the origin and development of a number of ideas, e.g. atomism. In any case, medieval atomism is conceptually flawed in the same manner, as it fails to decouple itself both (either) from theology and (or) paradoxical frameworks.

³And interesting debates such as the one elicited from a reported macroscopic superposition of half a meter [Kovachy *et al.*, 2015]. It was questioned whether the different fringe pattern shot-to-shot would prevent claims of having achieved a coherent superposition [Stamper-Kurn *et al.*, 2016]. Later this challenge received yet another reply [Kovachy *et al.*, 2016], drawing analogies from classic quantum optics experiments.

The development of sophisticated miniaturised [Xin *et al.*, 2018] and transportable [Geiger *et al.*, 2011; Bidel *et al.*, 2018; Ménoret *et al.*, 2018] sensor systems based on cold atoms has even found its way into the commercial arena [Fang *et al.*, 2016]. These atom interferometers could profit not only from technological developments (e.g. [Schkolnik *et al.*, 2016]), but also from new, more compact, and simpler schemes. Trapped atom interferometers [McDonald *et al.*, 2013; Marti *et al.*, 2015] hold the promise of providing long interrogation times in these miniaturised setups. These interferometers will circumvent the need for either microgravity, or the very long baseline tower of a freely falling-cloud interferometer, by guiding the atomic cloud in matter-waveguides. However, new challenges arise. Firstly, atom-guide interactions can rapidly decrease the coherence time of the atomic superposition states after a first beam-splitter. Secondly, beam-splitters are delivered by light or AC magnetic fields, which may modify the trapping potential or contribute themselves to dephasing. If a laser field is used, its orientation with respect to the waveguide needs to be extremely precise. Thirdly, fluctuations in the fields generating the waveguide may cause dephasing too. On the upside, in an ideal guided interferometer, the limit is the cloud's lifetime, that can typically be of the order of minutes for a thermal sample. All in all, compact atom interferometers are to be ready for field-applications in a decade or two.

Guided atom-clock interferometry [Stevenson *et al.*, 2015; Navez *et al.*, 2016; Fernholz *et al.*, 2016] has recently become a topic of intensive interest⁴ in this context. It relies on the measurement of frequency shifts⁵ induced on a local oscillator as the superposition states probe an area (Sagnac [Sagnac, 1913; Post, 1967; Schreiber *et al.*, 2014]) or a potential hill (gravimetry) [Roura, 2018]. The main advantage is that the beam-splitters can be MW/RF pulses, not laser light. This provides a system free of mechanical elements, such as mirrors [Navez *et al.*, 2016]. Magnetically trapped atoms can be guided -which allows for long distance transport without cloud spreading [Pandey *et al.*, 2019]- in a state-dependent fashion. The main drawback is that they are subject to dephasing induced by differential shifts from magnetic field fluctuations. Moreover, optically trapped atoms suffer from cloud spreading when

⁴In [Luo *et al.*, 2017] they propose to use many-body entanglement in a similar configuration to reach Heisenberg-limited sensitivity.

⁵See the following references for context. 1) A measurement of the recoil frequency of ^{133}Cs [Shau-Yu *et al.*, 2013] via the Compton frequency. 2) A discussion on atom-interferometer clocks [Peil and Ekstrom, 2014]. 3) A measurement of the time difference between two clocks travelling in opposite directions on Earth [Hafele and Keating, 1972]

applying a laser-light beam-splitter, and MW/RF beam-splitters are useless without a means to control spin-states independently.

The effects of RF-dressing on the hyperfine Zeeman structure of ^{87}Rb have been studied in depth since the early 70s (see [Cohen-Tannoudji and Haroche, 1969a; Haroche *et al.*, 1970; Cohen-Tannoudji and Dupont-Roc, 1972; Pegg, 1973] among others). This thesis incorporates detailed experimental studies especially of the *clock* transition between the -dressed- $|1, -1\rangle$ and $|2, 1\rangle$ states. Amplitude and polarisation of the RF-field, together with the configuration of the DC-magnetic field that decides the quantization axis affect the MW-spectrum between Zeeman sub-states of the two ground hyperfine manifolds of ^{87}Rb . RF-dressing can also be used for trapping, and, as we outlined just above, this thesis treats two relevant cases: the adiabatic shell trap [Zobay and Garraway, 2001] and a TAAP ring [Lesanovsky and Von Klitzing, 2007].

1.2 Content of this thesis

This work demonstrates key components for the development of a guided atom-clock interferometer in a TAAP waveguide. Together with [Pandey, 2019] it constitutes a guide for the state of the art regarding the proposal in [Navez *et al.*, 2016] and a presentation of the limitations that need to be overcome. This thesis is divided in the following chapters. Chapter 1 gives a general introduction and motivation of this work. Chapter 2 delivers a review of concepts related to laser cooling and ultra-cold atoms that will be used in the following chapters. Chapter 3 presents a detailed description of the physics of ground state ^{87}Rb atoms interacting with DC and AC fields. Chapter 4 deals with Radio-Frequency dressed potentials. It contains for the first time the concept of a bi-chromatic adiabatic shell, one of the key components of this work and it describes the TAAP ring. Chapter 5 provides an overview of the experimental setup. Chapter 6 gives a detailed account of BEC production and loading of BECs in a TAAP ring waveguide. Chapter 7 is probably the most important part of this thesis and it includes relevant results on RF and MW spectroscopy in RF-dressed states, including the experimental demonstration of a $\times 10$ reduction in line-width in the *clock* transition in the bi-chromatic shell. Finally, Chapter 8 summarises and underlines the results presented throughout, and offers some ideas for future research. These results may prove important for

the development of compact, portable guided-atom interferometers for fundamental experiments and applications like gravity mapping or inertial navigation.

2

Fundamentals of ultracold atoms

This chapter outlines the basic concepts of laser cooling in Section 2.1. It introduces the physics of Doppler and sub-Doppler cooling in Section 2.1.1 and the Magneto Optical Trap (MOT) and Molasses in Section 2.1.2. Afterwards, it reviews red-detuned optical traps (Section 2.1.3) and quadrupole magnetic traps (Section 2.1.4). To finalize, Section 2.2 focusses on the definition of the Bose Einstein Condensate and discusses the role of collisions in trapped ultra-cold gases (Section 2.2.1).

2.1 Laser cooling and trapping of neutral atoms

The concept of temperature in cold atomic gases is far from trivial. Usually, one assumes a cloud where atoms' velocities obey a Maxwell distribution with a mean value $\langle v \rangle$ and dispersion Δv [Cohen-Tannoudji and Guery-Odelin, 2011], where changes in $\langle v \rangle$ constitute an acceleration (the case of a Zeeman slower) and lowering Δv is a reduction in temperature (since the spread in the velocity distribution narrows down)¹. The internal degrees of freedom of the atoms are neglected: one does not define temperature by taking into account the spin. Such distinction between external and internal degrees of freedom is explicit in the particular atom-light interactions involved in laser cooling and trapping: we will see that it is indispensable to take into account the internal state of atoms to explain the pervasive experimental evidence of sub-Doppler cooling.

One important quantity to understand laser cooling and trapping is the photon

¹A good intuitive example to understand this is a time of flight measurement: even though the atoms fall with a $\langle v \rangle$ determined by gravity, the temperature measurement only *cares* about Δv

recoil energy $E_r = \hbar^2 k_L^2 / 2M$. E_r is the change in energy of an atom when it absorbs a photon. This energy implies a change in momentum of the atom's center of mass that is proportional to the momentum of the impinging photon². With a simple order-of-magnitude calculation [Metcalf and van der Straten, 1999b] one sees that the absorption of a single photon does not change the momentum of an atom significantly, but that many absorption processes are needed (this is easily accomplished with any laser). Also, one needs to take into account the fact that absorbed photons are emitted as fluorescent light after some time τ_R . Consequently, there are two competing processes of absorption and emission that result in a random walk with a net momentum transfer in the direction of the light beam. While we have so far considered the atom's center of mass only, absorption processes are relevant -for changes in momentum- only if the interacting light is resonant or near-resonant, and this depends on the internal degrees of freedom. Therefore, it is necessary that they can be formally de-coupled. As we have seen, the decay time of the atom τ_R determines the timescale of internal state changes; conversely, the recoil energy is associated to the center of mass motion. After defining the natural half-width of the transition as $\Gamma = 1/\tau_R$ we find that [Cohen-Tannoudji and Guery-Odelin, 2011]:

$$T_{ext} = \frac{\hbar}{E_r} \gg T_{int} = \frac{1}{\Gamma} \quad (2.1)$$

which for Rubidium becomes $T_{ext}/T_{int} = 1600$. At this point, the internal and external degrees of freedom of the atom can be decoupled and a mean force exerted by the light on the atom can be derived. The mean radiative force can be found in the literature [Cohen-Tannoudji and Guery-Odelin, 2011; Metcalf and van der Straten, 1999c]. The phase, amplitude and frequency of the light field determine whether the result of the interaction favours either of the two main possible physical processes of the system (which is fundamentally a damped-driven oscillator): absorption or dispersion [Grimm *et al.*, 2000].

2.1.1 Doppler and sub-Doppler cooling

Velocity dependent absorption processes can be used to narrow down the velocity distribution in an atomic cloud. For neutral-atom clouds, one can use a pair of counter-propagating beams with similar amplitude and a light frequency ω_L red detuned from the resonance $\delta = \omega_L - \omega_A$. At low-enough atom velocities, within the

²see that we now consider the atom as a billiard ball, i.e. we have ignored the internal degrees of freedom

capture range given by:

$$(\Delta v)_{capture} \approx \Gamma/k_L \quad (2.2)$$

the radiation pressure force can be expanded such that [Cohen-Tannoudji and Guery-Odelin, 2011]:

$$F = F_0 - \alpha v + \dots \quad (2.3)$$

with a friction coefficient given by:

$$\alpha = \hbar k_L^2 \frac{s}{(1+s)^2} \frac{(-\delta)\Gamma}{\delta^2 + \frac{\Gamma^2}{4}} \quad (2.4)$$

and the saturation parameter:

$$s = \frac{1}{2} \frac{\Omega^2}{\delta^2 + \frac{\Gamma^2}{4}} \quad (2.5)$$

where Ω is the Rabi frequency of the driving field, δ is the detuning from the transition frequency and Γ is the natural half-width. The friction force (the part in Eq. 2.3 that depends on the atom's velocity) drives the narrowing of Δv . The first term F_0 accelerates the atom in one direction. This fact can be problematic if one intends to confine a cloud of atoms in space. However, as mentioned above, the atom's displacement in the beam axis can be damped by a counter-propagating scheme where each beam's force is compensated by one of equal magnitude and opposite direction. In such scenario, atoms *at rest* experience no net force, except for the friction. The result is the accumulation of atoms in a narrower momentum dispersion at the point where all light-field forces cancel. This point is normally designed to exist in 3 dimensions, with three pairs of counter-propagating beams in the \hat{e}_x , \hat{e}_y and \hat{e}_z axes. In this type of configuration, the Doppler cooling lower bound temperature is given by balancing off the heating due to the atoms recoil after photon emission and the friction force:

$$k_B T_D = \frac{\hbar\Gamma}{2} \quad (2.6)$$

This limit can be overcome with cooling methods that address the internal structure of the atom and some of the first experiments in laser cooling of atoms already found lower temperatures than the Doppler limit [Lett *et al.*, 1988]. Sub-Doppler cooling was then explained by polarisation gradient-cooling mechanisms [Dalibard and Cohen-Tannoudji, 1989; Walhout *et al.*, 1992; Devlin and Tarbutt, 2016], which normally

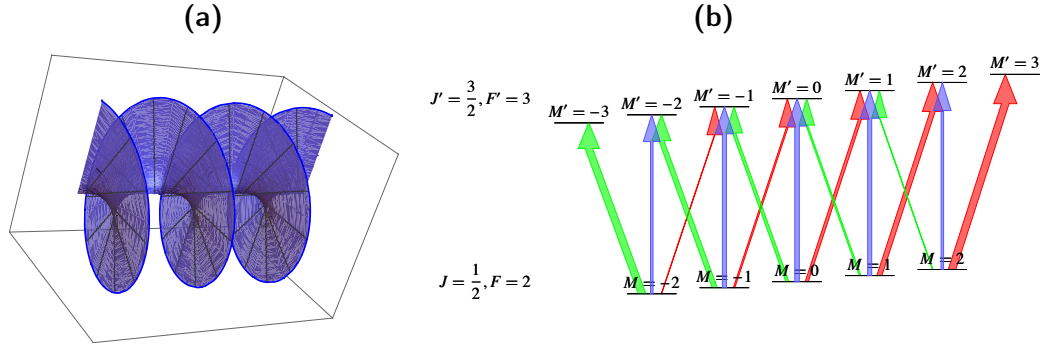


Figure 2.1: a) Shows the resulting rotating linearly polarised light field from two counter-propagating circularly polarised light fields, typical of a Molasses. b) shows the level diagram of the MOT transition in ^{87}Rb D2 line in the presence of a small magnetic field. Red lines correspond to σ_+ , green to σ_- and blue to π transitions. The width of the arrows indicate schematically the strength of each transition. Choosing the adequate polarisation results in optical pumping to each of fully stretched states.

rely on the non-adiabatic following of the internal and external degrees of freedom of the atom: optical pumping occurs at a much faster rate than atomic motion³. One example of a polarisation gradient cooling mechanism is the Sisyphus effect. It relies on spatially state-dependent atom-light coupling. However, in our experimental work we deal with counter-propagating light-beams of opposite circular helicity, contrary to the linearly-polarised light fields employed for Sisyphus cooling. In our case, the forces beyond cooling -albeit still originated from the multi-level atomic structure-cannot be explained in terms of a potential landscape. As we show in Fig. 2.1a) the resulting light polarisation in our case is linear and rotates in z . Therefore, there are no state-dependent potential gradients created by the changing polarisation of the light in space. The mechanism is explained in [Dalibard and Cohen-Tannoudji, 1989] and [Ungar *et al.*, 1989], among others. In short, Fig. 2.1 shows⁴ that when atoms move in the direction of the σ_+ beam, they are optically pumped into the $m_F = 2$ state, as they absorb more photons from the counter-propagating beam. The result is a net force opposing the atoms velocity vector. The same argument holds in the antiparallel direction, and this leads to a friction-like force akin to Doppler cooling, but with a cooling temperature limit that depends on the laser power. The physics of sub-Doppler cooling remain relatively unchanged in the presence of small magnetic fields [Steane and Foot, 1991].

³We will only address the case of red-detuned cooling laser beams.

⁴Diagram realised using the Mathematica package *AtomicDensityMatrix* from Rochester scientific <http://rochesterscientific.com/ADM/> (also Fig. 2.2)

2.1.2 The Molasses and the Magneto Optical Trap

The 3D optical *molasses* consists of a six-beam configuration where a viscous-like damping of the atomic motion leads to slow diffusion and cooling of a gas of atoms [Hodapp *et al.*, 1995]. The driving forces have been introduced in the previous section. Firstly, Doppler cooling takes place with a capture range given by Eq. 2.2. Secondly, sub-Doppler cooling may occur, in our case through the mentioned σ_+, σ_- configuration (with a shorter capture range [Dalibard and Cohen-Tannoudji, 1989]). In the 3D optical molasses three pairs of laser beams with detuning δ from the cooling transition and with the appropriate helicity [Tarbutt, 2015] are aligned in the three axes $\hat{e}_x, \hat{e}_y, \hat{e}_z$ of the lab frame. Even though the Molasses can confine atoms for some time, typical diffusion constants do not allow for trapping. For this purpose, one makes use of the Magneto Optical Trap (MOT). The MOT (be it in 2D or 3D) is the first building block of most cold-atom experiments with Rubidium [Foot, 2005]. The MOT differs from the molasses previously introduced by a spatially dependent force given by the Zeeman splitting caused by a weak quadrupole field. In the 3D version, six circularly-polarised counter-propagating laser beams are set in the three axes of a cartesian laboratory frame. They all have the same red-detuned frequency from the D2 line, the same saturation parameter (see Eq. 2.5), and they carry opposite circular polarisations (with respect to the spatially dependent quantization axis defined by the quadrupole field, on each of the axes). Atoms at rest at the center of the MOT (which is also the zero of the quadrupole field) experience a zero net radiative force. However, when an atom moves in either direction, it sees a force given by the mentioned selective Zeeman sub-level transition scheme. In the case of ^{87}Rb , there is a decay channel to the $F = 1$ hyperfine state from the excited state $F' = 2$ hence a re-pumper beam to carry on with the cycling MOT transition is needed. In order to increase the Phase Space Density in the MOT [Townsend *et al.*, 1995] one needs to reduce scattering processes once the atoms have reached cold temperatures (see Fig. 2.2). Several methods to pump atoms to a dark state [Townsend *et al.*, 1996] have been reported. In our experimental work we make use of a *temporal* dark MOT (to be discussed in section 6.1.1), where a slow switch-off of the re-pumper light leads to cold and highly compressed clouds ready for transfer into a Magnetic Trap in the *dark* hyperfine ground state $F = 1$. Table 2.1 presents a summary of the relevant frequencies.

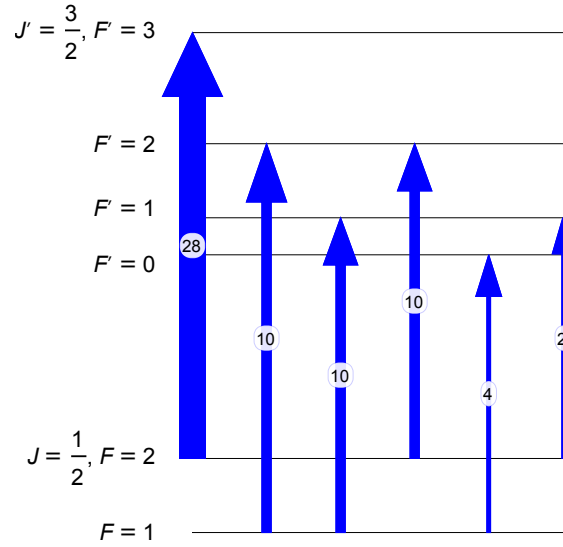


Figure 2.2: Energy level structure of ^{87}Rb with the corresponding, scaled, transition strengths. The MOT transition goes from $F = 2$ to $F' = 3$ and the Re-pumper transition goes from $F = 1$ to $F' = 2$. See Fig. 2.2 as well.

^{87}Rb D2 line	$\lambda_{lock} = 780\text{nm}$	$\nu_{lock} = 384.615\text{ THz}$
F1 \rightarrow F2	ν_{hf}	$\nu_{hf} = 6.8346826\text{ GHz}$
F'2 \rightarrow F'3	$\nu_{2',3'}$	$\nu_{2',3'} = 266.7\text{ MHz}$
F2 \rightarrow F'2	$\nu_{2,2'}$	$\nu_{2,2'} = \nu_{lock} - 54.85\text{ MHz}$
MOT	$\nu_{MOT} = \nu_{2,3'} + \delta_{MOT}$	$\delta_{MOT} = 0 \dots 40\text{ MHz}$
Re-pumper	ν_r	$\nu_r = \nu_{hf} + \nu_{2,2'}$

Table 2.1: Relevant frequencies for laser cooling in ^{87}Rb

2.1.3 Optical dipole traps

Dipole traps need of light beams that result in negligible radiation pressure when interacting with the atoms. They are based on the spatial variation of the atom's energy (Stark) shift given by the shape of the light beam. The difference between this section and the previous atom-light interaction physics is that now we focus on far-detuned laser light with respect to *the* atomic transition whereas in the cases where radiative forces were important we dealt with near-resonant light. The mathematical construction of this system is generally that of a simple oscillator subject to a classical radiation field [Grimm *et al.*, 2000]. In order to find the trapping potential we begin from the relationship -derived from semiclassical

arguments- between energy and light field intensity distribution $U(\mathbf{r}, z) \propto I(\mathbf{r}, z)$. These quantities are related to the ratio between the transition decay rate and the detuning from it. This detuning needs to be large-enough such that the upper level is minimally populated and the transition does not saturate, i.e. the scattering rate needs to be very small. We can write the relationship as:

$$V_{dip} = \frac{3\pi c^2 \Gamma}{2\omega_0^3 \Delta} I(\mathbf{r}) \quad (2.7)$$

where $\Delta = \omega - \omega_0$, being ω_0 the *targeted* atomic transition. Let's assume a Gaussian beam:

$$I(\mathbf{r}) = \frac{2P}{\pi w^2(z)} \exp\left(-\frac{2r^2}{w^2(z)}\right) \quad (2.8)$$

where the beam size along the propagation axis is defined by:

$$w(z) = w_0 \sqrt{1 + \left(\frac{z}{z_R}\right)^2} \quad (2.9)$$

and the Rayleigh range is $z_R = \frac{\pi w_0^2}{\lambda}$, with w_0 being the beam waist. We can find the second order expansion of V_{dip} , which delivers a strong trapping frequency orthogonal to the propagation axis with a weaker one in the propagation axis. The trapping frequencies are given by:

$$\begin{aligned} \omega_r/2\pi &= \sqrt{\frac{8V_0 P}{M\pi w_0^4}} \\ \omega_z/2\pi &= \sqrt{\frac{4V_0 P}{M\pi w_0^2 z_R^2}} \end{aligned} \quad (2.10)$$

where $V_0 = 3\pi c^2 \Gamma / 2\omega_0^3 \Delta$. This trap, however, is not very useful if one needs fast re-thermalization/collisional rates, which is the case in evaporation cooling. Therefore another *crossed* beam can be added to overcome this limitation, or a weak quadrupole⁵ [Lin *et al.*, 2011]. For simplicity, we will assume now that both beams have the same waist (which is roughly the case in our experiment). In this calculation the cylindrical symmetry used before does not apply and we need to use a cartesian reference system. Let's introduce the angle between both beams 2θ and rotate the system according to

⁵There are other solutions, like the dimple trap [Xie *et al.*, 2018]

the transformation:

$$\begin{pmatrix} z' \\ x' \end{pmatrix} = \begin{pmatrix} \cos \theta & \sin \theta \\ -\sin \theta & \cos \theta \end{pmatrix} \begin{pmatrix} z \\ x \end{pmatrix} \quad (2.11)$$

which corresponds to a rotation around the y axis (the beams are propagating in the x - z plane). One now applies this rotation to the coordinates in one of the beams using θ , and using $-\theta$ in the other beam. The total potential is proportional to the direct sum of the two intensities $V_{dip} \propto I_1 + I_2$. Now one expands x' , y' , z' to find each of the trapping frequencies. To second order we find (the coordinates with $'$ are relabelled to x , y , z to simplify the notation):

$$\begin{aligned} V_{dip,x} &\approx \frac{4V_0P}{\pi w_0^2} \left(1 + x^2 \left(\frac{-2 \cos^2 \theta}{w_0^2} - \frac{\sin^2 \theta}{z_R^2} \right) \right) + \dots \\ V_{dip,z} &\approx \frac{4V_0P}{\pi w_0^2} \left(1 + z^2 \left(\frac{-2 \cos^2 \theta}{z_R^2} - \frac{2 \sin^2 \theta}{w_0^2} \right) \right) + \dots \\ V_{dip,y} &\approx \frac{4V_0P}{\pi w_0^2} \left(1 - \frac{2y^2}{w_0^2} \right) + \dots \end{aligned} \quad (2.12)$$

Notice that P is the power in each beam. From Eq. 2.12 one can collect the following trapping frequencies:

$$\begin{aligned} \omega_x/2\pi &= \sqrt{\frac{4V_0P}{M\pi w_0^2} \left(\frac{2 \cos^2 \theta}{w_0^2} + \frac{\sin^2 \theta}{z_R^2} \right)} \\ \omega_z/2\pi &= \sqrt{\frac{4V_0P}{M\pi w_0^2} \left(\frac{\cos^2 \theta}{z_R^2} + \frac{2 \sin^2 \theta}{w_0^2} \right)} \\ \omega_y/2\pi &= \sqrt{\frac{8V_0P}{M\pi w_0^4}} \end{aligned} \quad (2.13)$$

where M is the mass of ^{87}Rb . The crossed dipole trap therefore has a long axis that depends on the angle θ , reaching a unit aspect ratio only when $2\theta = \pi/2$. One can also notice that, even with small angles, the *long* axis (previously) weak-trapping-frequency has a new contribution from the beams waist apart from the term related to the Rayleigh range A useful quantity is the Phase Space Density (PSD). In this case of a harmonic trap given by:

$$V(\mathbf{r}) = \frac{1}{2}M (\omega_x^2 x^2 + \omega_y^2 y^2 + \omega_z^2 z^2) \quad (2.14)$$

the density of states $\rho(\epsilon)$ is [Pethick and Smith, 2008]:

$$g(\epsilon) = \frac{\epsilon^2}{2\hbar^3\omega_{ho}^3} \quad (2.15)$$

where ϵ stands for energy and $\omega_{ho} = (\omega_x\omega_y\omega_z)^{1/3}$. Now we can find the partition function to be (with $\beta = 1/k_B T$):

$$Z = \int_0^\infty \rho(\epsilon) \exp(-\beta\epsilon) d\epsilon = \left(\frac{1}{\hbar\beta\omega_{ho}} \right)^3 \quad (2.16)$$

and, from here, the PSD $D_0 = N/Z$, where N is the number of atoms in the trap, is:

$$D_0 = N (\hbar\beta\omega_{ho})^3 = N \left(\frac{\hbar\omega_{ho}}{k_B T} \right)^3 \quad (2.17)$$

In the case of alkali atoms -or in any atom where the internal structure is more complex than a TLS- the state-dependent atom-light coupling needs to be considered. Whilst it is normally neglected when the laser is far-detuned and thus transitions are either undistinguishable or practically non-existent, it could be important in atom clock applications, where broadening due to differential energy shifts matters. The theory for an atom in a weak magnetic field where the Zeeman structure is resolved has been derived in the literature [Cohen-Tannoudji and Dupont-Roc, 1972; Chicireanu *et al.*, 2011]. However, in some of our experiments a strong RF-field is present. This RF-field shifts the energy levels -RF-dressed states- hence differential shifts diverge from those between the bare states. In fact, one could think of using the RF-dressing field in a similar way to that of the DC-field in [Chicireanu *et al.*, 2011], so as to cancel or compensate the differential light-shift in a TLS.

Let's comment shortly on the line broadening caused by the distribution of atoms in the trap. In our case, we use a red-detuned laser and therefore the atoms experience a space-dependent Stark shift that is the origin of the trapping potential, but also the source of broadening when driving an atomic transition. The difference between the spatially dependent transition frequency⁶ $\omega_{\text{hfs}}(\mathbf{r})$ and the *central* transition frequency ω_{hfs} can be approximated by (for large trapping laser detuning from ω_{hfs}) [Kaplan *et al.*, 2005]:

$$\omega_{\text{hfs}}(\mathbf{r}) - \omega_{\text{hfs}} \approx \frac{\omega_{\text{hfs}}}{\delta} \frac{U(\mathbf{r})}{\hbar} \quad (2.18)$$

⁶Not taken into account 1) Laser power fluctuations, 2) Laser alignment fluctuations 3) State-dependent Differential Stark shifts related to the Zeeman sub-levels.

where δ is the detuning of the trapping laser and ω_{hfs} is the ground states hyperfine splitting. This detuning depends on the internal state of the atoms and it can indeed cause atoms to be trapped in different potentials, similarly to what Section 4.2 presents for the case of a bi-chromatic shell trapping potential. However, in the optical trapping case this effect is smaller and it is normally easy to observe relatively narrow peaks (~ 20 Hz). $U(\mathbf{r})$ is the dipole potential. The fact that Eq. 2.18 contains the spatially dependent Stark shift $U(\mathbf{r})$ leads to inhomogeneous broadening, with a standard deviation of the atomic transition given by:

$$\sigma(\omega_{\text{hfs}}) = \frac{\omega_{\text{hfs}}}{\hbar\delta} \sqrt{\langle U^2(\mathbf{r}) \rangle - \langle U(\mathbf{r}) \rangle^2} \approx \sqrt{\frac{3}{2}} \frac{\omega_{\text{hfs}}}{\delta\hbar} k_B T \quad (2.19)$$

where I quote the result for a thermal cloud in a harmonic trap from [Kaplan *et al.*, 2005]. In the case of a cloud of ^{87}Rb at $T = 100$ nK in a trap with $\lambda = 1064$ nm one finds a frequency spread of $\sigma(\omega_{\text{hfs}}) \approx 1$ Hz when driving the hyperfine transition at $\omega_{\text{hfs}} \approx 6.834$ GHz. To calculate Eq. 2.19 for an arbitrary potential one needs to evaluate the quantities $\langle U(\mathbf{r}) \rangle$ and $\langle U^2(\mathbf{r}) \rangle$, which are simply:

$$\langle U(\mathbf{r}) \rangle = \frac{\int_{-\infty}^{\infty} \sigma_c(\mathbf{r}) U(\mathbf{r}) d\mathbf{r}}{\int_{-\infty}^{\infty} \sigma_c(\mathbf{r}) d\mathbf{r}} \quad (2.20)$$

where $\sigma_c(\mathbf{r}) = \exp\{\beta(U(\mathbf{r}) - U_0)\}$ where $\beta = (k_B T)^{-1}$. With our trap parameters $\theta \approx 0.015$ rad, $\lambda = 1064$ nm $\omega_{\text{hfs}} = 6.834$ GHz, and with 1W in each beam one finds the following scaling for the inhomogeneous broadening $\sigma(\omega_{\text{hfs}}) = \sigma_0 - \exp\{-(T + T_0)/T_h\}$ where $\sigma_0 \approx 10.44$ Hz, $T_0 \approx -1.18 \cdot 10^{-5}$ and $T_h \approx 5 \cdot 10^{-6}$. This dependence saturates at around $10\mu\text{K}$ to a frequency spread given by σ_0 . Evaluating this function at 100 nK, with the trapping parameters quoted above (which yield trapping frequencies $\omega_z/2\pi \approx 200$ Hz and $\omega_\rho/2\pi \approx 30$ Hz) the result is of $\sigma_{\omega_{\text{hfs}}} \approx 0.2$ Hz.

2.1.4 Magnetic trapping: the quadrupole trap

Instead of using light forces, one can take advantage of the magnetic properties of atoms and the precise control of spatially-dependent Larmor frequencies to create magnetic traps. In our experiment we use a magnetic quadrupole field to trap and RF-evaporate atoms after the MOT/Molasses stage and before the use of a dipole-trapping potential to reach BEC. Since this is a very common configuration, we refer to conventional literature on the topic [Foot, 2005]. Let's nonetheless compute the phase space density (PSD), which is needed to tackle the performance

of RF-evaporation in the magnetic trap. Let's calculate it from the density of states in a *linear* trap⁷. The density of states already integrated in momentum space is [Luiten *et al.*, 1996]:

$$\rho(\epsilon) = \frac{(2\pi(2m)^{3/2})}{2\pi\hbar} \int_{U(r)\leq\epsilon} \sqrt{\epsilon - U(r)} dr^3 \quad (2.21)$$

with

$$U(r) = \sqrt{(b_q x)^2 + (b_q y)^2 + (2b_q z)^2} \quad (2.22)$$

where $b_q = g_F \mu_B \alpha$ is the quadrupole magnetic field gradient in energy units. It is convenient to write this in spherical coordinates by using $x = r \sin(\theta) \cos(\phi)$, $y = r \sin(\theta) \sin(\phi)$ and $z = r \cos(\theta)$. Now, the condition $U(r) \leq \epsilon$ sets the limit:

$$r^2 \leq \frac{2\epsilon^2}{b_q^2(3 \cos(2\theta) + 5)} \quad (2.23)$$

And then the integral becomes

$$\rho(\epsilon) = \frac{(2\pi(2m)^{3/2})}{2\pi\hbar} \int_{-r_0}^{r_0} \int_0^\pi \int_0^{2\pi} r^2 \sin(\theta) \sqrt{\epsilon - \frac{\sqrt{b_q^2 r^2 (3 \cos(2\theta) + 5)}}{\sqrt{2}}} d\phi d\theta dr \quad (2.24)$$

where $r_0 = \sqrt{(2\epsilon^2)/b_q^2(5 + 3 \cos(2\theta))}$. From here, one finds that:

$$\rho(\epsilon) = \frac{16\sqrt{2}m^{3/2}\epsilon^{7/2}}{105\pi b_q^3 \hbar^3} \quad (2.25)$$

We can find now the partition function as:

$$Z = \int_0^\infty \rho(\epsilon) \exp(-\beta\epsilon) d\epsilon = \frac{(105\sqrt{\pi}) \beta^{-9/2} (16\sqrt{2}m^{3/2})}{16b_q^3 (105\pi\hbar^3)} = \frac{A_{Q0}(k_B T)^{9/2}}{b_q^3} \quad (2.26)$$

where A_{Q0} includes all constants except k_B . Now one can simplify this expression to be

$$Z = \frac{\sqrt{\frac{2m^3}{\pi}} (k_B T)^{9/2}}{(b_q \hbar)^3}. \quad (2.27)$$

⁷By linear we mean a trap without curvature, and given only by a 3D gradient

The PSD is related to the partition function [Christodoulou, 2015] via $D_0 = N/Z$, where N is the total number of atoms (particles):

$$D_0 = N/Z = N \sqrt{\frac{\pi}{2m^3}} \frac{(b_q \hbar)^3}{(k_B T)^{9/2}} \quad (2.28)$$

We will use this result in Section 6.1.2 to understand compression and evaporative-cooling processes occurring in the quadrupole trap.

2.2 Bose-Einstein Condensates

In this Section we first introduce the basic concepts related to BECs and in chapter 6 (Section 6.1) outline our BEC preparation procedure. First, we will briefly recall the definition of the Bose Einstein Condensate and then we will shortly discuss collisions in ultra-cold gases (Section 2.2.1).

The invention of laser cooling opened up the way for the preparation of atomic clouds at μK temperatures without the need for cryogenic methods. However, cooling with the dissipative light forces used in the MOT and Molasses stage is limited by re-scattering processes (see Section 2.1.1) and therefore the attainable phase space density is far from the BEC phase transition. For this, conservative traps need to be used, where re-thermalisation processes at very low temperatures become possible, and thus evaporative cooling is efficient [Metcalf and van der Straten, 1999a; Ketterle and Druten, 1996]. Evaporative cooling after the MOT preparation led to the Bose Einstein Condensate (BEC) [Davis *et al.*, 1995; Anderson *et al.*, 1995]. Until the first *measurable*⁸ achievement in 1995, BECs had been chased for more than 50 years after Einstein's proposal in the 1920s. BECs are not a topic of study in this thesis, but a *tool* with which to perform experiments on RF-dressed traps. The properties of BECs have been reviewed in many great works [Dalfovo *et al.*, 1999; Pethick and Smith, 2008; Fetter, 2009; Bloch *et al.*, 2008] (among others) and I refer the interested reader to them. In this thesis the BEC of ^{87}Rb acts as a probe of our ring waveguides and the mastering of its manipulation in complex adiabatic traps helps in their understanding, albeit most spectroscopy experiments have been performed with ultra-cold thermal clouds.

Although virtually all cooling techniques mentioned so far need inter-particle interactions, these are not the cause of the BEC phase transition: it is a consequence

⁸For a review of previous attempts with liquid Helium see [Legget, 2000]

of quantum statistics and the symmetric wavefunction under exchange of boson particles. The discovery of the existence of BECs arose departing from Bose's conceptualisation of the statistical distribution of bosons. The average occupation number for photons in the same energy state is (see chapter 12 in [Huang, 1987]):

$$n_i = \frac{1}{e^{\beta\epsilon_i} - 1} \quad (2.29)$$

with the usual definition $\beta = 1/k_B T$ and $\epsilon_i = \hbar^2 \mathbf{k}^2 / 2m$. In the limit of low temperature, and without any modification, photons are simply lost in the continuum and a condensate is not possible. It is precisely at this point where Einstein's contribution becomes pivotal: he proposed the corresponding distribution for mass particles with integral spin⁹. In this case, one needs to include the chemical potential $\mu < \text{Min}(\epsilon_i)$ to take into account particle conservation ($N = \sum n_i$). The mean occupation number for single-particle states i of non-interacting massive bosons is:

$$n_i = \frac{1}{e^{\beta(\epsilon_i - \mu)} - 1} \quad (2.30)$$

The total number of particles can thus be written as [Griffin *et al.*, 1995] (p. 235):

$$N = \sum_i n_i = \sum_i \frac{1}{\zeta^{-1} e^{\beta\epsilon_i} - 1} \quad (2.31)$$

where the fugacity is $\zeta = e^{\beta\mu}$. The integral in the continuum of the expression just above yields the following equation of state:

$$n = \frac{1}{\Lambda^3} g_{3/2}(\zeta) \quad (2.32)$$

where $\Lambda = \sqrt{2\pi\hbar^2/mk_B T}$ is the thermal de Broglie wavelength and:

$$g_{3/2}(\zeta) = \frac{1}{\Gamma(3/2)} \int_0^\infty dx \frac{x^{x-1}}{\zeta^{-1} e^x - 1} \quad (2.33)$$

The temperature at which $\zeta = 1$, where the equation of state Eq. (2.32) ceases to be valid, is the critical temperature T_c :

$$T_c = \frac{2\pi\hbar^2}{mk_B} \left(\frac{n}{g_{3/2}(1)} \right)^{2/3} \approx \frac{2\pi\hbar^2}{mk_B} \left(\frac{n}{2.612} \right)^{2/3} \quad (2.34)$$

⁹Nevertheless, BECs have been achieved with photons [Klaers *et al.*, 2010], polaritons [Kasprzak *et al.*, 2006] and surface plasmon polaritons [Hakala *et al.*, 2018] by ensuring that the statistical distribution in these experiments mimics that of a massive particle's BEC, such that they can emulate particle number conservation.

Below this critical temperature some states can have occupations higher than 1, even reaching close to the total N . The mathematical treatment of this regime involves separating the *zero-momentum* state in a new term before the summation of Eq. 2.31 [Foot, 2005]:

$$n = n_0 + \frac{1}{\Lambda^3} g_{3/2}(1) \quad (2.35)$$

which results in the condensate density fraction formula:

$$n_0 = n \left(1 - \left(\frac{T}{T_0} \right)^{3/2} \right) \quad (2.36)$$

This is the result of a uniform gas [Gaunt *et al.*, 2013]. However, in this thesis we deal with the more common case of a gas in a harmonic trap; I refer to the relevant literature for further detail.

2.2.1 Collisions in ultra-cold gases

We may study collisions in ultra-cold gases at two different levels. In the first place, we may distinguish between a single-component or a mixture gas. At this level, we may talk of mixtures of spin-states (this work), of isotopes [Bentine *et al.*, 2017; Sugawa *et al.*, 2011], or even of atomic species [Extavour *et al.*, 2006; Burchianti *et al.*, 2018]. In our experiment, we are interested both in a mixture of two spin-states of ^{87}Rb and also in a single-component ultra-cold gas. At another level, we may distinguish between elastic and inelastic collisions. One characteristic example of inelastic collisions is that of spin-exchange collisions. For instance, atoms in the $|1, -1\rangle$ and $|2, 1\rangle$ behave differently under spin-exchange collisions. The fully stretched $|1, -1\rangle$ cannot decay, but two colliding $|2, 1\rangle$ atoms may end up in one $|2, 0\rangle$ and one $|2, 2\rangle$ (this results in one atom lost in the magnetic trap - $m = 0$ - and one atom that finds itself suddenly with twice the curvature - $m = 2$ -). On the other hand, we also mentioned elastic collisions. Most of the theory on two-body elastic collisions (i.e. those where the internal states remain unchanged) in a BEC is characterised by the scattering length a associated to s-wave scattering processes [Pethick and Smith, 2008]. BECs of alkali atoms are normally in this regime, since they need to be produced at low-enough density such that three-body recombination is mostly avoided. Roughly, the reason behind it is that at very low temperatures the de Broglie wavelength of an atom is of the size, or larger, than the inter-particle distance. Therefore, one can use the “asymptotic expression of the wave function of the relative motion” [Pitaevskii and Stringari, 2003] of two particles,

which corresponds to the scattering *amplitude*. When the gas is very dilute and cold, its description depends on the s-wave scattering length¹⁰ but not on the microscopic interatomic potential details of the particles involved [Dalibard, 1998]. The boson scattering cross section in this regime is [Altin, 2016]:

$$\sigma = 8\pi a^2 \quad (2.37)$$

As we introduced above, this quantity depends on whether collisions occur between atoms in the same or different spin state, and the scattering length is important to understand the line broadening in atom-clock applications. It determines, together with the density, all contributions to the collisional mean-field shifts [Gibble, 2009]. These shifts are especially important in the case of trapped atoms, since densities are higher than atoms in free fall, and they may not be uniform within the trap. Also, the collision rate, proportional to the cross section, sets the efficiency of evaporative cooling. In addition, the stability of the BEC depends on the sign of the scattering length ($a < 0$ is not stable) [Weiner *et al.*, 1999]. In atom-clock based systems -i.e. when the interrogation of the coupling in a TLS-, collision-led interactions between atoms may thus become a source of line broadening [Gibble and Chu, 1993]. This shift can be written as [Reinhard, 2009; Harber *et al.*, 2002]:

$$\Delta\nu = \frac{2\hbar}{m}n((a_{22} - a_{11}) + f(2a_{12} - a_{22} - a_{11})) \quad (2.38)$$

for thermal atoms, and:

$$\Delta\nu = \frac{\hbar}{m}n((a_{22} - a_{11}) + f(2a_{12} - a_{22} - a_{11})) \quad (2.39)$$

for condensed atoms, where the difference stems from the fact that atoms are considered to be initially in the same state. In these expressions a_{ij} are the scattering lengths for collisions between atoms of type i and/or j . $f = (n_1 - n_2)/(n_1 + n_2)$ where n_k correspond to the density of each of the states. This expression is derived from a two-atom four-level hamiltonian that considers only s-wave collisions. The cloud density for condensed atoms is [Dalfovo *et al.*, 1999]:

$$n(\vec{\mathbf{r}}) = \frac{1}{g}(\mu - V_{ext}(\vec{\mathbf{r}})) \quad (2.40)$$

where g is the interaction parameter $g = 4\pi\hbar^2 a/M$ and the chemical potential is:

$$\mu = \frac{\hbar\omega_{ho}}{2} \left(\frac{15Na}{a_{ho}} \right)^{2/5} \quad (2.41)$$

¹⁰The s-wave scattering length is the low-energy limit of the scattering amplitude

where $a_{ho} = \sqrt{\hbar/M\omega_{ho}}$ is the harmonic oscillator length and $\omega_{ho} = (\omega_x\omega_y\omega_z)^{1/3}$, with $\omega_{x,y,z}$ being the harmonic potential trapping frequencies. We can find the peak density:

$$n_{0,c} = \frac{1}{8\pi} \left(15N \left(\frac{M\omega_{ho}}{\hbar\sqrt{a}} \right)^3 \right)^{2/5} \quad (2.42)$$

On the other hand, the density of the thermal cloud is:

$$n_{0,t} = N\omega_{ho}^3 \left(\frac{2\pi k_B T}{M} \right)^{-3/2} \quad (2.43)$$

If we now consider, as is the case in this work, the two states of ^{87}Rb $|1, -1\rangle$ and $|2, 1\rangle$, where $a_{11} = 100.44a_0$, $a_{22} = 95.47a_0$, $a_{12} = 98.09a_0$ ([Rosenbusch, 2009] and references 14,18 therein), with $a_0 \approx 0.5310^{-10}$ being the Bohr radius, we can see in Fig. 2.3 the different dependence with the density for both cases.

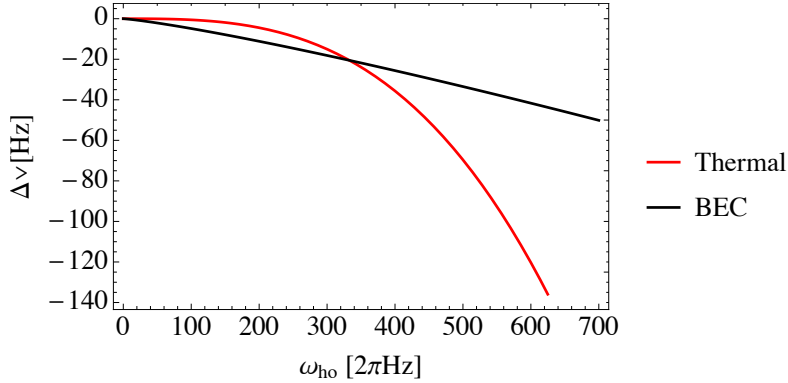


Figure 2.3: Collisional shift induced frequency spreading for the transition between the bare states $|1, -1\rangle$, $|2, 1\rangle$ in the case of a thermal and a BEC cloud.

Fig. 2.3 shows the calculated transition line-shift in the case of $f = 0$ (typical of a Ramsey experiment) for a fixed atom number of 10^5 both for thermal and condensed clouds. It follows that, although at low densities a trapped thermal cloud will present less broadening, at higher densities the line-shift with a BEC cloud is smoother. Notice that Fig. 2.3 has been calculated with the peak density, without taking into account the spatial distribution of the atoms. Moreover, thermal atoms have been demonstrated to experience the so-called self-rephasing effect, which improves the expected coherence time by several multiplication factors [Solaro *et al.*, 2016; Deutsch *et al.*, 2010; Rosenbusch, 2009]. To my knowledge, this effect has not been shown

with a BEC¹¹. Inelastic collisions [Owens and Hutson, 2017], which are a source of atom loss due to recombination occur at a factor of 6 lower rate in a condensate than in a thermal cloud for the same density [Burt *et al.*, 1997]. This fact also plays in favour of using condensates for spectroscopy/clock applications if one needs large densities. The frequency shifts calculated above depend on the density distribution when atoms are trapped. One can use the fact that the energy shifts induced by the trap can have the opposite sign to compensate one with another [Kaplan *et al.*, 2003]. An important quantity to be used later is the elastic collision time for thermal atoms, which is directly related to the efficiency of evaporation. The elastic collision rate is [Shvarchuck *et al.*, 2003]:

$$\tau_{el} = \frac{1}{\sqrt{2}n\bar{v}_{th}\sigma} = \frac{1}{32a^2n\sqrt{\frac{\pi k_B T}{M}}} \quad (2.44)$$

where we have used Eq. 2.37 for the elastic cross section, and the thermal velocity $\bar{v}_{th} = (8k_B T_0/\pi M)^{1/2}$.

¹¹Spin self-rephasing occurs when non-degenerate atoms undergo velocity changing elastic collisions [Solaro *et al.*, 2016]

3

Hyperfine Theory of ^{87}Rb

Así, lo que usualmente se enfoca en la representación matemática de una variable no es el concepto entero sino sólo su(s) parte(s) numérica(s).

– Mario Bunge, *Teoría y Realidad*

One of the central problems addressed in this thesis is the achievement of coherent splitting between two RF-dressed states in the adiabatic trap [Zobay and Garraway, 2001]. In this section we build up the theory of inter-manifold microwave transitions between RF-dressed states from the extensively studied hyperfine magnetic-field interaction Hamiltonian of ^{87}Rb . We begin by including only a static field interacting with the atomic spin, then add the time-dependent RF magnetic field to finalise, in the last step, with a bi-chromatic Hamiltonian where a MW magnetic field is also present.

This chapter investigates microwave transitions between RF-dressed states. It follows a similar formalism to that introduced in a series of papers by Kastler, Cohen-Tannoudji and Haroche (among others). The idea is to treat the atom plus RF-field as a *coupled* system, where one can define a basis of eigenstates that are coherent superpositions of the Zeeman substates mediated by the RF-photons. This same notion of dressing has been used to describe polarisation gradient cooling [Dalibard and Cohen-Tannoudji, 1989] or optical dipole traps [Grimm *et al.*, 2000], although in these cases the dressed system is comprised by atoms plus light. Since angular momentum is conserved under rotations, one can diagonalise the system in the new eigen-basis and study its interaction with the MW-field, which results in transitions between the RF-dressed states.

A number of pioneering theoretical [Cohen-Tannoudji and Haroche, 1969b] and experimental [Kastler, 1963] developments established a first model for hyperfine tran-

sitions between dressed states¹ [Cohen-Tannoudji and Haroche, 1969a]. These models dealt with an off-resonant dressing field and its description in terms of Bloch-Siegert shifts of the transition lines. These shifts can be understood from the modification of the gyromagnetic coupling g -factor. The matching of the coupling to a magnetic field for two isotopes [Haroche and Cohen-Tannoudji, 1970] or of two spin-states are ideas predicated on this synthetic g -factor. The modification of a g -factor by RF-dressing was recently employed in Chromium [Beaufils *et al.*, 2008]. A similar scheme has also been proposed in the context of atomic clocks in optical lattices [Zanon-Willette *et al.*, 2012]. Moreover, the system at hand can be thought of as synthetic field engineering with a periodic modulation of the spin system [Trypogeorgos *et al.*, 2018]². This body of work predicts and measures a modified spectrum in the microwave or optical regime of transitions between RF-dressed atomic states [Haroche *et al.*, 1970]. More recently, different approaches have populated the literature. Particularly, the case of ^{87}Rb arose interest for quantum computing applications [Merkel *et al.*, 2008; Merkel *et al.*, 2009; Mischuck *et al.*, 2012; Saiko *et al.*, 2014].

For the derivation of the microwave transition matrix elements between RF-dressed states, we employ twice the Rotating Wave Approximation, after describing the physics of ^{87}Rb atoms in the presence of a DC field (Section 3.1). Firstly, to neglect contributions other than the fundamental mode of the RF-field (Section 3.2). Secondly, to uncouple the multi-frequency oscillations between hyperfine Zeeman dressed sub-states once the MW-field is introduced too, according to the known energy differences between these states (Section 3.3). Previous work focused on the off-resonant behaviour of the interaction, with particular interest in the action of strong RF-fields. We will briefly address this issue. Moreover, we will also present the basic theory for RF intra-manifold transitions between dressed states (Section 3.2.1). A summary of ideas of this chapter is given in Section 3.5.

¹I may suggest the reader to review their measurements of Hanle curves with RF-dressed states [Kastler, 1973]

²In this case, the formalism is that of continuous dynamical decoupling (CDD). In CDD, the modulation of a field that interacts with a TLS (or higher-order system) yields low sensitivity to noise with respect to its fluctuations [Hirose *et al.*, 2012; Stark *et al.*, 2018]. Yet another interpretation of a similar phenomenon can be found in [Upadhyay *et al.*, 2018].

3.1 Atoms in the presence of a static field B_{DC}

Transition spectra found in alkali atoms can be explained from a theory where the adiabatic coupling between angular momenta arising from the electronic structure intrinsic spin (\mathbf{S}) and the electron's orbital (\mathbf{L}) and nuclear (\mathbf{I}) angular momentum leads to a magnetic moment which mediates the atom's coupling with external magnetic fields. The magnetic angular momentum associated to a given angular momentum operator \mathbf{X} can be written in the following form:

$$\boldsymbol{\mu}_x = \mu_B g_X \mathbf{X} \quad (3.1)$$

where $\mu_B = e\hbar/2m_e$ is the Bohr magneton. With this, one can write an interaction Hamiltonian of the form $\boldsymbol{\mu} \cdot \mathbf{B}$, where \mathbf{B} is an arbitrary magnetic field, g_X is the scaling g -factor of such interaction, in units of μ_B . The total magnetic moment is:

$$\boldsymbol{\mu} = \mu_B (g_I \mathbf{I} + g_S \mathbf{S} + g_L \mathbf{L}) \quad (3.2)$$

where (for ^{87}Rb): $g_S = 2.002319$ and $g_L = 0.9999$ and $g_I = -0.0009951414$. As we can see, the g -factor depends strongly on the nature of the associated angular momentum operator. For instance: since the mass of the proton m_p is much larger than that of the electron m_e , the nuclear magnetic moment is much smaller than the magnetic moment associated to the electron, and therefore it is reasonable to first treat separately the expectedly stronger $\mathbf{S} \cdot \mathbf{L}$ coupling, that leads to a level splitting called the fine³ structure, in the basis $\mathbf{J} = \mathbf{L} + \mathbf{S}$. The hyperfine structure, on the other hand, is a result of the coupling $\mathbf{J} \cdot \mathbf{I}$, that arises from the interaction of the magnetic field created by the orbiting-electron and the nuclear-magnetic moments. In this case one can also define a *total* angular momentum operator such that $\mathbf{F} = \mathbf{J} + \mathbf{I}$. Let's include now a magnetic field in the adiabatic approximation, where one assumes that the Larmor precession frequency is faster than the motion of the atom. As a consequence, the magnetic fields determine the polarisation of the atom. In our experiments this is always the case since $\mu_B B/h \gg k_B T/h$, therefore we can write:

$$H_0 = \frac{A_{\text{hfs}}}{\hbar^2} \mathbf{I} \cdot \mathbf{J} + \frac{\mu_B}{\hbar} (g_I \mathbf{I} + g_J \mathbf{J}) \cdot \mathbf{B}_0 \quad (3.3)$$

where A_{hfs} is the hyperfine structure splitting constant and \mathbf{B}_0 is a homogeneous magnetic field that defines the quantization axis. We can re-write Eq. 3.3 in terms

³The g -factor associated to this new operator is listed as $g_J = 2.00233113$ for $5^2S_{1/2}$, the case of interest in this thesis. See [Steck, 2001] and references therein

of \mathbf{F} , for weak magnetic fields:

$$H_0 = \frac{A_{\text{hfs}}}{\hbar^2} \mathbf{I} \cdot \mathbf{J} + \frac{g_F \mu_B}{\hbar} \mathbf{B}_0 \cdot \hat{\mathbf{F}} \quad (3.4)$$

where

$$g_F = g_J \frac{F(F+1) + 3/4 - I(I+1)}{2F(F+1)} + g_I \frac{F(F+1) - 3/4 + I(I+1)}{2F(F+1)} \quad (3.5)$$

This results in a diagonal matrix where $H_0|F, m_F\rangle = E_{m_F}|F, m_F\rangle$ with $E_{m_F} = m_F g_F \mu_B B_{\text{DC}}$ for small magnetic fields. In the case of ^{87}Rb , $I = 3/2$, $J = 1/2$, which in turn leads to two hyperfine ground states ($|J+I| = 2$ and $|J-I| = 1$) with 3 $m_F = -1, 0, 1$ states for $F = 1$ and 5 $m_F = -2 \dots 0 \dots +2$ states for $F = 2$. The static Hamiltonian can be written as:

$$H_0 = H_{\text{hfs}} + H_0 = \sum_{F=1,2} \frac{A_{\text{hfs}}}{2\hbar^2} (F(F+1) - 9/2) \hat{P}^F + \frac{\mu_B}{\hbar} \sum_{F=1,2} g_F \hat{F}_z^F B_{\text{DC}} \quad (3.6)$$

where \hat{P}^1, \hat{P}^2 (\hat{F}_z^1, \hat{F}_z^2) are projectors (operators) into the respective two subspaces with the definitions:

$$\begin{aligned} \hat{P}^F &= \sum_{m_F=-F}^F |F, m_F\rangle \langle F, m_F| \\ \hat{F}_z^F &= \sum_{m_F=-F}^F m_F |F, m_F\rangle \langle F, m_F| \end{aligned} \quad (3.7)$$

These are two sets of matrices of rank 3 and rank 5, identity matrices for I^1, I^2 and diagonal matrices with matrix elements proportional to the m_F substate for \hat{F}_z^1, \hat{F}_z^2 . The gyromagnetic factors, calculated from Eq. 3.5, are: $g_1 = -0.501827$ and $g_2 = 0.499837$. They are usually approximated by $|g_F| = 0.5$, but, as we will see later, the fact that $g_1 \neq g_2$ is crucial in magnetic trapping schemes involving several hyperfine substates. The states $|F, m_F\rangle$ of the coupled basis are related to the states $|I, m_I, J, m_J\rangle$ of the uncoupled basis by the Clebsch-Gordan decomposition or, more conveniently written, by the following expression that makes use of Wigner 3j-symbols (see Appendix A for the full decomposition):

$$|F, m_F\rangle = \sum_{m_I=-3/2}^{3/2} \sum_{m_J=-1/2}^{1/2} (-1)^{m_F+1} \sqrt{1+2F} \begin{pmatrix} I & J & F \\ m_I & m_J & -m_F \end{pmatrix} |m_I, m_J\rangle \quad (3.8)$$

The ladder operators (see Appendix A) acts on the m_J sub-states of \mathbf{J} (equivalently for \mathbf{I} and \mathbf{F}). Let's look back at Eq. 3.3, from where we calculate the eigen-system. This equation is of particular interest to understand the magnetic field dependence of the difference in energy between two states. In particular, it shows the existence of *clock transitions*, where the second derivative of the differential shift with respect to a potential source of broadening (in this case B_{DC}) becomes zero. We also intend to compare the current results with the case of RF-dressed atoms. The eigen-energies of the clock states can be expanded to second order for small B_{DC} :

$$\begin{aligned} E_{|1,-1\rangle} &\approx -\frac{5}{8}\hbar\omega_{\text{hfs}} + \frac{1}{4}(-5g_I + g_J)\mu_B B_{\text{DC}} - \frac{3}{16\hbar\omega_{\text{hfs}}}\left((g_I - g_J)\mu_B B_{\text{DC}}\right)^2 \\ E_{|2,1\rangle} &\approx \frac{3}{8}\hbar\omega_{\text{hfs}} + \frac{1}{4}(3g_I + g_J)\mu_B B_{\text{DC}} + \frac{3}{16\hbar\omega_{\text{hfs}}}\left((g_I - g_J)\mu_B B_{\text{DC}}\right)^2 \end{aligned} \quad (3.9)$$

from where the two linear terms of the form $g_X\mu_B B_{\text{DC}}$ give us a the g_F factors cited above, only that now we follow the simple argument developed from Eq. 3.1:

$$\begin{aligned} |g_1| &= \frac{1}{4}(-5g_I + g_J) = 0.501827 \\ |g_2| &= \frac{1}{4}(3g_I + g_J) = 0.499836 \end{aligned} \quad (3.10)$$

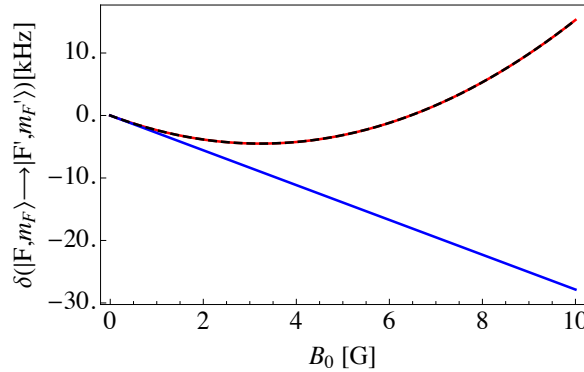


Figure 3.1: Breit-Rabi splitting between the magnetically sensitive clock states $|1, -1\rangle$ and $|2, 1\rangle$ as a magnetic field B_0 varies. Full calculation from in red, quadratic approximation from Eq. 3.9 in dashed black and linear approximation in blue

Fig. 3.1 shows that the quadratic term leads to a parabola shaped shift between the magnetically sensitive clock states of ^{87}Rb . This particular differential line-shift dependence with B_{DC} has been widely used in trapped atom clock applications [Szmuk *et al.*, 2015], leading to long coherence times that are further improved by collisional

shift-cancelling effects [Rosenbusch, 2009]. To test the theory presented above we prepared a cold cloud in a mixture the $F = 1$ Zeeman sub-levels and performed two-photon spectroscopy with the atomic cloud in free fall. We scanned over a relatively small range of MW-frequencies centred on the hyperfine line (we quote the detuning with respect to $\omega_{\text{hfs}}/2\pi$). The procedure consisted in letting the cloud fall in a homogeneous field B_{DC} that had previously been calibrated. Fig. 3.2 shows our measurement, together with the predicted energy-shifts for three transitions. We see that the measured transitions in the green and purple lines are shifted in *opposite* directions at a certain bias field. The RF-photon was chosen close to the resonance $\hbar\omega_{\text{RF}} \approx g_F\mu_B B_{\text{DC}}$ as B_{DC} was scanned. We can see that the line shift matches the resonant ω_{RF} of the LC circuit driving the RF-coil, where the strength of B_{RF} is maximum (see Section 5.5.3). In Fig. 3.2b we show a simple theoretical curve calculated with the methods presented in the next sections. Notice that the orange curve is not shifted because it is a MW one-photon transition. To cross-check the peaks-assignment, we considerably reduced the RF-power and drove the *clock* transition again. Black dots in Fig. 3.2 show the result of this measurement: they fall in the predicted curve from the Breit-Rabi formula. These measurements are a good preview of the next section, where we address the situation of alkali atoms in the presence of both a DC and (strong) RF field.

3.2 Hyperfine theory with Radio-frequency fields $B_{\text{DC}} + B_{\text{RF}}$

Let's study the interaction of ^{87}Rb atoms with the following time-dependent Hamiltonian:

$$H = \frac{A_{\text{hfs}}}{\hbar^2} \mathbf{I} \cdot \mathbf{J} + \frac{\mu_B}{\hbar} (g_I \mathbf{I} + g_J \mathbf{J}) \cdot (B_{\text{DC}} \hat{\mathbf{z}} + \mathbf{B}(t)) \quad (3.11)$$

where $\mathbf{B}(t) = \mathbf{B}_{\text{RF}}(t)$. Since $\hbar\omega_{\text{MW}} \approx \Delta E_F$ and $\hbar\Omega_{\text{RF}} \approx \Delta E_{m_F}$, we uncouple the general problem (that includes the MW-field too in Section 3.3) in these two energy scales. Section 3.3 studies transitions between different hyperfine manifolds, therefore it is not convenient to treat the problem at hand within only one of the subspaces. Instead let's solve the more general problem [Merkel *et al.*, 2008; Merkel *et al.*, 2009] in the tensor product space of I and J . In the case of ^{87}Rb , as we have seen, this reduces to two subspaces, which are $F = 2$ and $F = 1$, rendering a total

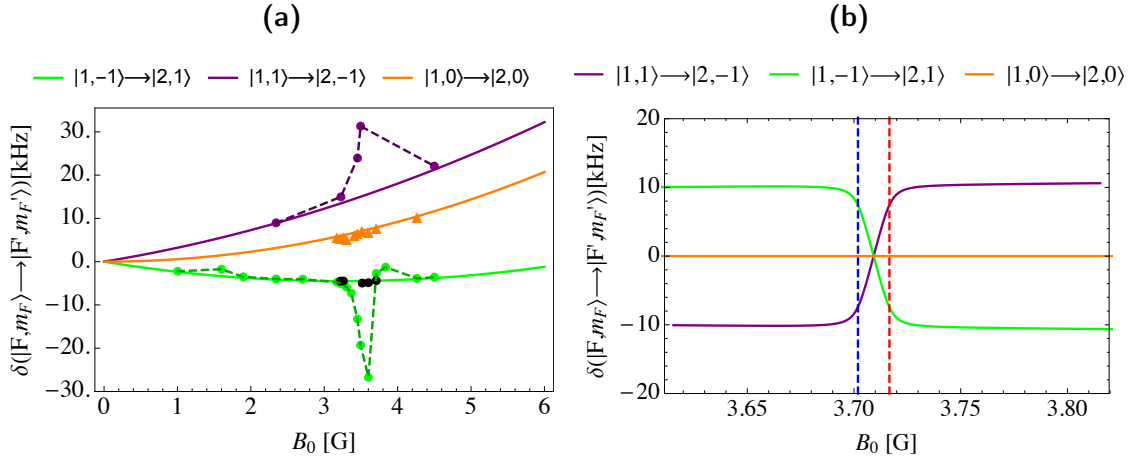


Figure 3.2: Differential energy shift between three transitions. All starting from the Zeeman sub-states of the $F=1$ manifold. In purple (to $|1, 1\rangle \rightarrow |2, -1\rangle$), in green (to $|1, -1\rangle \rightarrow |2, 1\rangle$) and in orange ($|1, 0\rangle \rightarrow |2, 0\rangle$). In a) we show the case of bare states in the presence of a static DC-field, which is scanned in the abscissa. In b) we show an estimation of the AC Stark shift. Here, the blue line shows the resonance point for a given frequency for the $F=1$ states and the red line shows it for the $F=2$ states. Dots in a) show experimental points, with the same colour code as the theory lines. Due to a strong RF-field resonant close to 3.5G we observe large line-shifts that we identify with AC Stark shifts induced by the RF radiation. Black dots correspond to measurements of the $|1, -1\rangle \rightarrow |2, 1\rangle$ transition for a low RF-amplitude. We do not observe line-shifts departing from the theoretical prediction of the Breit-Rabi formula.

dimension⁴ of $(2j_1 + 1)(2j_2 + 1) = 8$. Now, if we assume that the static fields are small-enough such that there is no hyperfine substates mixing, one can write the time-independent part of the Hamiltonian as in Eq. 7.6. This time-dependent term -also- corresponds to a magnetic dipolar interaction with the total spin operator, that is $H_{\text{RF}} = \mathbf{F} \mathbf{B}_{\text{RF}}(t)$. The first aim in any quantum mechanical problem involving a spin is generally to align the operators that contain the relevant observables with whatever is causing that spin to precess. In our case, since the RF-field is of the order of the Larmor frequency, it is reasonable to move into its reference frame.

Parallel components to the quantisation axis do not couple, so we consider the case of an arbitrary RF-field in the orthogonal plane defined by:

$$\mathbf{B}_{\text{RF}}(t) = B_x \cos(\omega_{\text{RF}}t + \phi_x) \hat{e}_x + B_y \cos(\omega_{\text{RF}}t + \phi_y) \hat{e}_y \quad (3.12)$$

⁴For a comprehensive review of quantum angular momentum see [Walraven, 2017]

Now, we use:

$$\begin{aligned}\hat{\mathbf{e}}_+ &= -\frac{1}{\sqrt{2}}(\hat{\mathbf{e}}_x + i\hat{\mathbf{e}}_y) \\ \hat{\mathbf{e}}_- &= \frac{1}{\sqrt{2}}(\hat{\mathbf{e}}_x - i\hat{\mathbf{e}}_y)\end{aligned}\tag{3.13}$$

to write Eq. 3.12 in the circular basis:

$$\begin{aligned}\mathbf{B}_{RF}(t) &= \frac{1}{\sqrt{2}}(B_x \cos(\omega_{RF}t + \phi_x) + iB_y \sin(\omega_{RF}t + \phi_y))\hat{\mathbf{e}}_+ \\ &+ \frac{1}{\sqrt{2}}(B_x \cos(\omega_{RF}t + \phi_x) - iB_y \sin(\omega_{RF}t + \phi_y))\hat{\mathbf{e}}_-\end{aligned}\tag{3.14}$$

It is evident from this equation that these are the circular components $\hat{\mathbf{e}}_+$ and $\hat{\mathbf{e}}_-$ into the spin projections \hat{F}_+ and \hat{F}_- . Now, we can write the Hamiltonian associated to the time evolution of a state $|\psi(t)\rangle_{rot} = U_z^\dagger |\psi(t)\rangle$:

$$\hat{H} = U_z^\dagger (H_0 + H_{RF}) U_z - i\hbar U_z \delta_t U_z^\dagger\tag{3.15}$$

The following operator provides the rotation in the $\hat{\mathbf{e}}_z$ axis:

$$U_z(\omega_{RF}t) = \prod_F \exp\left(\frac{-g_F i\omega_{RF}t \hat{F}_z^F}{|g_F| \hbar}\right)\tag{3.16}$$

The static part then reads:

$$\begin{aligned}U_z^\dagger H_0 U_z - i\hbar U_z^\dagger \delta_t U_z &= \frac{5\hbar\omega_{\text{hfs}}}{4} P^2 + \left(g_2 \mu_B B_{\text{DC}} - \frac{g_2}{|g_2|} \hbar\omega_{\text{RF}}\right) \hat{F}_z^2 + \\ &- \frac{3\hbar\omega_{\text{hfs}}}{4} P^1 + \left(g_1 \mu_B B_{\text{DC}} - \frac{g_1}{|g_1|} \hbar\omega_{\text{RF}}\right) \hat{F}_z^1\end{aligned}\tag{3.17}$$

Let's now look explicitly the time-dependent term -using some of the angular momentum algebra listed in Appendix A. We assume that the RF-frequency is much smaller than the hyperfine splitting, therefore we can neglect all terms of the form $\langle 2, m_F | U_z^\dagger H_{RF} U_z | 1, m_F \rangle$ and $\langle 1, m_F | U_z^\dagger H_{RF} U_z | 2, m_F \rangle$. This operation results in a Hamiltonian of the form:

$$\hat{H} = \begin{pmatrix} \hat{H}_1 & 0 \\ 0 & \hat{H}_2 \end{pmatrix}\tag{3.18}$$

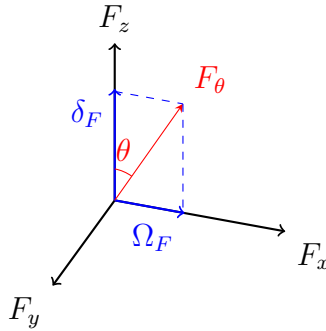
As an example, the sub-matrix for $F = 1$ after dropping the terms rotating at $2\omega_{\text{RF}}t$ (Rotating Wave approximation, from now on RWA) is:

$$\hat{H}_1 = \begin{pmatrix} \mu_B g_1 B_z - \hbar\omega_{\text{RF}} - \frac{3\hbar\omega_{\text{hfs}}}{4} A & \mathbf{B}_{\Phi,1} & 0 \\ \mathbf{B}_{\Phi,1}^* & \frac{3\hbar\omega_{\text{hfs}}}{4} A & \mathbf{B}_{\Phi,1} \\ 0 & \mathbf{B}_{\Phi,1}^* & -(\mu_B g_1 B_z - \hbar\omega_{\text{RF}} + \frac{3\hbar\omega_{\text{hfs}}}{4} A) \end{pmatrix} \quad (3.19)$$

where $\mathbf{B}_{\Phi,1} = g_1 \mu_B \sqrt{2}/4 (-B_x e^{i\phi_x} + i B_y e^{i\phi_y})$. From Eq. 3.19, one can find that the (non-zero) eigen-energies with an offset of $3/4A$ are $E_{\bar{m}} = \hbar \bar{m} \sqrt{\delta_1^2 + \Omega_1^2}$ where $\delta = \Omega_L - \omega_{\text{RF}}$ and $|\Omega_1| = \frac{|g_1 \mu_B|}{2\hbar} \sqrt{B_x^2 + B_y^2 + 2s B_x B_y \sin(\phi_x - \phi_y)}$ [Garraway and Perrin, 2015]. Note here that the sign of g_F sets the sense of rotation in U_z and, consequently, the circular component with non-zero coupling. In Fig 3.5 one can visualise the full coupled matrix in the bare basis. These operators contain terms in \hat{F}_z and \hat{F}_x that can be written as:

$$\hat{H}_1 = \delta \hat{F}_z + |\Omega_1| \hat{F}_x \quad (3.20)$$

Let's now apply a second rotation along \hat{F}_y to align the system into a new axis defined by $\hat{F}(\theta_F) = \hat{F}_z \cos \theta_F + \hat{F}_x \sin \theta_F$. From Eq. 3.20 we can retrieve the following relations:



$$\begin{aligned} \cos \theta_F &= \frac{\delta_F}{\Omega_{\text{eff}}} \\ \sin \theta_F &= \frac{\Omega_F}{\Omega_{\text{eff}}} \\ \tan \theta_F &= \frac{\Omega_F}{\delta_F} \end{aligned} \quad (3.21)$$

where $\Omega_{\text{eff}} = \sqrt{\delta_F^2 + \Omega_F^2}$ and $\delta_F = \Omega_{L,F} - \omega$ (here we make explicit the g_F dependence of the Larmor frequency $\Omega_{L,F}$, and the RF Rabi frequency Ω_F). We have used the notation θ_F to refer to the angle of rotation for each of the hyperfine manifolds. This angle can be written also as Sinuco-Leon *et al.*, 2019:

$$\theta_F = \frac{\pi}{2} - \tan^{-1} \left(\frac{B_{\text{DC}} - \hbar\omega_{\text{RF}} / (\mu_B |g_F|)}{\sqrt{2} B_{\text{RF}}} \right) \quad (3.22)$$

Given that $g_1 \neq g_2$, then g_F , and therefore $\delta_F = 0$ at different B_{DC} in each manifold.

As a consequence, to exactly diagonalise the system, distinct rotations should be applied at this stage to the two manifolds. The associated rotation operator is:

$$U_y(\theta_F) = \prod_F \exp\left(\frac{-g_F}{|g_F|} \theta_F \hat{F}_y^F\right) \quad (3.23)$$

After these two transformations the system's Hamiltonian is:

$$\begin{aligned} \bar{H} = U_y^\dagger(\theta_F) U_z^\dagger(\omega_{\text{RF}}t) H U_z(\omega_{\text{RF}}t) U_y(\theta_F) = \\ \sum_F \left[(\Omega_F \sin \theta_F - \delta_F \cos \theta_F) \hat{F}_z + \left(\delta_F \sin \theta_F - \frac{\Omega_F}{\sqrt{2}} \cos \theta_F \right) \hat{F}_x \right] \end{aligned} \quad (3.24)$$

One can see right away that this becomes a diagonal matrix when the RF-frequency is resonant with the static field, that is, when $\Omega_L = \omega_{\text{RF}}$ and $\delta = 0$. Note, however, that, as we mentioned just above, δ_F is state-dependent and therefore the eigen-system becomes a diagonal matrix for slightly different resonant conditions. This difference can be simply computed from $(|g_2| - |g_1|)\mu_B B_{\text{DC}}$. The dressed states -i.e. the eigen-states of the time-independent Hamiltonian in Eq. 3.24- can be obtained by applying the same transformations we used to reach Eq. 3.24 to the bare states. It is convenient to notice here that the operator in Eq. 3.23 is equivalent to an Euler rotation (unitary transformation) in the (F_z, F_x, F_y) orthogonal system and therefore one can use the Wigner summation formula with the $d_{m,m'}^j$ matrix elements.

$$\begin{aligned} |F, \bar{m}_F\rangle = U_y(\beta) U_z(\gamma) |F, m_F\rangle = R(0, \beta, \gamma) |F, m_F\rangle = \\ \sum_{m'} |F, m'\rangle \langle F, m'| R(0, \beta, \gamma) |F, m\rangle = \sum_{m'} D_{m',m}^F(0, \beta, \gamma) |F, m'\rangle \end{aligned} \quad (3.25)$$

where we use the definition [Biedenharn and Louck, 1981]:

$$R(\alpha, \beta, \gamma) = e^{-i\alpha \hat{F}_z} e^{-i\beta \hat{F}_y} e^{-i\gamma \hat{F}_z} \quad (3.26)$$

and

$$D_{m',m_F}^F(0, \beta, \gamma) = e^{-im_F\gamma} d_{m',m_F}^F(\beta) \quad (3.27)$$

where $d_{m_F m'}^F(\theta_F)$ is a Wigner d matrix representing the rotation:

$$d_{m',m_F}^F(\theta_F) = \langle F, m'| U_y(\theta_F) |F, m_F\rangle \quad (3.28)$$

where we make use of $\gamma = -i/s\omega_{\text{RF}}t$ and $\beta = \theta_F$. Therefore, the dressed states become time-dependent superpositions of the bare states $|F, m_F\rangle$ where the detuning

δ determines the relative weight of the components. Note that here we made use of the fact that the dimension of F and therefore of m_F and m remain invariant under any rotation on $\hat{F}_x, \hat{F}_y, \hat{F}_z$. Following this argument, let's re-label the dressed states definition following explicitly the correspondence $m' \longleftrightarrow \bar{m}_F$ and write the final result:

$$|F, \bar{m}_F\rangle = \sum_{m_F} e^{-ism_F\omega_{\text{RF}}t} d_{\bar{m}_F, m_F}^F(\theta_F) |F, m_F\rangle \quad (3.29)$$

where we use $s = g_F/|g_F|$ just like before.

3.2.1 Intra-manifold transitions between RF-dressed states

One method to measure the Radio-Frequency field amplitude consists in inducing intra-manifold transitions with a second (ideally weaker) RF-field (see Section 7.1). These transitions can also be used to evaporate and cool the atom cloud [Garrido Alzar *et al.*, 2006]. Now let's derive the transition probabilities for the cases of π, σ_+, σ_- polarisations of the impinging second RF-field. The intra-manifold Hamiltonian for spin $F=1$ reads:

$$H = \frac{\mu_B g_F}{\hbar} \mathbf{F} \cdot (\mathbf{B}_q(\mathbf{r}) + \mathbf{B}_1(t) + \mathbf{B}_2(t)) \quad (3.30)$$

We select $\mathbf{B}_1(t) = B_1 \cos(\omega_1 t) \hat{\mathbf{e}}_x$ as the RF-dressing field, and we assume for now that $\mathbf{B}_1(t) \gg \mathbf{B}_2(t)$. We ignore the spatial dependence of the Rabi frequency coupling with $B_q(\mathbf{r})$, and consider that $\mathbf{B}_q(\mathbf{r}) = B_{\text{DC}} \hat{\mathbf{e}}_z$. Now we choose a π -polarised $\mathbf{B}_2(t) = B_2 \cos(\omega_{ev} t) \hat{\mathbf{e}}_z$ with $\omega_{ev} \ll \omega_{\text{hfs}}$. We proceed by calculating the time-evolution in the rotating frame at ω_1 and then applying the rotation in \hat{F}_y from Eq. 3.23. The resulting Hamiltonian after these transformations is:

$$H_\pi = \left[\cos(\theta) (\delta - \Omega_\pi \cos(\omega_{ev} t)) + \frac{1}{2} \Omega \sin(\theta) \right] \hat{F}_z + \left[\Omega \cos(\theta) + 2(\delta + \Omega_\pi \cos(\omega_{ev} t)) \sin(\theta) \right] \hat{F}_x \quad (3.31)$$

We can follow the same method to find the Hamiltonian for a sigma-polarised rf, that we write as $\mathbf{B}_3(t) = B_3 \cos(\omega_{ev} t) \hat{\mathbf{e}}_y$, which contains both σ_\pm components. In

this case we find:

$$\begin{aligned}
H_\sigma = & \left[\cos(\theta)\delta - \frac{1}{2}(\Omega - \Omega_\sigma \sin(\Delta t)) \sin(\theta) \right] \hat{F}_z + \\
& + [\cos(\theta)(\Omega_\sigma \sin(\Delta t) - \Omega) + 2\delta \sin(\theta)] \hat{F}_x + \\
& \Omega_\sigma \cos(\Delta t) \hat{F}_y
\end{aligned} \tag{3.32}$$

The diagonal terms in H_σ and H_π are suggestive of a modulation of the energy levels induced by, in one case, $\Delta = \omega - \omega_{ev}$ and, in the other case, Ω . These modulations occur at two energy regimes that are significantly apart, and thus it is reasonable to study the temporal evolution of each system separately, in particular, by calculating the time-independent Hamiltonians after the application of separate rotations of $U_z(\Omega t)$ for H_π , and of $U_z(\epsilon\Delta_{ev} t)$ for H_σ . After performing the RWA (just like in the previous section) we find that:

$$\begin{aligned}
H_\pi^{\text{RWA}} &= [\omega_{ev} + \Omega_{\theta,\pi}] \hat{F}_z + \Omega_\pi \sin(\theta) \\
H_{\sigma_+}^{\text{RWA}} &= [\Delta + \Omega_{\theta,\sigma}] \hat{F}_z + \frac{\Omega_\sigma}{2}(1 + \cos(\theta)) \hat{F}_y \\
H_{\sigma_-}^{\text{RWA}} &= [\Delta + \Omega_{\theta,\sigma}] \hat{F}_z + \frac{\Omega_\sigma}{2}(\cos(\theta) - 1) \hat{F}_y
\end{aligned} \tag{3.33}$$

where we have defined:

$$\begin{aligned}
\Omega_{\theta,\sigma} &= \delta \cos(\theta) + \frac{1}{2}\Omega \sin(\theta) \\
\Omega_{\theta,\pi} &= \delta \cos(\theta) - \frac{1}{2}\Omega \sin(\theta)
\end{aligned} \tag{3.34}$$

H_π^{RWA} is thus the time-independent Hamiltonian in the RWA in a frame that rotates at Ω and the Hamiltonians labelled with σ_+, σ_- are time-independent in frames that rotate at $\pm\Delta$. Now we can find the eigen-energies for the three cases, which are to be compared with the known result for the dressed states, that we quote for completeness:

$$\begin{aligned}
E_{\bar{m}}(\omega) &= \hbar\epsilon_{\bar{m}} \sqrt{\delta^2 + \Omega^2} \\
E_{\bar{m}}(\omega, \omega_{ev}, \pi) &= \hbar\epsilon_{\bar{m}} \sqrt{(\omega_{ev} - \Omega_{\theta,\pi})^2 + (\Omega_\pi \sin(\theta))^2} \\
E_{\bar{m}}(\omega, \omega_{ev}, \sigma_+) &= \hbar\epsilon_{\bar{m}} \sqrt{(\Delta - \Omega_{\theta,\sigma})^2 + \Omega_\sigma^2(1 - \cos(\theta))^2} \\
E_{\bar{m}}(\omega, \omega_{ev}, \sigma_-) &= \hbar\epsilon_{\bar{m}} \sqrt{(\Delta - \Omega_{\theta,\sigma})^2 + \Omega_\sigma^2(\cos(\theta) - 1)^2}
\end{aligned} \tag{3.35}$$

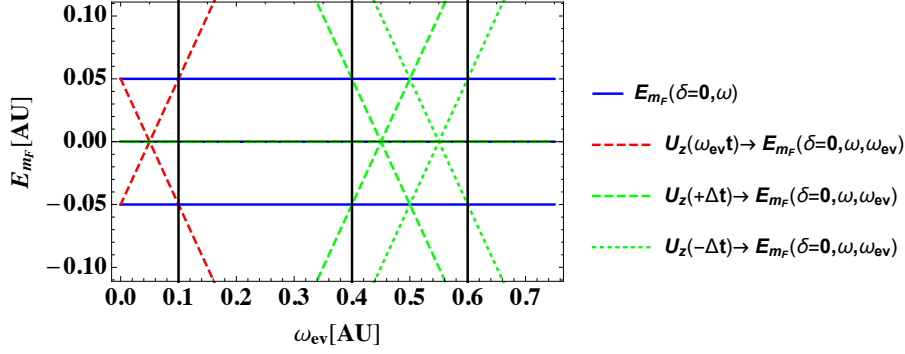


Figure 3.3: Eigen-energies of the dressed F=1 Zeeman substates in the case of only one dressing field and in the case where a second, weaker, RF-field is included. This second RF-field is considered with π , σ_+ and σ_- polarisations, and with a frequency ω_{ev} . The blue lines show the dressed states originated from the first dressing field. As one scans the frequency of the second RF, these lines are unperturbed. In red (green) we show the modified eigen-energies when a second RF with π (sigma plus and minus) polarisation is included and its frequency is scanned. Vertical black lines indicate the relevant crossing points at Ω (related to pi transitions) and $\omega \pm \Omega$ (related to sigma transitions).

where $\epsilon_{-1} = 1$, $\epsilon_0 = 0$ and $\epsilon_1 = -1$. Transitions are induced where the eigen-energies in Eq. 3.35 cross with the eigen-energies of the dressed states corresponding to ω , quoted above as $E_{\bar{m}}(\omega)$. Fig. 3.3 shows these energies. The blue lines depict the energy of the F=1 dressed manifold on resonance, i.e., when $\delta = 0$. We also draw the eigen-energies of the three cases calculated above (for a π , σ_+ , σ_- impinging second, weak RF) as a function of ω_{ev} . It is clear that if this field is weak (this is the approximation we made) the blue lines are unperturbed. However, in the new rotating frames related to Ω and $\epsilon\Delta_{ev}$, energies are shifted. The crossing points as ω_{ev} is scanned correspond to degeneracies where spins can be flipped⁵. The transition probabilities can be found through Eq. 3.33. This result holds also when the second RF-field has a large amplitude. However, in this case one needs to take into account a perturbation of the diagonal term mediated by non-negligible contributions that stem from the effects beyond the RWA. The result is a periodical modulation of the energy levels that typically results in multi-photon spectra where a modulation parameter, in this case $\xi = \Omega_{\pi,\sigma}/\Delta$. Now, we will outline the derivation, from a conveniently simple Hamiltonian, of the typical spectrum in a two-level system without applying

⁵Notice that when $\omega_{ev} = \omega$ both the dashed and the dotted green lines cross with the blue lines. These do not induce transitions, since this crossing corresponds physically to $\Delta m = 0$.

the RWA:

$$H = -\Omega_\theta \hat{F}_z + \Omega_{ev} (e^{-it\Delta} + \text{c.c.}) \hat{F}_x \quad (3.36)$$

where Ω_θ is the effective energy in the dressed basis after applying the RWA in the ω time-evolved Hamiltonian and $\Delta = \omega - \omega_{ev}$. Let's apply a transformation that translates the system into a rotating frame that accounts for the accumulated phase over an oscillation period $U_\phi(t) = e^{-i\phi(t)}$:

$$\phi(t) = \int_0^{2\pi} \Omega_{ev} \cos(\Delta t) dt = \frac{\Omega_{ev}}{\Delta} \sin(\Delta t) \quad (3.37)$$

in the rotating frame we find that:

$$H_\phi = (-\Omega_\theta - \Omega_{ev} \cos(\Delta t)) \hat{F}_z + \Omega_{ev} \left(e^{-\left(it\Omega_{ev} + \frac{\Omega_{ev}}{\Delta} \sin(t\Delta)\right)} + \text{c.c.} \right) \hat{F}_x \quad (3.38)$$

Now one can use that:

$$e^{-\left(it\Omega_{ev} + \frac{\Omega_{ev}}{\Delta} \sin(t\Delta)\right)} = \sum_n e^{-in\Delta t} J_n(\Omega_{ev}/\Delta) \quad (3.39)$$

where $J_n(\Omega_{ev}/\Delta)$ are Bessel functions of the first kind. After discarding the time dependent terms we can find a spectrum where the n th photon transitions have weights given by $J_n(\Omega_{ev}/\Delta)$ (see [Perrin and Garraway, 2017] for a detailed analysis).

3.3 Hyperfine theory of Radio-frequency dressed atoms in the presence of a microwave field $B_{\text{DC}} + B_{\text{RF}} + B_{\text{MW}}$

Now that we have solved the problem of an atom in the presence of a homogeneous field and an arbitrarily polarised radio-frequency field, let's look back at Eq. 3.11 and introduce one more term in the time-dependent magnetic field:

$$\mathbf{B}(t) = \mathbf{B}_{\text{RF}}(t) + \mathbf{B}_{\text{MW}}(t) \quad (3.40)$$

The radio-frequency magnetic field $\mathbf{B}_{\text{RF}}(t)$, as we established earlier, is near-resonant with the hyperfine sub-levels splitting at moderate homogeneous fields ($B_{\text{DC}} \ll 10 \text{ G}$). Now, the microwave frequency is of the order of the hyperfine splitting $\omega_{\text{hfs}}/2\pi$ and therefore we only consider the coupling between the two hyperfine subspaces, and

not within them. As a consequence, we can begin this derivation from the result in Eq. 3.24. For simplicity, we will further assume that the RF-frequency is resonant with the sub-levels splitting, i.e. $\delta = 0$. We make this assumption to derive the spectral profile of the two-frequency driven system in the simplest possible case, which is a good reference to compare non-linear effects, out of resonance behaviour or physics beyond the RWA. Having established our framework, we can now proceed by writing the microwave part of H_{MW} in the dressed-states basis. To do that, we apply the same rotations as before (Eqs. 3.16,3.23) in the same order:

$$H_{\text{MW}}^{\text{D}} = U_y^\dagger(\theta_F) U_R(\omega_{\text{RF}}t)^\dagger H_{\text{MW}} U_R(\omega_{\text{RF}}t) U_y(\theta_F) \quad (3.41)$$

To write H_{MW} and to calculate the action of \mathbf{J} onto $|F, m_F\rangle$, we will use that $g_J \gg g_I$ and the fact that, for frequencies close to the hyperfine splitting, only changes in the precession of F can follow adiabatically the magnetic field. Firstly, we need to write the states $|F, m_F\rangle$ (coupled basis) in terms of the states $|I, m_I, J, m_J\rangle$ (uncoupled basis) to elucidate the action of \mathbf{J} . We already did this in Eq. 3.9. Fig. 3.4 illustrates the result of the rotations in Eq. 3.41. It shows the transition matrix elements in a schematic arrayplot for the a MW-field orthogonal both to the RF and static fields, for two cases. Fig. 3.4(a) depicts H_{MW} in the bare basis and Fig. 3.4(b) shows \hat{H}_{MW} in the dressed basis. It is apparently clear that, in the dressed basis, transitions further from $\Delta\bar{m}_F = -1, 0, 1$ emerge. We now find the transition frequencies and transition matrix elements in several examples for the initial state $|1, -1\rangle$. We will not solve the problem generally, since that is shown in [Sinuco-Leon *et al.*, 2019]. In any case, let's have a look at several important examples and find the spectral response. As we have seen above, the dressed states at the resonant condition form a diagonal matrix in the dressed basis. The microwave interaction Hamiltonian includes oscillating terms at frequencies of the order of the hyperfine splitting, and therefore does not couple the m_F (or, for that matter, the \bar{m}_F levels), hence they are neglected.

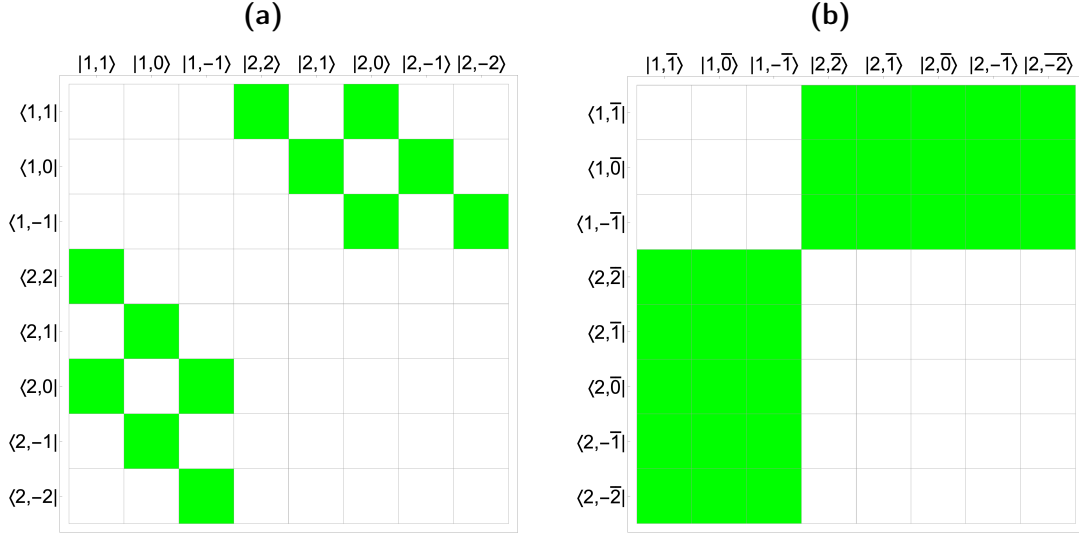


Figure 3.4: (a) Matrix array plot showing the non-zero matrix elements of H_{MW} for a linearly polarised mw-field orthogonal to a DC field in the Zeeman basis and (b) potentially non-zero matrix elements for \hat{H}_{MW} in the dressed basis. One can see already from (b) that seven groups of transitions appear. These are illustrated by the filled diagonals in each of the coloured areas.

3.3.1 Example case: $B_{\text{MW}} \perp B_{\text{RF}} \perp B_{\text{DC}}$

In this case, the fields are:

$$\begin{aligned}
 B_{\text{DC}} &= (0, 0, B_z) \\
 B_{\text{RF}} &= (B_{\text{RF},x} \cos(\omega_{\text{RF}}t), 0, 0) \\
 B_{\text{MW}} &= (0, B_{\text{MW}} \cos(\omega_{\text{MW}}t), 0)
 \end{aligned} \tag{3.42}$$

By following the procedure detailed above, one can calculate the matrix elements as $T_{\bar{m}_F, -1} = \langle F, \bar{m}_F | H_{\text{MW}}^D | 1, -1 \rangle$. This calculation results in complicated expressions with terms oscillating at multiples of Ω_{RF} and ω_{RF} . Therefore, and since here we are only interested in a broad description of the spectral features, let's calculate the Fourier transform of such elements, which will result in the weighted frequency domain response of the two hyperfine sub-matrices coupling. In this case we find two symmetric groups of five transitions at:

To	Transition Frequency	Transition Matrix Element
$ 2, -2\rangle$	$\omega_{\text{hfs}} \pm 3\omega_{\text{RF}} - 3\Omega_{\text{RF}}$	$\frac{1}{8}\sqrt{\frac{3}{2}}$
$ 2, -1\rangle$	$\omega_{\text{hfs}} \pm 3\omega_{\text{RF}} - 2\Omega_{\text{RF}}$	$\frac{1}{4}\sqrt{\frac{3}{2}}$
$ 2, 0\rangle$	$\omega_{\text{hfs}} \pm 3\omega_{\text{RF}} - \Omega_{\text{RF}}$	$3/8$
$ 2, 1\rangle$	$\omega_{\text{hfs}} \pm 3\omega_{\text{RF}}$	$\frac{1}{4}\sqrt{\frac{3}{2}}$
$ 2, 2\rangle$	$\omega_{\text{hfs}} \pm 3\omega_{\text{RF}} + \Omega_{\text{RF}}$	$\frac{1}{8}\sqrt{\frac{3}{2}}$

and two more symmetric groups of five transitions at:

To	Transition Frequency	Transition Matrix Element
$ 2, -2\rangle$	$\omega_{\text{hfs}} \pm \omega_{\text{RF}} - 3\Omega_{\text{RF}}$	$\frac{3}{8}\sqrt{\frac{3}{2}}$
$ 2, -1\rangle$	$\omega_{\text{hfs}} \pm \omega_{\text{RF}} - 2\Omega_{\text{RF}}$	$\frac{1}{4}\sqrt{\frac{3}{2}}$
$ 2, 0\rangle$	$\omega_{\text{hfs}} \pm \omega_{\text{RF}} - \Omega_{\text{RF}}$	$1/8$
$ 2, 1\rangle$	$\omega_{\text{hfs}} \pm \omega_{\text{RF}}$	$\frac{1}{4}\sqrt{\frac{3}{2}}$
$ 2, 2\rangle$	$\omega_{\text{hfs}} \pm \omega_{\text{RF}} + \Omega_{\text{RF}}$	$\frac{1}{8}\sqrt{\frac{3}{2}}$

These transitions are plotted in Fig. 3.6 a). Fig. 3.5 shows schematically the process we followed to calculate the transition matrix elements with Matrix Arrays that show the non-zero matrix elements in the full 8x8 system for three relevant cases. The first case is for atoms coupled by a static magnetic field plus an RF-field: here we see that the RF-coupling is intra-manifold. The second case in this figure shows the diagonal matrix of the dressed states eigen-energies on resonance $\delta_F = 0$. The third case depicts how each state of each of the two manifolds is coupled to any state of the other hyperfine manifold once a MW-field is included in the dressed basis according to Eq. 3.41. As it was mentioned above, these transitions occur at different combinations of ω_{RF} and Ω_{RF} .

3.3.2 Other examples

Fig. 3.6 shows three more cases. In b):

$$\begin{aligned}
 B_{\text{DC}} &= (0, 0, B_z) \\
 B_{\text{RF}} &= (B_{\text{RF},x} \cos(\omega_{\text{RF}}t), 0, 0) \\
 B_{\text{MW}} &= (0, 0, B_{\text{MW}} \cos(\omega_{\text{MW}}t))
 \end{aligned} \tag{3.43}$$

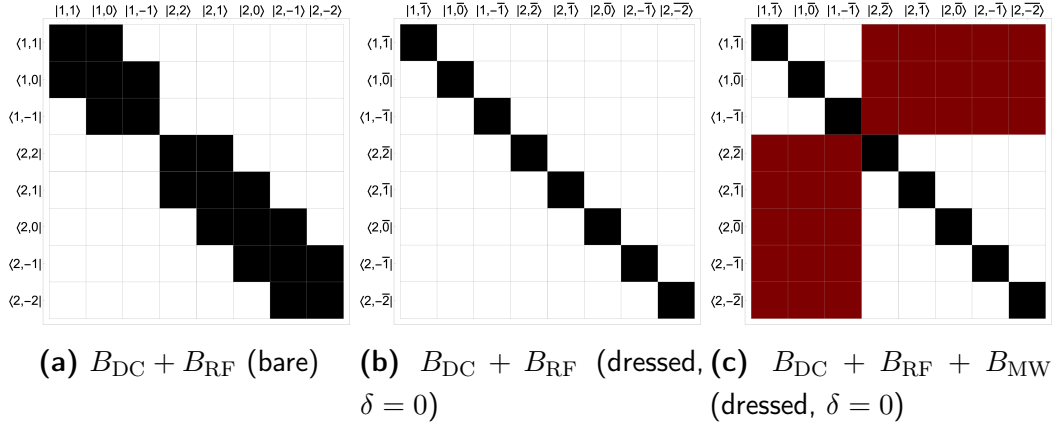


Figure 3.5: Matrix Array Plots for three cases: bare states in the presence of a static plus RF magnetic fields, dressed states on resonance and, finally, dressed states on resonance in the presence of a MW-field (in the same dressed basis). Black represents non-zero matrix elements. Red represents potentially non-zero transition matrix elements for RF-dressed atoms in the presence of a microwave field. These TME are time-dependent. An additional RWA is needed at each of the oscillation frequencies. We find these elements by calculating the Fourier components associated to each possible transition.

And Fig. 3.6 c) and d) show the spectrum for a σ_+ and σ_- mw polarisation respectively:

$$\begin{aligned}
 B_{\text{DC}} &= (0, 0, B_z) \\
 B_{\text{RF}} &= (B_{\text{RF},x} \cos(\omega_{\text{RF}}t), 0, 0) \\
 B_{\text{MW}} &= (B_{\text{MW}} \cos(\omega_{\text{MW}}t), \pm B_{\text{MW}} \sin(\omega_{\text{MW}}t), 0)
 \end{aligned} \tag{3.44}$$

The MW transitions between RF-dressed states present a spectrum of 7 groups (spaced by the RF-dressing frequency) of 5 transitions (spaced by the RF-dressing Rabi frequency). These transition frequencies are given by the condition: $\omega_{\text{MW}} + n\omega_{\text{RF}} = \omega_{\text{hyperfine}} + m_1\Omega_1 + m_2\Omega_2$, with $n = -3\dots0\dots3$ and $m = -3\dots0\dots1$. Here, Ω_1 and Ω_2 are the circular projections of the RF-field into the quantization axis. To be clear: a linearly polarised RF-field orthogonal to the quantisation axis and of total Rabi frequency Ω_l has two circularly polarised components of opposite handedness Ω_+ and Ω_- , each of which couples atoms from only one manifold. Noticeably, on resonance ($\delta = 0$), the transition strength does not depend on the RF-field polarisation. Even more importantly (again, on resonance $\delta = 0$): the Rabi frequency of the RF-field does not play any role in the transition driving, being only the MW-field Rabi frequency the responsible for any two-level system coupling. If the fields are not

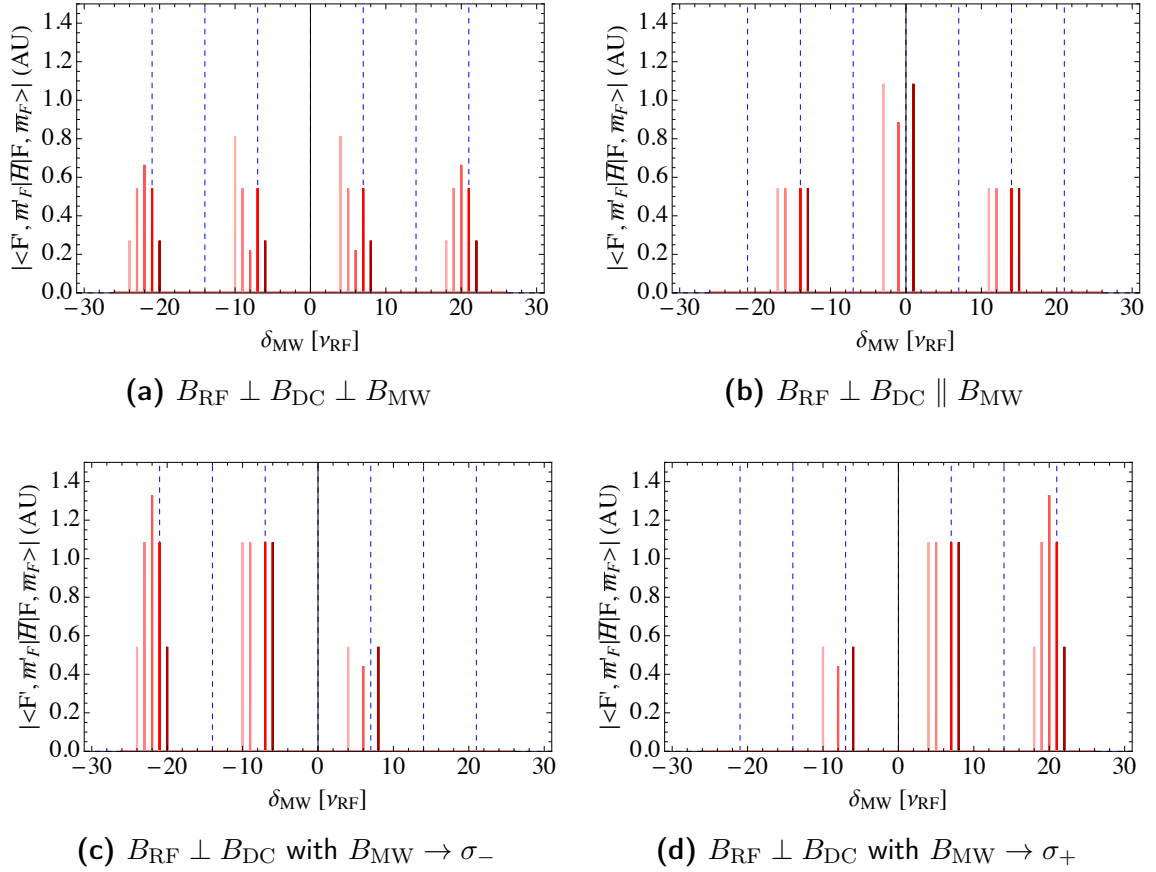


Figure 3.6: Expected spectrum of MW transitions between RF-dressed states for the four main configurations of magnetic fields. a) $B_{\text{RF}} \perp B_{\text{DC}} \perp B_{\text{MW}}$ b) $B_{\text{RF}} \perp B_{\text{DC}} \parallel B_{\text{MW}}$ c) $B_{\text{RF}} \perp B_{\text{DC}}$ with $B_{\text{MW}} \rightarrow \sigma_-$ d) $B_{\text{RF}} \perp B_{\text{DC}}$ with $B_{\text{MW}} \rightarrow \sigma_+$. In this figure, different colours indicate different final states. These colours are shadows of red. The darkest red corresponds to the final state with $m_F = 2$, the lightest red to the final state with $m_F = -2$ and so on.

perfectly aligned along the $(\hat{F}_x, \hat{F}_y, \hat{F}_z)$ axes or transitions are not driven on resonance this is modified, but the general features remain. Moreover, if the RF Rabi frequency is large (and especially if it reaches the magnitude of ω_{RF}) then off-resonant terms (such as the counter-rotating circularly polarised terms) cannot be neglected and therefore the energy levels experience Bloch-Siegert shifts. These shifts are better described by a modification of the g_F factor [Haroche *et al.*, 1970]. In this case:

$$g'_F = g_F J_0 \left(\frac{\Omega_F}{\omega_F} \right) \quad (3.45)$$

where J_0 is a Bessel function of 0th order [Haroche *et al.*, 1970]. Note that, at the zeroes of this Bessel function the RF-field cancels the magnetic moment and atoms are *de-magnetised*. These RF-induced Bloch-Siegert shifts can be used to match the g_F gyromagnetic factors for different spin states [Zanon-Willette *et al.*, 2012] or even different isotopes [Haroche and Cohen-Tannoudji, 1970]. We can find an approximate condition for the two ground hyperfine manifolds of ^{87}Rb by using that:

$$g'_F = g_F \sum_k^{\infty} (-1)^k \frac{\left(\frac{1}{4}\xi_F^2\right)^k}{(k!)^2} \approx g_F \left(1 - \left(\frac{\xi_F}{2}\right)^2 \right) \quad (3.46)$$

where we have introduced $\xi_F = g_F \mu_B B_{\text{RF}} / \hbar \omega_{\text{RF}}$. By equating $g'_2 = g'_1$ we can find the condition:

$$\frac{\mu_B B_{\text{RF}}}{\hbar \omega_{\text{RF}}} = \frac{\sqrt{|g_1| - |g_2|}}{\sqrt{|g_1|^3 - |g_2|^3}} = 2.3 \quad (3.47)$$

being the first zero calculated numerically 2.507, and the second 8.145. One can see here that the RF-field amplitude is much larger than in conventional adiabatic traps, where usually $\mu_B B_{\text{RF}} < \hbar \omega_{\text{RF}}$. In fact, such high RF-field amplitudes are rather inconvenient in shell traps, as we will see in Section 4.1.2, given the existence of an anti-trapped solution of the potential. The modification of g_F via RF-dressing was used to demonstrate the Hanle effect [Cohen-Tannoudji and Haroche, 1969a; Kastler, 1973]. Current systems for non-destructive imaging of cold clouds of ^{87}Rb are suitable for the detection of the Hanle effect produced in [Cohen-Tannoudji and Haroche, 1969a]. In [Lakshmi and Agarwal, 1985] it is shown that several tuneable parameters of a Hanle resonant system can lead to the production of squeezed light [Loudon and Knight, 1987], which in principle should make RF-dressed states a very convenient choice to observe this phenomenon.

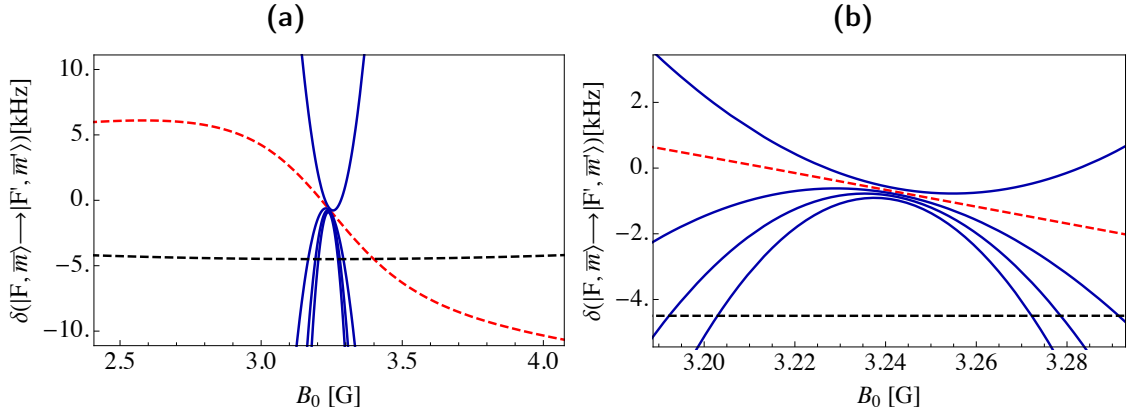


Figure 3.7: (a) Energy shift in a broad range of B_{DC} . The red-dashed line corresponds to the transition of interest between the dressed states $|1, -1\rangle \rightarrow |2, 1\rangle$. The RF-field is chosen to be resonant close to the magic field. The black-dashed line corresponds to the same energy shift yet with the bare states of ^{87}Rb . Blue lines correspond to all other possible transitions from $|1, -1\rangle$ to the rest of sub-levels in $F=2$. (b) Energy shift in a narrow range of B_{DC} . The color code is the same as in a). One can see how at resonance all lines cross (compensating for the Rabi frequency difference), which makes all transitions potentially insensitive to DC-field fluctuations in a narrow range of B_{DC} .

3.4 Protected transitions

Close to the resonance point $\delta = 0$, all differential energies between $|1, -1\rangle$ present the maximum/minimum of a parabolic shape when changing the DC field B_{DC} (except for the transition to $|2, 1\rangle$), which is a clear signature of a field fluctuations insensitive behaviour in the vicinity of such point. Moreover, we have seen that it is possible to drive in principle all transitions from any one state to the other hyperfine subspace. Therefore, ideally, microwave transitions become much narrower at $\delta_F \approx 0$, when the radio-frequency field is properly tuned. As we will show later, this result holds in the linear regime and within the RWA. Moreover, at larger radio-frequency Rabi frequencies, these parabolic line shapes present slightly different shapes that can limit the line-width of the MW transitions. Let's find numerically, still in the RWA, the eigen-energies from Eq. 3.11 in the presence of an RF-field orthogonal to the quantization axis. These energies can now be shifted both by B_{DC} and B_{RF} . The modification of the eigen-energies provokes that the magic field that we showed in Fig. 3.1 changes for large enough RF-fields [Kazakov and Schumm, 2015], which is generally the case in this thesis, since we are interested in RF-dressed states.

Fig. 3.7 shows the energy difference between all the possible TLS in the RF-

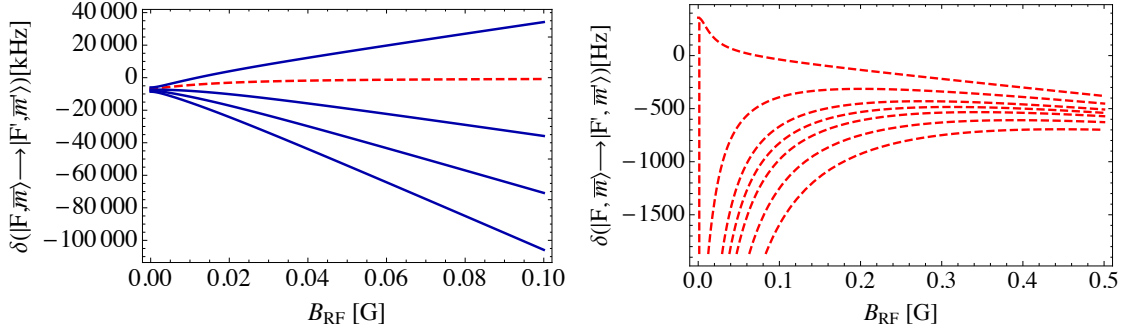


Figure 3.8: Differential energy shifts with B_{RF} between $|1, -1\rangle$ and the $F=2$ dressed hyperfine sub-levels (a) In red-dashed, the transition of interest. The blue lines correspond to the other 4 possible transitions between the dressed $|1, -1\rangle$ and the $F=2$ manifold sub-levels (b) Energy shift of the transition of interest for different detuning of B_{DC} with respect to the resonance with ω

dressed picture: the dashed red curve indicates the energy difference between the dressed *clock* transition states $|1, -1\rangle, |2, 1\rangle$. The blue curves show the rest of energy shifts. Notice that all curves are rearranged by compensating for the RF Rabi frequency Ω_0 . In black we plot the bare transition energy difference between the two clock states, also as B_{DC} is scanned. In the zoomed version in Fig. 3.7 (b) we show how close to the resonance point all energy differences find a turning point, where all transitions become minimally sensitive to fluctuations in B_{DC} . These transitions are therefore DC-field-protected. Notice that in the case of bare states the difference in g_F leads to the minimum of the parabola at 3.22 G, but in the case of (resonantly coupled) dressed states at the magic field it leads to a comparatively steep energy gradient.

Fig. 3.8a shows the same set of energy differences, now with a fixed B_{DC} at the resonance with ω_{RF} , as the RF-field amplitude is scanned. We can see that the transition of interest is the one that presents the smallest differential shift as the RF-amplitude increases. Fig. 3.8 (b) shows the differential energy shift as B_{RF} is scanned for several values of δ . Neglecting the non-physical solution of *very small* amplitudes of RF-field, we can see how all curves tend to converge. This result in turn becomes meaningless for very large fields, since then one needs to include effects beyond the RWA. We can see, in any case, that there is a flatter region where the transitions are less sensitive to fluctuations in B_{RF} .

3.4.1 Bi-chromatic protected transitions

We have just seen that the line-shifts associated to transitions between RF-dressed states present displaced absolute extrema. We now propose to use a bi-chromatic RF-field so as to compensate for this mismatch, and thus find the point in parameter space where all (or some) transitions have a maximum/minimum in their line-shift. The reason why the parabolic line-shifts are displaced is the difference in g_F factor. In fact, the resonant condition of the RF-field with the DC-field becomes different for this reason. To match the resonant points one can employ a bi-chromatic RF-field that contains two circularly polarised components of opposite handedness. Each of these components couples atoms from either hyperfine manifold. Therefore, one has access to the selective manipulation of spin states from each manifold with RF-fields that differ in amplitude and frequency. We can then write each of the subspace's eigen-energies:

$$\begin{aligned}\hbar\Omega_{1,\bar{m}} &= s\bar{m}\hbar\sqrt{(\Omega_{L,1} - \omega_1)^2 + \Omega_1^2} \\ \hbar\Omega_{2,\bar{m}} &= s\bar{m}\hbar\sqrt{(\Omega_{L,2} - \omega_2)^2 + \Omega_2^2}\end{aligned}\tag{3.48}$$

where $\Omega_{L,1} = |g_1\mu_B B_{DC}|$ and $\Omega_{L,2} = |g_2\mu_B B_{DC}|$ and $s = g_F/|g_F|$. If we now expand these expressions for small detunings, that is, small $\delta_F = \hbar\omega_0 - \hbar\omega_F$ -likewise for δ_{F+1-} , we can find the first derivative with respect to B_{DC} for the selected three states. The matching conditions are:

$$\begin{aligned}B_{DC} &= \frac{\hbar\omega_2}{\mu_B g_2} \\ \omega_1 &= \frac{g_1}{g_2}\omega_2\end{aligned}\tag{3.49}$$

Fig. 3.9 (a) shows four line-shifts where the the fields configuration fulfils the criteria in Eq. 3.49. Fig. 3.9 (b) shows the first derivative of these line-shifts. We promptly see all the lines crossing zero at the same point. Our result is similar to that obtained by continuous dynamical decoupling, which in the work of Stark et al. (see [Stark *et al.*, 2018]) also involves a 3-level system. In this configuration, there are 15 inter-manifold DC-field protected transitions (that couple each of the states from each manifold to all the states from the other manifold).

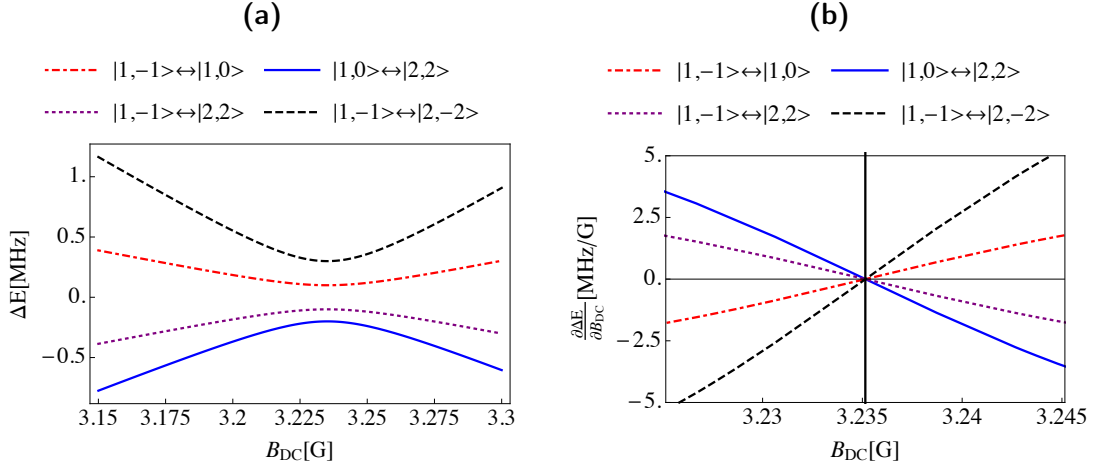


Figure 3.9: (a) Line shift for the transition between the dressed states $|1, -1\rangle \rightarrow |1, 0\rangle$ (red, dot/dashed), $|1, 0\rangle \rightarrow |2, 2\rangle$ (blue), $|1, -1\rangle \rightarrow |2, 2\rangle$ (purple, dotted) and $|1, -1\rangle \rightarrow |2, -2\rangle$. (b) Derivative $\partial\Delta E/\partial B_{DC}$. The colour code is the same as in a). A horizontal grey line shows where $\partial\Delta E/\partial B_{DC}$ is zero. We observe all line-shifts crossing exactly at the same B_{DC} , where they simultaneously fulfil that $\partial\Delta E/\partial B_{DC} = 0$.

3.5 Summary and concluding remarks

Radio-frequency dressing is a mathematical construction used to treat the interaction between the atomic spin and an AC field on top of a DC field. Atomic spins, as represented semi-classically, tend to align with a quantization axis, and to precess around it. There exist only a well defined number of precession amplitudes, which are integer multiples of the same unit amplitude (i.e. they are quantised). These integer multiples are given by *quantum numbers*. The unit amplitude is proportional to the g-factors associated to a variety of angular momentum operators, and to the Bohr magneton. In Eq. 3.1, we defined what I just called “precession amplitude” as a magnetic angular moment. Now, this magnetic angular moment changes together with the magnetic field. This results in different measurements of the energy associated to the different spin states (that we labelled with quantum numbers) as the magnetic field changes. In some regimes of the magnetic field amplitude, these energy levels cross, or evolve in such a way that a particular set of quantum numbers lose meaning, and we need to re-label -if possible- the spin states to make sense of the physics (one good example is that of the Zeeman lines for strong DC magnetic fields and the use of the coupled and uncoupled basis). However, what happens when one includes an AC field on top of the DC field? More concretely, an AC field whose amplitude oscillates in a range where the quantum numbers hold. We saw that one

can approximate the time-dependent hamiltonian by a time-independent one after using the RWA. This approximation leads one to define a new set of states, which are combinations of the ones that describe the atomic spin behaviour under the DC field. These new sets of states are called the dressed states, and they describe the atomic spin coupling with the RF photons. In fact, they contain a quantised number of RF photons. RF-dressing is a characteristically resonant phenomenon. If we pay attention to the behaviour of the eigen-energies of the dressed states we can see that they reach closest to degeneracy (an analogous situation to the magnetic field zero of the Zeeman lines) when $\hbar\omega_{\text{RF}} \approx g_F\mu_B B$. Degeneracy would mean that the magnetic moments are aligned; in the case of strong-enough RF-dressing the Rabi frequency of the RF-field prevents it from happening. However, for small-enough RF-dressing Rabi frequencies, atom spin flips occur, precisely because energy levels become degenerate at $\hbar\omega_{\text{RF}} \approx g_F\mu_B B$. These two limiting cases of the Landau-Zenner crossing lead, in first case, to the coherent superpositions that we call RF-dressed states and, in the second case, to radio-frequency evaporation. In this chapter, we studied transitions between dressed states considering two cases. In the first case, we looked at transitions within each of the hyperfine manifolds. These transitions can be driven with a weak, second RF. In the second case, we studied transitions between states in the two ground hyperfine manifolds of ^{87}Rb . These transitions are driven with a weak MW field, that is added to the *stronger* dressing RF-field. The following chapter explains how to use RF-dressing to create trapping potentials for ultra-cold atoms. Furthermore, Chapter 7 treats experimentally atomic transitions in the RF-dressed regime together with some aspects of RF-dressed potentials.

4

Radio-Frequency Dressed Potentials

This chapter contains three main sections, that develop the theoretical aspects of the three RF-dressed potentials that are presented experimentally in later sections. Firstly, we give an introduction to the adiabatic shell trap (Section 4.1). Then, we propose the bi-chromatic shell trap (Section 4.2) to overcome the traps mismatch between different magnetic Zeeman sub-levels. Finally, we give a short review of Time Averaged Adiabatic Potentials (TAAP), with special focus on the ring trap (Section 4.3).

4.1 The adiabatic Shell trap

The spatial dependence of the RF-coupling in inhomogeneous magnetic fields can be used to trap atoms, much in the same way as in an optical trap, where the spatially dependent Stark shift creates the adequate potential landscape for a localised minimum. This very definition entails a number of drawbacks for some applications that we set forth in the following pages, notably for trapped atom-clock interferometry. Nonetheless, it offers powerful tools for state-dependent trapping [Hofferberth *et al.*, 2006; Lesanovsky *et al.*, 2006b], and also for guiding [Navez *et al.*, 2016] ultra-cold thermal clouds and BECs, as we indicate in Section 6.2. The adiabatic shell trap was proposed in [Zobay and Garraway, 2001], and, since then, there have been many experiments that employ RF-dressed traps [Berrada *et al.*, 2013; Merloti *et al.*, 2013; Morizot *et al.*, 2007; Bentine *et al.*, 2017]. Its many applications range from the formation of adiabatic bubbles¹ to, as we suggest later, atom interferometry. In [Bolpasi *et al.*, 2014], the shell trap allowed to break the record for the brightest atom laser to date. In this experiment, they gravitationally

¹See N. Lundblad proposal in <https://coldatomlab.jpl.nasa.gov/scienceresearcher/>

out-coupled a BEC by shining a strong RF-field that modified the trapping potential into a magnetic cliff from where atoms would coherently fall. In contrast to this case, gravity normally plays the antagonist role in most experiments as the gravitational sag, which we shall deal with in Section 7.5.4. In this chapter we first derive the spatially dependent coupling of a radio frequency field in a quadrupole magnetic field (Section 4.1.1), then we derive the trapping frequencies including the effect of gravity, and also the trap equilibrium point (Section 4.1.2). Therein we will come to realise that the shell trap is rather inconvenient for atom clock applications since the two spin states involved have significantly dissimilar traps due to the different $|g_F|$. Later, we propose a novel bi-chromatic state-dependent adiabatic potential that brings down the traps mismatch (Section 4.2).

4.1.1 RF coupling in the quadrupole

The key to understanding the RF-dressed shell trap is the spatially inhomogeneous coupling of the RF-field when atoms are trapped in a quadrupole magnetic trap. A quadrupole field with the *fast* axis in gravity's direction can be written as:

$$B_q(\mathbf{r}) = \alpha x \hat{\mathbf{e}}_x + \alpha y \hat{\mathbf{e}}_y - 2\alpha z \hat{\mathbf{e}}_z \quad (4.1)$$

We can find the unit vector to be:

$$\mathbf{u}_{q3} = \frac{x \hat{\mathbf{e}}_x + y \hat{\mathbf{e}}_y - 2z \hat{\mathbf{e}}_z}{\sqrt{x^2 + y^2 + 4z^2}} \quad (4.2)$$

Now, we find the circular projection of an RF-field onto that unit vector. First we transform Eq. 4.1 to spherical coordinates which will leave us with the unit vectors:

$$\begin{aligned} \mathbf{u}_{q1} &= -\cos \theta \cos \phi \hat{\mathbf{e}}_x - \cos \theta \sin \phi \hat{\mathbf{e}}_y + \sin \theta \hat{\mathbf{e}}_z \\ \mathbf{u}_{q2} &= \sin \phi \hat{\mathbf{e}}_x - \cos \phi \hat{\mathbf{e}}_y \\ \mathbf{u}_{q3} &= \cos \phi \sin \theta \hat{\mathbf{e}}_x + \sin \theta \sin \phi \hat{\mathbf{e}}_y + \cos \theta \hat{\mathbf{e}}_z \end{aligned} \quad (4.3)$$

where:

$$\begin{aligned} \rho &= \sqrt{x^2 + y^2 + 4z^2} \\ \theta &= \arccos \frac{2z}{\rho} \\ \phi &= \arctan \frac{y}{x} \end{aligned} \quad (4.4)$$

From here we can construct a rotation matrix to transform any magnetic field into the quadrupole basis (u_{q1}, u_{q2}, u_{q3}) :

$$R_{QS} = \begin{pmatrix} -\cos\theta \cos\phi & \sin\phi & \cos\phi \sin\theta \\ -\cos\theta \sin\phi & -\cos\phi & \sin\theta \sin\phi \\ \sin\theta & 0 & \cos\theta \end{pmatrix} \quad (4.5)$$

In the RWA, only the circular components of the RF in the quadrupole basis couple the atoms. We can construct the spherical operators in this basis as:

$$\begin{aligned} \mathbf{u}_{q+} &= \frac{1}{2} (\mathbf{u}_{q1} + i\mathbf{u}_{q2}) \\ \mathbf{u}_{q-} &= \frac{1}{2} (\mathbf{u}_{q1} - i\mathbf{u}_{q2}) \end{aligned} \quad (4.6)$$

These operators allow us to write the projection matrix of the circular components, analogously to a quarter waveplate in Jones calculus, as:

$$Q_{\sigma+} = \begin{pmatrix} 1 & i & 0 \\ -i & 1 & 0 \\ 0 & 0 & 0 \end{pmatrix}, Q_{\sigma-} = \begin{pmatrix} 1 & -i & 0 \\ i & 1 & 0 \\ 0 & 0 & 0 \end{pmatrix} \quad (4.7)$$

Let's now consider the case of an elliptic RF-field in the circular basis of \mathbf{e}_+ and \mathbf{e}_- :

$$B_{RF} = B_x \cos\alpha \hat{\mathbf{e}}_x + iB_y \sin\alpha \hat{\mathbf{e}}_y \quad (4.8)$$

where α is a polarisation angle: $\alpha \pm \pi/4$ are circularly polarised fields and $\alpha = 0, \pi/2$ are linearly polarised fields. The coupling results in:

$$\begin{aligned} \Omega &= \frac{g_F \mu_B}{\hbar} |Q_{\sigma_s} R_{QS}^T B_{RF}| = \\ &= \frac{g_F \mu_B}{2\hbar} \sqrt{2 \cos^2\phi (B_x \cos\alpha \cos\theta - B_y \sin\alpha)^2 + 2 (B_x \cos\alpha - B_y \cos\theta \sin\alpha)^2 \sin^2\phi} \end{aligned} \quad (4.9)$$

where $s = \text{sgn}(g_F/|g_F|)$. This equation simplifies greatly for the two general cases of linear and circularly polarised RF-fields. After some algebra it can be shown that (for $B_x = B_y = B_0$):

$$\Omega_\sigma = \frac{g_F \mu_B |B_0|}{2\hbar} \sin^2(\theta/2) = \frac{g_F \mu_B |B_0|}{2\hbar} \sqrt{1 + \frac{4z^2}{\rho^2} - \frac{4z}{\rho}} = \frac{g_F \mu_B |B_0|}{2\hbar} \left(1 - \frac{2z}{\rho}\right) \quad (4.10)$$

and, for instance, for an RF-field linearly polarised along x:

$$\Omega_\pi = \frac{g_F \mu_B |B_0|}{\hbar \sqrt{2}} \sqrt{\cos^2 \theta \cos^2 \phi + \sin^2 \phi} = \frac{g_F \mu_B |B_0|}{\sqrt{2} \hbar} \frac{\sqrt{y^2 + 4z^2}}{\rho} \quad (4.11)$$

One can also find a similar expression for an RF linearly polarised along z, which will be useful later:

$$\Omega_\pi = \frac{g_F \mu_B |B_0|}{\sqrt{2} \hbar} \frac{\sqrt{y^2 + x^2}}{\rho} \quad (4.12)$$

A general expression where the three components are nonzero can also be found:

$$\begin{aligned} \Omega^2 = \left(\frac{g_F \mu_B}{\hbar \sqrt{2}} \right)^2 & (-B_x \cos(\alpha) \cos \theta \cos \phi + B_y \cos \phi \sin \alpha + B_z \sin \theta)^2 + \\ & + (B_x \cos(\alpha) - B_y \cos \theta \sin(\alpha))^2 \sin^2 \phi \end{aligned} \quad (4.13)$$

The handedness of the circular RF-field components that couple the atoms is determined by the sign of g_F . Although we did not mention it explicitly, our derivation includes this fact in Eq. 4.7. Depending on which of the two matrices we choose, the calculated Rabi frequency corresponds to an opposite circular projection into the local basis of the quadrupole. In the following, we typically consider either perfectly circular or perfectly linear RF-fields in our analytical calculations. We will quote the explicit formula of the RF-coupling when necessary for the reader's convenience.

4.1.2 Trap characteristics

Let's consider the case of an atom in the presence of a quadrupole field $B_q(\mathbf{r}) = \alpha(x\hat{\mathbf{e}}_x + y\hat{\mathbf{e}}_y - 2z\hat{\mathbf{e}}_z)$, where α is a magnetic quadrupole gradient and $(\hat{\mathbf{e}}_x, \hat{\mathbf{e}}_y, \hat{\mathbf{e}}_z)$ are the vectors of a cylindrically symmetric coordinate system, and an RF-field of arbitrary polarisation $\mathbf{B}(t)$. The Hamiltonian for weak fields $|g_F \mu_B B_q(\mathbf{r})| \ll \hbar \omega_{\text{hfs}}$, as we have seen previously, reads:

$$H = \frac{A_{\text{hfs}}}{\hbar^2} \mathbf{I} \cdot \mathbf{J} + \frac{\mu_B}{\hbar} (g_I \mathbf{I} + g_J \mathbf{J}) \cdot (B_q(\mathbf{r}) + \mathbf{B}(t)) \quad (4.14)$$

where A_{hfs} is the hyperfine splitting between the ground states of ^{87}Rb , \mathbf{I} and \mathbf{J} are the nuclear and electronic angular momentum operators, with g_I and g_J being their respective gyromagnetic ratios. If magnetic fields are weak, the total angular momentum $\mathbf{F} = \mathbf{I} + \mathbf{J}$ with eigenstates in a coupled basis $|F, m_F\rangle$ can be used instead of $|I, m_I, J, m_J\rangle$. For ^{87}Rb ($I = 3/2$, $J = 1/2$) there are two hyperfine subspaces

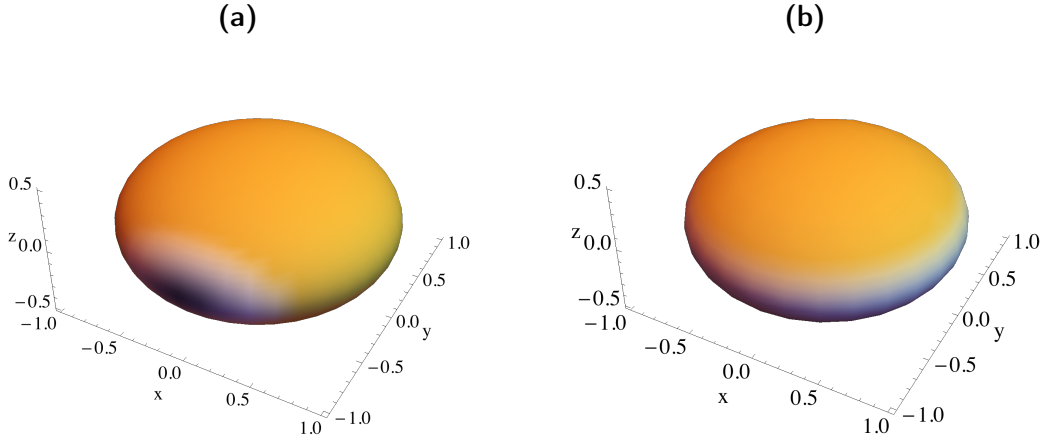


Figure 4.1: Radio frequency field coupling in a quadrupole field for (a) a linearly polarised RF-field along the y axis and (b) a σ_- polarised RF-field. The grey area indicates a low coupling region and the orange/red area indicates a high coupling region. Trappable states would experience the same coupling in the case depicted in a). However, in b) the high and low coupling region depend on the spin-state manifold.

with $F = I \pm 1/2$ and hyperfine Zeeman sub-states given by $m_F = -F \dots 0 \dots F$ in each one, as we saw in chapter 3. The total angular momentum gyromagnetic factor g_F was given previously in Eq. 3.10 ($g_1 = -0.5018$ and $g_2 = 0.4998$). The solution of Eq. 4.14 is generally found after the application of the Rotating Wave Approximation (RWA) and in a *dressed* basis $|F, \bar{m}_F\rangle$ of the same dimension as $|F, m_F\rangle$. Then the adiabatic dressed potential is [Zobay and Garraway, 2001]:

$$V^F(\mathbf{r}) = s \left(I + \frac{1}{2} \right) \frac{\hbar\omega_{\text{hfs}}}{2} + s\bar{m}_F\hbar\sqrt{\delta_F^2 + \Omega_F^2(\mathbf{r})} + Mgz \quad (4.15)$$

where $s = 1$ ($s = -1$) for $F = 2$ ($F = 1$), g is the gravitational acceleration and M is the atomic mass of ^{87}Rb . Furthermore, $\delta_F = \Omega_L^F(\mathbf{r}) - \omega_F$ (with $\hbar\Omega_L^F(\mathbf{r}) = m_F g_F \mu_B |B_q(\mathbf{r})|$, where $\Omega_L(\mathbf{r})$ is the Larmor frequency) and $\Omega_F(\mathbf{r})$ is the spatially dependent Rabi coupling [Garraway and Perrin, 2015]. In the RWA only circularly polarised RF with respect to the local quantization axis couples the spin of the atoms. A compelling corollary is that the different sign in g_F leads to anti-parallel magnetic moments that are only resonant to the co-rotating RF-field components, i.e. either to σ_+ or σ_- polarised fields. A circularly polarised RF in the laboratory frame can be written as:

$$\mathbf{B}_{\text{RF}} = B_0 (\cos(\omega_F t)\hat{\mathbf{e}}_x + s \sin(\omega_F t)\hat{\mathbf{e}}_y) \quad (4.16)$$

Each sense of rotation, specified with $s = \pm 1$ and defined with respect to $\hat{\mathbf{e}}_z$, couples

only atoms to either of the F manifolds. In the quadrupole trap we need to find the local coupling with respect to the spatially dependent unit vector of $B_q(\mathbf{r})$ (we can retrieve this result from Eq. 4.10):

$$|\Omega_F(\mathbf{r})| = \frac{\Omega_0}{2} \left(1 - \frac{2z}{\sqrt{x^2 + y^2 + 4z^2}} \right) \quad (4.17)$$

where $\hbar\Omega_0 = |g_F|\mu_B B_0$. The final potential is an isomagnetic surface defined by the resonance of ω_F and $B_q(\mathbf{r})$ [Lesanovsky *et al.*, 2006a]. Trapping occurs for the states with $g_F m_F > 0$ when $\frac{Mg}{2m_F |g_F| \mu_B \alpha} < 1$ [Merloti *et al.*, 2013]. If these conditions are fulfilled, in the harmonic limit and within the RWA, we can calculate the trapping frequencies. In order to derive them we will expand the trapping potential around the equilibrium point z_0 . Let's define the following spatially dependent functions:

$$\begin{aligned} r_q &= \sqrt{\rho^2 + 4z^2} \\ f_c &= \frac{1}{2} \left(1 - \frac{2z}{r_q} \right) \end{aligned} \quad (4.18)$$

With these definitions we can rewrite, using $b_q = g_F \mu_B \alpha$:

$$V(\mathbf{r}) = \sqrt{(\hbar\omega_{\text{RF}} - b_q r_q)^2 + \hbar^2 \Omega_0^2 f_c^2} + Mgz \quad (4.19)$$

where we set $\rho = 0$. Then we can retrieve the trap equilibrium position by finding z_0 from the equation $\partial V / \partial z = 0$. This gives two solutions, but only one of them corresponds to the trap. If we define:

$$\gamma = \frac{2b_q}{gM} \quad (4.20)$$

after some algebra we find that:

$$z_0 = -\frac{\hbar\omega}{2b_q} \left(1 + \frac{1}{\sqrt{\gamma^2 - 1}} \frac{\Omega_0}{\omega} \right) \quad (4.21)$$

which is the vertical displacement of the trapping position. We are interested in the two particular shell trap potentials corresponding to $|1, -1\rangle$ and $|2, 1\rangle$. From the previous results, we can promptly see that the quantities z_0 and ω_z differ for the two states due to unequal g_F factor, even for $\gamma^{-1} \ll 1$. When γ^{-1} becomes larger, the radial frequency is unmatched as well. On top of it, one may notice that the other trappable state in the system, $|2, 2\rangle$ presents even larger differences in trapping

frequencies and equilibrium position due to the different $|\bar{m}|$. Now, in order to find the axial trapping frequency, we expand V around z_0 for $\rho = 0$. We find:

$$\omega_z = \sqrt{\frac{2b_q^2}{M\hbar\Omega_0} \left(\frac{\gamma^2}{\gamma^2 - 1}\right)^{-\frac{3}{4}}} \quad (4.22)$$

To find the radial trapping frequency we set $z = z_0$ and then expand in ρ around 0. By using the reasonable approximation $\sqrt{\gamma^2 - 1} \rightarrow \gamma$ we find that:

$$\omega_\rho = \frac{b_q}{2\Omega_0 + \gamma\omega_{\text{RF}}} \sqrt{\frac{(3 - \gamma^2)\Omega_0 + \gamma\omega_{\text{RF}}}{\hbar M}} \quad (4.23)$$

These three results $-z_0, \omega_z, \omega_\rho$ - fully determine the trap in the harmonic limit. One can gather at first sight from Eq. 4.21 that states with different gyromagnetic factor $|g_F|$ have different equilibrium positions. Moreover, Eqs.(4.43, 4.41) show that the same occurs with the trap curvature. This traps mismatch sets a stringent limit in the dephasing time of the transition between the $|1, \bar{m}_F = -1\rangle$, $|2, \bar{m}_F = 1\rangle$ states, which severely complicates the performance of the proposal in [Navez *et al.*, 2016]. We will study the result of the traps mismatch when driving MW transitions between RF-dressed states in Section 7.1.1. In Section 4.2 we introduce a method to match the traps based on state-dependent manipulation of two different spin states. This is not a sensible proposal for the $|2, 2\rangle$ state, since one would have to compensate for the difference in m_F too.

4.2 The Bi-chromatic Shell Trap

Our proposal to overcome the traps mismatch is a bi-chromatic shell adiabatic potential where the different $\text{sgn}(g_F)$ permits to address selectively the $F = 1$ and $F = 2$ states depending on the handedness of the RF-dressing (circular) polarisation [Hofferberth *et al.*, 2006]. Atoms in the $F = 1$ ($F = 2$) manifold are only coupled by RF-fields with σ_- (σ_+) polarisation (with respect to \hat{e}_z). The RF-dressing field would then be composed by a σ_- component with ω_1, Ω_1 and a σ_+ component with ω_2, Ω_2 :

$$\begin{aligned} \mathbf{B}_{\text{RF}} = \mathbf{B}_1 + \mathbf{B}_2 = & (B_{x1} \cos(\omega_1 t) + B_{x2} \cos(\omega_2 t)) \hat{e}_x \\ & + (-B_{y1} \sin(\omega_1 t) + B_{y2} \sin(\omega_2 t)) \hat{e}_y \end{aligned} \quad (4.24)$$

where one sets $B_{xF} = B_{yF} = B_F$ for circularly polarised RF. The resulting potential entails separate traps for the two states, with independently tunable position and

trapping frequencies. We first set $B_1 = \frac{g_2}{g_1} B_2$, which yields identical Rabi frequency Ω_0 for both states. Leaving the RF-frequency as a free parameter, we can now find the traps matching position from Eq. 4.21:

$$|g_1|\omega_2 - |g_2|\omega_1 = \Omega_0 \left(\frac{|g_2|\gamma_1}{\sqrt{1-\gamma_1^2}} - \frac{|g_1|\gamma_2}{\sqrt{1-\gamma_2^2}} \right) \quad (4.25)$$

where γ_F corresponds to the quantity in Eq. 4.20. For $\alpha \gg 15$ Gpc/cm and $B_1 = \frac{g_2}{g_1} B_2$ Eq. 4.25 remains good approximation, and corrections can be found experimentally². Figs. 4.2 (a) and (b) illustrate the matching condition. In Fig. 4.2 (a) we plot the potential energy of the two states $V^1(z)$ and $V^2(z)$ in the z direction for three different pairs of ω_1, ω_2 . We fix the RF-frequency in $V^2(z)$ to ω_2 (red) and then plot together both $V^1(z)$ with ω_2 (blue) and $V^1(z)$ with several ω_j (black, dashed). As we see from Figs. 4.2 (a) and (b), at a certain $\omega_j = \omega_1$, that corresponds to the solution of Eq. 4.25, the traps positions are matched and the curvature in the potential energy difference $\Delta E = V^2(z) - V^1(z)$ becomes minimal at z_0 ($\delta V^2(z, \omega_2) / \delta z|_{z_0} = 0$). From Fig. 4.2 (b) one can see that the sampled energy difference by an atom -when the two states are coupled by a weak MW field- is minimal at such matching condition. Here we show $\Delta E(\omega_2) = V^2(z, \omega_2) - V^1(z, \omega_2)$ (blue), $\Delta E(\omega_j) = V^2(z, \omega_2) - V^1(z, \omega_j)$ (black, dashed) and $\Delta E(\omega_1) = V^2(z, \omega_2) - V^1(z, \omega_1)$ (green); together with a vertical black, dashed line drawn at the trap position for $V^2(z, \omega_2)$. Moreover, the effect of the curvature mismatch is already evident, as it leads to a parabola-shaped deviation from $\Delta E = 0$ further from z_0 .

Fig. 4.3 aims at showing how the line-width would be reduced as the matching condition is approached. For each ν_1 there is a corresponding ν_2 that becomes optimum (in this case the RF-amplitudes and gradient are fixed). This figure shows the convolution of a gaussian-shaped sized cloud trapped in the shell for $|1, -1\rangle$ with the energy difference, at the cloud's position, between the two potentials, such that:

$$h\Delta\nu = \Delta E = |V^2(z) - V^1(z)| \quad (4.26)$$

In order to make this estimation of the frequency spread for a thermal cloud in the bi-chromatic shell trap as it changes from the initial to the final state we will assume

²Note that this is a solution in the RWA. Therefore, one expects to find deviations at the range of Rabi frequencies typically used in our experiments.

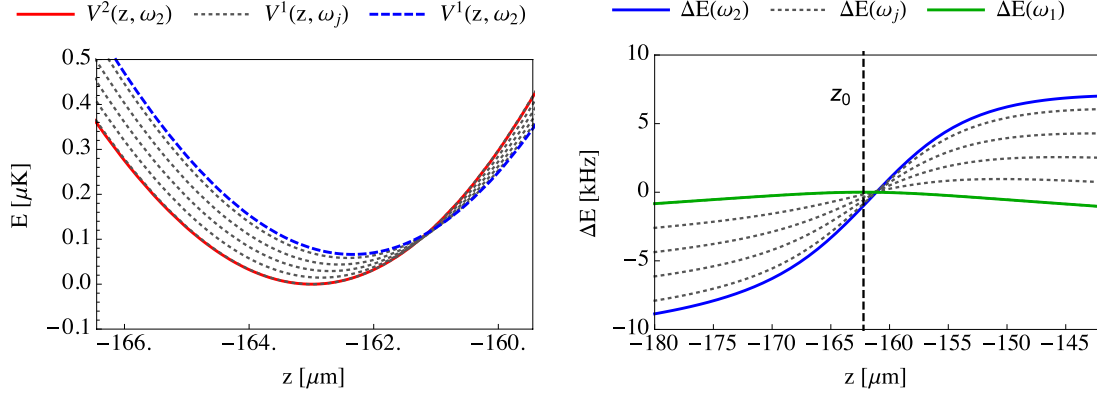


Figure 4.2: (a) Potential energy (in μK) vs distance from the center of the quadrupole for the RF-dressed potential Eq. 4.15. We fix $\alpha = 100$ Gpcm and $\omega_2/2\pi = 2.25891$ MHz, $B_2 = 200$ mG and $B_1 = g_2/g_1 B_2$. In red, $V^2(z)$, with ω_2 . In blue $V^1(z)$ with ω_2 . Dotted black lines correspond to $V^1(z)$ for several different ω_j spaced by 2 kHz. (b) Difference in potential energy (in kHz) $\Delta E = V^2(z) - V^1(z)$, calculated from (a). In blue $V^2(z)$ and $V^1(z)$ have the same ω_2 . In black (dotted), ΔE for $V^2(z)$ with ω_2 and $V^1(z)$ for each of the ω_j , spaced by 2 kHz. In green, ΔE for the matched traps. The vertical black (dashed, thick) line indicates the trap minimum z_0 of $V^2(z)$ calculated from the red curve in (a).

a Gaussian distribution of atoms placed at the center of the trap:

$$n(z) = \frac{N}{\Delta z \sqrt{2\pi}} e^{-\frac{(z-z_0)^2}{2(\Delta z)^2}} \quad (4.27)$$

with $\Delta z = \sqrt{\frac{2k_B T}{M\omega_z}}$ and where we can obtain ω_z according to Eq. 4.43. To calculate the standard deviation of the frequency spread:

$$\sigma_{bc}^2 = \langle (\Delta E/h)^2 \rangle - \langle \Delta E/h \rangle^2 \quad (4.28)$$

with the mean values defined by:

$$\langle \Delta E/h \rangle = \frac{1}{hN} \int_{-\infty}^{\infty} n(z) \Delta E dz \quad (4.29)$$

With $T = 100$ nK, $\alpha = 100$ Gpcm and $B_{RF} = 0.2$ G (for the F=2 shell, and using the adequate B_{RF} for the matching of the shell in F=1) one finds a standard deviation of $\sigma_{bc} \approx 4$ Hz, (for the matching condition we choose $\nu_2 = 2.25891$ MHz and calculate via Eq. 4.25 $\nu_1 = 2.2679903$ MHz) which should deliver a $1/e$ contrast decay time in a Ramsey experiment of $\tau_{bc} \approx 350$ ms (see Appendix B). Fig. 4.3 shows the calculated frequency spread σ_{bc} for several pairs of RF-dressing frequencies in the two shell

traps, spanning for about 1kHz with respect to the ideal matching condition. The white dots indicate the analytical solution of this matching condition for each pair of frequencies. One can see that they fall where the frequency spread becomes minimum.

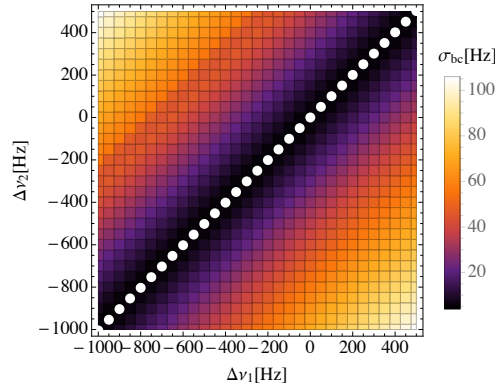


Figure 4.3: Calculated frequency spread according to Eq. 4.28 for a cloud at $T = 100$ nK, with shell traps with $\alpha = 100$ Gpcm and $B_2 = 0.2$ G (and $B_2g_2 = B_1g_1$). The white dots are the corresponding matching condition calculated from Eq. 4.25. Both axes depict the deviation of the RF-frequencies $\Delta\nu_1$ and $\Delta\nu_2$ from $\nu_1 = 2.2679903$ MHz and $\nu_2 = 2.25891$ MHz, respectively.

To give an idea of the matching precision needed $\tau_{bc} \approx 0.001$ ms if ω_1 deviates from the matching condition by 2kHz. As we will see in Section 7.5.1, the RF-polarisation in most experiments is not exactly circular, with the amplitudes mismatch being the main source of imperfection, and this modifies the actual matching conditions. Simulations similar to that shown in Fig. 4.3 can be used to understand which of the trapping parameters causes deviations from the ideal situation. Fig. 4.4 shows the frequency spread if the RF-field amplitude in one of the shells deviates from the matching given by $B_1g_1 = B_2g_2$. We can see that very small changes of only 2.5 mG provoke a frequency spread 4 times larger than in the case where $\Delta B_{\text{RF}} = 0$. As it was stated above, one could scan $\Delta\omega_{\text{RF}}$ and find a *new* matching condition, but it remains true nonetheless that the system is greatly affected by small changes in the Rabi frequencies of the RF-field. Moreover, these changes contribute to broadening through fluctuations -not only through drifts. This contribution scales linearly with the difference in ΔB_{RF} (see Section 7.5.3).

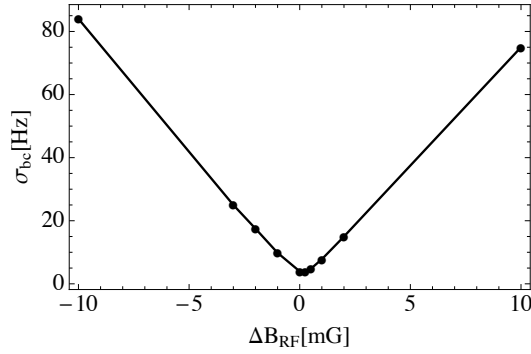


Figure 4.4: Calculated frequency spread according to Eq. 4.28 for a cloud at $T = 100$ nK, with shell traps with $\alpha = 100$ Gpcm and $B_2 = 0.2$ G (and $B_2 g_2 = B_1 g_1$) where we change $B_1 = B_2 g_2 / g_1 + \Delta B_{\text{RF}}$

4.3 Time Averaged Adiabatic Potentials

Time averaged adiabatic potentials (TAAP) were proposed by I. Lesanovsky and W. von Klitzing [Lesanovsky and Von Klitzing, 2007] and first demonstrated in the group of C. Foot [Sherlock *et al.*, 2011; Gildemeister *et al.*, 2010] and later in [Navez *et al.*, 2016; Pandey *et al.*, 2019] (also within this thesis). TAAPs add a time-averaging magnetic field to a RF-dressed magnetic trap. By choosing appropriately the relative orientation of the RF-field and time-averaging field polarisation one can produce a number of trapping potentials: from double wells in any spatial direction to ring traps or dumb-bell traps. Their operation relies on the fulfilment of the following condition:

$$\omega_{\text{trap}} \ll \omega_{\text{TA}} \ll \Omega_L \quad (4.30)$$

where ω_{trap} is the trapping frequency, ω_{TA} is the time-averaging AC field frequency and Ω_L is the Larmor frequency. This condition is easily satisfied with ^{87}Rb atoms, since typically $\omega_{\text{trap}} < 1$ kHz, $\Omega_L \propto 1$ MHz, and one can choose an audio frequency $\omega_{\text{TA}} \propto 10$ kHz. Eq. 4.30 guarantees the adiabatic following of Ω_L by the atomic spin at the frequency of the TA field, and consequently the effective modification of the trapping potential. This idea is similar to that of the TOP trap, except that in the TAAP case atoms are dressed with a strong Radio Frequency field. This chapter contains a description of the TAAP ring trap. To produce a flat ring, there are two possible RF-field configurations: a π -polarised RF-field along \hat{e}_z or a σ polarised RF-field propagating in \hat{e}_z . The former is a state-independent potential (except for the divergence stemming from different $|g_F|$) and the latter needs the *correct* circular polarisation handedness to trap either spin state.

TAAP rings offer reliably smooth waveguides and spin-state-dependent coherent control, transport and atom-optics manipulation. We have demonstrated record transport distances of BECs [Pandey *et al.*, 2019] and state-dependent potentials [Navez *et al.*, 2016]. Apart from applications in atom interferometry, neutral atoms in ring traps have been proposed to simulate the quantum Hall regime [Roncaglia *et al.*, 2011], with access to the low order Laughlin states [Viefers, 2008]. The high ratio of angular momentum per atom needed to reach this regime can in principle be attained in TAAP rings in a controllable way. TAAP rings could also be employed in spatial adiabatic passage experiments [Polo *et al.*, 2016; Menchon-Enrich *et al.*, 2016]

TAAP rings compete with many other ring-shaped trapping schemes. Static magnetic traps [Crookston *et al.*, 2005] or optical potentials based on phase-masks [Lee and Hill, 2014] or passive optical elements [Turpin *et al.*, 2015] are inherently incapable of performing any sort of controlled displacement of BEC. Time-averaged ring traps [Bell *et al.*, 2016] trade complexity for smoothness: only very small sampling distances produce smooth-enough rings. TAAP rings, on the other hand, are perfectly smooth, since the field-generating wires lie very far from the trap. They offer state-dependent and state-independent control, and the needed equipment is of Audio and Radio-Frequency, which are two seasoned technologies. TAAP potentials are an interesting system also for studying effects beyond the rotating wave approximation [Hofferberth *et al.*, 2007] or beyond the linear Zeeman effect [Sinuco-Leon and Garraway, 2012].

4.3.1 The TAAP ring trap

The total field in a TAAP potential contains three components: a spatially dependent DC magnetic field, a RF-field, and one more magnetic field that oscillates at audio frequencies. The two most important parameters of the ring potential are the trapping frequencies and the radius of the ring. The ring topology does not allow for high radial trapping frequencies, but the confinement of the atoms is determined by the axial trapping frequency (pointing parallel to the radius of the ring), which can be of the order of a kHz [Lesanovsky and Von Klitzing, 2007]. In the following we derive the analytical solution for the radius of the ring. Let's then consider the case where such field is oriented along $\hat{\mathbf{e}}_z$:

$$g_F \mu_B B_{TAAP}(\mathbf{r}) = b_Q(\rho \hat{\mathbf{e}}_\rho - 2z \hat{\mathbf{e}}_z) + b_M \sin(\omega_m t) \hat{\mathbf{e}}_z \quad (4.31)$$

with $b_M = g_F \mu_B B_m$, $b_Q = g_F \mu_B \alpha$. Now, from the following condition in the vertical direction:

$$-2\alpha z + B_m \sin(\omega_m t) = 0 \quad (4.32)$$

we can define the temporally parametrized z_0 :

$$z_0 = \frac{b_M}{2b_Q} \sin(\omega_m t) \quad (4.33)$$

so as to set a new $z' = z + z_0$. Following Eq. 4.15, we can write the full TAAP potential:

$$V(\mathbf{r}, t) = \sqrt{(\hbar\omega_{\text{RF}} - b_Q r'_q(t))^2 + \hbar^2 \Omega_0^2 f_c^2} + Mgz \quad (4.34)$$

where $r'_q = \sqrt{\rho^2 + z'^2}$. For now, we assume that the Rabi frequency coupling is spatially independent (this is the same as letting $f_c = 1$, which is a sensible approximation for ultra-cold clouds in TAAP potentials generated from perfectly circularly polarised RF-fields -with respect to $\hat{\mathbf{e}}_z$ - or linearly polarised RF-fields along $\hat{\mathbf{e}}_z$). The radius of the ring in that case is the solution for:

$$\int_0^{2\pi} \frac{\partial V(\mathbf{r}, t)}{\partial \rho} dt = 0 \quad (4.35)$$

Using Eq. 4.35 one finds that:

$$\rho_0 = \frac{2}{\pi} \frac{\hbar\omega_{\text{RF}}}{g_F \mu_B \alpha} E[\beta^2] \quad (4.36)$$

with the modulation factor $\beta = b_M/(\hbar\omega_{\text{RF}})$. One can see that the pre-factor to the Elliptical function in Eq. 4.36 is the radius r_0 from [Lesanovsky and Von Klitzing, 2007]. Let's find that result shortly: since the elliptical function only modifies slightly this term as B_m changes, it seems convenient to find a setting of the fields that simplifies it to unity. The proposed solution in [Lesanovsky and Von Klitzing, 2007] is to modulate the frequency ω_{RF} . The reason to use this modulation is found by solving³:

$$\frac{\partial V(\mathbf{r}, t)}{\partial \rho} = r_0 \quad (4.37)$$

³This condition forces the ring radius to be constant. From here, one then finds which ω_{RF} satisfies it.

from where we retrieve:

$$\omega_{\text{RF}} = \omega_{\text{RF}}^0 \sqrt{1 + \beta^2 \sin^2 \omega_m t} \quad (4.38)$$

After inserting this modulation in Eq. 4.34 one finds that:

$$r_0 = \frac{\hbar \omega_{\text{RF}}}{b_q} \quad (4.39)$$

Let's now re-define $\rho_0 = r_0$ to simplify further calculations. We will find the trapping frequencies of the time-average of $V(\mathbf{r}, t)$, which becomes a toroidally-shaped potential of radius ρ_0 (for the fields configuration from Eq. 4.31). By expanding the first term inside the square root in Eq. 4.34 around ρ_0 we find that:

$$\hbar \omega_{\text{RF}} - b_q r'_q(t) \approx \hbar \omega_{\text{RF}}^0 \frac{\Delta \rho}{\rho_0} \frac{1}{\sqrt{1 + \beta^2}} \quad (4.40)$$

where $\Delta \rho = \rho - \rho_0$. Now we insert Eq. 4.40 into Eq. 4.34, expand around $\Delta \rho$ and time-average. The term that accompanies ρ^2 gives the following harmonic trapping frequency:

$$\left(\frac{\omega_\rho}{2\pi}\right)^2 = \frac{2}{M} \frac{\omega_m}{2\pi} \int_0^{2\pi/\omega_m} \frac{b_q^2}{2\hbar\Omega_0 \left(1 + \left(\frac{b_m}{b_q\rho_0}\right)^2 \sin^2(\omega_m t)\right)} dt = \frac{b_q^2}{\hbar\Omega_0 M} \left(\frac{1}{\sqrt{1 + \beta^2}}\right) \quad (4.41)$$

In order to find the trapping frequency along $\hat{\mathbf{e}}_z$, we proceed similarly by expanding around z the first term of the potential and, with $\rho \rightarrow \rho_0$, we find:

$$\hbar \omega_{\text{RF}} - b_q r'_q(t) \approx \frac{2b_m z \sin(\omega_m t)}{\rho_0 \sqrt{1 + \beta^2 \sin^2(\omega_m t)}} = \frac{2b_q \beta z \sin(\omega_m t)}{\sqrt{1 + \beta^2 \sin^2(\omega_m t)}} \quad (4.42)$$

Now, we derive the quadratic term from the potential in z , like we did before for ρ , and we perform the same calculation as in Eq. 4.41.

$$\left(\frac{\omega_z}{2\pi}\right)^2 = \frac{2}{M} \frac{\omega_m}{2\pi} \int_0^{2\pi/\omega_m} \frac{2b_q^2 \beta^2 \sin^2(\omega_m t)}{\hbar\Omega_0 (1 + \beta^2 \sin^2(\omega_m t))} dt = \frac{4b_q^2}{M\hbar\Omega_0} \left(1 - \frac{1}{\sqrt{1 + \beta^2}}\right) \quad (4.43)$$

In order to characterise the TAAP ring, it is important to understand both the role of gravity and the coupling strength Ω_{RF} . Firstly, we see that mathematically there is no constraint as for how small Ω_{RF} can be. However, Landau-Zener losses set a lower limit for the coupling strength that needs to be overcome in order for the

atomic cloud to live in the dressed potential regime. Said otherwise: the RF-coupling strength needs to be large-enough for the atoms to avoid spin-flip losses to other hyperfine sub-states at the resonance eigen-energies crossing [Allegrini and Arimondo, 1971; Rubbmark *et al.*, 1981]. The role of gravity needs to be thought of along with the polarisation-dependent radio-frequency dressing coupling. Gravity imposes a *sag* that has to be compensated with the vertical modulation, which thus brings the resonance area far from the bottom of the trap where major losses occur⁴ (notice that we have neglected the contribution of gravity in the trapping frequencies calculation). The introduction of the modulated magnetic field with amplitude B_m and frequency ω_m in the dressed potential has a defining consequence in the Landau-Zener criterion, that is: the frequency ω_m sets the time-scale of the dressed potential coupling rates. From [Navez *et al.*, 2016] we see that, for a TAAP ring where the dressing is perfectly linear in the vertical direction z :

$$\omega_m \ll \frac{\Omega_{\text{RF}}^2 r_0}{\omega_{\text{RF}} a_{ho}} \quad (4.44)$$

where $a_{ho} = (\hbar/m\omega_z)^{1/2}$ is the harmonic oscillator length. Therefore, for *very small radiuses*, the dressing condition does not apply. As we have discussed earlier, this is the case when the time-averaged energy term that scales with B_m is smaller than the gravitational potential sag. The takeaway results close to the trap bottom of the ring potential are [Lesanovsky and Von Klitzing, 2007; Navez *et al.*, 2016]:

$$V = \hbar\Omega_{0c} + \frac{1}{2}m\omega_r^2(r - R)^2 + \frac{1}{2}m\omega_z^2 z^2 \quad (4.45)$$

with trapping frequencies in the radial and the axial directions:

$$\begin{aligned} \omega_\rho &= \omega_0(1 + \beta^2)^{-1/4} \\ \omega_z &= 2\omega_0 [1 - (1 + \beta^2)^{-1/2}]^{1/2}, \end{aligned} \quad (4.46)$$

where β is the modulation index defined above and $\omega_0 = b_q (M \hbar\Omega_0)^{-1/2}$.

As we have seen previously, the RF-field coupling depends on the sign of g_F . Similarly to the case of the shell trap, if the RF is circularly polarised as σ_- only atoms in the $F = 1$ manifold states⁵ are trapped in the ring potential, and the same happens for σ_+ and⁶ $F = 2$. Therefore, if one intends to trap the two *clock* states, the RF-polarisation needs to be linear in \hat{e}_z for a flat ring. Even in this case, the different

⁴for the case of a linearly polarised RF-field along \hat{e}_z

⁵In fact, only $|1, -1\rangle$, as we discussed earlier

⁶Both $|2, 1\rangle$ and $|2, 2\rangle$ can be trapped.

magnitude in g_F leads to slightly unmatched traps, again similarly to the case of the shell trap (one could think of a bi-chromatic ring trap to tame this shortcoming). However, the different coupling to the RF-polarisation can provide state-dependent control of the two spin states in the appropriate configuration. For instance, if one includes some ellipticity in the default vertically aligned RF-field, it will create different traps for the two states. In addition, the modulation field can also be tilted by including in-phase or out of phase smaller components in the x-y plane to the default modulation in \hat{e}_z . In this case, since the trap is tilted as a result of the gravitational potential, both states experience the same changes in the trapping potential. These two experimental knobs are the ones used in [Navez *et al.*, 2016] to design an experimental sequence where under the same evolution of the trap parameters each of the spin states travels along the ring waveguide in opposite directions, thus leading to a Sagnac phase shift that can be measured in a Ramsey-type interferometer.

The ring trap can be loaded from a shell trap by slowly ramping up a modulation field b_z in the \hat{e}_z direction. Fig.4.5 shows an x-z section from a numerical simulation of a $5\mu\text{K}$ cloud in an adiabatic potential as the amplitude of the modulation field increases -the plots are in re-scaled spatial units. The RF-field is circularly polarised, since a shell trap cannot be loaded with a vertically polarised RF in \hat{e}_z due to the zero coupling point at its center. In this example, if all fields are perfectly aligned, increasing B_m modifies the shell to a torus-like potential that reaches its maximum radius at $B_m \approx 0.8\text{ G}$. It is important to note that, since the RF-frequency is not being modulated, the analytic tools developed above are not exact. Moreover, the ring-radius is far from constant as B_m changes and it is important to set this field to a value lower than that at which the trap begins to shrink (in the case depicted on the figure, that would correspond to $B_m \approx 1\text{ G}$). Normally, it is not convenient to split the cloud. Therefore one chooses a slightly tilted modulation field such that all atoms enter the ring from the same side.

The ring trap depicted in Fig. 4.5, however, is not state-independent and cannot be used for both clock-states as a default waveguide. Therefore, one needs to load a TAAP ring-trap with a linearly polarised RF-field in \hat{e}_z . One can load this trap more easily from a crossed dipole trap, which has become the standard method in our laboratory (see Section 6.1.3). In addition, we developed a sequence that builds upon the loading of a tilted ring-trap with circularly polarised RF, starting from the

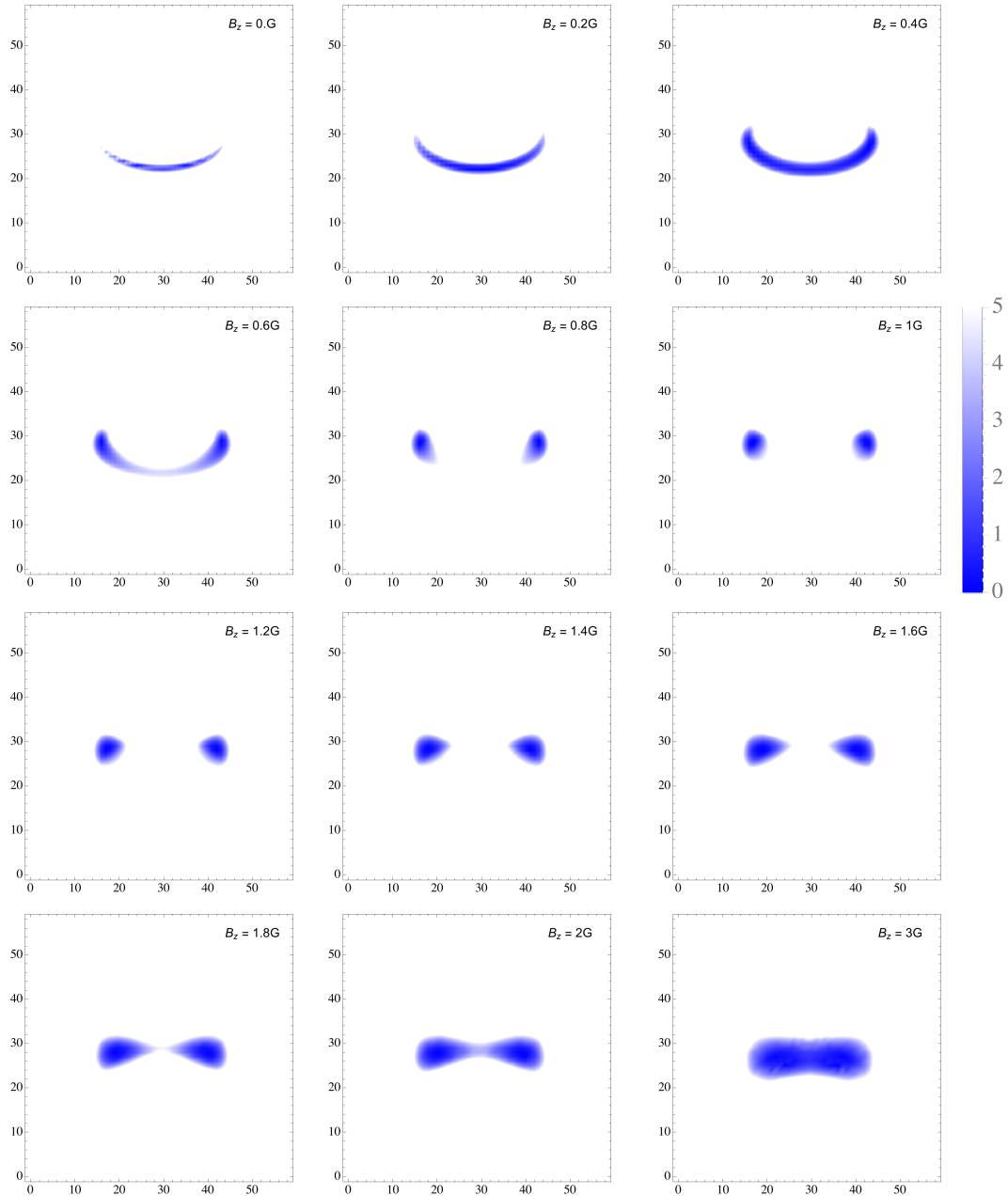


Figure 4.5: Simple Ring Loading $\omega_{\text{RF}} = 2$ MHz, $B_q = 100$ Gpcm. The RF-field polarisation is σ_- . We consider atoms in the $|1, \bar{m}_F = -1\rangle$ state. Notice that, in this particular example, the ring radius changes drastically right before $B_m \approx 1$ G and right after $B_m \approx 1.5$ G. Therefore, one should choose the value of B_m to be in this range in order to avoid big changes in the radius in case of magnetic field fluctuations.

shell trap⁷. This method would not work if the cloud is prepared in a spin mixture, but it allows for transferring the atoms between the spin-states at a later stage. The sequence is as follows:

- Load a shell trap with the appropriate circularly polarised RF
- Introduce a tilted modulation field by adding a small component in $\hat{\mathbf{e}}_x$ to the stronger one in $\hat{\mathbf{e}}_z$.
- Once the cloud has reached the steady tilted ring trap, ramp down the RF-field pointing along $\hat{\mathbf{e}}_x$. Now the RF-field is linearly polarised along $\hat{\mathbf{e}}_y$.
- Ramp up the RF-field along $\hat{\mathbf{e}}_z$. One can choose either proper circular polarisation (by choosing $\pm\pi/2$ with respect to the RF-field in $\hat{\mathbf{e}}_y$) or an effective tilted RF-field such that the phase is $2\pi k$ with respect to the RF-field in $\hat{\mathbf{e}}_y$.
- Ramp down the RF-field in $\hat{\mathbf{e}}_y$ and also the small modulation component in $\hat{\mathbf{e}}_x$. Now the atoms are trapped in a flat TAAP ring with a vertically polarised RF-field.

This sequence, although it proved successful in the loading of clouds between $2 - 5\mu\text{K}$, did not work well with BECs. The reason is that, in each of the steps from right above, numerous lossy channels associated to the modification of the polarisation are present. In any case, this was the procedure that we employed to demonstrate the results from [Navez *et al.*, 2016]. In Section 6.2 we will explain the loading of the TAAP ring trap from a crossed dipole trap, which has become the standard procedure in our laboratory.

⁷This was needed when preparing the sample in a TOP trap

5

Experiment Setup

This Chapter gives an outline of the experimental set-up components, together with a short explanation of the programming. First, it gives a general overview of the experiment in Section 5.1. Then, it introduces the laser system used to produce and distribute the MOT and Imaging light, which relies on the spectroscopical locking of a diode laser to the 780nm D2 line of ^{87}Rb (Section 5.2). Afterwards, it gives a description of the imaging system (Section 5.3), and the dipole trap laser system at 1064nm (Section 5.4). In our laboratory, the experiment is well enclosed within a box with gates controlled by air-pressure locking mechanisms, yet in an *open* lab space. Therefore we needed to design and build an interlock system to prevent any high-power IR light from exiting the experiment area (this interlock system is described in [Pandey, 2019]). The description of the laser systems is followed by an account of the magnetic fields involved in the experiment -Table 5.1 classifies them conveniently according to their frequency and indicates some of the purposes they are employed for in the experiments. To conclude this Chapter I will shortly describe the experiment computer control (Section 5.6).

DC	AF	RF	MW
Quadrupole	TOP	Evaporation	Spectroscopy
MOT	TAAP	RF-dressing	
Offset fields		Spectroscopy	

Table 5.1: Classification of the different magnetic fields employed in the experiment divided in DC, AF (audio-frequency), RF (radio-frequency) and MW (microwave) with their purposes.

5.1 Cretan BEC1 experiment

For a detailed description of the experiment setup before I joined the laboratory, see the work of previous students [Pappa, 2011; Pappa *et al.*, 2011; Sahagun *et al.*, 2013; Bolpasi, 2008; Bolpasi and von Klitzing, 2010; Bolpasi, 2014]. Here, I will describe more thoroughly additions or modifications to the original experiment.

The experiment cell is shaped as an octagon, with optical access from eight sides in the horizontal plane (25cm) and two larger vertical windows (40cm). The two vertical and four of the horizontal openings are used for the MOT beams. The vertical MOT openings also carry the vertical imaging light. A pair of the horizontal windows is used for the horizontal absorption imaging beam. A MW dipole antenna was installed close to the cell and next to one of the overtures. The remaining opening is connected to the 2D-MOT vacuum cell. The principal glass cell is surrounded by a *macor* octagon-shaped protective structure and held with metallic arms that rest on a granite rectangular stone sitting on a thick marble piece that, in turn, rests on a Newport vibration control system made of four air-pressure stabilised valves. A larger glass cell dedicated to the 2D-MOT is connected to the science cell via a 1mm link.

The original design used two ion pumps, one for the 2D-MOT and one for the 3D-MOT vacuum cell. These two cells are connected by the differential pumping tube mentioned above. The 3D-MOT cell would work at 10^{-11} mbar and the 2D-MOT cell at 10^{-7} mbar¹. Shortly after joining the laboratory, the 2D-MOT pump broke², but this did not damage the vacuum, which stayed steady at 10^{-11} mbar for four years -and, to date, counting. We did bake the vacuum system in a gradient-like procedure at our arrival, given that the Rubidium atoms had deposited on the pump plates after some idle time. We included a Peltier element close to the 2D-MOT vacuum cell to set the vapour pressure within, and to prevent the atoms from moving away from the experiment volume.

The experiment was initially built with a TOP trap [Petrich *et al.*, 1995] setup

¹This use of a differential pressure system between both cells is explained by the particular requirements of the 2D, 3D-MOT [Schoser *et al.*, 2002] and the remaining stages in the experiment. For instance: one aims at low pressure to avoid background collisions in the BEC stage. This means that, although the atom-capture rate might be faster at higher pressure in the MOT, one needs to find a compromise.

²Without anybody involved. Not even me.

(i.e. two quadrupole coils and a three-axis Helmholtz-pair coils setup). The highest condensed atom number that we achieved after re-starting the machine was of the order of 60000 atoms in $|2, 2\rangle$. However, our project required, first and foremost, the loading of (ideally large) BECs in TAAP ring traps. The loading of BECs in a TAAP ring had been already achieved in [Sherlock *et al.*, 2011; Gildemeister *et al.*, 2010] but the RF-polarisation needed in our interferometer proposal [Navez *et al.*, 2016] made it complicated to achieve large BEC atom numbers in the ring, as the loading from the TOP trap became cumbersome. After demonstrating state-dependent manipulation and the loading of (small) BECs in the ring we decided to upgrade our BEC production by installing a crossed dipole trap and by working with the $|1, -1\rangle$ spin state. Insomuch as most of the experiments shown in this thesis were performed after this set-up upgrade, no detail will be given on the TOP trap, although it can be found elsewhere [Pappa, 2011; Hodby *et al.*, 2000].

5.2 780nm lasers system

Section 2.1.2 showed that to form a MOT and eventually produce a BEC, one needs a cooling and re-pumper transition together with control of the light frequency in the low MHz regime. In our set-up -which has been partially introduced elsewhere [Pappa, 2011; Pappa *et al.*, 2011; Sahagun *et al.*, 2013]- a Master laser locked to the D2 line of ^{87}Rb is the frequency reference for the laser-light used in cooling and imaging. After that, a slave laser, a distribution board with a three-axis independent frequency tuning, and a Taper laser for the MOT light amplification, deliver all the needed light beams. See Table 2.1 to find the relevant frequencies in the experiment.

The master laser is based on an External Cavity diode scheme [Bolpasi, 2014] that uses a diffraction grating attached to an electronically-controlled piezoelectric element as frequency selector. By monitoring a saturated absorption spectroscopy signal from a Rubidium vapour and tuning the cavity characteristics via the orientation of the piezoelectric, one can achieve a highly stable mode-locked laser beam at the spectroscopical line of interest. In our setup, an RF-coil wrapped around the vapour cell creates a time-dependent modulation of the spin alignment. The laser light is shone through the vapour cell in a double-pass configuration and recorded in a photodiode. In order to retrieve the atomic spectrum, the photodiode signal is demodulated (at the RF frequency that drives the vapour's reference Zeeman

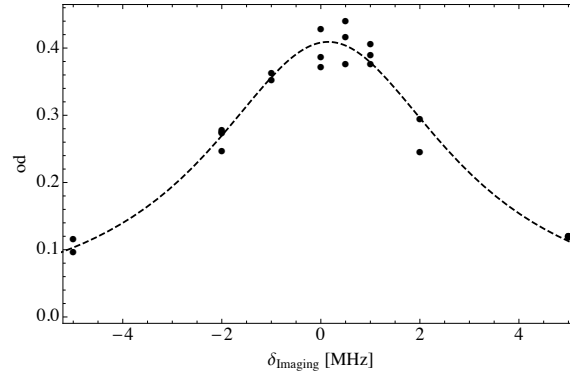


Figure 5.1: Imaging light calibration. Black dots are experimental optical depth measurements of a cold cloud sample of ^{87}Rb . The black, dashed line is a fit to a Lorentzian curve. The fit results are full-width 6 ± 0.3 MHz, Detuning 0.15 ± 0.07 MHz. The quoted detuning is the one set by the experiment's script such that the addition of frequencies of the locking light, AOM1, AOM4 and the AOM at the Taper board are on resonance with the MOT atomic transition (see Fig. 5.2 for detail)

splitting) in a mixer (Mini Circuits ZAD-6). This results in the typical Doppler-free saturation spectroscopy signal for ^{87}Rb and ^{85}Rb . Then its temporal derivative is calculated electronically (see [Bolpasi, 2014; Pandey *et al.*, 2018] for details) and sent to an oscilloscope, where one can visualize the locking point. Our Master laser is locked at the $|5S_{1/2}, F = 2\rangle \rightarrow |5P_{3/2}, F = 1/3\rangle$ cross-over, blue detuned from the $F2 \rightarrow F'2$, $\nu_{\text{lock}} = \nu_{2,2} + 54.85$ MHz. We use this laser for three different experiments, with 5 mW arriving at each one. Fig. 5.1 shows a measurement of the optical density of a cold cloud for several detunings set by the imaging AOM. The expected linewidth for noiseless amplification (assuming no further broadening, which is fair) is the natural linewidth of the D2 transition, which matches with our observation.

The slave laser is a custom-designed/built system that integrates a 780nm diode (Panasonic 200mW 780nm LNC728PS01WW) into an aluminium mount with a small Thorlabs lens C230TMD-B $f=4.51$ mm used to collimate the laser beam. The current is driven from a Thorlabs LDC 202 B, and the temperature is stabilised with a Thorlabs PID TED 200 C connected to a Peltier element attached to the laser mount. A heat sink is attached to the mount and we have also included a fan to ease heat dissipation. The current that drives this laser diode is added with a microwave signal before feeding it. This microwave field is used to modulate the current and produce sidebands detuned by the hyperfine-line transition frequency from the D2 line. The microwave source is also custom-built and has a TTL selector that can

deliver up to three different MW frequencies. The amplitude of the sideband can be tuned in a frequency mixer (Mini Circuits ZMX-8GLH) externally controlled from an analog channel (see Section 5.6), and it is amplified by a Stealth Microwave amplifier (SM6471-37HS). Two sidebands appear on either side of the carrier when this current modulation is applied. One of the sidebands corresponds to the re-pumper light, that can be up to 3% of the carrier peak. The microwave sideband injection is used in the operation of the MOT, the C-MOT and for state-transfer between the two ground hyperfine manifolds. We will briefly discuss these cases.

MW sideband injection in the MOT and C-MOT. In the MOT and C-MOT, we choose proportionally the sideband frequency according to the MOT or C-MOT main frequency set by AOM3 (see Fig. 5.2). This frequency tuning is necessary because both the carrier and sidebands are shifted at the AOM by the same amount. However, the re-pumper should stay on resonance, even if the carrier (the pumper) is detuned. One limitation of our system is that the MW generation set-up is limited to only three frequencies and does not feature a frequency ramp function.

MW sideband injection for state transfer. A state-transfer sequence (F2→F1) is used in the *temporal dark MOT* (see Section 2.1.2), for which only the re-pumper sideband amplitude needs to be reduced, keeping the main peak constant in amplitude. An inverse state-transfer sequence (F1→F2) is needed after a sample has been manipulated in F=1. In this latter case, we employ a less conventional approach. The principle of operation of the F1→F2 state-transfer with a MW injected sideband can be reduced to studying the scattering rates of the two peaks (we neglect the far off-resonant second re-pumper sideband) that come out of the slave laser after microwave injection. One should remember that the re-pumper sideband will not be larger than a 3% of the main peak (this means that the saturation parameters will normally follow $s_r/s_p < 0.01$, where the sub-indices r and p stand for re-pumper and pumper, respectively). We can write generally the scattering rates for both beam wavelengths:

$$\begin{aligned} r_p &= \frac{\Gamma}{2} \frac{s_p}{1 + s_p + \delta_p^2} \\ r_r &= \frac{\Gamma}{2} \frac{s_r}{1 + s_r + \delta_r^2} \end{aligned} \tag{5.1}$$

from where the quotient r_p/r_r is larger than one for any s_r in the working range, assuming that the detuning from the respective transitions is the same. Now, however,

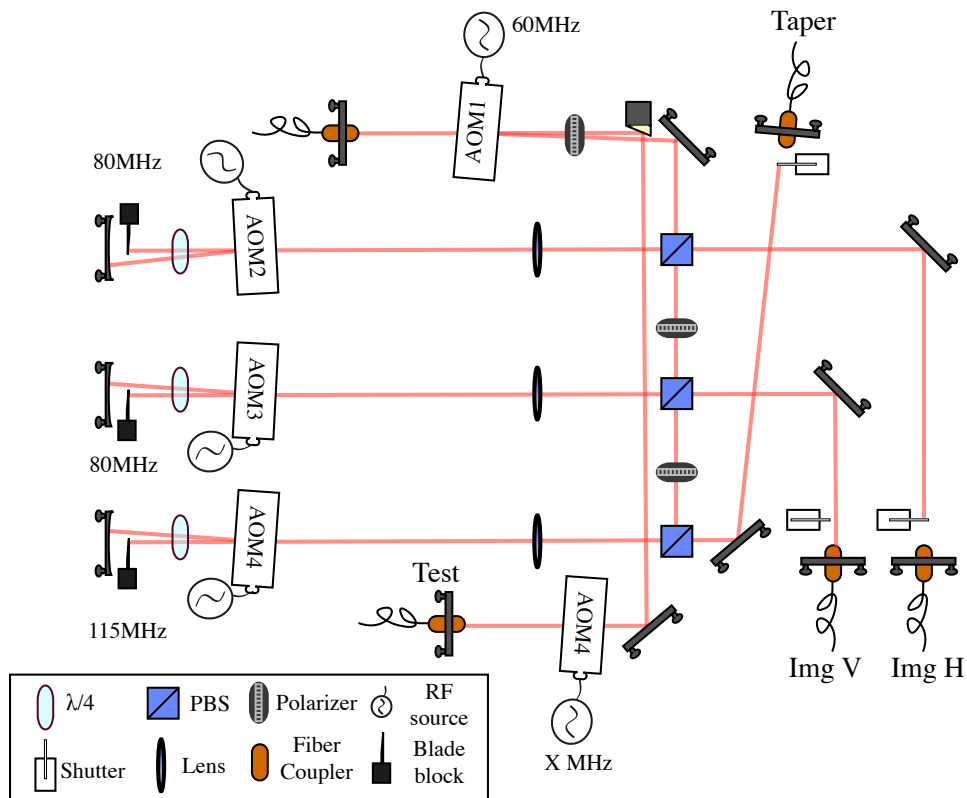


Figure 5.2: Main frequency setting board of the experiment. The input light arrives after the spectroscopically tuned Master laser and the amplification and sideband-setting slave laser, right before “AOM1”. Then, the light is distributed in up to 4 paths with independently tuneable frequency and power. The “Test” fiber goes to the experiment table through a polarisation maintaining fiber. AOM4 is usually not used, but it can be tuned to a frequency X of approx. 100MHz.

if we can tune the pumper and the re-pumper peaks with a different detuning, it is possible to modify the scattering rate dramatically. See for instance the case when $\delta_r = 0$ but $\delta_p \neq 0$:

$$\begin{aligned} r_p &\approx \frac{\Gamma s_p}{2 \delta_p^2} \\ r_r &\approx \frac{\Gamma}{2} s_r \end{aligned} \tag{5.2}$$

These equations yield $r_p/r_r \approx s_p/(s_r \delta_p^2) < 1$ for large enough detuning of the pump beam. This corresponds to a MOT where the scattering rate of the re-pumper is much higher than that of the pumper. This allows for fast transfer of all atoms from F=1 into F=2 whilst minimising scattering for atoms in F=2, which would heat the cloud and result in atom loss.

Practically, we tune the light in the following way: with AOM3 we apply a total detuning of -37.5MHz. Then we change the frequency of the re-pumper MW-modulation by +37.5MHz (to 6700 MHz), making it resonant with the re-pumper transition. Fig. 5.3 a) shows the loading curves from F=1 to F=2 for three different amplitudes of the sideband current modulation. This experiment was performed by preparing a sample in $|1, -1\rangle$ in a magnetic trap, then releasing it and finally applying the sequence explained above. In this figure, the blue curve, where the re-pumper light is 2.5% of the pump beam light, clearly saturates close to 100 μ s. Provided that these clouds have relatively low optical density, one can conclude that all atoms have been transferred to the upper state³. Fig. 5.3 b) shows how some of the relevant parameters in this sequence change in a typical experiment. Blow-away light-pulses are required both in the de-pumping (during temporal dark MOT) and re-pumping (during state-transfer for imaging) stages. These pulses are usually performed with several of the MOT beams plus one of the imaging beams tuned on-resonance and applied for short periods of time. Note that in this figure the grey-coloured "Experiment time" includes the sample preparation from the Magnetic trap up until evaporative cooling, plus the sample manipulation/interrogation with RF or MW-fields.

Tapered amplifier The total power at the output labelled "Taper" in Fig. 5.2 after setting all necessary light frequencies is of less than 2mW. To achieve a reasonably large MOT one needs of the order of 1W of near-resonant light [Bolpasi

³When the cloud is optically thick and large pumping can become cumbersome for low laser intensities.

and von Klitzing, 2010]. We used a tapered laser for about two years and then a double-pass tapered amplifier. The tapered laser exhibits normally narrower locking plateaus, similarly to a slave laser⁴, whereas the double-pass tapered amplifier is usually both easier to lock and provides some leeway in the current control. These systems need currents between 1-2A and very good thermal stability at rather low temperatures⁵ to avoid heating of the electronics and semiconductor components. The double-pass laser (in our setup, an Eagleyard 2W GaAs semiconductor laser diode) offers an advantageous low injection power, normally below 1mW, whereas the tapered laser threshold is of the order of 3-5mW. The low injection power can make a difference if the light source has been split in many paths, as it has been in our case. One needs to shape the output beam-shape carefully to achieve acceptably large coupling efficiencies in optical fibers (this CE is usually below 50%). For this purpose, we use a small lens (Thorlabs C230TMD-B $f=4.51\text{mm}$) close to the front side of the diode in order to collimate the vertical axis and a cylindrical lens ($f=50\text{mm}$) in order to shape the horizontal axis of the beam that exits the taper. In the double-pass configuration, another lens (Thorlabs C230TMD-B $f=4.51\text{mm}$) is placed at the back of the diode mount. This lens can be used either to collimate or focus the back-beam into the back-injection mirror, which is placed at approximately 5cm. It is an interesting question what should be the ideal distance between the mirror and the lens. We found that focussing the beam onto the mirror *reduces* the sensitivity to the alignment by up to a factor of 1000 at short distances⁶. As the mirror is placed further away, the difference becomes smaller, since the *focussed* and *collimated* beams become equivalent by definition.

MOT set-up. The laser light after amplification in the Taper travels 5m in a polarisation maintaining fiber to the enclosed experiment table. There, a fiber output collimator sends the light into a distribution board. This board contains 16 fiber couplers. Among them, 12 are for the 3D-MOT beams and 2 for the 2D-MOT beams. One more output is for a push beam used to feed the 3D-MOT from cold

⁴The principle of operation is the same

⁵For Cretan standards. This is a serious question, insomuch as humidity within the laboratory can reach up to 60-70% in the worst summer days even with two dehumidifiers working at full power. If one is not careful and the temperature at the diode drops below the dew point, water condensation may occur at the laser's mount and result in permanent damage to the diode.

⁶I measured this quantity by comparing the alignment sensitivity (defined as the number of degrees turned in a knob in the mirror mount where the output power would half from the maximum) for several back mirror positions both for collimated and a focused beam. These distances ranged from 2cm to 50cm

2D-MOT atoms. The light from the output labelled as “Img H” in Fig. 5.2 is also sent to this distribution board and then into one of the 3D-MOT beams in \hat{e}_z , so as to be aligned with the vertical imaging camera (see Section 5.3). All the fiber couplers are mounted in aluminum posts that are glued unto a granite plate. Elements such as shutters, quarter-wave plates or PBS are also mounted in similar posts and arranged in the same manner. These elements are used to tune the relative power between the beams or to selectively remove them from the experiment site. The MOT beams need to have a large diameter. Therefore, after passing through the optical fibers that exit the distribution board, the light goes through a collimating lens that delivers beams of 2.5cm. Moreover, these light beams need to be circularly polarised. For this purpose, the same standard Thorlabs tube that holds the collimating lens includes a quarter-wave plate as well [Pappa, 2011].

5.3 Imaging system

The two principal techniques used to probe cold atom clouds are fluorescence and absorption imaging. Fluorescence imaging is based on a process of near-resonant absorption and re-emission of laser light by the atoms and it can provide information on atom number, but great care needs to be taken to avoid blurring of the cloud. Images of the scattered light are collected with a camera. We use this method to monitor the MOT loading. Absorption imaging is based on the absorption of near-resonant light by the atom cloud as a weak laser beam traverses it and relies on the detection of the shadow imprinted onto the beam with a camera. When using the absorption imaging technique (which is the default technique in most experiments) we take three pictures in each run of the experiment: 1) the cloud 2) the imaging beam and 3) the background. Then we perform the operation:

$$T = \frac{I_{\text{cloud}}(z, y) - I_{\text{background}}(z, y)}{I_{\text{light}}(z, y) - I_{\text{background}}(z, y)} \quad (5.3)$$

and we calculate the optical density [Pappa *et al.*, 2011]:

$$\text{od}(z, y) = -\log(T) + \frac{1}{\log(10)} \frac{I_0}{I_{\text{sat}}} \frac{1}{1 + \delta^2} (1 - T) \quad (5.4)$$

where z and y are two axes that define the plane of imaging. The total magnification of the imaging system is the quotient of the objective magnification and the binning

at the camera's CCD array⁷. Our setup uses up to four cameras. Two small CCDs record a fluorescence signal of the loading of the MOT and are used for the alignment of the MOT beams and also to optimise the free molasses expansion when needed. A third low-noise high-resolution camera Andor Ikon-M 934 is placed on top of the cell and facing downward. This is particularly useful to visualize the ring traps and *horizontal* double wells. The fourth camera is another Andor Ikon placed in the horizontal plane with a field of view of 3 mm. This camera is most useful in free fall measurements, for instance, of temperature, or of the different expansion of a thermal and a condensed clouds. The small CCDs use commercial objectives, and there is no particular interest in the accurate knowledge of the cloud size based on those images. The absorption imaging cameras are equipped with interchangeable microscope objectives and they are set after a $4f$ -type objective that is set close to the experiment cell [Pappa, 2011; Pappa *et al.*, 2011].

Two-states imaging. When performing some spectroscopy experiments, it is important to know the population of the different spin states involved in the atomic transitions. Acquiring this information typically involves imaging two different spin-states. In our case, we are interested in imaging atoms in the $F = 1$ and $F = 2$ ground hyperfine manifolds of ^{87}Rb , which are set apart by 6.834 GHz. In our sequence, we use the two Andor Ikon cameras to image atoms in each of the spin states. Fig. 5.4 shows schematically the experimental sequence. A sample initially prepared in the $F=1$ manifold, undergoes a MW transition that sets the cloud in a mixture of $F=2$ and $F=1$ atoms (notice that in order to distinguish between m_F states one would need an additional Stern-Gerlach pulse). At this stage, and after a short ToF ($t < 3$ ms), one short ($t < 200\mu\text{s}$) pulse of near-resonant light images the atoms just transferred from $F=1$ to $F=2$. After 1ms, a 3ms MOT+resonant light pulse illuminates the cloud in order to heat and remove all $F=2$ atoms. Afterwards, a short ($t < 200\mu\text{s}$) MOT tuned for *state transfer* (see Section 5.2) pumps all atoms from the $F=1$ manifold into the $F=2$ manifold, and these atoms are imaged in the last step in one of the other Andor Ikon cameras. For absorption imaging, one needs three pulses of near-resonant light in the D2 line. Therefore, the two remaining images are taken with both cameras at the same time. Using two-cameras allows for faster operation and very simple handling of the image files for posterior analysis. Imperfections in the blow-away sequence, and especially, in the syncing of all pulses, have sometimes led to imprecise atom number counting. Normally this measurement

⁷for instance a $\times 1$ objective with binning 2 in the camera chip, corresponds to a magnification of 0.5

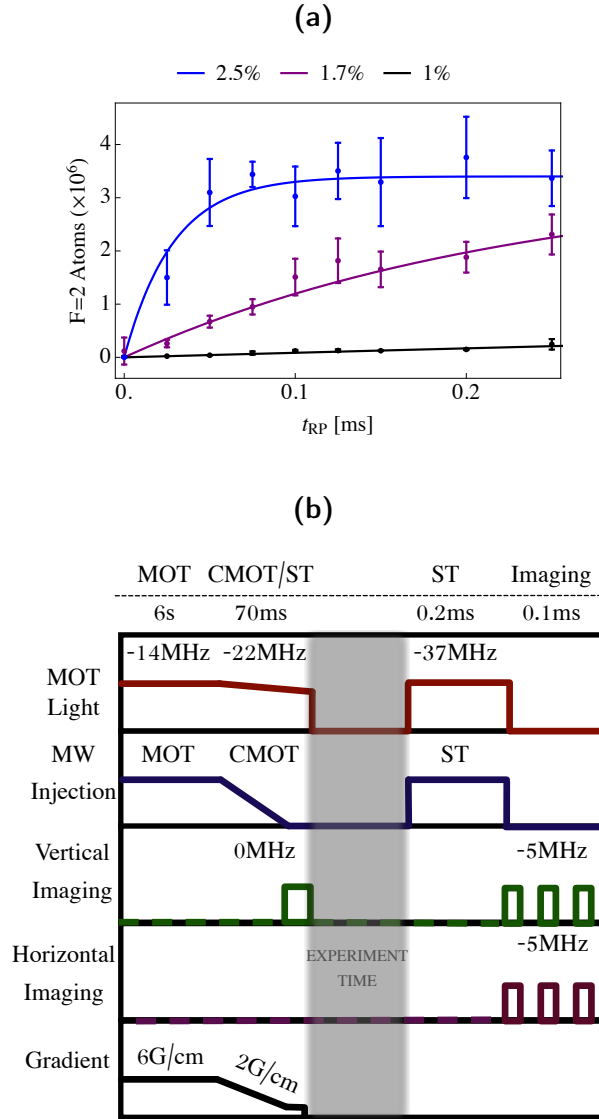


Figure 5.3: a) Transfer curves of atoms from the $F=1$ manifold into the $F=2$ manifold via laser pulses of MW sideband modulation for different amplitudes in the current modulation. b) A general experimental sequence. To obtain the data in (a), the gray coloured area in (b) consisted of a cloud evaporated in the quadrupole down to $T \propto 20\mu\text{K}$. Detunings from the D2 line are quoted in MHz in this figure for the several light sources used in the experiment. The parameters shown in the figure are valid in most of the experiments shown in this thesis, i.e., atoms may be manipulated in different ways within the grey coloured area, but both stages of state-transfer remain unchanged.

can be corrected in data post-processing, by counting the total atom number with each camera and re-scaling the *incorrect* measurement accordingly (see Appendix C).

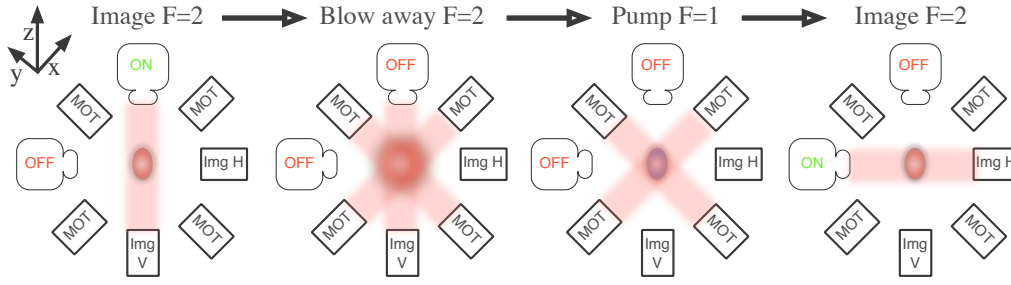


Figure 5.4: Two state imaging sequence in cross-cut schematic of the set-up. Rectangular shapes labelled “MOT” represent the horizontal MOT beams, “Img H” represents the horizontal imaging laser beam and “Img V” represents the vertical imaging beam. Both imaging beams are only resonant with atoms in the ground hyperfine manifold $F=2$. The target sample contains atoms both in sub-states of $F=1$ and $F=2$. First, we image the atoms in $F=2$ with a short pulse (atoms in $F=1$ remain unperturbed). Second, we blow away all atoms in $F=2$ with a resonant pulse in several directions. Third, we apply a pumping sequence (see Fig. 5.3 and accompanying text). Fourth, we image the $F=1$ atoms that were pumped to $F=2$.

5.4 Dipole trap laser system

In order to improve the repetition rate of the experiment, and also to ease the loading of BECs into the TAAP ring, we installed a dipole trap, which replaced the TOP trap as the sample preparation method⁸. This new system has allowed for production of BECs with a total of only 50 mW of laser light for the 2D-MOT and 3D-MOT [Pandey *et al.*, 2018], although we normally operate with approximately 500 mW. The current setup (see Fig. 5.5) has produced BECs in a single-beam plus quadrupole, double-beam plus quadrupole and double-beam without quadrupole⁹ configurations. We have also demonstrated a slight improvement in efficiency when a TOP-field is included¹⁰. Our dipole trap setup has been inspired by other works in the literature [Faber, 2011; Lin *et al.*, 2009]. The laser head (Azur Light Systems 20W 1064nm) delivers, in standard operation, 18W, as chosen by the user (we do not employ external control of the amplitude in the laser power supply). The beam diameter is of 1mm. To reach the desired waist at the atoms’ position, we use a beam

⁸The BEC production time with the TOP trap sequence would take up to 50s, whereas we managed to produce BECs with the dipole trap, after optimising the early stages too, as fast as 15s.

⁹During evaporation in the dipole trap

¹⁰However, we do not employ this method typically unless the final desired trap is a TOP trap, since this alternative provides a rather light gain.

expander with two 1 inch diameter lenses ($f_{L1} = -200\text{mm}$, $f_{L2} = 500\text{mm}$, with effective focal length of -60mm) that collimates the beam into a 2.1mm diameter size at the position of L3 and L4 lenses. In between, there are two AOMs (Intra Action ATM 803FB6), set at least 1MHz apart to avoid creating fringes at the trap position. The AOMs frequency can be set to fine tune the trap position once manual alignment has been performed. They are normally set close to 68MHz and 70MHz. These two AOMs are positioned in an orthogonal configuration, thus providing a total of four beams, of which we only use two. The AOMs are driven from a Rigol DG4162 that is connected to two Kuhne electronic VHF mosfet power amplifier KU PA 006008 - 30 HY (fed by their respective *Mean Well* Sp-150-13.5 supplies). The maximum voltage set in the Function Generators is 5Vpp and an attenuation of 17dB prevents damage of the AOMs, which receive in the end a maximum of 2.5W RF drive power and reach an 85% efficiency in the first mode. The RF-field that drives AOM1 (from Fig. 5.5) passes through a switch (Mini Circuits ZMSW-1111), and the amplifier is connected to a security interlock system such that if any of the experiment enclosure gates is opened during operation, it switches off. This same security system turns off the laser power supply if security is breached. Two half-inch diameter lenses, labelled in the sketch as “L3” and “L4” (with focal length 25.4cm) focus the expanded beam right at the center of the quadrupole trap. All optical elements are clamped down together with the laser head on a standard optics table. Lenses L3 and L4 are mounted on aluminium posts which are in turn glued to the marble table. This setup leads to two beams with waists $w_0 = 66\mu\text{m}$ at the center of the trap and a Rayleigh range of 0.8cm.

In order to align the dipole trap beams, we first matched a 780nm light-beam coming from the “Test” light output (right after AOM4, which is normally off) from the AOM board shown in Fig. 5.2 to the center of the quadrupole by extinguishing a free running MOT. Afterwards, via a two-pinhole alignment algorithm, we matched the beam path of both arms of the dipole trapping light with the 780nm light. This 780nm beam would be aligned passing, from one of the beam dumps, through a pinhole, the cell, and another pinhole, until the laser head output. Then, we used mirrors M2 and M4 to align one of the dipole beams and M2 and M5 for the other dipole beam (keeping always M1 fixed) to align the dipole beams onto the beam dumps, following the seam path as the 780nm light. Afterwards, we loaded atoms into each of the dipole beams and used the vertical camera and a reference image of a tight cloud in the quadrupole to adjust further the lenses position L3 and L4 (to set the focus of the trap exactly in place) and mirrors M4 and M5 to set the crossing point. This procedure yields excellent results in the $10\mu\text{m}$ regime. To

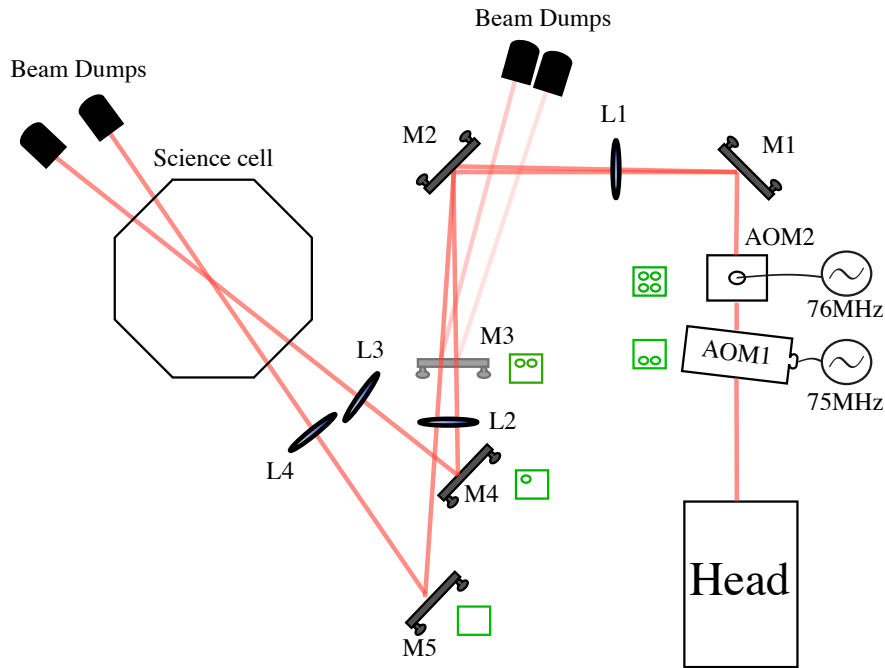


Figure 5.5: Dipole Trap laser setup sketch. The green squares indicate the distribution of the beam intensity in the vertical plane. The labelled “AOM1” splits the initial beam into a first and second mode (first green square) and the labelled “AOM2” splits these two beams further into a total of four beams. The two lower modes are then dumped and the two upper modes are used for trapping, as the three remaining green squares indicate. In this drawing, M refer to mirrors, with numbers 1,2,3... L refer to lenses.

fine-tune the height and beams-angle, we employed the frequency tuning of the AOMs.

One noteworthy problem faced when trying to load the BEC into a ring trap was that, initially, very large fluctuations in the transfer efficiency and *shaking* of the atomic cloud were present, especially with very cold clouds. These problems were due to the fact that we had placed the first set of beam dumps where M3 is shown in Fig. 5.5. These beam dumps, which are made of copper, would heat up to more than 100°C . These hot objects would modify the index of refraction of the air through which the laser beams travel. The rarified air caused the beam to wobble with a magnitude as high as $40\mu\text{m}$ at the center of the trap (measured with absorption imaging of a small cloud). By changing the beam dumps position to where the sketch indicates, this wobbling went down to about $3.5\mu\text{m}$, BEC production improved by a factor of 3 and we could successfully load BECs in the ring traps. In normal conditions, the BEC atom number stability is of 12%.

5.5 Magnetic fields

This section reviews all magnetic fields used in the experiment. sub-section 5.5.1 deals with DC magnetic fields, sub-section 5.5.2 with Audio Frequency magnetic fields, sub-section 5.5.3 with Radio Frequency magnetic fields, and sub-section 5.5.4 with Microwave frequency magnetic fields.

5.5.1 DC magnetic fields

We employ a quadrupole trap field created by a pair of coils in anti-Helmholtz configuration in the vertical direction, and several bias fields. There are two sets of three pairs of Helmholtz-configured coils. One of these sets is close to the experiment cell and it can drive either DC or Audio fields (with an LC resonator). The other set consists of large coils, of the size of the experiment gates, and they are used for weak (< 1 G) magnetic fields compensation. Fig. 5.6 shows a scheme of all DC-field generating coils.

Quadrupole fields Strong quadrupole magnetic fields (up to 300Gpcm) for the magnetic trapping are generated through the pair of anti-Helmholtz coils (see brown coils in Fig. 5.6) from a Delta Electronika SM 15-400, externally controlled via the AO32 from the PC (see Section 5.6). A locally-made fast switching system with rise-times of the order of $100\mu\text{s}$ and fall times of the order of $5\mu\text{s}$ [Pappa, 2011] allows for proper manipulation of the atomic cloud. We use another power supply Delta Electronika ES015 10, connected to the same coils through a similar switching circuit, to be used in the MOT sequence. This configuration, with one PSU dedicated to the MOT stage and another to the Magnetic Trapping stage, allows for reliably sharper switching between low and high current in the magnetic trapping loading.

Residual quadrupole fields. An interesting quantity to be known in spectroscopy measurements is the residual quadrupole field with the PSU turned off and, especially, in stand-by mode. We used the spatially dependent coupling of an atomic transition associated to the quadrupole field to estimate the residual field fluctuations. For a freely falling cloud in $F=1$, atoms are transferred via a MW pulse to the $F=2$ manifold at the point in space where the MW field is resonant. We found that, when the switching circuit between the PSU and the coils is set to *ON* and the PSU is in stand-by mode, the residual quadrupole field is $B_q = 0.159 \pm 0.002\text{Gpcm}$. When the switching system is set to *OFF*, $B_q \approx 0.018\text{Gpcm}$. This means that there

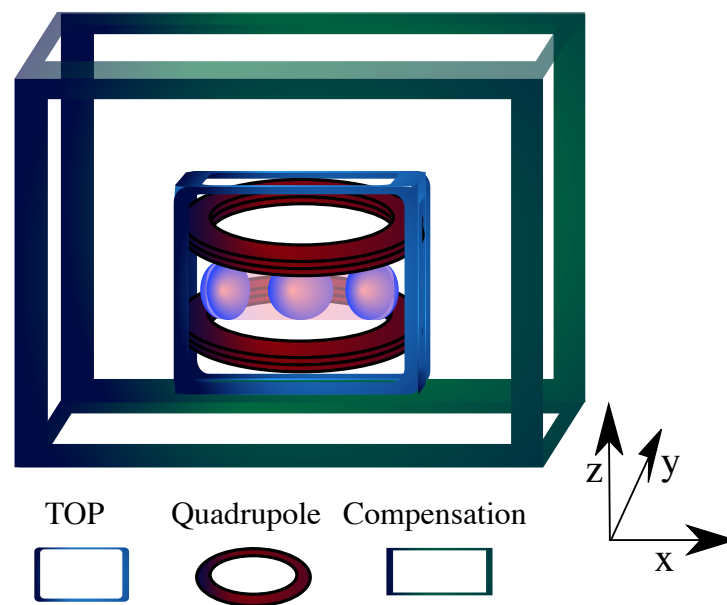


Figure 5.6: Schematic drawing of all the DC-field generating coils that surround the experiment cell (placed in the center of the image). The green square coils represent the compensation coils, which are in reality much bigger compared to the TOP and Quadrupole coils, as the text explains. The TOP coils (blue) are also used for DC magnetic fields. The quadrupole coils are represented by brown rings.

Field direction	B_{\perp} (G)	$\xi(G/A)$	$I_0(A)$
\hat{e}_x	0.083 ± 0.0004	-0.1256 ± 0.0004	-1.782 ± 0.004
\hat{e}_y	0.089 ± 0.003	0.124 ± 0.004	-0.74 ± 0.03
\hat{e}_z	0.09 ± 0.02	0.47 ± 0.02	0.08 ± 0.02

Table 5.2: Earth’s magnetic field compensation coils (see Fig. 5.6) calibration.

is some residual quadrupole field even when the PSU driving the coils is off.

DC-fields Three pairs of 14cm wide Helmholtz coils¹¹ lie in the three axes close to the experiment cell (these are the blue coils in Fig. 5.6). Another set of four coils with dimensions $1.5 \times 0.85\text{m}$ is attached to the structure that surrounds the experiment. These two pairs are oriented in the x and y directions. One more pair of dimensions $1.5 \times 1.5\text{m}$ rests on the same structure and creates a nearly homogeneous field in the vertical direction z. These coils are represented in Green in Fig. 5.6. These bigger coils were initially designed to compensate the Earth’s magnetic field. They have approximately 0.125G/A (\hat{e}_x direction), 0.125G/A (\hat{e}_y direction) and 0.5G/A (in the z direction). They are all driven from a Delta Electronika EST 150.

DC-fields calibration. To calibrate DC-fields we employed inter-manifold atomic transitions between Zeeman sub-levels. We used the two-photon transitions between $|1, -1\rangle \rightarrow |2, 1\rangle$ and $|1, 1\rangle \rightarrow |2, -1\rangle$ and the one photon transition $|1, 0\rangle \rightarrow |2, 0\rangle$. These transitions are simple to find and address even when the DC-field is unknown, since the detuning -from $\omega_{\text{hfs}}/2\pi$ - needed in the MW is smaller according to their differential Breit-Rabi shifts (see Section 3.1). The Earth compensation coils calibration was performed based on this idea, and assuming a linear Zeeman shift with total magnetic field $|B| = \sqrt{B_z^2 + B_{\perp}^2}$. We used one-photon MW-transitions with $\Delta m_F = \pm 1$. We would prepare a Molasses in free fall and shine a MW pulse close to the hyperfine splitting. Then, we assume the simple dependence of ν -the MW transition frequency-, $\hbar\nu = g_F\mu_B\sqrt{B_{\perp}^2 + \xi(I - I_0)^2}$ where ξ gives us the G/A scaling, B_{\perp} is the orthogonal field component and I_0 is the current at which the field in the scanned direction is minimum. By scanning the current I , in independent experiments, in all $\hat{e}_x, \hat{e}_y, \hat{e}_z$ directions, we find Table 5.2, from where the most important number is ξ , for it gives a very precise calibration of the G/A and it is independent of the measurement day’s overall DC-homogeneous field background.

¹¹These coils are also used in the production of audio-frequency fields

5.5.2 Audio-frequency magnetic fields

The audio-frequency fields are generated from an audio card that feeds two audio amplifiers. One amplifier (CROWN XLS 200) usually drives the Blue coils from Fig. 5.6 in the \hat{e}_x and \hat{e}_y directions, whereas the other amplifier (Cambridge Audio P500) drives the coils in the \hat{e}_z direction. These amplifiers receive an input of $< 1V_{pp}$ and deliver a magnetic field of up to 48G at the atoms position after passing an LC resonator circuit tuned to 5.02KHz. The TOP coils are the same set introduced earlier, in Helmholtz configuration, close to the experiment cell. Beforehand, we saw how to use them to drive DC-fields in all directions but both fields can be driven at the same time, or alternatively. In the \hat{e}_z direction a relay switch prevents cross-coupling with the quadrupole coils¹². The audio-fields waveforms are written in Mathematica. The user employs the intuitive nomenclature of polarisation for these fields. For instance, a π_z polarised TOP-field would contain only a one component in the \hat{e}_z direction. Another example: a $\sigma_{x,+}$ would contain one field component in \hat{e}_z and another in \hat{e}_y with a difference of phase of $\pi/2$.

Audio-fields calibration To calibrate the amplitude of the audio fields we used RF-spectroscopy in a TOP trap. With this method, it is relatively simple to achieve a precision of 5 mG, especially when one works with very cold clouds or, ideally, with a BEC. It works by inducing intra-manifold transitions with a weak RF-field. Atoms undergo transitions when the TOP-field amplitude is resonant with the RF-field frequency. Provided an accurate knowledge of this frequency, one can retrieve the magnetic field amplitude from the resonant condition. Now, if one employs a TOP-field with some ellipticity, then the longer axis will be *first* resonant with the RF-field, thus allowing for independent calibration of two pairs of coils. The phase was calibrated by measuring in an oscilloscope after the field would traverse the coils and several water-cooled a 6Ω resistor.

5.5.3 Radio-frequency magnetic fields

Radio-frequency fields are used in RF-dressing experiments, RF-evaporation and also RF-spectroscopy. In each case, different features are needed. For instance, the control of RF-fields polarisation is key in RF-dressed traps whereas it is important to

¹²In this direction, both DC and AC fields should not be run together, given that cross-coupling from the quadrupole is very strong.

achieve smooth frequency ramps in RF-evaporation. We typically use conventional Function Generators (such as the Rigol 1062, Rigol 4162 and Lecroy waveStation 2012) that are connected to the main external reference clock and receive the adequate control inputs from the DIO64 and AO32 cards. Our set-up has three pairs of custom-made Helmholtz-type antennae with LC resonators tuned to 2.2 MHz (along \hat{e}_x and \hat{e}_y) and 2.6 MHz (along \hat{e}_z) with ceramic capacitors. We measured a FWHM of 100kHz in all cases with a Network Analyser Rhode and Schwarz ZVB. The three pairs of coils are fed by their respective Minicircuits LZY-22+ amplifier. RF-evaporation could be generated with either function generator or from an AD9854. We used a Research Amplifier 25A250A that drives a one loop coil without a resonator placed in the horizontal plane. In this case, the polarisation is not very important.

Radio-frequency evaporation. It is useful to know the efficiency of RF-evaporation cooling. One can start by checking the Phase Space Density and the collisional rate as the cloud is evaporating. Another solution is to use of a powerful empirical law, which states that in *good* RF-evaporation, the atom number and the temperature will scale as:

$$\xi = \frac{d \ln(T)}{d \ln(N)} \quad (5.5)$$

This establishes by how much temperature decreases as atoms are lost from the trap [Christodoulou, 2015]. It has been found that ξ remains constant throughout evaporation and, more importantly, that its value is close to $\xi \approx 1.1$ in the Ioffe, TOP or quadrupole traps. The actual scaling if the trapping frequency changes during evaporation is $N \propto (T/\omega)^\xi$, where ω is the trapping frequency. Therefore, a reasonable figure of merit if one needs to know whether their RF-evaporation is working well is by checking whether $\xi \approx 1.1$. An efficient evaporation not always leads to BEC. The initial PSD needs to be large enough such that this cooling rate reaches the condensation point before the regime of runaway evaporation (or, said bluntly, when there are no collisions left).

Radio-Frequency fields calibration

Amplitude calibration. To calibrate the RF-field amplitude (especially the dressing RF-field) we use either RF transitions between RF-dressed states (see Section 3.2.1 and Section 7.1) or MW transitions between RF-dressed states (see Sections 3.3, 7.2 and 7.3). This is somewhat inconvenient for newcomers to dressed

trap experiments: how can one know what is the Rabi frequency before loading the trap? And it is not a trivial question: if the Rabi frequency is too low, no RF-dressed trap will be formed. One possible solution is to drive a two photon transition with the RF-frequency set to the desired RF-dressing frequency. Then, one should observe a line-shift, similar to a Stark shift, that depends on the RF-field amplitude as it is increased. From this shift, one can estimate the RF-field amplitude. If one does not have access to a microwave source, then the solution is to calibrate a DC-field that will be used for dressing, program the theoretically ideal loading sequence into the RF-dressed adiabatic potential (see Section 7.1.1 for a description of the loading from a TOP trap and Section 7.3 for a description of the loading from the crossed dipole trap) and increase the RF-field amplitude until one observes a signature of transfer into the new trap. This signature is normally a change in position, aspect ratio or both. It is a good idea to use resonators in the field generating coils to achieve relatively easily fields of the order of 1 G.

Phase calibration. We calibrated the phase of the RF-fields with an atom cloud. In order to generate circularly polarised RF-fields of a given handedness $B(t) = \cos \omega t + \sin \omega t + \phi$, one needs to drive two of the sets of coils (say along \hat{e}_x and \hat{e}_y) with a phase difference that will be either $\phi = \pi/2$ or $\phi = -\pi/2$. Fig. 5.7 shows the normalised atom number (state $|2, 2\rangle$) in a dumb-bell trap [Sherlock, 2011] after loading from a TOP trap for a circularly polarised TOP-field that is rotated in the plane of the RF-field. In one case, we see that, for a linearly polarised RF at 45° , the coupling strength goes to zero when the RF-field and the TOP-field become parallel. In the case of a circularly polarised RF (b) we see that atoms are only trapped when the TOP trap is circularly polarised (regardless of handedness, which is depicted as Blue and Red dots) and aligned with the circularly polarised RF. However, we also see that this is an asymmetric distribution, coming from the fact that, when the RF-field is circularly polarised there is a state-dependent coupling (see Section 4.1.1). The yellow (grey) area indicates the simulated region of high (low) RF-field coupling. These can be retrieved also from Section 4.1.1, in particular from Eq. 4.9. Good references on this topic are [Sherlock, 2011; Gildemeister, 2010].

Radio-Frequency generation for the bi-chromatic shell

This sub-section gives a detailed description of the RF-fields generation needed for the bi-chromatic shell trap, that will be introduced later in Section 4.2 and studied

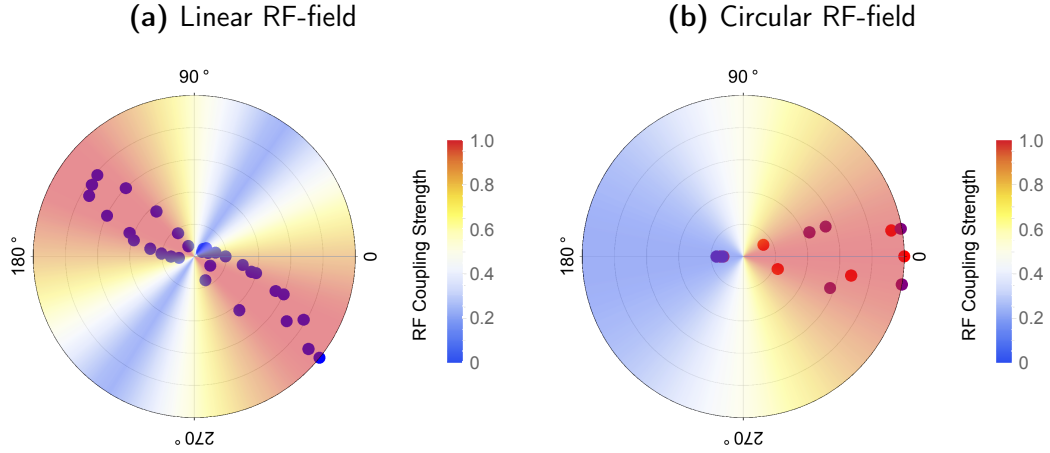


Figure 5.7: a) RF coupling strength for a linearly polarised RF at -45° in the xy plane
b) RF coupling strength for a circularly polarised RF. In both cases the dots represent experimental data. Red for vertical TOP rotation along X. Purple for rotation along Y.

experimentally in Section 7.4. As it was introduced before, the cell in the experiment is surrounded by three pairs of Helmholtz coils in the \hat{e}_x , \hat{e}_y and \hat{e}_z directions. The coils in the \hat{e}_x and \hat{e}_y have been tuned with LC circuits to a resonance with $Q \approx 20$ at $\nu \approx 2.2$ MHz. The desired RF-field consists of two circularly polarised components, at two different frequencies, with opposite handedness, as in Eq. 4.24. We feed each of the horizontal coils with the corresponding two-frequency component input, added from two function generators in separate power splitters. This is depicted in Fig. 5.8. The frequency generation sources are a Rigol DG4162 for the parameters with subindex 1 and a Rigol DG1062 for the parameters with subindex 2. The power splitters are a Minicircuits ZFRSC-42-S+ and ZFRSC-123-S+ and both amplifiers are Minicircuits LZY-22+. The microwave source used to drive the hyperfine transitions is a Rhodes and Swartz SMB 100A. The microwave dipole antenna is home-made and tuned to the hyperfine line at 6.834 GHz.

5.5.4 Microwave-frequency magnetic fields

The complexity of the microwave fields used in this thesis is far less from that of the RF-fields. We use short pulses to drive transitions, with no stringent control of the polarisation. Therefore, we use a custom-made dipole-type antenna set close to the experiment cell. We use a MW amplifier that is fed from a Rhode and Schwartz SMB 100A MW-field synthesiser. We measure a signal line-width of 10Hz with our Vector Network Analyzer. We use a switch (Mini-Circuits ZASWA-2-50DR+),

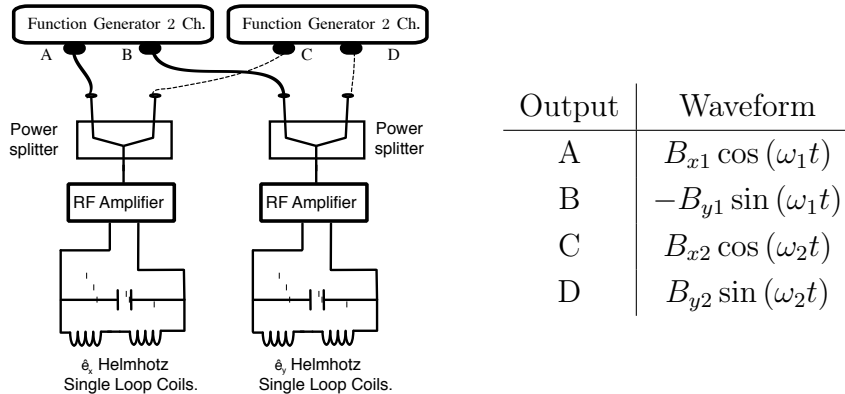


Figure 5.8: Sketch of the RF generation set-up. Two commercial function generators feed two power splitters where the \hat{e}_x and \hat{e}_y components of B_1 and B_2 are added and then fed, after amplification, to two pairs of single-loop Helmholtz coils oriented along the relevant axes, and tuned via resonators close to 2 MHz.

together with the switching capabilities of the MW synth. The signal is further amplified by a Stealth Microwave SM6471-37HS-06-23 whose output is connected to the antenna. The SMB Synthesiser produces up to 18dBm. The switch introduces a loss of 15dB and the amplifier a gain of 40dB. Finally, the 1m-long cable from the amplifier to the antenna introduces a loss of 3dB/m. A simple LabView script sends a frequency and amplitude setting for the MW field for each experiment run, and it cannot be changed in its duration. We would normally work with a dipole antenna with a sharp resonance at 6.83 GHz placed close to the vacuum cell. The setup includes also a waveguide antenna that is mounted close to the experiment cell, at 45° from the z-axis.

5.6 Experiment control

Two interface cards perform most data transfer tasks between the computer-generated control sequences and the equipment used for the atoms manipulation. These are the 64 TTL channel FPGA DIO-64 from Viewpoint Systems¹³ and a 16-bit 32 channels PXI analog card from National instruments (model 6723). From now on we will call these cards DIO64 and AO32. In order to generate the audio-frequency waves necessary for the TOP and TAAP traps we have used several audio cards, always with the corresponding ASIO drivers. These have been: AudioFire12, the

¹³This is a discontinued product according to the website <https://www.viewpointusa.com/product/pxi/dio-64-event-detection-control>

0	Quadrupole_Gradient	120
0	RF_OnOff	off
1.5	x-----x	x----x
0	Quadrupole_Gradient	10;200
0.5	x-----x	x----x
0	AOM_Dipole_Total_Amplitude	0.97
1	x-----x	x----x
0	AOM_Dipole_Total_Amplitude	0.48;500
1	x-----x	x----x
0	AOM_Dipole_Total_Amplitude	0.3;200
1	x-----x	x----x
0	AOM_Dipole_Total_Amplitude	0.2;200
1	x-----x	x----x
0	AOM_Dipole_Total_Amplitude	0.19;200
1	x-----x	x----x
0	AOM_Dipole_Total_Amplitude	0.18;200
1.3	x-----x	x----x
0	AOM_Dipole_Total_Amplitude	0.165;200
0.5	x-----x	x----x
0	AOM_Dipole_Total_Amplitude	0.165
0	Quadrupole_Gradient	2;500

Figure 5.9: Example of a script in the user-friendly Microsoft Excel interview. Colors can be used to highlight devices or time-events and sequenced-block manipulation is easily at hand.

M-Audio 1010LT and also the MOTU 828 Mk III Hybrid. These cards were typically set at 48kHz and 16bit and all of them matched the experiment noise level requirements, with no noticeable difference. The fastest time-scale needed is set by the imaging light pulses, which need transients faster than μs . This is easily achieved with standard AOMs and the specifications of the digital and analog cards. In order to synchronise all actions in any experimental sequence a 10 MHz Rubidium clock feeds the chassis hosting the AO32 card, the Word Clock input of the audio cards and the external clock reference of the DIO64. This same clock is used eventually in RF generation too. In order for all events to be fully synced when sound is present in the experimental sequence, a synthesised TTL pulse is included in the .wav file read by the sound-card, which afterwards passes as the external initial trigger for the DIO64, and this is in turn cascaded into the AO32. When included in the experimental sequence, the RF-generation card AD9854 would also receive this external clock reference.

In a typical experiment, we employ Microsoft Excel sheets to write temporal intervals linked to events, which are clearly stated by user-friendly naming of the devices (examples could be "AOM Imaging" or "Andor Ikon Trigger"). See Fig. 5.9, where I show how one would write the dipole trap evaporation sequence. This

format facilitates highlighting relevant parts of the sequence, re-structuring whole sections of it, or copying and pasting them from one sheet to another. Moreover, it reduces the training time of new users (spreadsheets are of general usage outside the laboratory). A Mathematica file-handling-script running in the background is tasked with converting the .xlsx files into .xml files. At the same time, it translates and classifies the sequence of events and device names into the proper I/O final channel. To do this, it uses the information encoded in a settings database written in C++. This processing will assign a time, a card name and a channel according to the database setting. At this stage, one can also program needed time-delays, which are most convenient when using light shutters. Afterwards, another Mathematica script translates the temporal sequence of classified events into HEX code for the DIO64 card, and into a sequence of events -real numbers- for the AO32 card. The DIO64 is programmed in a FIFO streaming mode, which yields a loading of the order of seconds for sequences below 5000 steps (this number of steps includes ramps in the AO32, for which *empty* events need to be programmed in the DIO64 card as well). For a number of steps well below 10000, the time-limiting factor for the script full compilation is the sound-generation. This is due to the fact that sound files need to last as much as the whole experiment sequence, even if the audio-frequency magnetic fields are needed for only few seconds, because the sound wave is the one setting the initial trigger. For a 3 channel .wav file with a Sample Rate of 96kHz and a Sample Depth of 8bit the time constant is of 0.12s/s (i.e. 0.12s per second in the 3 channel wav file). This translates into times of the order of 3s for a typical experiment of 20-30s and in consequence the experimenter can change parameters safely from one run to the next without blank time.

6

BEC in a TAAP

This chapter includes two main sections. In the first part, we explain all the steps leading to BEC in a typical experimental sequence in our setup (section 6.1). In the second part, we explain the loading of BECs and ultra-cold thermal clouds into a TAAP ring waveguide from a crossed dipole trap (section 6.2). In this second part, we also show some experimental characterisation of the ring trap, as well as demonstrations of manipulation of BECs.

6.1 BEC Production

This section includes a detailed description of the stages involved in the experimental realisation of a BEC in our laboratory. The first stage is a MOT-CMOT where the atomic vapour is trapped, cooled, and finally compressed and pumped to one of the of hyperfine ground state manifolds of ^{87}Rb . The second stage is the magnetic trapping, where atoms in a weak-field-seeking state ($g_F m_F > 0$) are captured. The magnetic trap capture is followed by adiabatic compression and Radio Frequency evaporation. Finally, in the last stage, atoms are transferred to a trap formed by a weak quadrupole magnetic field and an IR crossed-dipole optical potential [Lin *et al.*, 2009; Colzi *et al.*, 2018], where a ramp downwards in the trapping laser power cools down the gas until reaching the BEC transition.

6.1.1 MOT-CMOT

During the MOT stage, we drive the D2 line transition with the MOT laser beams detuning set to $\delta = -14$ MHz and a saturation parameter $s \approx 3$. The repumper frequency is set to $\nu = 6582$ MHz such that it is on resonance with the

$S^{1/2}F = 1 \rightarrow P^{3/2}F' = 2$. In consequence, the scattering rates fulfill that $r_p/r_r \gg 1$ and we have a functioning MOT. A weak quadrupole gradient is set at $\alpha = 6$ Gpcm. Afterwards, we follow a *temporal dark MOT* sequence (see Section 6.1.1) in order to pump the atoms to the $F = 1$ ground state and also achieve higher compression, thanks to the smaller scattering rate for these spin states. The transfer to $F = 1$ could be accomplished by only switching off the re-pumper beam, but a slow and controlled decay yields better results. In our scheme, we first perform a compressed MOT in F2 by increasing δ_p and δ_r up to 6Γ ($\delta_{MOT} = -37$ MHz, with the re-pumper frequency re-scaled by the same amount to $\delta_r = 6605$ MHz). Then we ramp down the quadrupole gradient field in $\Delta t = 45$ ms ($\alpha = 6 \rightarrow 1.9$ Gpcm) whilst, at the same time, ramping down the re-pumper sideband amplitude (to 50% of the maximum). When $> 90\%$ of the atoms have populated the F1 states we switch on a resonant pump beam with $r_r \approx 0$ to blow away any remaining atoms in F=2. The result is 5×10^8 atoms at $40\mu\text{K}$, a temperature that lies between the Doppler and the Recoil limit. The cloud position in the MOT needs to be aligned with the quadrupole trap to achieve an efficient loading into the magnetic trap. To fulfil this requirement, we adjust the counter-propagating laser-beams power accordingly, and we use the Earth's magnetic field compensation coils (see Fig. 5.6). We use the CCD cameras mentioned in Section 5.3 to inspect the traps matching, and also a Molasses expansion. By tuning the beams alignment, we reach an almost isotropic expansion. Both position and power ratio can be easily adjusted from the MOT laser-light distribution board (see Section 5.2). For BEC production in the $|2, 2\rangle$ state, the re-pumper is kept constant during the whole sequence. The CMOT is kept to 20ms and a Molasses stage of 10ms follows. Similar temperatures can be achieved, but there is poor compression efficiency.

6.1.2 Magnetic Trap

The magnetic trapping stage -in our case, a trap created by a magnetic quadrupole field $\mathbf{B}_q(\mathbf{r}) = (\alpha x, \alpha y, -2\alpha z)$ with a maximum gradient of $\alpha = 300$ Gpcm- comprises three steps: 1) capturing atoms from the MOT stage, 2) adiabatic compression of the trap by increasing the quadrupole gradient such that collisions are increased and 3) RF-evaporation to reach optimal conditions for the loading of the crossed-dipole trap. The well known drawback of the quadrupole trap is that it has a magnetic field zero zero at its center, where atoms may undergo spin-flip transitions. There are several methods to prevent these losses. From among them, we have employed a TOP trap, a hybrid trap with a crossed-beam dipole plus the quadrupole, and also a

Stage	Atom Number	Temperature (μK)	Gradient (Gpcm)	PSD
Capture	$2.5 \cdot 10^8$	70	50	$3 \cdot 10^{-6}$
Compression	$2 \cdot 10^8$	120	120	$3 \cdot 10^{-6}$
Evaporation	$2 \cdot 10^7$	40	120	$4 \cdot 10^{-5}$

Table 6.1: Atom Number, Temperature, Gradient and phase space density (PSD) at the end of the three stages in the quadrupole magnetic trap.

one-beam dipole trap plus the quadrupole.

In our sequence, we re-capture the CMOT atoms in the $|1-1\rangle$ state in a magnetic trap that we found to be optimum¹ at $\alpha = 50$ Gpcm. Then we compress the trap by ramping $\alpha = 50 \rightarrow 120$ Gpcm in 1s. Afterwards, we perform RF-evaporation with a weak RF-field frequency ramp $21\text{MHz} \rightarrow 5.5\text{MHz}$. Table 6.1 shows relevant measured and calculated quantities during this process. We observe that the compression is an adiabatic process, except for a small atom loss². After these stages, one still needs to increase the PSD (see Eq. 2.28 in section 2.1.4) by 5 orders of magnitude, and this will be achieved in the optical trap, that is described in the following section.

6.1.3 Hybrid trap and crossed dipole

Following RF evaporation in the quadrupole trap, the magnetic field zero is displaced by a distance one beam waist (i.e. approx. $70\mu\text{m}$) with a vertical homogeneous magnetic field, and the dipole trap laser is switched on right after. Then, the quadrupole gradient is ramped down in $\Delta t = 1.5\text{s}$, $\alpha = 120 \rightarrow 10$ Gpcm. The final gradient chosen at this step is only relevant to increase the longitudinal confinement in the hybrid trap, but BECs of 10^5 atoms can consistently be produced for a relatively wide range of parameters. The atom number loss during the transfer to the hybrid trap is approximately 30%. After the atomic cloud has been transferred to the crossed dipole hybrid trap, an eight step piecewise exponential ramp from a maximum total power of 18W (of which 12W arrive to the atoms position) down to approximately 700 mW per beam yield the BEC. The total laser power-ramp

¹This gradient value depends on the compression at CMOT so we have chosen several α at this stage over time

²See that the PSD does not change and the temperature increase scales with the gradient

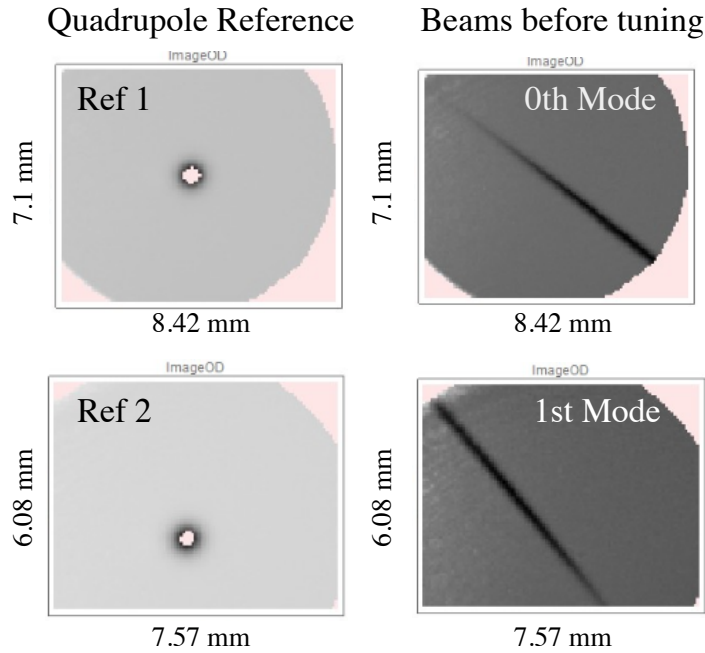


Figure 6.1: Reference images taken from the vertical imaging system (Ref 1 and Ref 2) of a tight quadrupole trap and atoms trapped in a single beam dipole trap for the zeroth and first mode of the *horizontal* AOM. The center of the tight clouds appears pink simply because the image-processing algorithm was set to show saturation for optical depths larger than 1 in this manner.

duration is 5-6s. The gradient is ramped down at the same time $11 \rightarrow 2 \text{ Gpcm}^3$. We have produced BECs with a number of approaches at this step, hence we do not find the choice of parameters particularly critical. For instance, one can ramp down the quadrupole to zero during the dipole evaporation, and still reach a BEC, now in a fully optical potential. One can also have the TOP additional magnetic fields on during the evaporation procedure⁴, which facilitates the transfer from the crossed dipole to a fully magnetic TOP trap after evaporation.

The coarse alignment of the crossed dipole trap was performed as explained in Section 5.4. In order to tune further the exact position of the focusing lenses

³This ramp is not critical, and one can find good evaporation with different combinations of laser-power ramps and gradient ramps.

⁴Preliminary data indicates that this in fact improves the evaporation efficiency

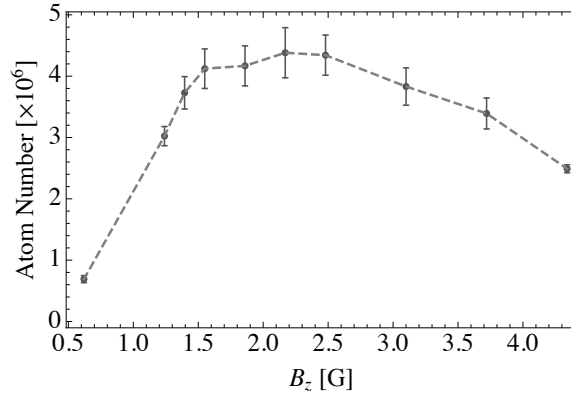


Figure 6.2: Atom number after short evaporation in the hybrid quadrupole + crossed-dipole trap for several values of B_z . B_z is a vertical homogeneous magnetic field that displaces the quadrupole field zero away from the dipole beams focus.

we used, for reference, absorption images (from the vertical camera⁵) of an atomic cloud in the quadrupole trap. After determining the quadrupole trap position, and loading each one of the two trapping laser beams with cold atoms, we could find with great accuracy the traps mismatch, and correct it by displacing the lenses position. Fig. 6.1 shows atoms in a quadrupole magnetic trap used as a reference to set the position of lenses L3 and L4 (see Section 5.4). Figures labelled as “0th Mode” and “1st Mode” correspond to atoms in both available dipole trap beams before fine-tuning the position of the half-inch $f = 25.4$ cm lenses. We also employed the horizontal absorption imaging system to set the proper height of the beams (which gives a complete overlap with the center of the quadrupole field). As mentioned earlier, for the hybrid trap to work, the zero of the quadrupole field has to be displaced from the dipole trap position [Lin *et al.*, 2009] by using a vertical homogeneous magnetic field. We displace the quadrupole zero upwards and away from the dipole beams crossing point. Fig. 6.2 shows the atom number of a cloud evaporated in the crossed dipole for different vertical bias field values. We detect an optimum point, which corresponds to the cited distance of one beam waist away from the dipole trap beams⁶. There is a fast decay curve when the quadrupole zero swings through the cloud and a slower one when the trapping frequency becomes smaller as the quadrupole field moves away.

The dipole beams optimal position is sensitive to up to $5\mu\text{m}$. We measured this sensitivity by running the same script for one particular set of optimized alignment

⁵The dipole beams propagate in the \hat{e}_x, \hat{e}_y plane

⁶This is a tradeoff between Majorana losses and a good longitudinal confinement.

parameters. Then we changed the frequency of the *vertical* AOM by up to 2MHz, which results in a displacement at the trap position of $100\mu\text{m}$ in the vertical direction. One can see in Fig. 6.3 that, for a range of the beam position that corresponds, in standard deviation, to $50\mu\text{m}$ in the vertical direction and $5\mu\text{m}$ in the horizontal direction, the atom number remains at its highest. Since we have measured beam position fluctuations of $3.5\mu\text{m}$ (see Section 5.4), these should not affect the atom number stability further than the *inherent* deviation measured for each position in these density plots. It is important to note that these fluctuations (especially, in position) become important when transferring atoms to the dressed traps. In this case, the position fluctuations of both traps can lead to mismatches and heating of the cloud. We observed this rather strikingly when first loading BECs into TAAP ring traps. However, this was before correcting for the stability in the dipole trap beams position (see Section 5.4).

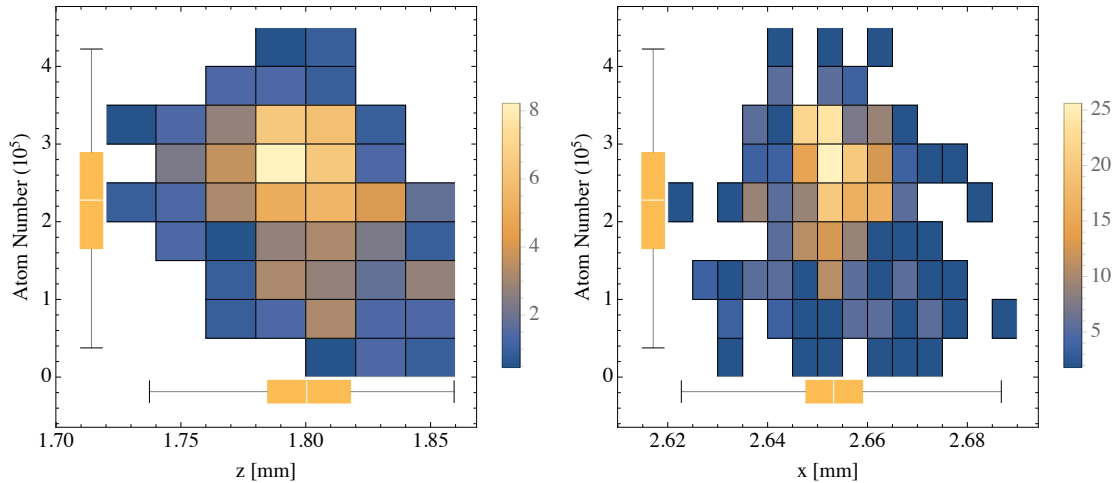


Figure 6.3: Histogram plot of the frequency for Atom number in the BEC depending on the vertical (a) and horizontal (b) positions of the trap.

Another aspect to take into account is the power ratio between the two beams forming the crossed dipole. The power ratio sets, together with the angle between the beams (17°), the aspect ratio of the confining potential and the trapping frequencies. Fig. 6.4 a) shows the aspect ratio (measured in a short ToF from the vertical absorption imaging system) of a cloud trapped in a crossed dipole without a quadrupole field. Fig. 6.4 b) shows the trapped atom number in the same trap after some evaporation. One can see that the aspect ratio increases together with the beams' power difference (this is set by the amplitude that drives the first AOM in the crossed-dipole optics board). We chose the minimum attainable aspect ratio

to run all experiments, so as to altogether facilitate the loading of the dressed traps.

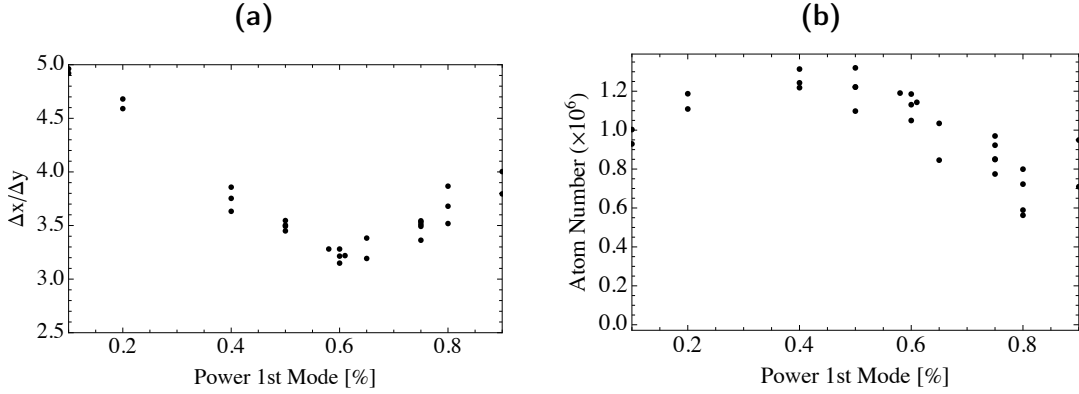


Figure 6.4: In (a) aspect ratio of the cloud for different power ratios between the 0th and 1st modes of the *horizontal* dipole trap beam AOM with only 2ms expansion time as seen from the vertical absorption imaging system. In (b) dependence of the atom number with the power ratio.

Trapping frequencies in the dipole trap can be measured by modulating the trapping laser amplitude and tracking atom number loss and heating. Once the modulation frequency hits the trapping frequency, the system becomes an overdriven oscillator that will drastically heat the cloud and result in atom loss. Fig. 6.5 shows one example of such an experiment, in this case in a hybrid trap with $\alpha = 10$ Gpcm, with the quadrupole field displaced by one beam waist. One observes two drops in atom number (accompanied by the cloud's heating, though this is not shown here) at $f_a = 101 \pm 2$ Hz and $f_b = 208 \pm 3$ Hz. The width of the fitted Lorentzian curves is of 45 Hz in both cases. This measurement is performed with 0.2 of a total power of 15W (of which a total of 9W reach the atoms position). The expected trapping frequencies according to Eq. 2.13 are $f_x \approx f_y \approx 180$ Hz and $f_z \approx 30$ Hz. The fitted f_b from Fig. 6.5 matches well with the fast axes⁷ and f_a is a sub-harmonic of this frequency. For reference, the trapping frequency measured in a single beam trap with 5W at the atoms position and a waist of $w = 68\mu\text{m}$ was measured to be of 450Hz, which also matches the theory from Section 2.1.3, that predicts a fast axis frequency of $f_{x,y} \approx 400$ Hz.

Fig. 6.6 a) shows clear evidence of BEC production with two absorption images taken with the vertical imaging system. One can see the atom cloud after only 5ms

⁷One should take into account the corrections coming from the presence of the quadrupole trap too, although they are expected to be small in the fast axes.

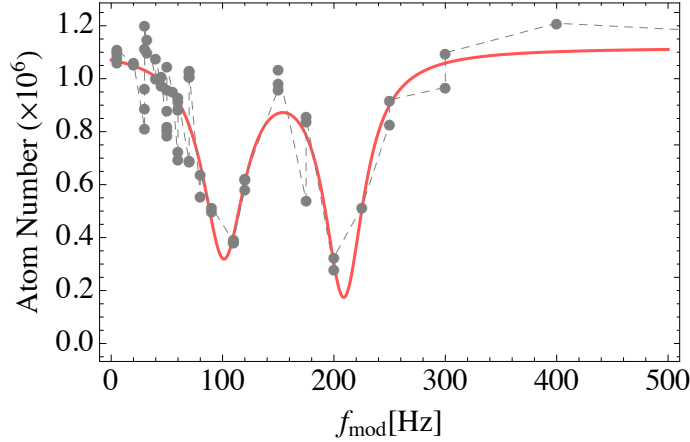


Figure 6.5: Grey dots indicate the atom number measured for different modulation frequencies of the power of the dipole trap. The dashed gray line is a guide to the eye. The red solid curve is a fit that contains an atom number offset where two Lorentzian-shaped curves are subtracted.

ToF expansion, where the observed aspect ratio is very close to the one in-trap. It also shows the atomic cloud after 25ms of expansion time. Here one can observe two distinctive features of the condensate: firstly, the aspect ratio is inverted in the central, higher optical density part of the atomic cloud and, secondly, there is a bi-modal distribution with a clear Gaussian thermal part, and the Bose-condensed part in the center. If one images the same cloud in the horizontal direction, a similar result can be found. Fig. 6.6 b) shows the condensed atom number with respect to the MOT loading time τ_{MOT} . One can see that, with a saturated MOT, the atom number fluctuations are reduced, with a total of $3 \cdot 10^5$ atoms in the BEC. However, if the MOT loading stops in the linear part of the loading curve, BEC might not be produced (there is a critical number in the initial MOT) or the relative fluctuations become larger.

6.2 The TAAP ring

This Section presents relevant experiments concerning the loading and manipulation of BECs in the TAAP ring trap. S. Pandey's thesis [Pandey, 2019] is devoted to providing further detail on this topic and I refer the interested reader to it. Fig.6.7 sketches the steps in the BEC loading from a crossed dipole trap to a TAAP ring waveguide. The evaporation in the dipole trap ends typically at very low gradients ($\leq 10\text{Gpcm}$). However, ring traps with reasonable parameters, i.e. $B_{\text{mod}} \approx 1\text{G}$ and

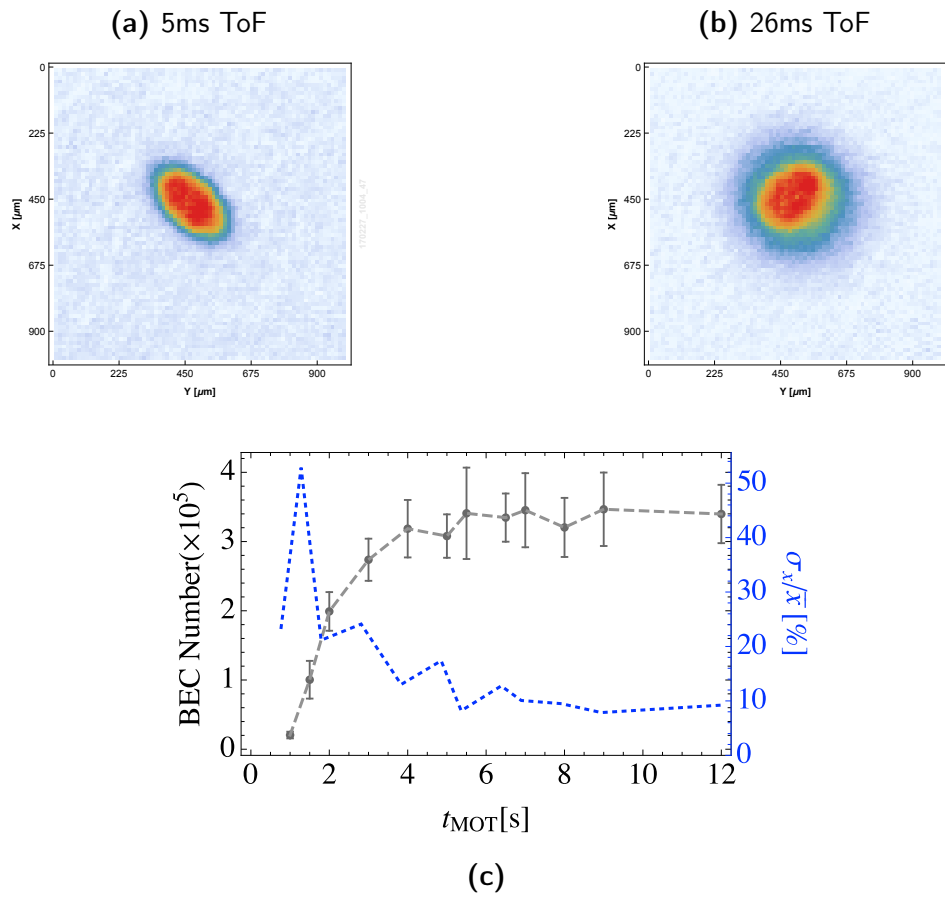


Figure 6.6: In a) $|1, -1\rangle$ BEC prepared in a crossed-dipole hybrid trap, imaged after 5ms expansion, and then after 25ms expansion as seen from the vertical absorption imaging system. One can clearly see the inversion of aspect ratio of the condensed part. In b) relative BEC atom number fluctuations (blue) and total BEC atom number (gray) versus the MOT loading time t_{MOT}

$\Omega_{\text{RF}} \approx 300\text{kHz}$, $\omega_{\text{RF}} = 0.5 - 3\text{MHz}$, need gradients well above 20Gpcm [Lesanovsky and Von Klitzing, 2007]. Since it is convenient to reach ring radii of some $\approx 300\mu\text{m}$ one needs to introduce a quadrupole gradient of the order of 50Gpcm . In order to do this whilst preventing heating of the cloud, we initially displace the quadrupole zero away (with a bias field in the x-y plane) from the crossed dipole trap where the BEC initially rests (as we said, at this point the quadrupole field is very low, with $\alpha \leq 10\text{Gpcm}$ and the ring radius $\rho(\alpha_A)$ is very large). Afterwards, the RF-field and the modulation field are switched on, creating a very shallow ring trap (Fig.4.5). Right away, the bias field displaces the quadrupole zero such that the the cloud's position lies at a magnetic field that is near-resonant with the ring radius. Finally, the gradient is increased until its final value, thus reducing the ring radius to $\rho(\alpha_B)$ and increasing the ring trapping frequencies to the order of magnitude of those of the crossed dipole. In order to conclude with the transfer, the power of the dipole lasers is ramped down and the BEC enters fully into the TAAP waveguide.

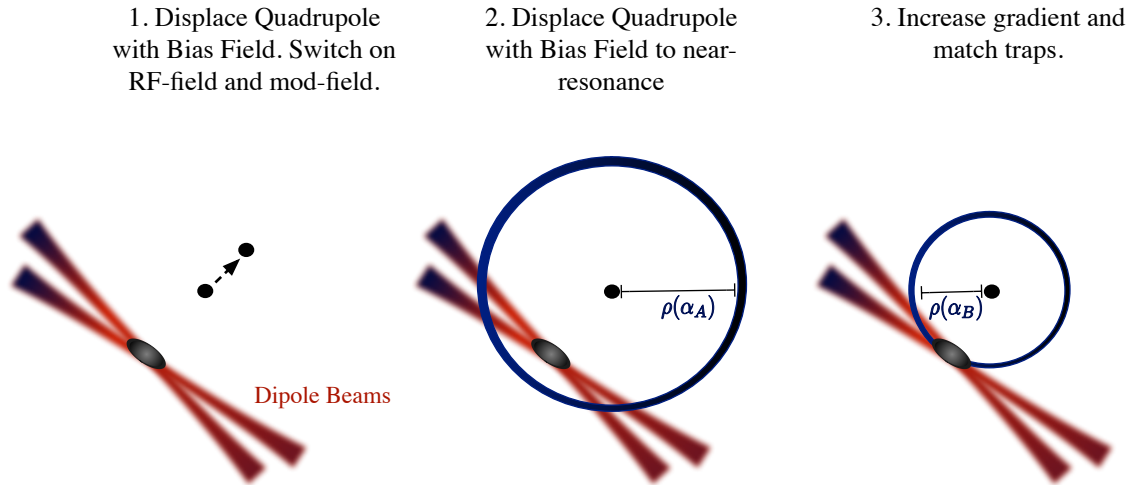


Figure 6.7: Sketch drawing of a summary of the steps for the TAAP ring loading from the crossed dipole trap. A BEC is prepared in a crossed-dipole trap. Then the quadrupole centre is displaced by using a homogeneous field in the x-y plane, aligned with the large axis of the dipole trap (Step 1). Afterwards an RF-field is switched on and the quadrupole zero is brought back closer (Step 2). Finally, the quadrupole gradient field is increased to match the radius of the ring with the atom-cloud's position (Step 3).

The vertical RF-component resonator was tuned to 2.55MHz , and this will be the RF-field frequency in the following, unless stated otherwise. The quadrupole gradient was normally applied in the range $\alpha = 50 - 100\text{Gpcm}$. As we have seen

in Eq. 4.36 the ring radius scales as an elliptical function with the modulation parameter β , which can be simply tuned by fixing all parameters except the amplitude of the audio-frequency modulation field B_m (In Section 5.5.2 we established that the modulation frequency is 5.02kHz in all our experiments). Fig. 6.8 shows how the ring radius changes for different values of B_m . In this case, we scanned this parameter to find the optimum matching point in order to load the ring at 100 Gpc/cm from the crossed dipole trap. Therefore, one could see how the size of the cloud after free fall expansion would be minimum in the vicinity of $B_m = 1.85$ G. One also observes that the numerical simulation -which does not make any assumptions further than the RWA- (dashed, red line) matches the data points within their error⁸. The black-dashed line, corresponding to Eq. 4.36 marks, for lower B_m the simplest prediction that is given by Eq. 4.39. However, this curve needs to be corrected by the effect of the spatially dependent Rabi frequency, and this is shown by the numerical simulation. We can see that the behaviour matches that of Fig. 4.5: after some maximum ring radius is attained as one scans B_m , the ring radius begins to shrink, until it loses the toroidal shape.

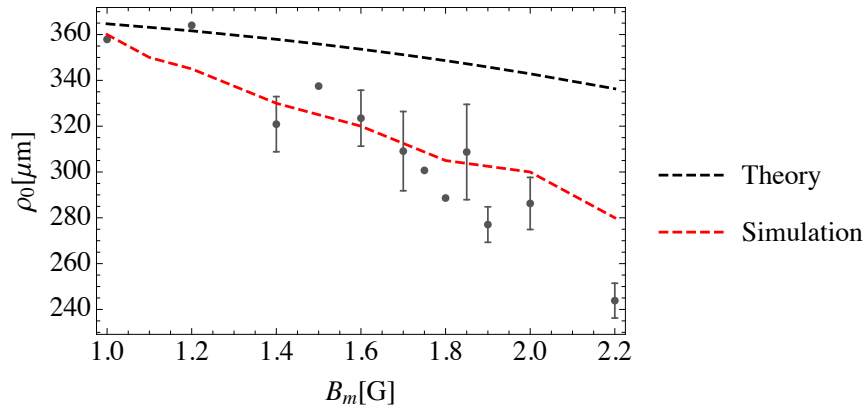


Figure 6.8: Theory given by Eq. 4.36 in a black, dashed line. Numerical simulation for the experimental parameters in red, dashed line. The experimental data was taken with a fixed gradient $\alpha = 100$ Gpc/cm and a radio frequency field aligned along \hat{e}_z with $\omega_{\text{RF}}/2\pi = 2.6$ MHz and Rabi frequency $\Omega_0/2\pi \approx 0.6$ MHz. I scan the vertical modulation field $B_m = 1 - 2.2$ G. The data without error bars correspond to single measurements. Error bars are unusually large in this experiment because the loading had not been optimised.

⁸The step size in the numerical simulation was of $5 - 10 \mu\text{m}$, and this is the error associated to the calculation

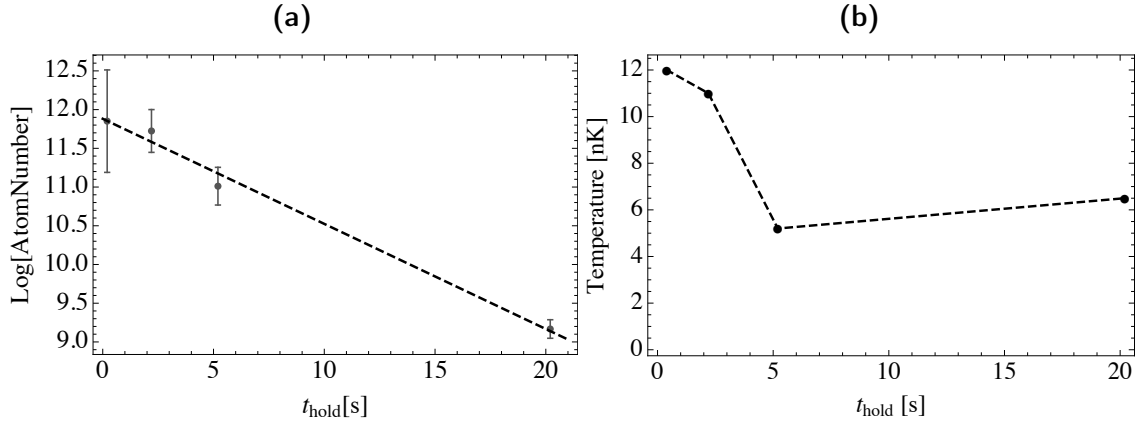


Figure 6.9: a) Logarithm of the atom number trapped in the TAAP ring after several holding times t_{hold} . b) Measured temperature of the cloud in ToF experiments after several holding times t_{hold} . The trap parameters were the same as in Fig. 6.8 with $B_m = 1.85$ G

After loading in similar conditions, and after fixing $B_m = 1.85$ G, we measured the lifetime of the cloud trapped in the (tilted) TAAP ring. Fig. 6.9 shows the atom number decay in the BEC (a) together with the evolution of the cloud temperature (b). We measure a lifetime of 7s and we observe some cooling in the first 5s of holding time, that leads to a final temperature of 6 nK. This is evidence for natural evaporation cooling occurring in the ring. The explanation for this effect could be related to spin-flip losses of hotter atoms that travel through the radially symmetric lower coupling strength regions, thus traversing higher-probability areas for Landau-Zenner losses. In the TAAP ring with a vertical linear RF the lifetime is fundamentally limited by the RF Rabi frequency, and it is different from the case of a ring created with a circularly polarised RF in that there is, in principle, no upper limit for this coupling strength for which the trap is lost. The maximum lifetime measured for thermal atoms at $1\mu\text{K}$ is of 28s in a ring at 110Gpm and with $\Omega_{0z} > 2\pi 400$ kHz

Fig. 6.10a) shows a BEC in a crossed dipole matched with the ring trap after 2ms ToF. Fig. 6.10c) shows the same cloud after releasing it into the ring -by ramping down the dipole-trap power-, also with 2ms ToF. Fig. 6.10b) shows the same cloud, in the case of Fig. 6.10a), but after 26ms of free flight. It presents the characteristic bi-modal distribution of a Bose-Einstein condensate with a thermal fraction. We loaded up to 3×10^5 atoms in the ring trap with a BEC lifetime of up to 4s. Loading a BEC into the ring from the dipole trap needs of precise control of the homogeneous magnetic field that displaces the quadrupole magnetic field zero,

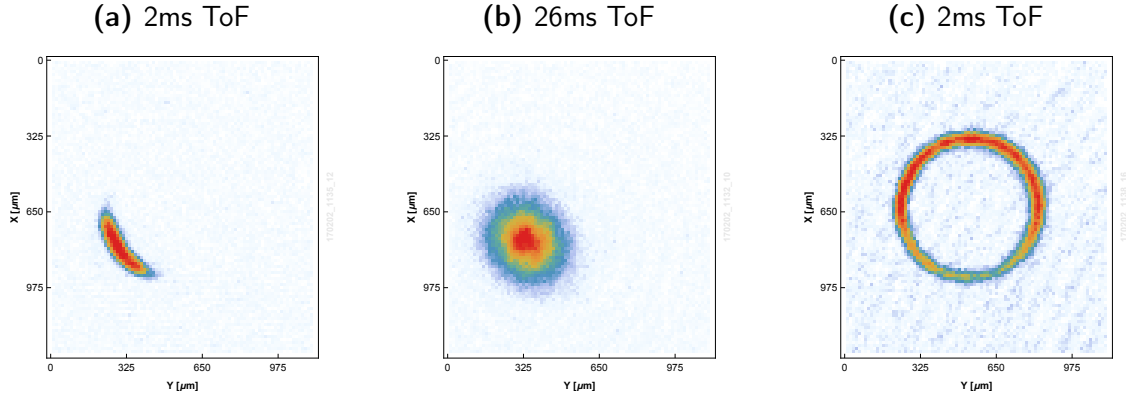


Figure 6.10: Absorption images (from the vertical imaging system) of a BEC in a TAAP ring waveguide. a) Shows a 2ms ToF image of BEC previously trapped in a crossed dipole matched to the ring trap b) Shows the cloud after 26ms ToF from a), with a clear a bi-modal distribution c) Shows the same cloud after the dipole trap laser power is ramped down after 2ms ToF.

and also of very good pointing stability of lasers forming the crossed dipole trap. The pointing stability shown in Fig. 6.3 was good-enough to load BECs into the TAAP ring reliably. One must also note that both the modulation field B_m and the RF-field amplitude change the radius of the ring-trap, and thus the loading condition.

The TAAP ring allows both for state-dependent manipulation by using the RF-field polarisation and also for state-independent manipulation by using the tilt of the modulation field B_m axis [Gildemeister *et al.*, 2012; Pandey *et al.*, 2019]. Fig. 6.11 shows a full rotation of an ultra-cold cloud in a ring formed with a quadrupole gradient of $\alpha = 85$ Gpcm and the RF-field linearly polarised along \hat{e}_z with parameters $\omega_{\text{RF}} = 2.6$ MHz, $\Omega_0 \approx 0.6$ MHz. Here we tilt the axis of the modulation field by 22° at the position $0, \pi/2, \pi, 3\pi/2$ of the resonant surface that defines the ring by choosing the appropriate three-component vector for \mathbf{B}_m . Notice how the shape of the clouds is non-uniform in all absorption imaging pictures. This is due to very small tilts introduced by misalignment of both \mathbf{B}_{RF} and \mathbf{B}_m . These can be corrected, but it is out of the scope of this chapter, and a detailed description of the manipulation of BECs in the ring trap can be found in S. Pandey’s PhD thesis [Pandey, 2019].

The smoothness of the loading permits splitting a condensate without destroying it, and causing non-measurable heating. Fig. 6.12 shows a simple scheme for BEC splitting using a TAAP ring waveguide and one dipole beam. The sequence is simple: one ramps down the power in one of the dipole beams and then displaces the ring trap

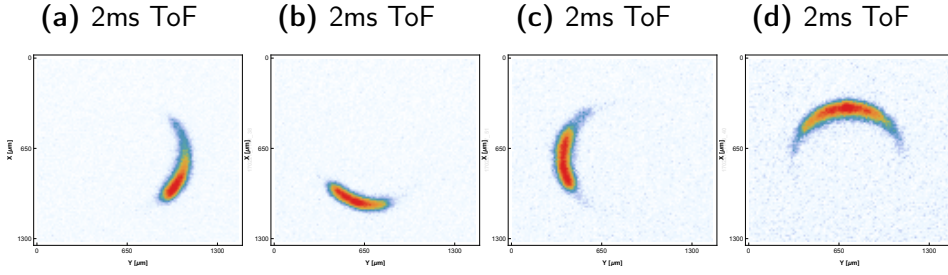


Figure 6.11: Absorption images of an ultra-cold cloud trapped in a tilted TAAP ring trap for the following parameters: a) 0.7G in $B_m \hat{e}_y$ 1.7G in $B_m \hat{e}_z$ ($\Delta\phi = \pi$), b) 0.7G in $B_m \hat{e}_x$ 1.7G in $B_m \hat{e}_z$ ($\Delta\phi = \pi$), c) 0.7G in $B_m \hat{e}_y$ 1.7G in $B_m \hat{e}_z$ ($\Delta\phi = 0$) and d) b) 0.7G in $B_m \hat{e}_x$ 1.7G in $B_m \hat{e}_z$ ($\Delta\phi = 0$). The holding time was 0.5s, $\omega_{RF}/2\pi = 2.6$ MHz, $\Omega_0/2\pi \approx 0.6$ MHz in \hat{e}_z and $\alpha = 85$ Gcpm

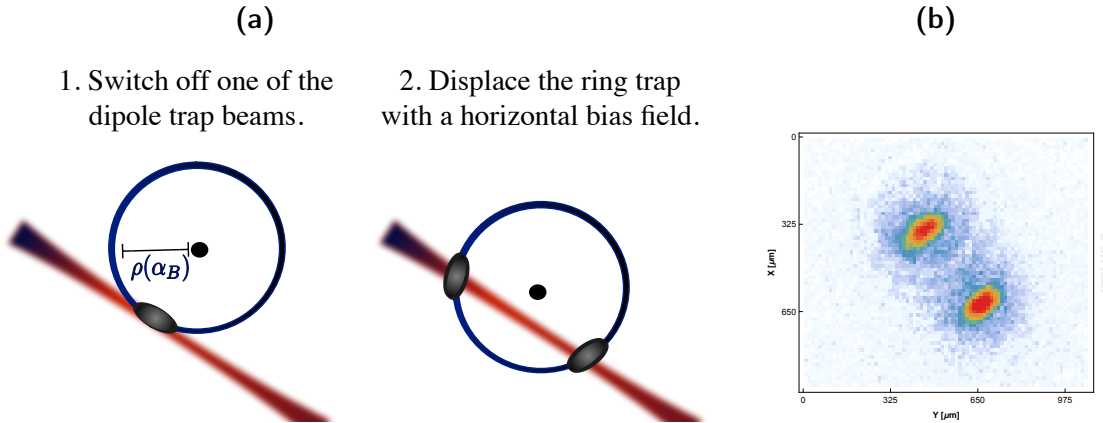


Figure 6.12: a) Shows a sketch of a BEC splitting by using a dipole trap and a TAAP ring. b) Shows an absorption image of the split condensate after 20 ms ToF. In this image, we observe both anisotropic expansion and a bi-modal distribution in both clouds.

across, such that the combined confinement of the optical and magnetic potential result in cloud splitting. The experimental parameters need to be adjusted carefully (preliminary results indicate that it should be down to 2mW in the dipole laser power) to obtain a roughly equal population distribution in the two wells. Fig. 6.12 b) shows one example of a split cloud after 20ms ToF. We observe clear signatures of BEC in both clouds. This experiment confirms the smoothness of the transfer between the optical and the RF-dressed traps.

7

Spectroscopy with Radio-Frequency Dressed ^{87}Rb ultra-cold atoms

This chapter collects experiments on spectroscopy with RF-dressed states. Section 7.1 deals with intra-manifold transitions within each hyperfine subgroup of Zeeman levels. Section 7.2 presents results concerning inter-manifold transitions with RF-dressed atoms trapped in a crossed-dipole optical potential. Section 7.3 gathers fundamental studies on MW-transitions in an RF-dressed shell potential. Finally, Section 7.4 offers a selection of experiments that test the ideas presented in Section 4.2.

7.1 RF-spectroscopy in Adiabatic Potentials

Weak radio-frequency fields can be used to evaporate and cool atom clouds trapped in RF-dressed adiabatic potentials. As we introduced in Section 3.2.1, there are several allowed intra-manifold transitions that depend on the parameter previously defined as θ_F in Eqs. 3.21. We use RF-spectroscopy to determine Ω_0 , which is an important measurement in the bi-chromatic shell experiments that we present in Section 7.4. Since the theory in Section 3.3 allows us to measure Ω_0 with MW-transitions, we have used both methods alternatively in the laboratory. This Section presents a series of RF-spectroscopy experiments in the shell and TAAP ring. In some cases, we observed higher order transitions, with up to 3 photons. As Section 3.2.1 introduces, this phenomenon is explained by the breakdown of the *first* RWA when the RF-field inducing the transitions is strong.

7.1.1 RF-spectroscopy in the shell trap

A BEC is prepared in a crossed-dipole trap plus a TOP trap with $\mathbf{B}_m(t) = B_0 \cos(\omega t)\hat{\mathbf{e}}_x + B_0 \sin(\omega t)\hat{\mathbf{e}}_y$ ($B_0 = 10\text{ G}$, $\omega/2\pi = 5.02\text{ kHz}$) and $\alpha = 13\text{ Gpcm}$. Each dipole trap beam has 0.9 W at the end of evaporation. After reaching BEC, the gradient is ramped in $\Delta t = 200\text{ ms}$ to $\alpha = 13 \rightarrow 70\text{ Gpcm}$. Then, the dipole power is ramped down in both beams to zero in $\Delta t = 150\text{ ms}$. At this point, atoms remain trapped in a TOP. In order to dress the cloud, B_0 is ramped to 6.5 G (such that $g_F\mu_B B_{\text{DC}} \approx 2\hbar\omega_{\text{RF}}$, with $B_{\text{DC}} = B = 0$ in this case) in $\Delta t = 100\text{ ms}$. Simultaneously we ramp $\alpha = 70 \rightarrow 55\text{ Gpcm}$ to improve slightly the lifetime. At this point an RF-field with $\nu_{\text{RF}} = 2268400\text{ Hz}$ linearly polarised along $\hat{\mathbf{e}}_y$ is switched on. A $\Delta t = 250\text{ ms}$ ramp $B_0 = 6.5 \rightarrow 0\text{ G}$ adiabatically transfers the atoms into the shell trap. Afterwards the gradient is decompressed to 24 Gpcm and a second, weaker, RF-field is switched on. The sample is held in this situation for 2.01 s . In the end, we measure via absorption imaging the remaining atom number in $|1, -1\rangle$. By looking at the Lorentzian-shaped dips in atom number as the frequency of the second RF-field is scanned, we can identify the transitions predicted by the theory and measure the RF Rabi frequency (see Fig. 7.1). We obtain $\Omega_0/2\pi \approx 250\text{ kHz}$ from all the transitions observed. One must be careful when interpreting these data since the actual line-shape is not exactly Lorentzian¹ [Easwaran *et al.*, 2010]. We checked that the higher order peaks disappear for lower amplitudes of the evaporation RF, thus ensuring that these transitions are the ones predicted in Section 3.2.1.

This technique allows for the calibration of all RF-field antennae amplitude versus Voltage and also with the frequency variation (which is important since we make use of resonators with a large Q). It is limited by the geometrical uncertainty of the polarisation. To calibrate more fully the RF-dressing fields one can measure the Rabi frequency with the method mentioned above for several values of quantities of interest. Fig. 7.2 shows the Rabi frequency measurement for several amplitudes with a fixed RF-dressing frequency at 2268400 Hz . It also shows the Rabi frequency for two different RF-frequencies (the previously quoted, and 2258410 Hz) and a fixed amplitude. In the zoomed version of Fig. 7.1 we can see up to two higher order transitions that occur at $\Omega/2$ and also at $\Omega/3$. We can see from Fig. 7.2 that the precision that one can achieve with this measurement is of the order of 10 kHz . This method can also be used to cool down the sample and even reach BEC (see [Sherlock, 2011]).

¹In fact, it is a non-symmetric function

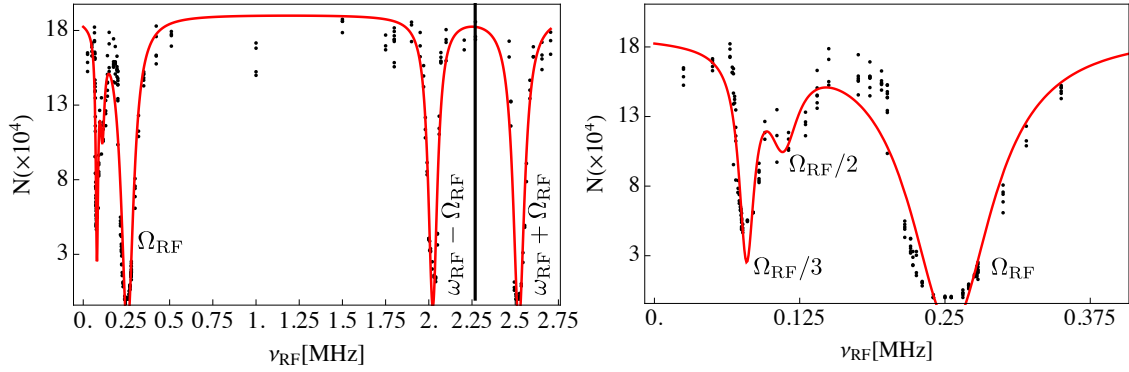


Figure 7.1: Measured atom number in a shell trap after a long RF pulse of a second, weaker RF-field for different frequencies. The vertical black line indicates the frequency of the dressing RF-field. The black dots are experimental atom number measurements. The Red line is a fit that includes up to 5 Lorentzian dips.

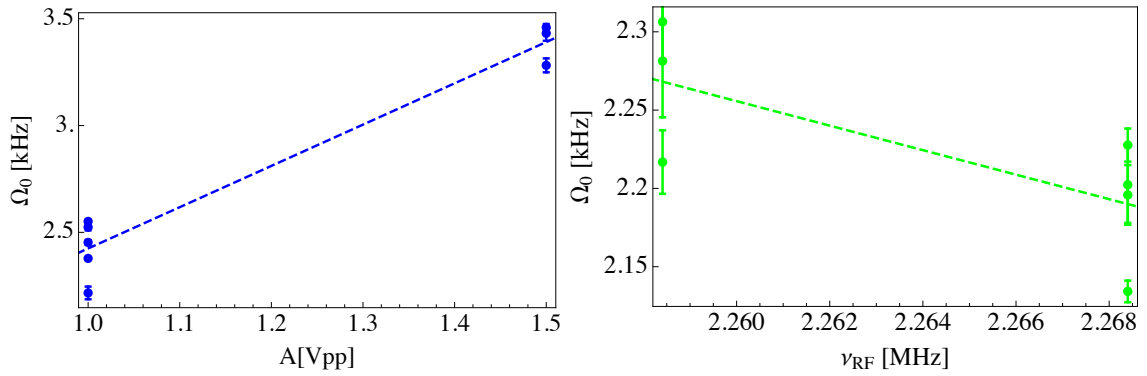


Figure 7.2: Measured Rabi frequency by the method of RF-evaporation with a second weaker RF (see Fig. 7.1) for two different amplitudes of the dressing RF and for two different frequencies. With this procedure one can obtain a calibration of the RF-fields generation.

7.1.2 RF-spectroscopy in a TAAP ring

Instead of loading the BEC into the ring trap (see Section 6.2), one could try to evaporate directly in the TAAP, which would produce a BEC in the ground state of the ring, thus avoiding the technical trouble that may come with the matching of different traps. In preliminary work, we performed spectroscopy in a tilted ring trap (that allows for higher trapping frequencies in both the axial and radial directions -of the order of 100 Hz- compared to the flat ring). The sample is prepared in a crossed-dipole trap $T < 1\mu\text{K}$ with a very weak quadrupole gradient $\alpha = 3\text{Gpcm}$ and a final

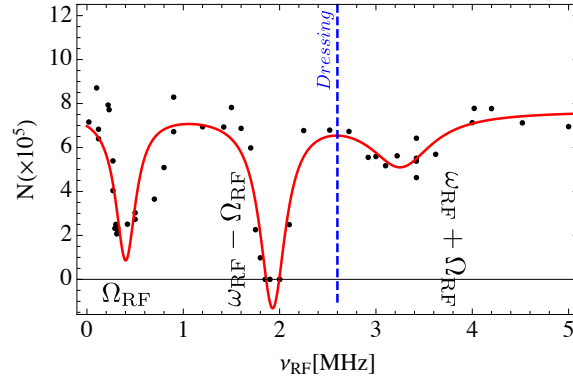


Figure 7.3: Atom number in a tilted ring trap after the application of a long pulse of a second weaker RF-field. The black dots are experimental points, the red line is a fit that includes three Lorentzian dips from an offset atom number (as we mention elsewhere, these transitions do not present Lorentzian line-shapes, therefore this is a very rough approximation). Notice that, especially in the transition at Ω_{RF} , the line-shape is far from Lorentzian, and the fit is rather inaccurate. The vertical dashed blue line indicates the RF-dressing frequency.

power of 0.9 W per beam. A homogeneous magnetic field b_z in the $\hat{e}_x - \hat{e}_y$ plane is then ramped up to the condition $g_F \mu_B b_z \approx 2\hbar\omega_{\text{RF}}$, where $\omega_{\text{RF}}/2\pi = 2.55\text{MHz}$. Then, the RF-dressing field is switched on. To load the tilted ring trap we employed a strong field along \hat{e}_z and a weaker² one, with the same phase³, along \hat{e}_x . In $\Delta t = 50\text{ms}$, b_z is ramped down to a near-resonant condition $g_F \mu_B b_z \approx \hbar\Omega_{\text{RF}}$. A $\Delta t = 200\text{ms}$ ramp of the quadrupole gradient $\alpha = 3 \rightarrow 110\text{Gpcm}$ and a 2s ramp to zero of the dipole trap power follow. To perform the spectroscopy measurement a 3.2s weak RF-pulse in the \hat{e}_y direction is shone and then an absorption image of the cloud is taken. Fig. 7.3 shows one spectrum in the tilted TAAP ring trap with the parameters detailed just above. Here we measure $\Omega_0 \approx 0.62\text{MHz}$ from a fit just like the one from Section 7.1.1. We observe the same transitions predicted in the RWA for the shell trap, although one of the sigma-polarised components is clearly weaker. One intuitive explanation is that, since the ring is tilted by a modulation field that is not perfectly horizontal, the circular projection coupling of the weaker RF corresponding to this transition becomes weaker. Although we did observe evaporation cooling in the tilted TAAP ring with the second RF-field, it was not efficient enough to cross the BEC threshold, probably due to the lack of collisions in this rather loose trap.

²The different resonators in the coils make this very simple even if the fields are unknown.

³This is to result in a linearly polarised RF-field tilted with respect to \hat{e}_z

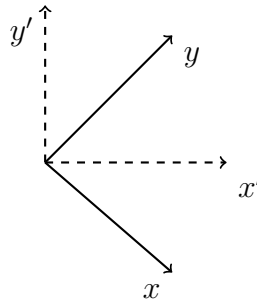


Figure 7.4: Coordinate system summary in the horizontal plane x', y' are the axes of the Earth compensation coils and the TOP coils. x, y are the axes of the RF-coils, which lie at 45° from x', y' .

7.2 MW-spectroscopy in a dipole trap

Section 3.3 introduced the theory for MW-transitions between the sub-states in the two ground hyperfine manifolds of ^{87}Rb . This section includes experimental results on this topic with RF-dressed atoms trapped in a crossed-dipole. We will elaborate on the sample preparation procedure as well as the spectroscopy results. The spectra presented in Section 3.3 correspond to the theory in the RWA and, in particular, to atoms set at the resonant condition of the impinging RF-dressing field with a homogeneous field that defines the quantization axis. In most experiments atoms were not perfectly on resonance. Moreover, non-linear effects for which we did not account may be present too.

Experiment geometry. Fig. 7.4 shows a scheme of the experiment reference axes. In the following experiments, and unless stated otherwise, only the RF-antenna (in Helmholtz configuration) that lies along the x axis is used. The MW dipole antenna lies along the x' axis (see Fig. 7.4). Therefore, it can produce linearly polarised fields in the $y' - z$ plane depending on its orientation. Precession effects of the MW-field centred in $z = z'$ may occur if the antenna is tilted. The purity of the MW polarisation has not been tested. The RF antennae are aligned with the $x - y$ axes. We have demonstrated almost perfect circularly polarised RF by tuning the amplitude and phase of two antennae in the x and y axes respectively, as shown in Section 5.5.3.

7.2.1 Spectrum

In order to study the spectrum predicted in Section 3.3 we performed a scan of the MW frequency to interrogate atoms initially trapped in a crossed-dipole trap in the dressed $|1, -1\rangle$ state. The sample is normally prepared with 3×10^5 atoms at 50nK and a final axial trapping frequency -see Eq. 2.13- of $\omega_z/2\pi \approx 180$ Hz and radial trapping frequency of $\omega_\rho/2\pi \approx 30$ Hz. At this point the vertical bias field b_z is ramped up to the off-resonant point given by $|g_F|\mu_B b_z \approx 2\hbar\omega_{\text{RF}}$. Then the RF-field ($\omega_{\text{RF}}/2\pi = 2.27$ MHz, $\Omega_0/2\pi \approx 350$ kHz) is switched on, linearly polarised in the x-y plane along \hat{e}_x . Afterwards b_z is ramped in $\Delta t = 200$ ms down to a near-resonant condition $|g_F|\mu_B b_z \approx \hbar\omega_{\text{RF}}$ where $b_z = 3.1$ G, so as the atoms are dressed. One way to know whether the atoms are well matched to the resonant ellipsoid is to slowly ramp up a quadrupole gradient and ramp down the dipole trap power: if the atoms remain trapped in the resulting adiabatic shell this is a clear indicator of good matching. We did not take special care in setting the bias field to the resonant condition with great accuracy, which means that⁴ $\theta_F \neq \pi/2$. In the final step, we image the atoms in the F=2 state. The MW-field was generated by a dipole antenna placed perpendicularly to the horizontal plane, aimed at producing a linearly polarised field oriented in the horizontal direction, at some 45deg from \hat{e}_x and orthogonal⁵ to the homogeneous DC-field along \hat{e}_z . However, the spectrum obtained after interrogating the sample with a 0.7 ms (a pulse shorter than the fastest $\pi/2$ cycle in all allowed transitions) indicates that other MW polarisation components might be present as a consequence of imperfect alignment or even reflections in neighbouring surfaces to the experiment cell. In any case, and as expected from the theoretical prediction, we observe seven groups of five transitions. In each of the groups we can see transitions from the initial dressed $|1, -1\rangle$ state to all the sub-states of the upper manifold. The overall coupling strength of the groups, with the even ones (group with n=0 - the closest to the hyperfine line- and n=2,-2) being clearly weaker than the odd ones, is that expected for $b_z \perp B_{\text{MW}}$ (we showed this in Fig. 3.6). This spectrum was fitted to the transition matrix elements dependencies with all parameters in [Sinuco-Leon *et al.*, 2019] and it showed small non-linear effects for which this thesis has not given an account. Nonetheless, our brief derivation of the allowed transitions is enough to understand the observation of 7 groups (spaced by $\omega_{\text{RF}}/2\pi$) of five transitions (spaced by $\Omega_0/2\pi$).

⁴Take the tan from Eqs. 3.21

⁵One can change this by simply rotating the MW dipole antenna on its axis

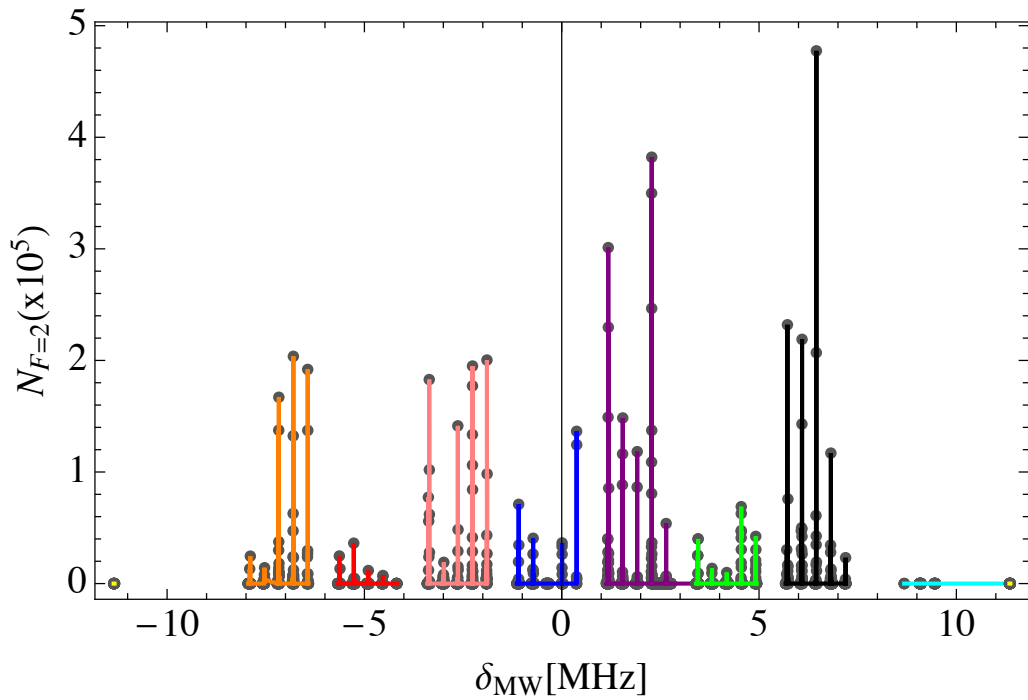


Figure 7.5: Full spectrum of MW inter-manifold transitions between RF-dressed states in a cloud trapped in a crossed-dipole. Colors are used to distinguish each of the 7 groups of 5 transitions predicted in Section 3.3. We observe transitions in all groups because there are MW field polarisation components of the three possible types (π and σ_{\pm})

7.2.2 Spectrum characteristics

We will analyse some of the relevant characteristics of the MW-transitions between RF-dressed states. Firstly we will present results regarding the line-shifts when varying the homogeneous magnetic field (this corresponds to changing θ_F in the dressed picture). Afterwards we will shortly present how the *clock* transition line-shift changes with the RF-field polarisation. Finally, we will show some preliminary work on the maximum coherence time attainable in such transition. We have added some comments on a yet unexplained peak-splitting phenomenon observed in several of the transitions.

Line-shifts with homogeneous fields

In Section 3.1 (see Fig. 3.1) we introduced the concept of *magic* field as that magnetic field for which the differential energy shift between two states attains a turning point, therefore yielding a set of parameters highly insensitive to fluctuations of *that* magnetic field. This was, however, the theory for bare states. Afterwards, we calculated several differential energy shifts in the RWA for the two-level systems involving the dressed $|1, -1\rangle$ state and all the $F=2$ manifold dressed sub-levels. In Section 3.4, Fig. 3.7 one could see that for a certain magnetic field, close to the resonance with the RF-dressing field, all transitions -except for the *clock* transition- undergo a similarly parabolic energy difference dependence. The *clock* transition that presents a turning point in the energy difference at a different θ_F . This transition, in any case, has a smoother linear slope, proportional to the difference in g_F factor. One can interpret these parabola-like energy dependencies in the same manner as for the standard *magic* field, since these transitions, which now involve states other than the clock pair, also show a minimally sensitive point to magnetic field fluctuations.

In this section we delve into experimental results on this multi-transition parabola-shaped differential energy shift with the static magnetic field for RF-dressed Rubidium 87 atoms. We have demonstrated, in particular, the parabolic transition-frequency behaviour with respect to a changing B_{DC} field for three transitions. We observe the narrowing of the line-width as one approaches the turning point of the line-shift as well. In addition, we have shown (this work was performed with G. Sinuco-Sussex-) that the physics beyond the rotating wave approximation remain relatively untouched. The sample was prepared similarly to the previous Section 7.2.1, with $b_z = 1.2\text{ G}$ during evaporation. Then we ramped $b_z = 1.2 \rightarrow 5\text{ G}$ and switched on an RF-field with $\omega_{\text{RF}}/2\pi = 2263410\text{ Hz}$ and $\Omega_{\text{RF}}/2\pi = 375\text{ kHz}$. Afterwards we

ramped $b_z = 5 \rightarrow 3$ G in $\Delta t = 400$ ms⁶. Before the MW-interrogation and subsequent independent state absorption imaging we change $b_z = 3 \rightarrow b_{\text{final}}$ G, which is the field in the abscissa of (Fig. 7.6a, b, c).

Fig. 7.6 a) shows the line-shape of the transition between the dressed states $|1, -1\rangle \rightarrow |2, 2\rangle$ for three different b_z . The horizontal axis is the detuning of the microwave frequency with respect to the maximum (minimum) of the parabola in Fig. 7.6 b) (c)). One can see that, as the transition frequency approaches the *magic* condition, the line becomes narrower. The narrowest line we measured in the transitions from $|1, -1\rangle$ to $|2, 2\rangle$ and $|2, 0\rangle$ was of 120 Hz for a 10ms pulse. Understanding each of the transitions shifts might be important also if one wants to determine Ω_{RF} with precision. During the same session we also measured the bare transition line-shift $|1, -1\rangle \rightarrow |2, 0\rangle$ with the same DC-field in order to have a real-time calibration of the homogeneous field present in the experiment. We found fields of the order of 0.5G, both orthogonal and antiparallel, to the the b_z coils. More precisely, that would be b_{\perp} and b_{\parallel} in $\sqrt{b_{\perp}^2 + (b_{\parallel} + b_z)^2}$.

The *clock* transition shows a different behaviour. One can already see in Fig. 7.6 d) that it has a linear slope at the resonance point. Fig. 7.7 shows a 2D scan where we measure the dressed $|1, -1\rangle \rightarrow |2, 1\rangle$ transition for several pairs of RF-field amplitude and bias field. There is not a real-time calibration of the bias field from this session. The RF-field was set to $\omega_{\text{RF}}/2\pi = 2267900$ Hz in the \hat{e}_x direction. The dressed atoms were trapped in the crossed-dipole. We can see that the behaviour of the line-shift corresponds to the one found in Section 3.4, with a parabola-like shaped curve that presents a *maximum* (this is a measurement with respect to the hyperfine line). Consequently, a magic condition is attainable too in this strong-RF-field regime, although in a narrower range of parameters (see Fig. 3.7). Moreover, amplitude fluctuations in the the RF-field contribute to the broadening of the lines, as one can clearly see this from Fig. 7.7, where the curves are shifted following the RF-field amplitude. The magnitude of this shift with the Rabi frequency for a fixed DC magnetic field is of approximately 7 Hz/kHz. On resonance we expect a shift of < 1 Hz/kHz if we do not include non-linear effects.

⁶The reason for ramping up and down the bias field is convenience. Initially, the dipole trap and the quadrupole are matched with a small bias field (of the order of 1 G). To load the shell trap one needs to cross adiabatically the resonant condition with $\omega_{\text{RF}}/2\pi$, wich in our case lies normally close to 3 G, thus the need to ramp b_z close to 5 G before dressing.

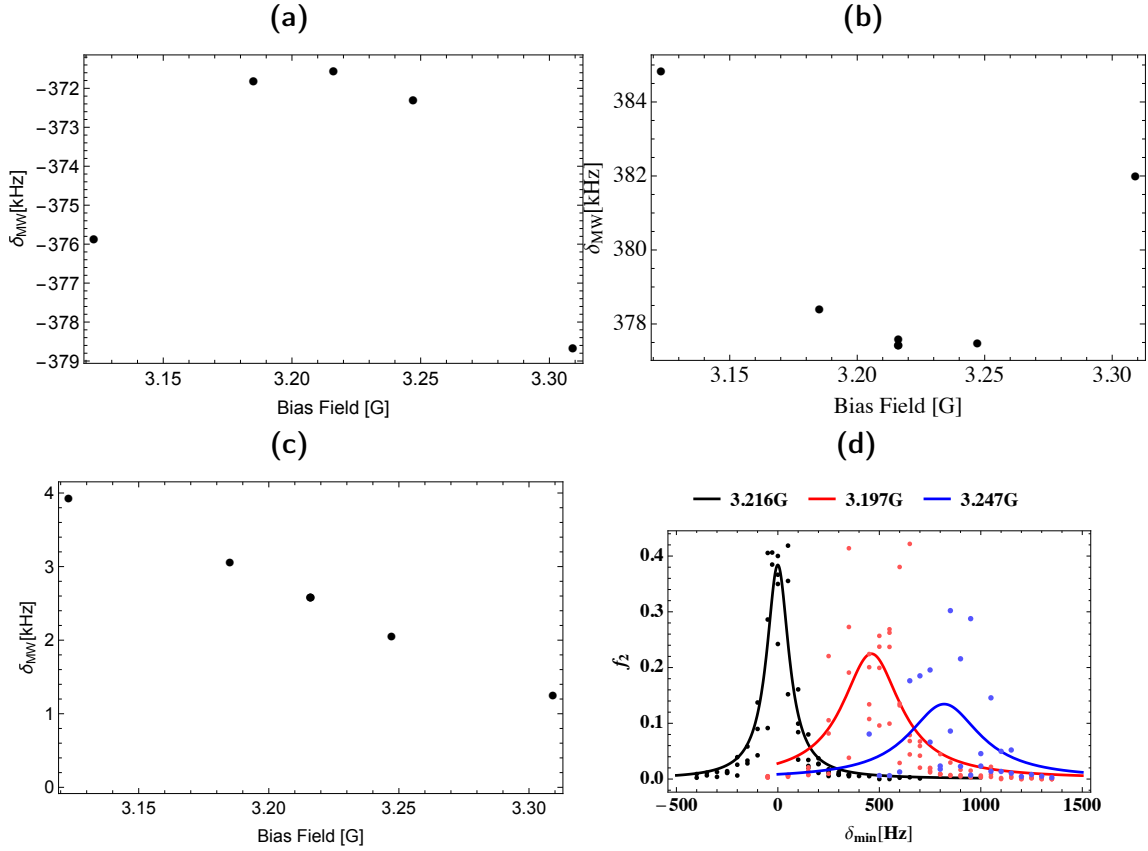


Figure 7.6: line-shift of the transitions (a) $|1, -1\rangle \rightarrow |2, 0\rangle$, (b) $|1, -1\rangle \rightarrow |2, 1\rangle$, (c) $|1, -1\rangle \rightarrow |2, 2\rangle$ with respect to the homogeneous field b_z . (d) Line measurement close to the bottom of the parabola in the $|1, -1\rangle \rightarrow |2, 2\rangle$. Line-widths are $\Delta\nu = 132 \pm 12$ Hz for the Black curve at $b_z = 3.216$ G, $\Delta\nu = 347 \pm 54$ Hz for the Red curve at $b_z = 3.197$ G and $\Delta\nu = 427 \pm 189$ Hz for the Black curve at $b_z = 3.247$ G. One can see how the noise increases greatly as the DC magnetic field is set away from the resonance.

Line-shifts with RF-polarisation

The difference in g_F leads to strong differential couplings with the circular projections of the RF-field into the local quantization axis for states in the two F manifolds. As we saw in Fig. 7.7, this difference ends up shifting the *clock* transition whenever RF-field amplitude fluctuations are present. In this section we outline a method to achieve the same shift in both states. This method consists of choosing an RF-polarisation that produces a symmetric coupling of the RF-fields in both manifolds. Hence, when the total RF-amplitude fluctuates, both states see the same shifts. These synced line-shifts add partially to the line broadening, which is inevitable if they are not compensated. Fig. 7.8 shows the line-shift as the phase

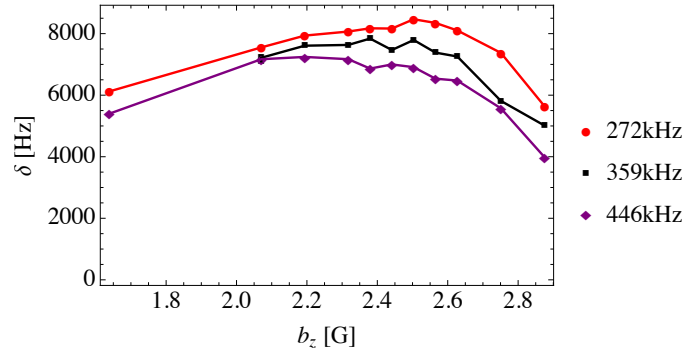


Figure 7.7: Measurement of the *clock* transition line-shift in a two-dimensional scan of the homogeneous bias field b_z and the RF-amplitude. Each color denotes the transition frequency as the homogeneous field is scanned for a different Rabi frequency. The lines are only a guide to the eye. Notice that, from the theory presented in chapter 3, we can identify these curves as being “left” from the resonance, which is close to 3 G in this case. Therefore, the pseudo-magic condition for RF-dressed states occurs off-resonance, and the sensitivity to DC-fields is maximum on-resonance.

between a strong RF-field (in the \hat{e}_x direction) and a weaker RF-field (in the \hat{e}_y direction) is scanned. One can see that the two curves cross at a certain point, at which the transition will be minimally sensitive to the fluctuations in the total RF-field amplitude. Of course, this does not prevent broadening related to fluctuations in the polarisation (that could be the result of relative amplitude fluctuations between the \hat{e}_x and \hat{e}_y components of the RF-field \mathbf{B}_{RF}). Even though it is not shown here, we measured the line-shift at the crossing point for a third set of RF-amplitudes and it matched with Fig. 7.8.

7.2.3 Coherent driving

Chapter 1 introduced the concept of atom-clock interferometry. This work has been largely motivated by the achievement of coherent driving of a two-level system of RF-dressed states, such that they can be used in this type of interferometers. In this section we present results of atoms trapped in an optical potential which, by itself, cannot provide the state-dependent control of, for instance, TAAP traps. However, it allows for testing the spectral characteristics without the large inhomogeneous broadening attached to magnetic trapping⁷, thus becoming a long-interrogation

⁷All traps present inhomogeneous broadening but, as we calculated in Section 2.1.3 the order of magnitude associated to the dipole trap is much smaller than for the shell trap (see Section 4.2)

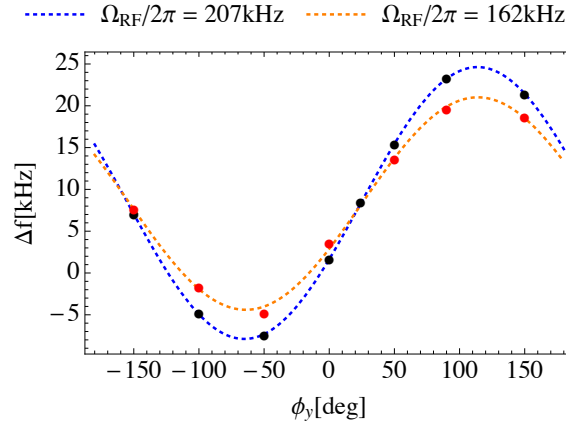


Figure 7.8: Measurement of the line-shift (dots) for two different RF amplitude settings as the phase of the weaker component (in this case the Y RF component in our convention) is scanned. One can see a crossing point.

time platform for spectroscopy and, potentially, interferometry. Here we will show evidence of coherent driving with decay times of the order of 100 ms of the *clock* transition between the dressed states $|1, -1\rangle$ and $|2, 1\rangle$ in the crossed-dipole trap. From Section 7.2.2, one could propose to extend this to other transitions between RF-dressed states, which can be of interest in long-coherence time quantum computing protocols with several spin-states or atom interferometry.

We performed two sorts of experiments: 1) Rabi oscillations, where a driving MW-field is shone for some time and the atom populations are recorded and 2) time domain Ramsey fringes (see Fig. 7.9). The sources of contrast decay depend on the particularities of the system, but they contain both homogeneous and inhomogeneous sources for the broadening of the atomic transition. Sources of homogeneous broadening affect all atoms equally whereas sources of inhomogeneous broadening affect them differently⁸ [Treutlein, 2008]. Sources of line broadening can be related to atomic collisions (see Section. 2.2.1), magnetic field fluctuations (see Section 4.2) or optical field fluctuations (see Section. 2.1.3). Rabi and Ramsey experiments will differ in that the driving field fluctuations are an important de-phasing mechanism during a Rabi experiment and, on the contrary, they are minimised in the Ramsey experiment (where the trapping or environmental fields are the main contributors to

⁸This is why spin echo techniques work only when dephasing is related to inhomogeneous broadening. Notice that in our experiments, the fact that different spin states are in different traps is a source of inhomogeneous broadening as well.

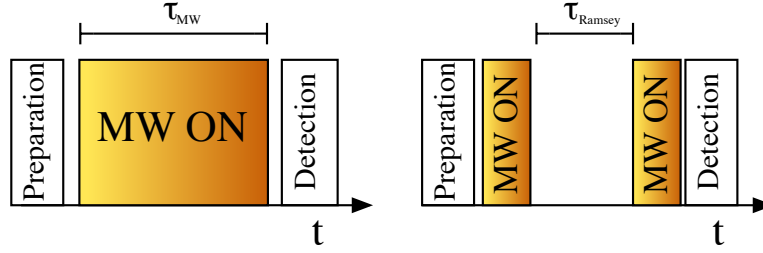


Figure 7.9: Schematic comparison between a Rabi experiment and a Ramsey experiment. In a Rabi experiment the MW pulse that drives the TLS is left on for a time duration τ_{MW} that begins right after the sample preparation and the sample detection. In a Ramsey experiment two MW pulses are applied onto the sample, which is let to evolve freely for a time duration τ_{Ramsey} . In this case, one can scan either τ_{Ramsey} , or the phase or frequency of the second MW pulse. We present experiments where τ_{Ramsey} is scanned.

the transition line broadening). Appendix B contains a short derivation of the decay curves in Rabi oscillations and time-domain Ramsey fringes for both Gaussian and Lorentzian noise profiles. The following table summarises the results for a Gaussian noise profile. Here, f_2 is the fraction of atoms in the upper state of a two level system:

$$\begin{array}{l}
 \text{Gaussian Noise} \\
 \text{Rabi} \quad G_{Ri} f_2 = \frac{1}{2} \left(1 + e^{-\frac{t^2 \sigma_\Omega^2}{2}} \cos(\Omega_r t) \right) \\
 \text{Ramsey} \quad G_{Ry} f_2 = \frac{1}{2} \left(1 + e^{-\frac{t^2 \sigma^2}{2}} \cos(2\pi t (\nu_{\text{MW}} - \nu_0)) \right)
 \end{array}$$

The following table summarises the results for a Lorentzian noise profile:

$$\begin{array}{l}
 \text{Lorentzian Noise} \\
 \text{Rabi} \quad L_{Ri} f_2 = \frac{1}{2} (1 + e^{-t\sigma_\Omega} \cos(\Omega_r t)) \\
 \text{Ramsey} \quad L_{Ry} f_2 = \frac{1}{2} (1 + e^{-t\sigma} \cos(2\pi t (\nu_{\text{MW}} - \nu_0)))
 \end{array}$$

from where σ_Ω describes a frequency spread that has a contribution of the driving field (i.e. fluctuations in Ω) and σ contains shifts in the local oscillator. σ_Ω is the noise in the MW field (since it drives transitions between RF-dressed states) and σ is the environmental noise (this can be AC or DC noise or a combination of both).

Rabi Oscillations. Fig. 7.10 shows Rabi oscillations between the dressed $|1, -1\rangle$, $|2, 1\rangle$ states trapped in the crossed-dipole trap ($\omega_z/2\pi \approx 180$ Hz, $\omega_\rho/2\pi \approx 27$ Hz -see Eq. 2.13) with the MW frequency $\nu_{\text{MW}} - \nu_{\text{hfs}} = 6417$ Hz. Atoms were dressed with

the RF-field at $\nu_{\text{RF}} = 2267900$ Hz along $\hat{\mathbf{e}}_x$ with $\Omega_0/2\pi \approx 200$ kHz and $b_z \approx 2.7$ G. These experimental conditions were chosen to minimise the cloud's heating during loading and holding times. We can see high contrast oscillations whose noise increases with the microwave pulse time τ_{MW} . We fit a curve that follows Eq. B.12 and find $\sigma = 13 \pm 2$ Hz and $\Omega/2\pi = 527.7 \pm 0.3$ Hz, from which we can infer using Eq. B.14 a $1/e$ decay time $\tau_{dG} = 100 \pm 15$ ms. From this figure one can find the duration of a $\pi/2$ pulse for this MW amplitude. Now it is a good time to remember that the strength of the transition between RF-dressed states depends on the MW-field amplitude but not on the dressing RF-field amplitude. This measurement was performed by imaging both spin states independently, as described in Section 5.3. In this case f_2 refers to the quantity $f_2 = N_{|2,1\rangle} / (N_{|2,1\rangle} + N_{|1,-1\rangle})$, measured at every experimental run and processed following Appendix C.

Ramsey Fringes. The two plots in Fig. 7.11 show the quantity f_2 in different Ramsey experiments. In these cases the atom cloud was detected via fluorescence imaging and f_2 is a measurement of the atoms in $|2, 1\rangle$ after two *detuned* $\pi/2$ pulses⁹ ($\Delta t = 400\mu\text{s}$) normalised to the total atom number in the sample. The sample was prepared in the crossed-dipole trap ($\omega_z/2\pi \approx 180$ Hz, $\omega_\rho/2\pi \approx 27$ Hz, see Eq. 2.13) and dressed at $b_z \approx 2.75$ G with $\omega_{\text{RF}}/2\pi = 2267900$ Hz in the $\hat{\mathbf{e}}_x$ direction. For the experiment in Fig. 7.11 (a) we set $\nu_{\text{MW}} - \nu_{\text{hfs}} = 6399$ Hz and for Fig. 7.11 (b) we set $\nu_{\text{MW}} - \nu_{\text{hfs}} = 6499$ Hz (we chose different ν_{MW} to cross-check that these were indeed Ramsey fringes). Then we use Eq. B.9 to fit the data, including a phase in the cosine¹⁰:

$$G_{\text{Ry}} f_2 = \frac{1}{2} \left(1 + e^{-\frac{t^2 \sigma^2}{2}} \cos(2\pi \nu_R \tau_{\text{Ramsey}} + \phi_0) \right) \quad (7.1)$$

where σ is the standard deviation of the transition line frequency and thus it is related to the local oscillator fluctuations, τ_{Ramsey} is the time between the two MW pulses, ϕ_0 is an arbitrary phase, and ν_R is the frequency of the Ramsey fringes, which is $\nu_R = |(\nu_{\text{MW}} - \nu_0)|$ where ν_0 is the transition frequency and ν_{MW} is the MW driving field frequency. The fitted function finds $\nu_R = 107.3 \pm 0.7$ Hz and $\sigma = 24 \pm 3$ Hz in (a) and $\nu_R = 200 \pm 3$ Hz in (b), where one cannot fit properly the decay due to the short data sample. We observe ν_R scaled accordingly with the ν_{MW} set in each experiment, thereby confirming the observation of Ramsey fringes. We find a total population decay that matches a typical lifetime and a contrast loss decay time of 58 ms. One

⁹These are MW pulses of the same duration of a $\pi/2$ but set away from resonance in order to observe Ramsey fringes with an oscillation period given by the detuning of the pulse MW frequency.

¹⁰This phase *corrects* for imperfections in the $\pi/2$ pulses.

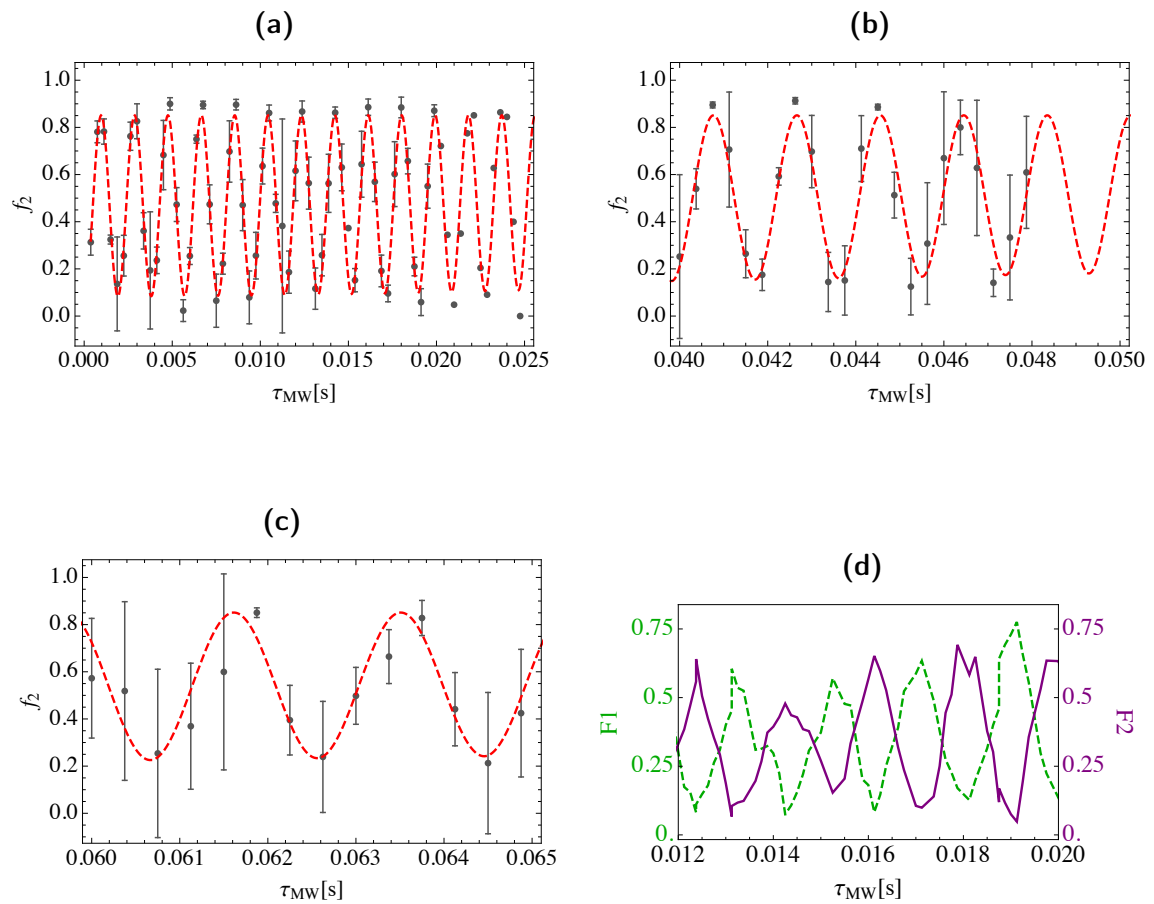


Figure 7.10: In (a,b,c) atom number $f_2 = N_{F=2}/(N_{F=2} + N_{F=1})$ after post-correction following Appendix C as the duration of a microwave pulse with frequency tuned to the atomic transition is increased. The red, dashed line is a fit to all data -from $\tau_{\text{MW}} = 0 \rightarrow 0.07$ - that includes one decay for the contrast (See Eqs. 7.2.3). d) shows the averaged atom number in $F = 1$ (green, dashed) and $F = 2$ (purple) separately. One can see how the two curves are complementary.

can see that for long τ_{Ramsey} times, close to 100 ms, the fringes contrast is washed away and the noise has increased due to the randomization of the process. One important remark is that we observed a $\times 20$ increase in coherence time in a Ramsey-like experiment as the one detailed above when comparing the case of a b_z close to the *maximum* in one of the parabola-like curves shown in Fig. 7.7 with respect to a b_z set closer to resonance, in the linear part. We can see from these results that the decay time is not limited by the inhomogeneous broadening of the crossed-dipole trap (see Section 2.1.3, where we estimated de-phasing times much larger than those reported here). Therefore, the observed broadening must be the result of magnetic field fluctuations. We measured previously a line-shift with the RF-field Rabi frequency, for a fixed b_z , of 7Hz/kHz. To get the measured $\sigma \approx 24\text{Hz}$ the Rabi frequency fluctuations should be of 3kHz, which corresponds to 2mG in B_{RF} units. We can estimate, very roughly, the relationship between the magnitude of the fluctuations in the static magnetic and the line broadening from Fig. 7.7. A reasonable assumption extracted from this figure is 1.5kHz/G. Therefore, the magnitude of the fluctuations in b_z should be of the order of 15 mG. The laser amplitude fluctuations, according to our simulations¹¹, should be unrealistically large to justify this decay. From Section 2.2.1 we can estimate, for the trap parameters at hand, a mean field collisional broadening of 4Hz if the cloud is thermal and 24Hz if there are 100×10^3 condensed atoms. It is not unlikely that there was a condensed fraction, which would lead to a collisional broadening of the order of 10 Hz. In conclusion, our observation is likely to be a combined effect, with collisions likely contributing significantly to the de-phasing.

Stark shifts

We used the relatively long coherence time and high contrast of the dressed clock transition Ramsey fringes to measure differential dipole trap Stark shifts. The error in each measurement is approximately 2Hz. Fig. 7.12 shows the experimental measurement of fringes like those presented in Fig. 7.12 for three different amplitudes in the dipole trapping light. The grey dots are the atom number in $|2, 1\rangle$ normalized to the total atom number, and the coloured curves correspond to fits like those introduced in previous sub-sections. Fig. 7.12 d) shows the result of the fitted frequency to the curves. Assuming a linear dependence, one finds an upper bound of the differential Stark shift of approximately 3Hz/W, with a total trapping power of

¹¹One can calculate the stark shift for an atom at two different laser powers and estimate how large amplitude fluctuations should be for the energy difference to match the reported de-phasing.

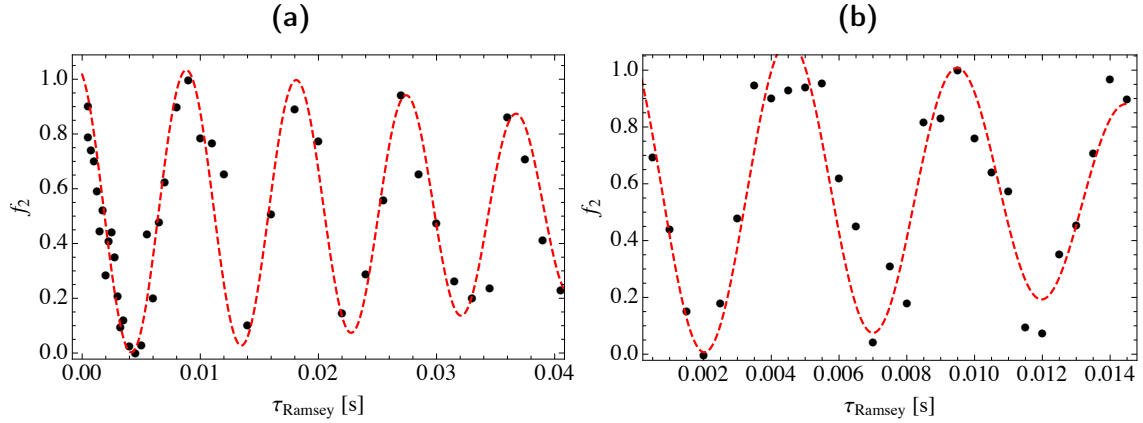


Figure 7.11: Measured atom number (black dots) as the time between two MW pulses of a frequency detuned by 200Hz from the resonance of the transition between the dressed $|1, -1\rangle \rightarrow |2, 1\rangle$ increases. The red, dashed line is a fit that includes a decay of the contrast together with another decay of the total population. In a) $\nu_{\text{MW}} - \nu_{\text{hfs}} = 6399$ Hz and in b) $\nu_{\text{MW}} - \nu_{\text{hfs}} = 6499$ Hz.

some 2W. This is only an illustrative example of the potential capabilities when using the relatively long coherence time in transitions between two trapped RF-dressed states in an optical potential. It could be particularly interesting to include small spatially inhomogeneous fields that would lead to state-dependent trapping, yet by using still the optical potential as a base waveguide.

7.3 MW-spectroscopy in a shell trap

The coherent driving of MW-transitions between RF-dressed states in a magnetic trap is of fundamental importance for the *bucket* interferometer proposed in [Navez *et al.*, 2016]. This section introduces the first experiments performed in the adiabatic shell potential. In [Navez *et al.*, 2016] the waveguide was formed by a TAAP, therefore the results presented here are not a complete characterisation of the transition broadening in the ring, given that in the shell trap there is no modulation field B_m . However, the underlying physics of the atomic transition of interest will remain fundamentally unchanged. Moreover, the shell trap is the ideal test-bed for magnetically trapped RF-dressed atoms. The shell trap potential, as we have seen in Section 4.1.2 is defined as:

$$V_{|F, \bar{m}\rangle}(\mathbf{r}) = s\bar{m}\hbar\sqrt{\delta_F^2 + \Omega_{\text{RF}}^2(\mathbf{r})} + Mg z \quad (7.2)$$

from where we had already established all relevant parameters in Eq.4.15. Both

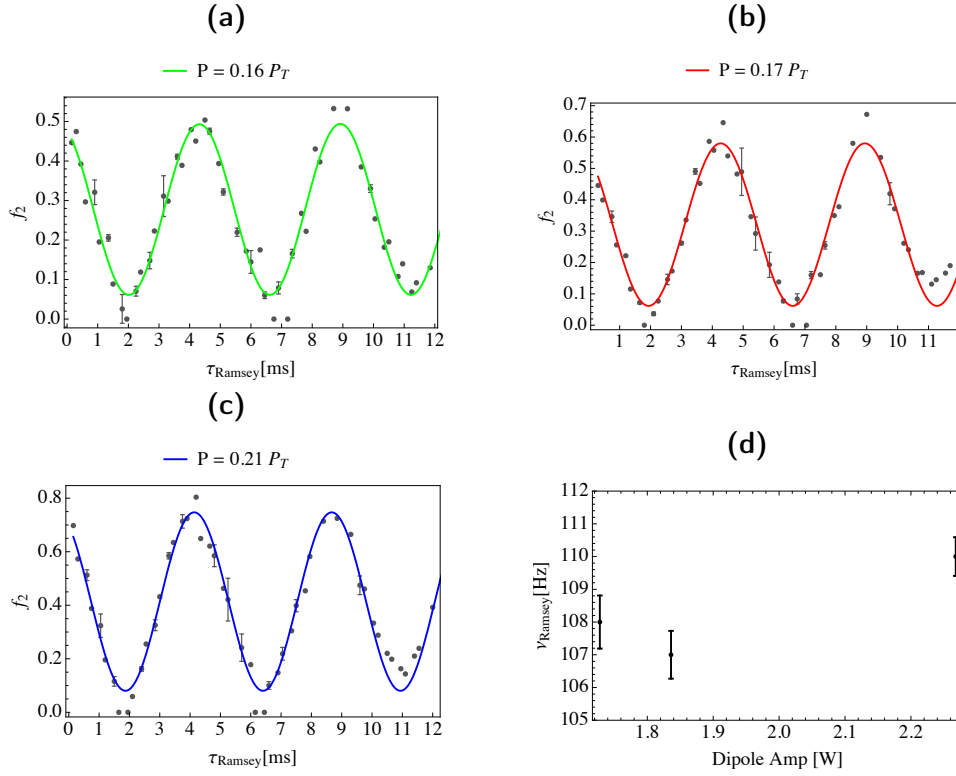


Figure 7.12: Measured atom number in $|2, 1\rangle$ (normalized to the total atom number $N = N_1 + N_2$ where N is measured using the two-state imaging technique explained in Section 5.3) for three different dipole trap settings in a Ramsey experiment. The numbers in the legends signal the fraction of the total dipole power during the interrogation time. The translation into Watt at the atoms position is: a) $0.16 \rightarrow 1.728\text{ W}$, b) $0.17 \rightarrow 1.836\text{ W}$ and c) $0.21 \rightarrow 2.268\text{ W}$ d) Shows the measured Ramsey frequency for each of the three cases.

δ_F and Ω_{RF} are spin-state dependent. As we present in Fig. 7.13 this leads to state-dependent traps, not only with regards to the RF-polarisation coupling g_F -dependences, but also on the quadrupole-field induced \bar{m} -dependent force. Fig. 7.13 shows the differences in energy $\Delta E_1 = V_{|1,-1\rangle} - V_{|2,1\rangle}$ and $\Delta E_2 = V_{|1,-1\rangle} - V_{|2,2\rangle} - \Omega_0$. These curves illustrate the inhomogeneous broadening induced by the energy gap that a cloud of size Δz would experience during atomic transitions (Ω_0 is the Rabi frequency at the center of the shell trap). Fig. 7.13 shows the effects of the traps mismatch: i) there is no trap for $|2, 0\rangle$, ii) there is less heating in $|2, 1\rangle$, and iii) the line-width is one order of magnitude narrower in the transition $|1, -1\rangle \rightarrow |2, 1\rangle$ compared to the other transitions (it is 1.5 kHz in one case and 20 kHz in the other two cases). To highlight this effect, in Fig. 7.13 (c,d,e) we show absorption pictures at the position of the trap 95ms after inducing the three different transitions.

One can observe the striking difference both in optical density and heating that the cloud experiences. Fig. 7.13 (a) shows the peak optical depth for a range of MW frequencies close to the three transitions of interest. The blue line is a measurement after 1ms of hold time after the MW pulse and the red diamonds are a measurement (at the resonance) after 95ms of hold time. One notices a total loss of atoms in $|2, 0\rangle$ and the short lifetime of the other two states, which is roughly of 100 ms for $|2, 1\rangle$ and 60 ms for $|2, 2\rangle$. Therefore, although the full MW spectrum remains unchanged in its structure, magnetic trapping, that relies on spatially dependent coupling of the atomic spin, leads to state-dependent trapping potentials. The dephasing time in the *clock* transition becomes shorter than 1 ms in this case and this prevents, at first sight, any clock-type atom-guided interferometer to work¹². In order to overcome it, one would need to compensate for the different g_F factor (in this case, $|\bar{m}|$ is the same). In an optical potential, the matching of the Rabi frequency of the RF-field could simply be done by tuning the polarisation of the RF, since the trapping position is determined by the optical force, which can be made state-independent. However, the trap position in the shell is determined by g_F and this can only be compensated by choosing different RF-dressing frequencies for the two states. This is precisely the idea behind the bi-chromatic shell trap, the central topic in Section 7.4.

To load the shell trap from the crossed-beam optical trap we first switch on a very weak quadrupole $\alpha < 15$ Gpcm, which is displaced upwards with a bias field in the z direction b_{z1} . Afterwards we switch on B_{RF} and then slowly ramp down the bias field from b_{z1} to b_{z2} ($t_{b_{z1} \rightarrow b_{z2}} = 200 - 400$ ms) until the crossed-dipole trap and the shell trap are overlapped. b_{z1}, b_{z2} are chosen according to $\hbar\omega_1 \approx \mu_B |g_1| b_{z2} \approx \mu_B |g_1| b_{z1} / 2$ (for an optimal loading, $g_F m_F \mu_B b_{z2}$ needs to be well matched to $\hbar\omega_1$). We tune all the parameters so that the trapping frequencies are close for the two traps. In the final step we ramp down the dipole trap laser power ($\Delta t_{\text{transfer}} = 200$ ms) and switch it off. We can load clouds without noticeable heating nor atom number loss. Fig. 7.14 shows the cloud after loading for several RF-frequencies. It is clear that only the ones that spatially match the dipole trap position result in no atom loss nor heating. The RF-amplitude is $\Omega_{\text{RF}} \approx 300$ kHz, the quadrupole gradient $\alpha = 80$ Gpcm, and the bias field $b_z \approx 3$ G.

¹²This dephasing time is limited by the large differential Zeeman shift between RF-dressed states.

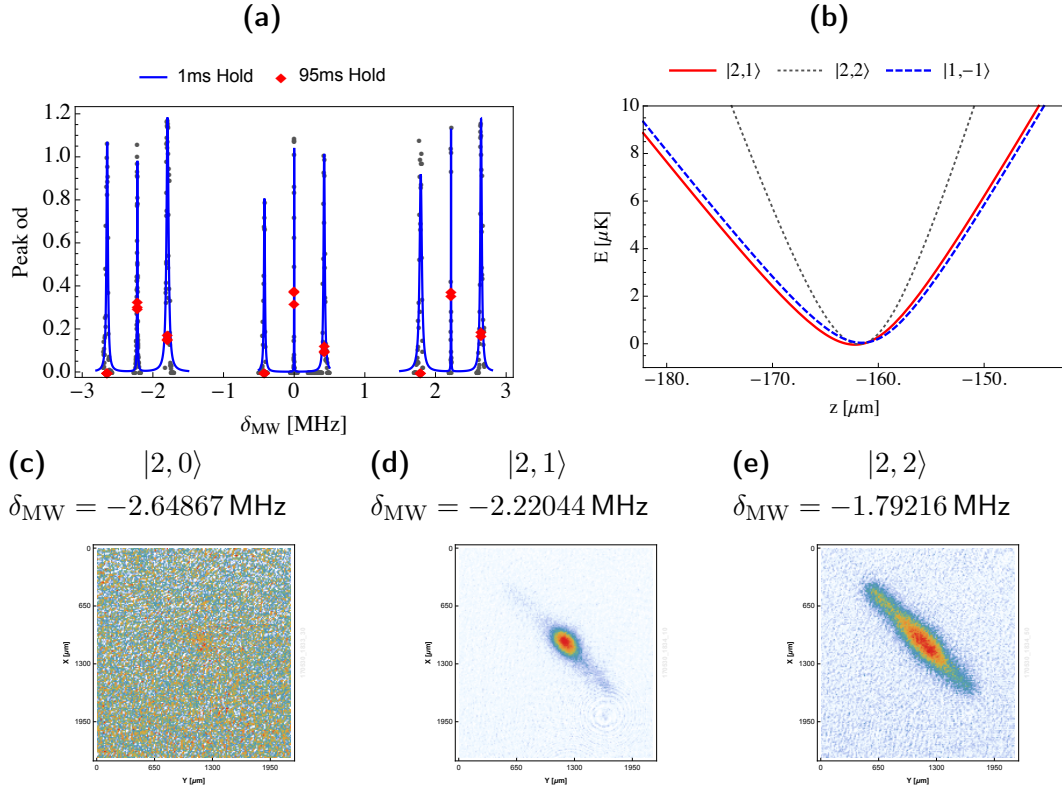


Figure 7.13: a) MW spectrum close to the hyperfine line that includes transitions from $|1, -1\rangle$ to $|2, 0\rangle$, $|2, 1\rangle$ and $|2, 2\rangle$ in the three central groups (See Section 3.3). Black dots represent the atom number measurements and the blue lines are Lorentzian fits. The red dots are atom optical depth measurements in the final state after being held in the shell for 95ms. b) Shows the traps mismatch, which leads to larger linewidth and heating in the transition to $|2, 2\rangle$ compared to $|2, 1\rangle$. It is important to notice that atoms transferred to $|2, 0\rangle$ are untrapped. (c,d,e) are absorption images 95ms after the application of the MW pulse. c) corresponds to $|2, 0\rangle$, d) to $|2, 1\rangle$ and e) to $|2, 2\rangle$. The transition frequency δ_{MW} corresponds to the detuning from the hyperfine line.

7.4 The bi-chromatic shell

The bi-chromatic shell trap is loaded by following the same procedure explained in Section 7.3. Trapping frequency measurements in both the mono-chromatic and the bi-chromatic shell are in agreement with Eq. 4.43 and Eq. 4.41. Their typical range is: $\omega_z/2\pi$ from 50 Hz to 300 Hz and $\omega_{x,y}/2\pi$ from 8 Hz to 13 Hz. Fig. 7.15 shows the cloud oscillation frequency for several gradients in the case of a mono-chromatic and a bi-chromatic shell, together with the expected trapping frequencies from theory -with and without the inclusion of gravity- (see Section 4.2). In these cases, $\omega_{\text{RF}}^{F=1}/2\pi = \omega_1/2\pi = 2267900$ Hz, $\omega_{\text{RF}}^{F=2}/2\pi = \omega_2 = 2258910$ Hz and

(a) Graphic representation of the evolution of b_z , α and the total dipole trap power in a typical experiment.

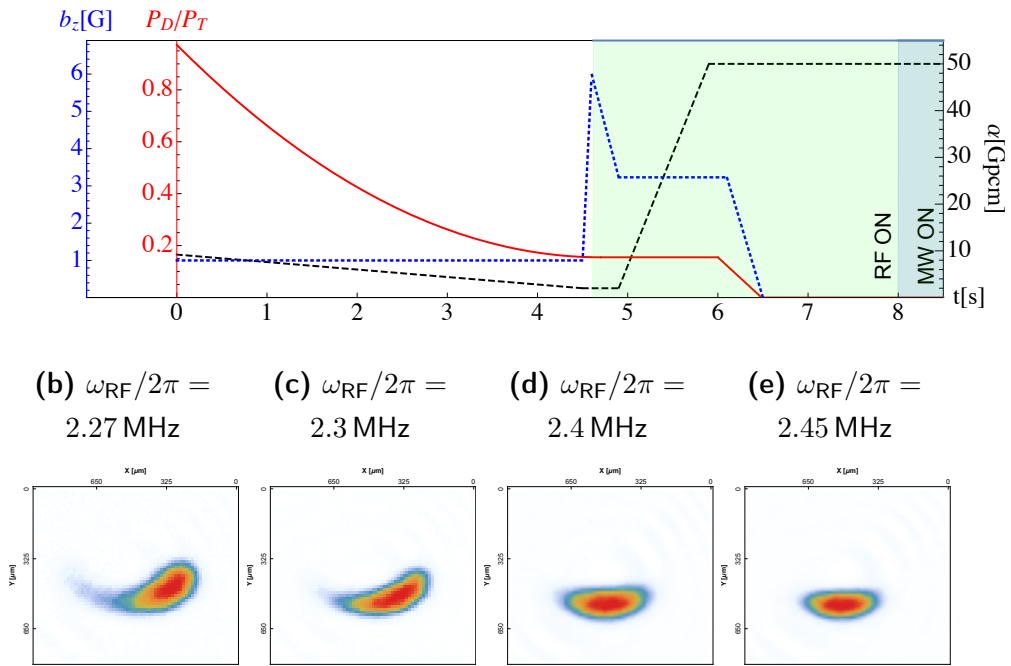


Figure 7.14: (a) A typical experimental sequence to load a shell trap, with a focus on three key parameters: the vertical bias field b_z , the total power in the dipole laser P_{Dipole} and the quadrupole field gradient α . The green, dimly shadowed area indicates the time that the RF-field is on. The doubly (blue and green) shadowed area indicates the time when a MW pulse is switched on. Notice that the time duration of the latter is exaggerated for the readers convenience. This figure shows how these parameters change from the onset of evaporation (where the solid red curve of P_D/P_T -where P_D stands for dipole power and P_T stands for *total* dipole power, i.e. 20W- begins its turn downwards) until right after a MW pulse is applied. After this sequence, the atom cloud is detected via absorption imaging. At $t \approx 4.5$ s the RF is switched on and the cloud is dressed with a sweep of the bias field. At this point, the quadrupole is very weak, and atoms are still trapped in the crossed dipole. Two slow consecutive ramps, first of α to a high curvature field, then of P_D to zero result in the atoms trapped in the adiabatic shell. All vertical axis begin at zero. Figures (b,c,d,e) are absorption images of the shell trap after loading. All parameters are fixed except the RF-frequency. In b) the dipole trap and final shell trap positions are unmatched and the cloud experiences heating and oscillates after transfer. In c) and d) the transfer improves. In e) we observe a smaller (colder) cloud nearly perfectly matched in position.

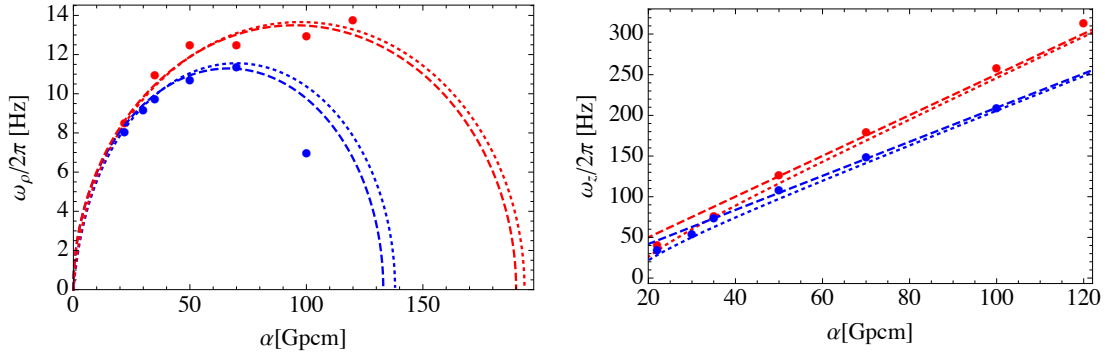


Figure 7.15: Measured trapping frequencies in a mono-chromatic (blue) and bi-chromatic shell (red). Dots represent the result from a fit to a product of a sine wave with an exponential of several cloud position oscillations in trap. ω_ρ is the radial trapping frequency and ω_z is the axial trapping frequency. Dotted (dashed) lines are the expected trapping frequency from the theory including gravity (without including gravity).

$\Omega_{\text{RF}}/2\pi \approx 260$ kHz for both shells. We observe a reduction in power after the RF amplification of 30 – 40% in Ω_1 when switching on the RF-field at ω_2 (as described in Section 5.5.3, both frequency components are driven from the same amplifier). As a consequence, the trapping frequencies scale accordingly (see that in this figure, the measured Rabi frequency is plugged into the analytical formula and there are no free parameters). One important point is the maximum in the trapping frequency at $\alpha \approx 70$ Gpcm. The minimum curvature at this point can be a good choice in more advanced atom-interferometry applications.

Fig. 7.16 shows the BEC lifetime as the gradient α changes. The RF-dressing frequencies are $\omega_1/2\pi = 2294336$ Hz, $\omega_2/2\pi = 2285238$ Hz¹³ and $\Omega_{\text{RF}}/2\pi \approx 260$ kHz. We load a BEC prepared in the crossed-dipole hybrid trap in the $|1, -1\rangle$ state. The thermal atoms lifetime in the same series of experiments is of up to 80s and the BEC lifetime reaches up to 7s. As in all RF-dressed potentials, Landau-Zener losses at the avoided crossing are the main source of lifetime shortening before background collisional losses become important¹⁴. Imperfections in the RF-generation produce trap-averaging effects that modify the shape of the trap, given that, in that case, each state is dressed by a bi-chromatic field. See that this situation contrasts with

¹³We only interrogate atoms in $F=1$ in experiments where transitions are not driven. The frequency ω_2 may shorten the lifetime if it is close to any of the possible intra-manifold transitions. In addition, it can produce parametric heating if it is very close to ω_1 and it modulates the trapping frequencies and the trap position.

¹⁴For *strong* RF-amplitudes LZ losses become smaller.

that of the ideal bi-chromatic trap, where each state is dressed only by one frequency. We know that these imperfections are present (see Section 7.5.1), but they do not seem to introduce additional lossy channels in the trap. We could achieve similar lifetimes at lower gradients, however, in this particular experiment, the loading was optimum at this range (i.e. the resonant surface was aligned better with the dipole trap at these gradients).

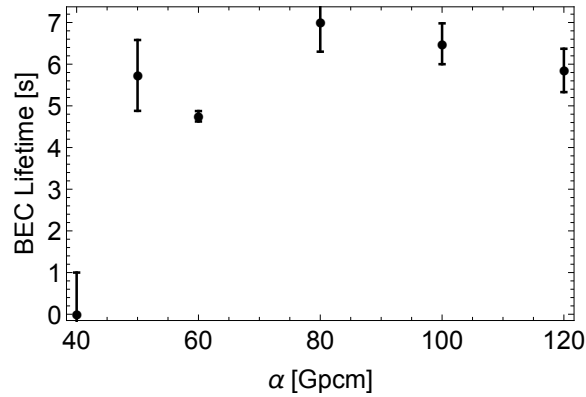


Figure 7.16: BEC lifetime in the bi-chromatic shell for different gradients in a span $\alpha = 40 - 120$ Gpcm. The thermal cloud lifetime in these experiments was of the order of 1min. This experiment is performed with a fixed RF-frequency and fixed RF-amplitude.

7.5 Spectroscopy in the Bi-chromatic Shell Trap

The key aspect of the bi-chromatic trap is that it allows for state-dependent control of both the curvature (via the Rabi frequency) and the position of the traps (via the RF-frequency). In this section we will make use of these experimental *knobs* to match the traps of the two spin states of interest so as to reduce the linewidth of the *clock* transition (we found it to be too broad to become of practical use in Section 7.3).

We have seen in previous sections that there is one transition available between the dressed $|1, -1\rangle, |2, 1\rangle$ states with $\Delta E \approx \hbar\omega_{\text{hfs}}$. This transition is shifted by the non-linear part of the energy splitting and, due to the difference in g_F , each state will experience altogether different Rabi frequencies for the same RF magnetic field B_{RF} . In addition, when we interrogate this transition, we find that the cross-coupling of B_2 (B_1) with $F = 1$ ($F = 2$) induced by imperfections in the RF-field polarisation results in a periodic modulation in time of the energy splitting that ends up provoking a

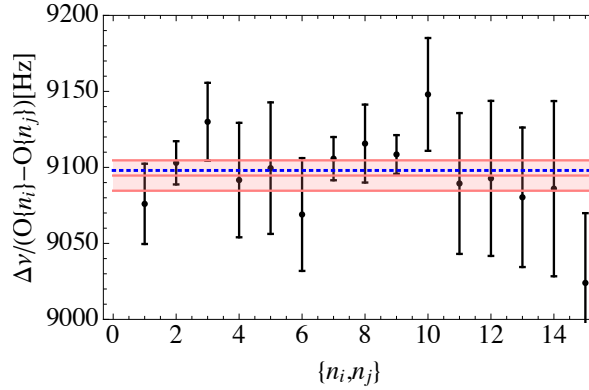


Figure 7.17: Measured frequency difference from a number of harmonics of the clock transition in the bi-chromatic shell. The horizontal axis shows a pair n_i, n_j out of a sample of 6 measured peaks. All possible pairs from this sample are therefore $(6 \times 6 - 6)/2 = 15$ points. The vertical axis shows the quotient between the frequency difference and the order of the peak. The order of the peak is defined with respect to an arbitrarily chosen central peak. The blue line indicates the expected line-shift. The orange area surrounds the mean value of all measurements excluding the highest and lowest points. Black dots correspond to fits to Lorentzian curves of the MW spectrum and the error is the one of the fit.

cascade of multi-photon transitions [Silveri *et al.*, 2017; Oliver *et al.*, 2005]. These imperfections result also in time-averaged reshaping of the traps. As a consequence, the bi-chromatic shell deviates from the spectral response explained in Section 3.3, i.e. 7 peaks close to $\omega_{\text{MW}} = \omega_{\text{hfs}} + n\Omega_{\text{RF}}$. The difference lies in the presence of a finite number of harmonics separated by $\Delta\omega = |\omega_1 - \omega_2|$ (we have only interrogated, alternatively, $n = 0, 1$ in our experiments). Fig. 7.17 shows a measurement of all differences in frequency divided by the peaks' distance between six of these harmonics. One can observe that they are separated by $\Delta\nu = \nu_1 - \nu_2$, which in this case is $\Delta\nu = 2294336\text{Hz} - 2285238\text{Hz} = 9098\text{Hz}$ (the measured mean distance between two peaks is $\Delta\nu = 9076 \pm 65\text{Hz}$). We address these multi-photon transitions with a semi-classical two-level toy model in Section 7.5.1.

7.5.1 Multi-photon spectrum

The multi-photon spectrum can be explained by imperfections in the RF-polarisation. We will derive an approximate expression to describe the resulting eigen-energies modulation due to cross-coupling from the RF-dressing field of the two manifolds.

In order to account for imperfections in the RF-fields polarisation we will find the circular projections of B_{RF}^1 (B_{RF}^2) in σ_- (σ_+) into the local basis of the quadrupole at the center of the traps, where it is aligned with $\hat{\mathbf{e}}_z$. We will assume that the phase at the RF-generation coils is $s\pi/2$, but that the RF-field amplitudes in the two coils are not the same. Then, for a generic case, we have:

$$B = B_x \cos(\omega t) \hat{\mathbf{e}}_x + B_y \sin(\omega t) \hat{\mathbf{e}}_y \quad (7.3)$$

Now we can use that $B_0 = (B_x + B_y)/2$ and $\Delta B = (B_x - B_y)/2$ to write:

$$B = (B_0 - \Delta B) \cos(\omega t) \hat{\mathbf{e}}_x + (B_0 + \Delta B) \sin(\omega t) \hat{\mathbf{e}}_y \quad (7.4)$$

where one can readily see a *counter-rotating* component of amplitude ΔB . The result is a total field with crossed components $\Omega_{1,2} = \frac{|g_1|\mu_B}{2\hbar} \Delta B_{B1}$ and $\Omega_{2,1} = \frac{|g_2|\mu_B}{2\hbar} \Delta B_{B2}$, where $\Delta B_{B1} = (B_{x1} - B_{y1})/2$ and $\Delta B_{B2} = (B_{x2} - B_{y2})/2$. We can now write the full magnetic field as:

$$\begin{aligned} \frac{g_F \mu_B}{2\hbar} B_{\text{RF}}(t) = & ((\Omega_1 - \Omega_{1,2}) \cos(\omega_1 t) + (\Omega_2 - \Omega_{2,1}) \cos(\omega_2 t)) \hat{\mathbf{e}}_x \\ & + (-(\Omega_1 + \Omega_{1,2}) \sin(\omega_1 t) + (\Omega_2 + \Omega_{2,1}) \sin(\omega_2 t)) \hat{\mathbf{e}}_y \end{aligned} \quad (7.5)$$

where $\Omega_j = \frac{g_F \mu_B}{2\hbar} B_{\text{RF}}^j$ are the circular projections of the Rabi frequency (magnetic field) into the circular basis. Notice that $\Omega_{1,2}, \Omega_{2,1}$ are the crossed contributions from B_{RF}^1 into $F = 2$ and from B_{RF}^2 into $F = 1$. The static part of the Hamiltonian in Eq. 4.14 is:

$$H_0 = H_0 + H_{\text{DC}} = \sum_{F=1,2} \frac{A_{\text{hfs}}}{2\hbar^2} (F(F+1) - 9/2) \hat{P}^F + \frac{\mu_B}{\hbar} \sum_{F=1,2} g_F \hat{F}_z^F B_{\text{DC}} \quad (7.6)$$

where P^1, P^2 (\hat{F}_z^1, \hat{F}_z^2) are projectors (operators) into the respective two subspaces with the definitions given in Eq. 3.7. Here we have chosen a B_{DC} that would correspond to the quadrupole field at the trap position z_0 (see Eq. 4.21). The time dependent part will be given by $H_{\text{RF}} = g_F \mu_B \mathbf{F} \mathbf{B}_{\text{RF}}(t)$. In the absence of a strong coupling between the hyperfine manifolds, and assuming that the atoms in the sub-states $|F, \bar{m}_F\rangle$ follow adiabatically Eq. 4.15, we can calculate the time evolution in the state-dependent rotating frames resulting from the application of:

$$U_z = \prod_F \exp\left(\frac{-i\omega_F t \hat{F}_z^F}{s\hbar}\right) \quad (7.7)$$

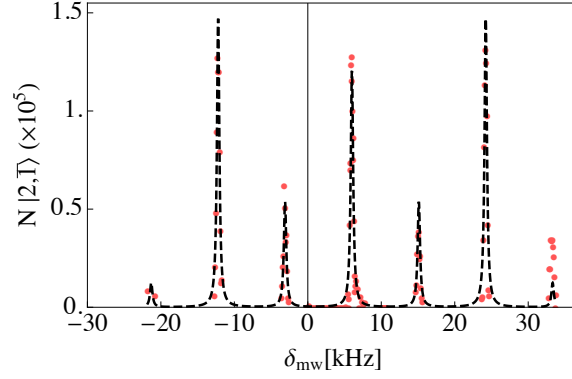


Figure 7.18: An example of a multi-photon spectrum. Red dots indicate experimental measurements and the black dashed line is a fit to the data employing the result in Eq. 7.13. The difference in RF-frequency between the two dressing fields is $\Delta\nu = \nu_1 - \nu_2$. In this particular case we have $\Delta\nu = 2294336\text{Hz} - 2285238\text{Hz} = 9098\text{Hz}$.

where we have assumed, for simplicity, that $g_1 = -g_2$. We calculate the time evolution $\hat{H} = U_z^\dagger(H_0 + H_{\text{RF}})U_z - i\hbar U_z^\dagger \delta_t U_z$, after which we define $\Delta = \omega_1 - \omega_2$, similarly to [Garrido Alzar *et al.*, 2006]. The resulting Hamiltonian is:

$$H = H_{hf} + \sum_F s (|g_F| \mu_B B_{\text{DC}} - s \hbar \omega_F) \hat{F}_z^F + \sum_{F, F'} \left[\delta_{F, F'} \Omega_F \hat{F}_x^F + (1 - \delta_{F, F'}) \Omega_{F, F'} \left[\hat{F}_x^{F'} \cos(\Delta t) - \hat{F}_y^{F'} \sin(\Delta t) \right] \right] \quad (7.8)$$

where the sum is over $(F, F') = 1, 2$ and $\delta_{F, F'} = 0, \delta_{F, F} = 1$. Close to resonance, \bar{m}_F remain *good* quantum numbers and we can find the eigen-energies:

$$E_{F, \bar{m}}(t) = s \left(I + \frac{1}{2} \right) \frac{\hbar \omega_{\text{hfs}}}{2} + |\bar{m}_F| \hbar \sqrt{\delta_F^2 + \Omega_{F, \text{m}}^2(t)} \quad (7.9)$$

with $s = 1$ ($s = -1$) for $F = 2$ ($F = 1$) and $I = 3/2$ and where $\delta_F = \mu_B |g_F| B_{\text{DC}} - \hbar \omega_F$, and:

$$\Omega_{F, \text{m}}^2(t) = \Omega_F^2 + \Omega_{F, F'}^2 + 2\Omega_F \Omega_{F, F'} \cos(\Delta t) \quad (7.10)$$

For small $\Omega_{2,1}$, $\Omega_{1,2}$ the time averaged potential resulting from Eq. 7.9 is well approximated by Eq. 4.15. Notice however that we did not account for the spatial dependence of the quadrupole field, since we have assumed a homogeneous field aligned with $\hat{\mathbf{e}}_z$, which is only a fair approximation for small clouds at the bottom

of the trap (and for perfect matching in the bi-chromatic shell). It is nonetheless illustrative enough to now develop this argument further by considering that any pair of $|1, \bar{m}_F\rangle, |2, \bar{m}'_F\rangle$ can be treated as a two-level system coupled by a weak microwave field. Particularly, in this two-level atom picture, for small $\Omega_{1,2}, \Omega_{2,1}$, the difference in energy between $|1, -1\rangle$ and $|2, 1\rangle$ is modulated according to:

$$\Delta\Omega(t) = \Omega_2 - \Omega_1 + (\Omega_{2,1} - \Omega_{1,2}) \cos(\Delta t) \quad (7.11)$$

now we can write the reduced matrix in a two-dimensional basis with $|2, 1\rangle \rightarrow |\uparrow\rangle$ and $|1, -1\rangle \rightarrow |\downarrow\rangle$:

$$H_m = \left(\frac{\omega_{\text{hfs}}}{2} + \frac{\Delta\Omega(t)}{2} \right) \hat{\sigma}_z + \Omega_{\text{MW}} \cos(\omega_{\text{MW}} t) \hat{\sigma}_x \quad (7.12)$$

where we have included a weak microwave link between the two states. This system is described in detail in [Silveri *et al.*, 2017], from where we retrieve the general solution for the spectral response:

$$P_\omega(\omega) = \sum_{j=-\infty}^{\infty} \frac{\Gamma |J_j(\xi)|^2}{(\delta + j\Delta\omega)^2 + \Gamma^2} \quad (7.13)$$

where Γ is the line-width of each transition, determined by all the involved dephasing and decoherence processes, and $\delta = \omega_{\text{MW}} - \omega_0$, $\Delta\omega = \omega_1 - \omega_2$. This expression corresponds to an infinite number of transitions centred at ω_0 and spaced by $\Delta\omega$ with relative amplitudes given by the family of Bessel functions of the first kind with argument $\xi = \Delta\Omega_{F,F+s}/\Delta\omega$, where $\Delta\Omega_{F,F+s} = |\Omega_{1,2} - \Omega_{2,1}|$ is the amplitude of the energy splitting modulation. ω_0 is the transition frequency. In the bi-chromatic shell spectrum, all 7 transitions corresponding to $n = -3, \dots, 0, \dots, 3$ will present this multi-photon resonance. Fig. 7.18 shows an example of a multi-photon spectrum measured in the bi-chromatic shell. We can fit the data, depicted in Red dots, to Eq. 7.13 to find an modulation amplitude of the two-levels eigen-energies of $|\Omega_{2,1} - \Omega_{1,2}|/2\pi = 118$ kHz and $\Delta/2\pi = 9098$ Hz for $\Omega_1/2\pi \approx \Omega_2/2\pi = 123$ kHz and $\omega_1/2\pi = 2.294336$ MHz and $\omega_2/2\pi = 2.285238$ MHz.

7.5.2 Line-shift with a bias field

Possibly the key potential advantage of the shell with respect to other magnetic traps in guided atom-clock interferometry applications is that homogeneous DC magnetic field fluctuations do not contribute to the broadening of the transition. The reason is that the bias field only translates in space the quadrupole trap, but

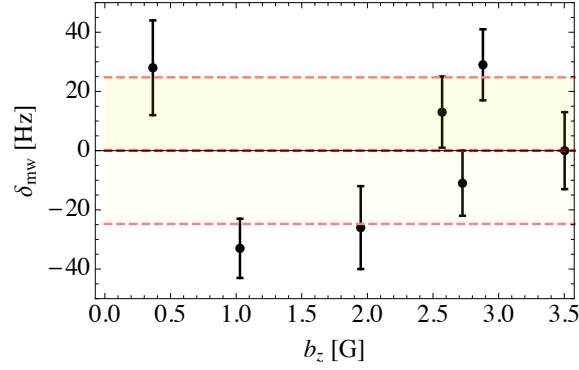


Figure 7.19: Measured $\delta_{MW} = (\omega_{MW} - \bar{\omega}_0)/2\pi$ where $\bar{\omega}_{MW}$ is the mean value of the transition frequency ω_{MW}^j corresponding to each b_{zj} . The trap parameters are $\omega_1/2\pi = 2.294336$ MHz, $\omega_2/2\pi = 2.285238$ MHz, $\Omega_1 \approx \Omega_2 \approx 240$ kHz, $\alpha = 70$ Gpcm. The MW pulse lasts $t_{MW} = 2$ ms and it lies within the first slope of a Rabi cycle.

the eigen-energies of the dressed states are still ultimately defined by the resonance point of the RF-frequency with the quadrupole field (see Fig 4.2). As a consequence: a DC homogeneous field offset does not shift the transition.

In Fig. 7.19 we show a measurement of the $|1, -1\rangle \rightarrow |2, 1\rangle$ transition for a range $\Delta b_z \approx 3.5$ G. We load a bi-chromatic shell with $\omega_1/2\pi = 2.294336$ MHz, $\omega_2/2\pi = 2.285238$ MHz, $\Omega_1/2\pi \approx \Omega_2/2\pi \approx 240$ kHz and $\alpha = 70$ Gpcm. We subsequently drive the transition at $n = 0, k = 0$ ($t_{MW} = 2$ ms) after ramping ($\Delta t = 0.2$ s) b_z from b_{z2} to a final b_{zj} . Fig. 7.19 shows $\delta_{MW} = (\omega_{MW} - \bar{\omega}_0)/2\pi$, with the shaded yellow area corresponding to one standard deviation from the mean $\bar{\omega}_0 = \sum_j \omega_j/n_\omega$, where n_ω is the total number of measurements of the transition frequency for a given b_z . From here, we can retrieve the fact that , experimentally, we have not observed any line-shift in the $|1, -1\rangle \rightarrow |2, 1\rangle$ transition for a range $\Delta b_z \approx 3.5$ G.

7.5.3 Line-shift with $\Delta\Omega_{RF}$

We can estimate from Eq. 4.15 the expected line-shift associated to the difference in Rabi frequency ($\Delta\Omega_{RF} = \Omega_2 - \Omega_1$). When the position of the two traps is matched, it becomes directly proportional to $\Delta\Omega_{RF}$. In Fig. 7.20 we show the transition frequency $\delta_{MW,j} = (\omega_{MW,j} - \omega_{hfs})/2\pi$ for several $\Delta\Omega_{RF}$. The Rabi frequencies had been calibrated using the methods outlined in Section 7.1.1 and Section 7.3. Initially, we set $\Omega_1/2\pi \approx \Omega_2/2\pi \approx 370$ kHz and $\alpha = 22$ Gpcm. The RF-frequencies for the

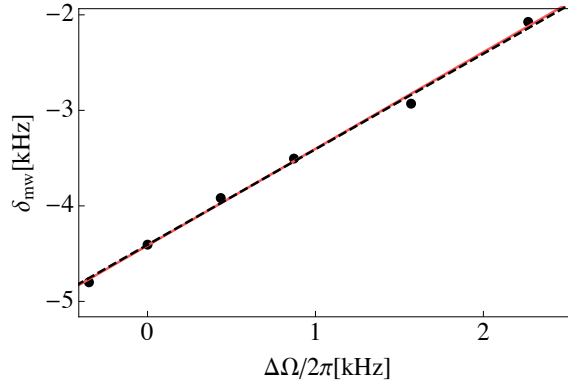


Figure 7.20: Measured shift for the dressed $|1, -1\rangle \rightarrow |2, 1\rangle$ transition for several values of the difference in Rabi frequency $\Delta\Omega_{\text{RF}} = \Omega_2 - \Omega_1$ between the V^1 and V^2 shell traps. The red line is a fit that yields a slope of 1.01 ± 0.01 Hz/Hz with an offset of -4412 ± 20 Hz. The black dashed line indicates a directly proportional shift of δ_{MW} with $\Delta\Omega_{\text{RF}}$. The errors in δ_{MW} are smaller than the black dots. There is a systematic error in the measurement of both Ω_F of the order of 2 kHz from the calibration -performed as shown in Fig. 7.2.

two traps were calculated according to Eq. 4.25 and fine-tuned experimentally. The chosen RF-frequencies were $\omega_1/2\pi = 2.267900$ MHz and $\omega_2/2\pi = 2.258910$ MHz. The black dashed line is the expected shift if the transition frequency scales linearly with $\Delta\Omega_{\text{RF}}$ ¹⁵ and the red line is a linear fit to the data. The resulting slope entails a 700 Hz/mG broadening with fluctuations in the RF-amplitude difference $\Delta\Omega_{\text{RF}}$ between the two shells, therefore becoming highly detrimental for the coherence time of the *clock*. As an example, achieving 1s coherence time would need a stability of $\Delta\Omega_{\text{RF}}$ of $\sim 10^{-5}$. It is important to note that line-shifts due to changes in the total Rabi frequency are negligible compared to those related to $\Delta\Omega_{\text{RF}}$.

7.5.4 Line-shift at low gradients

The effect of gravity in the transition line-shift is important. It leads to a mismatch of the trap position with respect to the exact resonance point. When gradients are very low, which might become necessary, for instance, to gain access to larger RF Rabi frequencies without the disappearance of the trap from over-compensation of the gravity field, one needs to address the problem as one of off-resonant RF-dressing. Fig. 7.21 shows a Ramsey-like measurement (one first prepares a bi-chromatic shell, then chooses one of the peaks and measures the

¹⁵There are no free parameters in this line

transition and then shines two short MW pulses spaced by some time t_R , just like in Section 7.2.3). We focus on the line-shift as measured from this spectroscopic sequence. The RF-frequencies were $\omega_1/2\pi = 2294336$ Hz and $\omega_2/2\pi = 2285238$ Hz and the Rabi frequencies $\Omega/2\pi \approx 200$ kHz. We observe a parabola-like shape close to 16 Gpcm and an asymptotic behaviour of the line-shift as the gradient is increased (we also observed a decay in contrast in this direction). Numerical simulations show that this curve is possible if the Rabi frequencies in each of the state-dependent traps were different. We can extract two conclusions from this experiment: 1) at low gradients, the contribution of the gradient field fluctuations to the line broadening becomes relevant and 2) (again) the RF-field mis-compensation leads to non-trivial behaviour and faster decoherence rates. A preliminary study can be found in Appendix D.

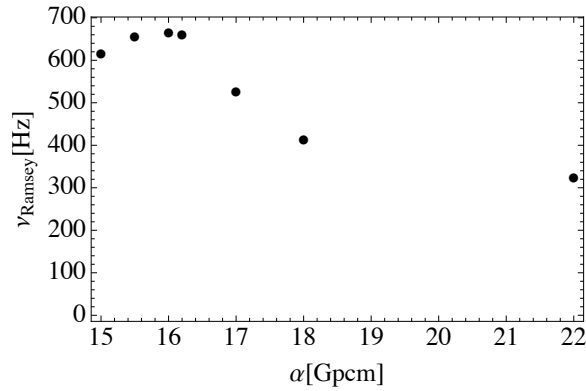


Figure 7.21: Ramsey fringe frequency ν_R measurement of the line-shift in the bi-chromatic shell as the quadrupole gradient α is changed close to the limit of gravity compensation. In this experiment the RF-frequencies are $\omega_1/2\pi = 2294336$ Hz and $\omega_2/2\pi = 2285238$ Hz, and the Rabi frequencies $\Omega/2\pi \approx 200$ kHz.

7.5.5 Tuning $\Delta\omega_F$

In Section 4.2 we advanced an approximate calculation of the needed $\Delta\Omega_{\text{RF}}$ to match the shell traps for the two states. However, as we have shown in the previous sections, one may encounter a number of deviations from this basic theory, related mostly to imperfections in the RF-field. In this section, we present a measurement of the position matching of the two traps by spectroscopic means: we choose a pair of frequencies ω_1, ω_2 , close to the simple prediction of Eq. 4.25 for $\alpha = 45$ Gpcm and $\Omega_1 \approx \Omega_2 \approx 250$ kHz. Then we determine the dependence of the line-width of the transition on $\Delta\omega_F$. Fig. 7.22 (a) shows the line-width after a microwave pulse of $t_{\text{MW}} = 10$ ms. The observed line-width is Fourier limited for this pulse duration. At

the matching condition -of this particular experiment-, we observe a reduction in line-width of $\times 10$ with respect to the mono-chromatic shell (measured in Section 7.1.1). In order to verify that the transition is in fact narrower in the bi-chromatic shell than in the mono-chromatic shell, we performed Rabi and Ramsey-type experiments. We observe very fast decay curves in the mono-frequency shell trap (where we had measured a line of $\Delta f \approx 10^3$ Hz for $t_{\text{MW}} = 10$ ms) whereas the bi-chromatic shell (where we had measured a line-width of $\Delta f \approx 10^2$ Hz for $t_{\text{MW}} = 10$ ms) presents Rabi oscillations with a decay time of ≈ 10 – 20 ms. Fig. 7.22 (b) shows an example of Rabi oscillations in the bi-chromatic shell trap, with $\alpha = 50$ Gpcm, $\omega_1/2\pi = 2.294336$ MHz, $\omega_2/2\pi = 2.285238$ MHz and $\Omega_1/2\pi \approx \Omega_2/2\pi \approx 270$ kHz. We fit the evolution of the population in $|2, 1\rangle$ to $f_2 = f_0 \left[1 - e^{-t^2 \sigma_R^2/2} \cos(\Omega_{\text{MW}} t) \right]$ (as in Eq. B.12) and find $\sigma_R = 57 \pm 6$ Hz and $\Omega_{\text{MW}}/2\pi = 146 \pm 1$ Hz.

This result is significantly far from the prediction from Section 4.2, where we found that it should be possible to reach a line-width of $\sigma_{bc} \approx 4$ Hz. We have commented on a number of potential de-phasing sources in previous sections, being the fluctuations in the difference in Rabi frequency between the two shell traps the major contributor in this case. We calculated that deviations of the order of 1 mG broaden the transition up to $\sigma_{bc} \sim 20$ Hz, and fluctuations of the order of 1 mG cause up to $\sigma_{bc} \sim 700$ Hz. This latter contribution needs to be addressed with technical improvements in the RF-fields generation. However, a more robust solution would be to find a configuration where the transition is less sensitive to fluctuations in ΔB_{RF} . This large sensitivity is dictated by the different g_F in the two states. Therefore, one approach could be to modify the effective g_F of one or both spin-states, so as to match them, as we saw at the end of Section 3.3. There are two avenues under consideration. First, the use of strong-enough RF-fields such that using the Bloch-Siegert matches the effective g-factors (it was the idea developed in Section 3.3). Second, the introduction of another magnetic field, in the audio regime, that would be used to modify the coupling of the dressed atoms to the RF-fields in a state-dependent way. This rather speculative idea is based on the claims from [Kunitomo *et al.*, 1977]. The first solution is not suitable for an ordinary shell trap, since strong RF-fields pull atoms against gravity, to the point of anti-trapping. The second solution has not been studied deeply in the context of adiabatic traps, and, as it was mentioned above, so far it remains as speculation.

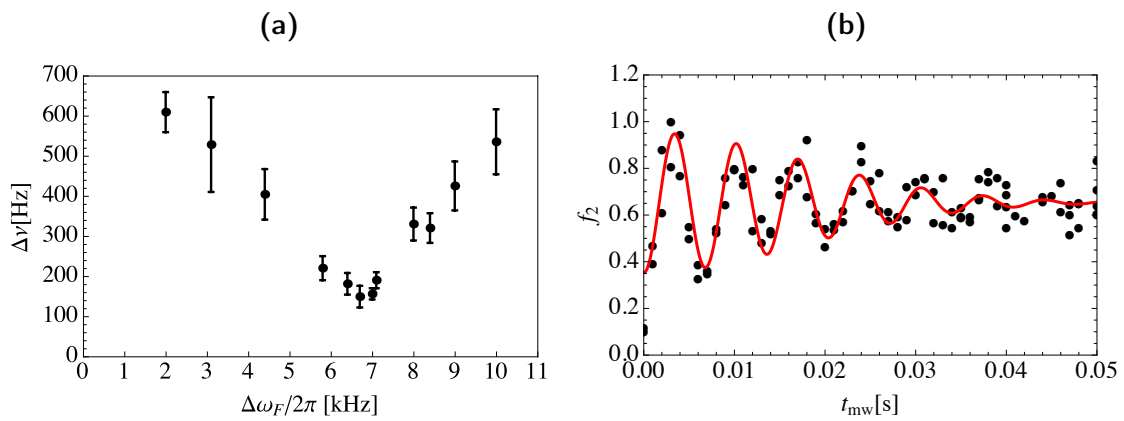


Figure 7.22: In a): measured line-width $\Delta\nu$ in the $n = 1$ transition with a microwave pulse of 10 ms for the clock transition in the dressed states for different values of $\Delta\Omega_{\text{RF}}$. $\Omega_1 \approx \Omega_2 \approx 250$ kHz, $\alpha = 45$ Gpc. In b): Example of Rabi oscillations in the bi-chromatic adiabatic potential.

8

Conclusions

In the introduction (chapter 1) we set out to answer two questions, regarding a trapped and guided atom-interferometer. First: is it possible to guide two spin-states adiabatically along opposite paths in a closed loop? Second: is it possible to reduce the de-phasing of the superposition state after a first beam splitter for a time span of the order of the guiding time? We fully demonstrated the former, and we have studied the limitations of the latter. This thesis presented the experimental realisation of two key elements for a guided atom-clock Sagnac interferometer using ultra-cold atoms of ^{87}Rb . Firstly, the adiabatic loading and manipulation of BECs in a ring waveguide. Secondly, a study of the clock transition in the strong RF-dressed regime with ultra-cold atoms trapped in optical and magnetic potentials.

This experimental work was carried out with a gas of dressed ultra-cold ^{87}Rb atoms. As we introduced in chapters 1 and 2, dilute alkali gases have become one of the most successful platforms to explore quantum matter in highly controlled environments. Particularly, the precise manipulation and understanding of the external and internal degrees of freedom (chapter 3) of ultra-cold atoms and BECs has proven a key component of very precise atom-clocks and matter-wave interferometers, for example. The possibility of creating RF-dressed traps (chapter 4), that allow for state-dependent control of atomic spin states, and also for the creation of ultra-smooth waveguides (e.g. TAAPs) has motivated to a large extent our research. Using this, we proposed a matter-wave Sagnac interferometer based on inferring a gravitational energy difference from a clock shift, using two spin states of ^{87}Rb [Navez *et al.*, 2016]. It is precisely from this proposal that the two questions posed at the beginning of this chapter were drawn. Very clearly, the coherence time of the superposition state needs to be of the order of one round trip along the closed

loop that defines the interferometer; and this displacement should only minimally perturb the atomic cloud. Therefore, one has to manipulate coherently both the external and internal degrees of freedom of ultra-cold clouds of RF-dressed atoms. Chapter 5 presents the experimental setup employed to accomplish these purposes. We described a dipole trap laser set-up to produce ultra-cold atom samples and BECs of up to 3×10^5 atoms of ^{87}Rb in the $|1, -1\rangle$ spin-state, together with all the experimental stages. This system enabled the lossless loading of BECs into a TAAP ring waveguide with no measurable heating altogether (chapter 6). Once in the the ring waveguides, BECs (lifetime 4s) and ultra-cold clouds (lifetime 28s) were manipulated in a state-dependent or state-independent fashion.

Spectroscopy of RF-dressed states. After the successful demonstration of coherent transport of BECs in the ring TAAP waveguides (see [Pandey, 2019; Pandey *et al.*, 2019]) we investigated the response of RF-dressed states to AC and DC fields (chapter 7), having the *clock* transition between $|1, \bar{m}_F = -1\rangle$ and $|2, \bar{m}_F = 1\rangle$ in the spotlight. Importantly, we presented experiments characterising the MW spectroscopy of trapped RF-dressed states. We found good qualitative correspondence between the observed spectra and the theory set out in chapter 3. Furthermore, we studied the line-shifts of several of these transitions with B_{DC} and the RF-field polarisation. An interesting property of RF-dressed states is that the B_{DC} -dependent eigen-energies present parabola-shaped features close to the resonant condition set by $\Omega_L - \omega_{\text{RF}} = 0$ (where Ω_L is the Larmor frequency and ω_{RF} is the RF-frequency). The differential energy shifts of the two-level systems that can be drawn from all Zeeman sub-levels are also parabola-shaped. This means that a number of transitions are *protected* against B_{DC} field fluctuations. Experimentally, we found dephasing times of the order of 100 ms for RF-dressed ultra-cold atoms in a crossed dipole trap in Ramsey and Rabi experiments involving the clock states. Additionally, we measured linewidths down to $\Delta\nu = 120$ Hz (for $\nu \approx 6.8$ GHz) at 3 G in the transitions between the dressed $|1, -1\rangle$ and both $|2, 0\rangle$ and $|2, 2\rangle$ (typically, without setting the fields to the pseudo-magic condition presented in Section 3.4, we measured line-widths much larger than 5 kHz in these two transitions). Having shown long de-phasing times in the crossed dipole, we suggest the implementation of a trapped interferometer where dressed atoms are optically trapped and a weak inhomogeneous magnetic field delivers the needed state-dependent manipulation, in a configuration where the inhomogeneous broadening related to the magnetic trap is much reduced. In addition, one can use a bi-chromatic dressing field to match the parabola-like minima of the differential line-shifts associated to several transitions at one particular B_{DC} , where

they become minimally sensitive to fluctuations in DC-fields 3.4.1. This configuration can produce, for example, a three-level system protected from DC-field noise [Randall *et al.*, 2015]. The transition strengths can be tuned by changing the polarisation of the MW-field¹. In optical dipole traps, we have been able to achieve long coherence times even with condensates, in the RF-dressed regime. An interesting idea is to use an atomic species where interactions can be tuned more easily [Fattori *et al.*, 2008]. In that case, one would not only be able to couple coherently two or more (dressed) spin states via microwave pulses with long dephasing times, but also to conditionally² switch on and off transitions via changes in, for instance, the scattering length.

RF-dressed states are particularly fragile to noisy RF-fields [Morizot *et al.*, 2008], and the superposition state used in the interferometer is also, by default, highly sensitive to magnetic field fluctuations. In consequence, the control of the time-dependent polarisation of the RF-fields and A-fields determines the successful adiabatic manipulation of the atom clouds. In our case, the magnetic fields stability was good-enough to manipulate BECs without measurable temperature increase or atom loss both in TAAP rings and in shell traps. The dephasing time of the transition between $|1, \bar{m}_F = -1\rangle$ and $|2, \bar{m}_F = 1\rangle$ was limited to a large extent by fluctuation in the RF-fields amplitudes. A succinct summary of these two observations is that the degree of stability of the magnetic fields did limit the control of the internal degrees of freedom, whereas it did not limit the control of the external degrees of freedom of the ultra-cold atoms.

A bi-chromatic shell trap. After characterising the spectroscopy in an optical trap, we studied ultra-cold atoms in adiabatic shell traps (Section 7.1). We focussed on the transition between the two *clock* states. The dephasing time of this transition in a RF-dressed trap is highly damped by inhomogeneous broadening caused by the different g_F of the two states. A method to match the traps and thus reduce this broadening was presented and tested: it consists of using a bi-chromatic dressing field, with two circularly polarised components of the opposite handedness and of different frequency. We observed a reduction in line-width of one order of

¹The MW-polarisation is defined with respect to the local quantization axis. In the case of atoms in an optical trap, this quantization axis is defined by a homogeneous magnetic field that points in a well established direction. To change the MW polarisation, in this case, is equivalent to tilting the axis of the homogeneous magnetic field.

²With the atom number, or the density, for example. One more application is, as in [Fattori *et al.*, 2008], minimising interactions to increase the coherence time in atom interferometers.

magnitude (Section 7.4). We expect further reduction of the line-width with better control of the magnetic fields polarisation stability. The observed null line-shift of the transition with³ B_{DC} makes the bi-chromatic shell trap an interesting platform to measure spatially dependent magnetic fields. The reason is that homogeneous DC-fields displace the trap but do not shift the transition. Therefore, one could compare the clock transition in different regions of space with no further broadening or shifts related to the displacement. We also suggest a method to construct from this a gravimeter based on the displacement of each of the spin states by means of changing the RF-dressing frequency independently. Similarly to an atomic gyroscope, the coherence time of the transition limits the performance of the interferometer. One more relevant observation is that the bi-chromatic shell spectrum showed a Landau-Zener-Stückelberg-Majorana interference pattern [Silveri *et al.*, 2017], which was a consequence of a modulation of the dressed clock-states eigen-energies resulting from non-perfect circularly polarised RF-fields. This type of interferometry has become very popular to demonstrate *quantumness* in solid-state systems [Oliver *et al.*, 2005; Gong *et al.*, 2016; Bogan *et al.*, 2018].

Other ideas. The full TAAP magnetic field configuration could be used to match the coupling to the RF-field in the two spin-states [Kunitomo *et al.*, 1977]. One could think of a dumbbell potential, instead of a ring, so as to achieve more easily uniform couplings. In any case, the study of the modified spectrum [Glenn *et al.*, 2013] of transitions between RF-dressed states in the TAAP case is needed to accomplish our proposal [Navez *et al.*, 2016]. We also saw that using the Bloch-Siegert shift could be used to match the modified g'_F of two spin states (see Section 3.3). For typical values of ω_{RF} in this experiment, one would need rather large Rabi frequencies in the RF-fields, at the limit of what is reasonably doable in our laboratory. However, with lower ω_{RF} , these shifts could be used to minimise broadening related to fluctuations in DC and RF fields. In an alternate future work, it would be worth investigating spin mixtures in the ring. It should be possible to first split a BEC in a superposition state in the dipole trap and then transfer it to the ring. Although, so far, a Ramsey sequence has a very short de-phasing time, this method gives access to high angular momentum states of spin mixtures⁴. On a different front, in [Ye *et al.*, 2018] they propose the use of a state-dependent dressed potential to study the dynamics of a two-component BEC. Both TAAPs and the bi-chromatic shell are good candidates for this type of experiment.

³Note the distinction with $B_Q(\mathbf{r})$.

⁴This could maybe be a good platform to implement what is proposed in [Pelegrí *et al.*, 2018].

The general aim of follow-up experiments should be related to narrowing the clock transition line-width in the dressed potential. The current work shows that de-phasing times of the order of 0.5s are possible by controlling magnetic field fluctuations [Szmuk *et al.*, 2015], and (or) also by installing μ -metal shields. Special care should be taken to stabilise and improve the generation of the RF-fields. A first step is the active stabilisation control of the RF-field polarisation⁵. Alternative approaches, such as some of those outlined above, are worth investigating. Firstly, the modification of g_F factors by using even stronger RF-fields should allow either for matching of g_F , or for robustness against fluctuations in the RF-fields amplitude⁶. Secondly, a mixed optical/magnetic potential, is worth studying, since, in principle, the traps mismatch for the two spin-states is much smaller compared to the shell trap case.

⁵Faster repetition rates would also help in the experimental search for corrections in the optimum parameters to increase the de-phasing times.

⁶This would occur at the maxima and minima of the Bessel-function shaped dependence of the modified gyromagnetic factor.

Appendices

Appendix A

Angular Momentum Algebra

Let us begin by writing the quantum angular momentum operator in the coupled basis that defines the hyperfine manifolds $|F, m_F\rangle$ (these are the angular momentum operators used in Chapter 3). They can be found in any Quantum Mechanics reference, for instance [Messiah, 1999]:

$$\begin{aligned}
 \hat{F}_z|F, m\rangle &= m\hbar|F, m\rangle \\
 \hat{F}_\pm|F, m\rangle &= \hbar\sqrt{F(F+1) - m(m\pm 1)}|F, m\pm 1\rangle \\
 \hat{F}_x &= \frac{1}{2}(\hat{F}_+ + \hat{F}_-) \\
 \hat{F}_y &= \frac{1}{2i}(\hat{F}_+ - \hat{F}_-)
 \end{aligned} \tag{A.1}$$

In order to perform some of the Hamiltonian transformations necessary to realise the Rotating Wave Approximation and thus reach a time-independent hamiltonian and to define the Dressed Basis we have used some standard rotation matrices in the coupled basis. A good reference for these operators can be found in [Garraway and Perrin, 2015; Walraven, 2017]:

$$\begin{aligned}
 R_z(\alpha) &= \exp\left[-\frac{i}{\hbar}\alpha\hat{F}_z\right] \\
 R_z^\dagger(\alpha)\hat{F}_zR_z(\alpha) &= \hat{F}_z \\
 R_z^\dagger(\alpha)\hat{F}_\pm R_z(\alpha) &= \exp\left[\pm i\alpha\hat{F}_\pm\right]
 \end{aligned} \tag{A.2}$$

As is typical in the literature related to adiabatic potentials, most of our treatment was performed in the coupled basis. However, when introducing a microwave field, at the hyperfine splitting energy scale, new couplings (i.e. degeneracies) appear between

the two manifolds and thus the quantum numbers of the uncoupled basis are needed to describe the system. The relation between the coupled $|F, m_F\rangle$ and uncoupled $|I m_I J m_J\rangle$ basis that we wrote in Eq. 3.8:

$$|F, m_F\rangle = \sum_{m_I=-3/2}^{3/2} \sum_{m_J=-1/2}^{1/2} (-1)^{m_F+1} \sqrt{1+2F} \begin{pmatrix} I & J & F \\ m_I & m_J & -m_F \end{pmatrix} |m_I, m_J\rangle \quad (\text{A.3})$$

can be shown to be, explicitly:

$$\begin{array}{ll} |F, m_F\rangle & |m_I, m_J\rangle \\ |1, -1\rangle & \frac{1}{2}|-1/2, -1/2\rangle - \frac{\sqrt{3}}{2}|-3/2, 1/2\rangle \\ |1, 0\rangle & \frac{1}{\sqrt{2}}|1/2, -1/2\rangle - \frac{1}{\sqrt{2}}|-1/2, 1/2\rangle \\ |1, 1\rangle & \frac{\sqrt{3}}{2}|3/2, -1/2\rangle - 1/2|1/2, 1/2\rangle \\ |2, -2\rangle & |-3/2, -1/2\rangle \\ |2, -1\rangle & \frac{1}{2}|-3/2, 1/2\rangle + \frac{\sqrt{3}}{2}|-1/2, -1/2\rangle \\ |2, 0\rangle & \frac{1}{\sqrt{2}}|-1/2, 1/2\rangle + \frac{1}{\sqrt{2}}|1/2, -1/2\rangle \\ |2, 1\rangle & \frac{\sqrt{3}}{2}|1/2, 1/2\rangle + \frac{1}{2}|3/2, -1/2\rangle \\ |2, 2\rangle & |3/2, 1/2\rangle \end{array}$$

These are essential to study microwave transitions between the hyperfine manifolds in magnetic field sensing applications Horsley and Treutlein, 2016a; Horsley and Treutlein, 2016b. When dealing with inter-manifold transitions, a set of orthogonal operators corresponding to \mathbf{J} , that act on m_J is needed. It can be written just like Eq. A.1:

$$\begin{aligned} J_z |m_I, m_J\rangle &= m_J \hbar |m_I, m_J\rangle \\ J_{\pm} &= \hbar \sqrt{J(J+1) - m_J(m_J \pm 1)} |m_I, m_J \pm 1\rangle \\ J_x &= \frac{1}{2}(J_+ + J_-) \\ J_y &= \frac{1}{2i}(J_+ - J_-) \end{aligned} \quad (\text{A.4})$$

We normally neglect the contribution from the I operator because the $g_I \ll g_J$.

Appendix B

Decay curves in Coherent Driving

To find the population evolution in our two-level system (normally with the dressed states $|1, -\bar{1}\rangle$ and $|2, \bar{1}\rangle$) we can find from the von Neumann equation using the density matrix:

$$\frac{\partial \rho}{\partial t} = \frac{i}{\hbar} [\rho, H] - \begin{pmatrix} 0 & \gamma_d \rho_{12} \\ \gamma_d \rho_{21} & 0 \end{pmatrix} \quad (\text{B.1})$$

where we have assumed lifetimes $\tau \gg 1/\gamma_d$, and where γ_d is the coherences decay rate. Here the Hamiltonian in the RWA is:

$$H = \begin{pmatrix} 0 & \Omega_R \\ \Omega_R^* & \Delta \end{pmatrix} \quad (\text{B.2})$$

with Ω_R being the Rabi frequency that couples the two states (in our case this is a linear term only with ω_{MW}) and Δ being the detuning of the driving field with the transition. We can now choose $\Delta = 0$ and solve the ODE system in Eq. B.1 to find:

$$f_2 = \frac{1}{2} (1 + e^{-t\gamma_d} \cos \Omega_R t) \quad (\text{B.3})$$

where we have assumed that $\Omega \gg \gamma_d$. When $\gamma_d = 0$ we recover the well known result of undamped Rabi oscillations:

$$f_2 = \frac{1}{2} (1 + \cos \Omega_R t) \quad (\text{B.4})$$

However, this result does not capture the physics of Gaussian-profiled noise sources, which are the typical ones in our experiment. To calculate this dependency we start from the correlator:

$$R_i f_2 = \int_{-\infty}^{\infty} S(\Omega_R) f_2^{ud}(\Omega_R) d\Omega_R \quad (\text{B.5})$$

The function $S(\Omega_R)$ captures the fluctuations in the driving field of the transition. However, we can also think of a Ramsey experiment, where the fringes are given by:

$$f_2 = \frac{1}{2} (1 + \cos(2\pi t \delta_r)) \quad (\text{B.6})$$

with $\delta_r = (\nu - \nu_{\text{MW}})$ and ν_{MW} being the MW field driving frequency. In this case the broadening would be attached to the local oscillator, so we write an equivalent relation:

$${}_{Ry}f_2 = \int_{-\infty}^{\infty} S(\nu_0) f_2^{ud}(\nu_0) d\nu_0 \quad (\text{B.7})$$

Let us now focus in this latter case of Ramsey fringes. If we consider a Gaussian noise profile on the trapping/environmental fields such that Ferreira Cao, 2017:

$$S(\nu_0) = \frac{1}{\sqrt{2\pi}\sigma} \exp\left(-\frac{(\nu - \nu_0)^2}{2\sigma^2}\right) \quad (\text{B.8})$$

then we find that:

$${}^G_{Ry}f_2 = \frac{1}{2} \left(1 + e^{-\frac{t^2\sigma^2}{2}} \cos(2\pi t (\nu_{\text{MW}} - \nu_0))\right) \quad (\text{B.9})$$

Conversely, if we insert use a Lorentzian-shaped noise profile into Eq. B.7:

$$S(\nu_0) = \frac{1}{\pi} \frac{\sigma}{(\nu - \nu_0)^2 + \sigma^2} \quad (\text{B.10})$$

then we find a linear decay:

$${}^L_{Ry}f_2 = \frac{1}{2} \left(1 + e^{-t\sigma} \cos(2\pi t (\nu_{\text{MW}} - \nu_0))\right) \quad (\text{B.11})$$

notice that the results in Eq. B.11 and Eq. B.3 are the same, which suggests that the processes leading to dephasing in the coherences of Eq. B.1 should be related to noise distributions of the form of Eq. B.10. Collisional broadening is one such example. We can find equivalent expressions for the Rabi decay.

$${}^G_{Ri}f_2 = \frac{1}{2} \left(1 + e^{-\frac{t^2\sigma_\Omega^2}{2}} \cos(\Omega_r t)\right) \quad (\text{B.12})$$

and

$${}^L_{Ri}f_2 = \frac{1}{2} \left(1 + e^{-t\sigma_\Omega} \cos(\Omega_r t)\right) \quad (\text{B.13})$$

with Ω_r being the Rabi frequency at the resonance. Notice that in this case the de-phasing is related to fluctuations in Ω_r . The Lorentzian and Gaussian noise

sources produce different de-phasing characteristic curves, with associated decay times at $1/e$:

$$\begin{aligned}\tau_{dG} &= \frac{\sqrt{2}}{\sigma} \\ \tau_{dL} &= \frac{1}{\sigma}\end{aligned}\tag{B.14}$$

We have compared the χ^2 and R parameters resulting from using both fitting functions in several decay curves and the Gaussian noise profile shows systematically better (although only of the order of 5%) results than the linear decay resulting from Lorentzian noise.

Appendix C

Two-states imaging processing

We introduced our two-state imaging procedure in Section 5.3. Imperfections in the imaging of either state can arise from wrongly synced shutter or AOM timings, or simply from one of the cameras not being properly focused. When imaging only one of the states, in a simpler sequence, we observe a difference in atom number count from the two cameras of $< 5\%$. However, especially in the early stages of the two-state imaging set-up, this would not work as well in the sequence described in the Chapter 5. Having access to *good* counts in the the Rabi oscillations in one the states allows us though to re-scale the other state, since they are perfectly correlated. To to this, we first find the interpolation function (Fig. C.1a) that relates the atom number count in both states (i.e. in both cameras). Then we re-scale the atom number count in the $F=2$ images (where we can clearly see a large divergence) following this dependence. Fig. C.1b shows the figure of merit of this correction: the total atom number. Orange marks the total atom number before correcting the images of $F=2$ atoms and Blue, Dashed shows the total atom number count after the correction. We see that after the correction the total atom number remains constant at times much shorter than the measured lifetimes of the cloud.

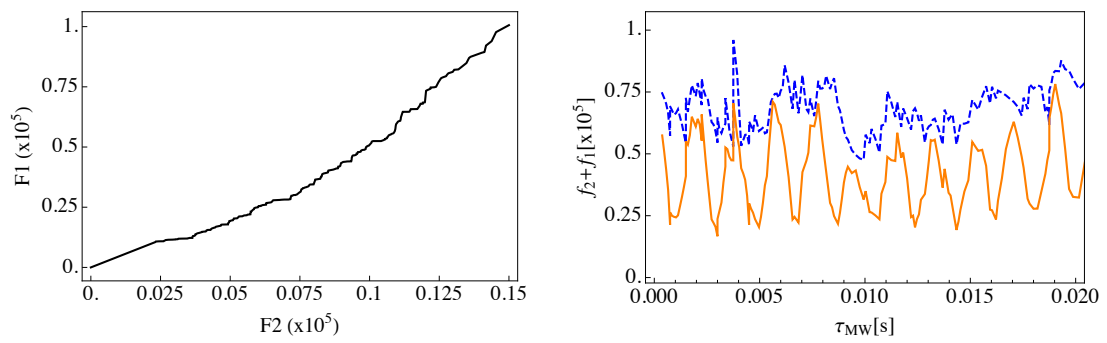


Figure C.1: a) Interpolation function for the atom number count in both spin states. b) In Orange total atom number count before corrections and in Blue total number count after corrections.

Appendix D

Quadrupole-field line-shifts in the bi-chromatic shell.

In Section 7.5.4 we study the energy shift with the magnetic quadrupole trapping field of the clock transition in the bi-chromatic shell. This appendix summarises some further preliminary analysis of the data presented in Fig. 7.21. The motivation behind this study is a numerical finding that suggests that the shape of the curve in Fig. 7.21 is the result of both low gradient and different Rabi frequencies for both states. The sample is prepared as explained in Section 7.5.5. Afterwards we first measure the transition line with a 10ms weak MW pulse, and the Rabi frequency on resonance with a stronger MW field to ensure that the Rabi oscillations do not decay before a clean π pulse. The results are shown in Fig. D.1, that represents the normalised atom number in $F=2$. A Lorentzian fit to Fig. 7.15a) yields a linewidth of $\Delta\nu_0 = 141 \pm 6$ Hz and $\nu_0 = 6019 \pm 3$ Hz (this measurement is performed at 22Gpcm, with $\omega_1 = 2294336$ Hz and $\omega_2 = 2285238$ Hz and the Rabi frequencies $\Omega \approx 200$ kHz). Here ν_0 is the transition frequency between the states $|1, -\bar{1}\rangle$ and $|2, \bar{1}\rangle$. A fit with Gaussian noise (see Eq. B.12) to the data in Fig. D.1b) yields $\Omega_{\text{MW}}/2\pi = 199 \pm 3$ Hz and $\sigma = 153 \pm 9$ Hz, where σ refers to the standard deviation in the frequency noise induced by the MW field amplitude. After this, we set-up a Ramsey experiment at several gradients. We fit Eq. B.9 to each of the cases and find the results in Table D.1.

Fig. D.2 shows one example of temporal Ramsey fringes, for $\alpha = 17$ Gpcm and all

Gradient (Gpcm)	ν_{Ramsey} (Hz)	σ (Hz)
15	616 ± 9	261 ± 38
15.5	658 ± 8	102 ± 41
16	666 ± 3	98 ± 13
16.2	661 ± 8	232 ± 40
17	528 ± 5	159 ± 19
18	414 ± 20	274 ± 80
22	325 ± 29	293 ± 100

Table D.1: Here ν_{Ramsey} is the measured temporal Ramsey fringe oscillation frequency as retrieved from a fit to Eq. B.9 and σ is the standard deviation of the local oscillator frequency, also retrieved from the fit. The errors are the ones of the fit, without weighing in the data-points error.

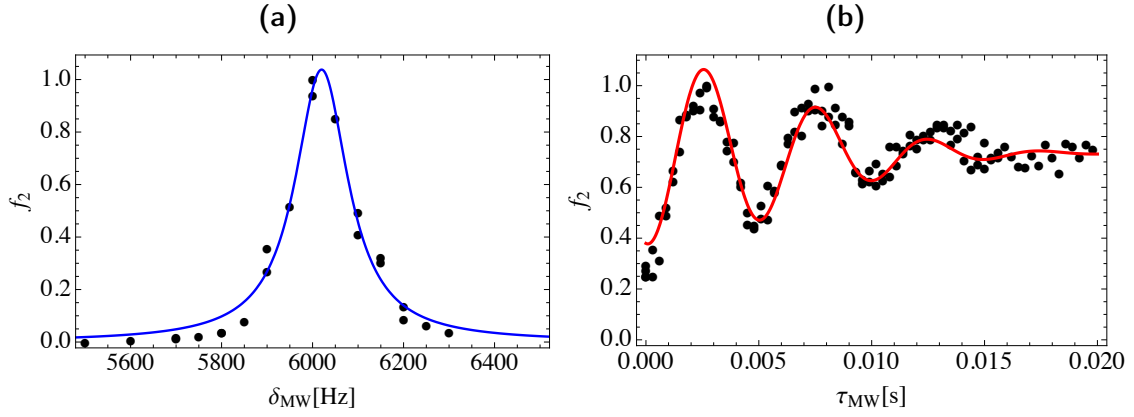


Figure D.1: a) One example of the transition line between the dressed clock states in the bi-chromatic shell. b) Rabi oscillations between the dressed clock states in the bi-chromatic shell.

ν_{Ramsey} plotted together. The dashed orange curve is a fit to the following function:

$$\nu_{Ramsey} = \xi_{off} + \xi_{amp} (v_1 - v_2) \quad (D.1)$$

with:

$$\begin{aligned} v_1 &= \sqrt{(\alpha - \xi_0)^2 + \xi_{\Omega_1}^2} \\ v_2 &= \sqrt{(\alpha - \xi_0)^2 + \xi_{\Omega_2}^2} \end{aligned} \quad (D.2)$$

Eq. D.1 has the same dependence as the energy difference between the two shell traps, assuming they are matched. The *Rabi frequency* is represented here by ξ_{Ω_1}

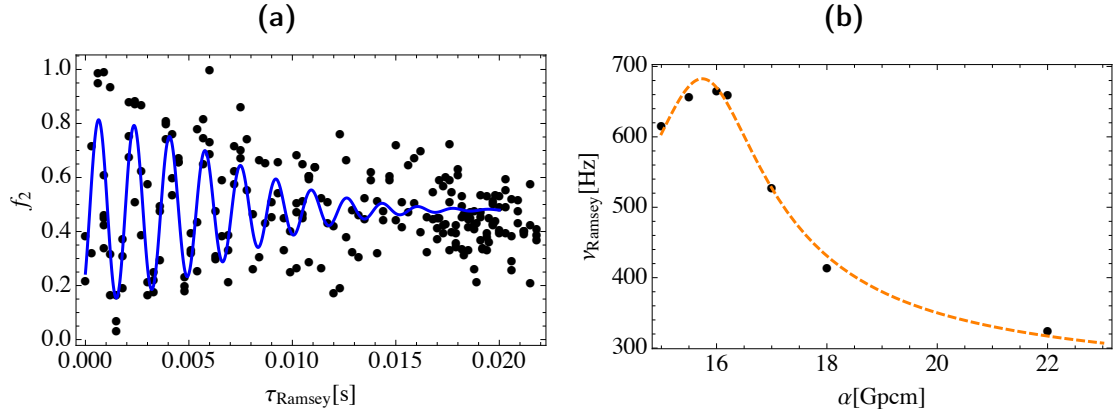


Figure D.2: a) Temporal Ramsey fringes at 17Gpcm in the bi-chromatic shell b) Ramsey fringes frequency ν_{Ramsey} for several quadrupole field gradients. Here, black dots are data points and the orange, dashed curve is a fit to the data ν_{Ramsey} using Eq. B.9.

and ξ_{Ω_2} . If we fit this curve to the data in Fig. D.2 b) we obtain the dashed, orange line. We find $\xi_{\Omega_1} = 1.067 \pm 0.18$ and $\xi_{\Omega_2} = 1.068 \pm 0.18$. However, this curve is mostly useful to find the dependence of the standard deviation of the transition frequency with fluctuations of the quadrupole field. To find this dependence, one can calculate the derivative of Eq. D.1 as fitted to Fig. D.2 b) and then integrate around each value of the quadrupole field for the span of the quadrupole field fluctuations. Assuming fluctuations of 0.3% we find the orange curve in Fig. D.3. The grey, dashed curve is an estimation of the broadening due to fluctuations of the order of $200\mu\text{G}$ in the RF-fields¹. It is interesting to note that the data points for higher gradients are expected to suffer less from fluctuations in the quadrupole gradient, yet the line-width remains the same or even increases. This can be explained intuitively by the fact that, as the gradient decreases, the atomic cloud leaves further from the resonance. Consequently, the fluctuations in Rabi frequency matter less. The *parabola*-like shape that we find can be explained by the difference in Rabi frequencies in both shells, as the fit indicates.

¹This is a blunt approximation, estimated from the point at 22Gpcm.

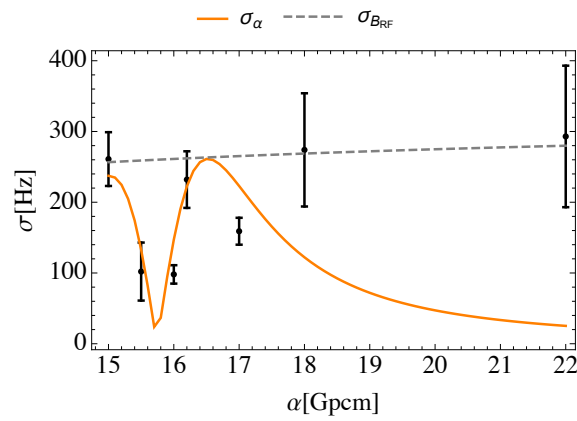


Figure D.3: Black dots are σ as fitted with Eq. B.9 to the data in Fig. D.2b). The error is the error of the fit. orange is a derivative of the orange, dashed curve from Fig. D.2b), considering quadrupole field fluctuations of 0.3%. The grey curve is a very rough estimate of the broadening caused by RF-field fluctuations of the order of $200\mu\text{G}$ in the RF-fields.

Bibliography

- Abend, S., Gebbe, M., Gersemann, M., Ahlers, H., Müntinga, H., Giese, E., Gaaloul, N., Schubert, C., Lämmerzahl, C., Ertmer, W., Schleich, W., and Rasel, E. (2016). *Atom-Chip Fountain Gravimeter*. Phys. Rev. Lett., **117**, 203003.
- Allegrini, M. and Arimondo, E. (1971). *Radiofrequency transitions in a dressed atom*. J. Phys. B At. Mol. Phys., **4**, 1008.
- Altin, P. A. (2016). *The role of interactions in atom interferometry with Bose-Condensed atoms*. PhD thesis.
- Anderson, M. H., Ensher, J. R., Matthews, M. R., Wieman, C. E., and Cornell, E. A. (1995). *Observation of bose-einstein condensation in a dilute atomic vapor*. Science, **269**, 198.
- Baily, C. (2013). *Early atomic models. From mechanical to quantum*. Eur. Phys. J. H, **38**, 1.
- Barrett, B., Geiger, R., Dutta, I., Meunier, M., Canuel, B., Gauguet, A., Bouyer, P., and Landragin, A. (2014). *The Sagnac effect: 20 years of development in matter-wave interferometry*. Comptes Rendus Phys., **15**, 875.
- Beaufils, Q., Zanon, T., Chicireanu, R., Laburthe-Tolra, B., Maréchal, E., Vernac, L., Keller, J.-C., and Gorceix, O. (2008). *Radio-frequency-induced ground-state degeneracy in a Bose-Einstein condensate of chromium atoms*. Phys. Rev. A, **78**, 051603.
- Bell, T. A., Glidden, J. A. P., Humbert, L., Bromley, M. W. J., Haine, S. A., Davis, M. J., Neely, T. W., Baker, M. A., and Rubinsztein-Dunlop, H. (2016). *Bose-Einstein condensation in large time-averaged optical ring potentials*. New J. Phys., **18**, 035003.

- Bentine, E., Harte, T. L., Luksch, K., Barker, A. J., Mur-Petit, J., Yuen, B., and Foot, C. J. (2017). *Species-selective confinement of atoms dressed with multiple radiofrequencies*. *J. Phys. B At. Mol. Opt. Phys.*, **50**, 094002.
- Berrada, T., van Frank, S., Bucker, R., Schumm, T., Schaff, J.-F., and Schmiedmayer, J. (2013). *Integrated Mach-Zehnder interferometer for Bose-Einstein condensates*. *Nat. Commun.*, **4**, 2077.
- Bidel, Y., Zahzam, N., Blanchard, C., Bonnin, A., Cadoret, M., Bresson, A., Rouxel, D., and Lequentrec-Lalancette, M. F. (2018). *Absolute marine gravimetry with matter-wave interferometry*. *Nat. Commun.*, **9**, 627.
- Biedenharn, L. C. and Louck, J. D. (1981). *Angular momentum in quantum physics : theory and application*. Addison-Wesley.
- Bloch, I., Dalibard, J., and Zwerger, W. (2008). *Many-body physics with ultracold gases*. *Rev. Mod. Phys.*, **80**, 885.
- Bloom, B. J., Nicholson, T. L., Williams, J. R., Campbell, S. L., Bishof, M., Zhang, X., Zhang, W., Bromley, S. L., and Ye, J. (2014). *An optical lattice clock with accuracy and stability at the 10^{-18} level*. *Nature*, **506**, 71.
- Bogan, A., Studenikin, S., Korkusinski, M., Gaudreau, L., Zawadzki, P., Sachrajda, A. S., Tracy, L., Reno, J., and Hargett, T. (2018). *Landau-Zener-Stückelberg-Majorana Interferometry of a Single Hole*. *Phys. Rev. Lett.*, **120**, 207701.
- Bolpasi, V. (2008). *High Power Laser System for the Creation of Bose-Einstein Condensations*. PhD thesis, University of Crete.
- Bolpasi, V. (2014). *An ultra-high flux matter-wave laser from a highly flexible Ioffe-Pritchard trap*. PhD thesis, University of Crete.
- Bolpasi, V., Efremidis, N. K., Morrissey, M. J., Condylis, P. C., Sahagun, D., Baker, M., and Von Klitzing, W. (2014). *An ultra-bright atom laser*. *New J. Phys.*, **16**, 033036.
- Bolpasi, V. and von Klitzing, W. (2010). *Double-pass tapered amplifier diode laser with an output power of 1 W for an injection power of only 200 μ W*. *Rev. Sci. Instrum.*, **81**, 113108.

- Burchianti, A., D'Errico, C., Rosi, S., Simoni, A., Modugno, M., Fort, C., and Minardi, F. (2018). *Dual-species Bose-Einstein condensate of K 41 and Rb 87 in a hybrid trap*. Phys. Rev. A, **98**, 063616.
- Burt, E. A., Ghrist, R. W., Myatt, C. J., Holland, M. J., Cornell, E. A., and Wieman, C. E. (1997). *Coherence, Correlations, and Collisions: What One Learns about Bose-Einstein Condensates from Their Decay*. Phys. Rev. Lett., **79**, 337(4).
- Canuel, B., Bertoldi, A., Amand, L., Pozzo di Borgo, E., Chantrait, T., Danquigny, C., Dovale Álvarez, M., Fang, B., Freise, A., Geiger, R., Gillot, J., Henry, S., Hinderer, J., Holleville, D., Junca, J., Lefèvre, G., Merzougui, M., Mielec, N., Monfret, T., Pelisson, S., Prevedelli, M., Reynaud, S., Riou, I., Rogister, Y., Rosat, S., Cormier, E., Landragin, A., Chaibi, W., Gaffet, S., and Bouyer, P. (2018). *Exploring gravity with the MIGA large scale atom interferometer*. Sci. Rep., **8**, 14064.
- Chicireanu, R., Nelson, K. D., Olmschenk, S., Lundblad, N., Derevianko, A., and Porto, J. V. (2011). *Differential Light-Shift Cancellation in a Magnetic-Field-Insensitive Transition of Rb 87*. Phys. Rev. Lett., **106**, 063002.
- Christodoulou, P. (2015). *Quantifying cold thermal clouds as a resource for Quantum Degeneracy in a Ioffe-Pritchard trap*. Msc thesis, National Technical University of Athens and IESL FORTH.
- Cohen-Tannoudji, C. and Dupont-Roc, J. (1972). *Experimental Study of Zeeman Light Shifts in Weak Magnetic Fields*. Phys. Rev. A, **5**, 968.
- Cohen-Tannoudji, C. and Guery-Odelin, D. (2011). *Advances in atomic physics : an overview*. World Scientific.
- Cohen-Tannoudji, C. and Haroche, S. (1969a). *Absorption et diffusion de photons optiques par un atome en interaction avec des photons de radiofréquence*. J. Phys., **30**, 153.
- Cohen-Tannoudji, C. and Haroche, S. (1969b). *Interprétation quantique des diverses résonances observées lors de la diffusion de photons optiques et de radiofréquence par un atome*. J. Phys., **30**, 125.

- Colzi, G., Fava, E., Barbiero, M., Mordini, C., Lamporesi, G., and Ferrari, G. (2018). *Production of large Bose-Einstein condensates in a magnetic-shield-compatible hybrid trap*. Phys. Rev. A, **97**, 053625.
- Crookston, M. B., Baker, P. M., and Robinson, M. P. (2005). *A microchip ring trap for cold atoms*. J. Phys. B At. Mol. Opt. Phys., **38**, 3289.
- Dalfovo, F., Giorgini, S., Pitaevskii, L. P., and Stringari, S. (1999). *Theory of Bose-Einstein condensation in trapped gases*. Rev. Mod. Phys., **71**, 463.
- Dalibard, J. (1998). *Collisional dynamics of ultra-cold atomic gases*. In: Inguscio, M., Stringari, S., and Wieman, C. (Eds.), *Proc. Int. Sch. Phys. Enrico Fermi*, chapter Course CXL.
- Dalibard, J. and Cohen-Tannoudji, C. (1989). *Laser cooling below the Doppler limit by polarization gradients: simple theoretical models*. J. Opt. Soc. Am. B, **6**, 2023.
- Davis, K. B., Mewes, M. O., Andrews, M. R., Van Druten, N. J., Durfee, D. S., Kurn, D. M., and Ketterle, W. (1995). *Bose-Einstein condensation in a gas of sodium atoms*. Phys. Rev. Lett., **75**, 3969.
- de Angelis, M., Bertoldi, A., Cacciapuoti, L., Giorgini, A., Lamporesi, G., Prevedelli, M., Saccorotti, G., Sorrentino, F., and Tino, G. M. (2009). *Precision gravimetry with atomic sensors*. Meas. Sci. Technol., **20**, 022001.
- Deutsch, C., Ramirez-Martinez, F., Lacroûte, C., Reinhard, F., Schneider, T., Fuchs, J. N., Piéchon, F., Laloë, F., Reichel, J., and Rosenbusch, P. (2010). *Spin Self-Rephasing and Very Long Coherence Times in a Trapped Atomic Ensemble*. Phys. Rev. Lett., **105**, 020401.
- Devlin, J. A. and Tarbutt, M. R. (2016). *Three-dimensional Doppler, polarization-gradient, and magneto-optical forces for atoms and molecules with dark states*. New J. Phys., **18**, 123017.
- Dutta, I., Savoie, D., Fang, B., Venon, B., Garrido Alzar, C. L., Geiger, R., and Landragin, A. (2016). *Continuous Cold-Atom Inertial Sensor with 1nrad/sec Rotation Stability*. Phys. Rev. Lett., **116**, 183003.
- Easwaran, R. K., Longchambon, L., Pottie, P.-E., Lorent, V., Perrin, H., and Garraway, B. M. (2010). *RF spectroscopy in a resonant RF-dressed trap*. J. Phys. B At. Mol. Opt. Phys., **43**, 065302.

- Extavour, M. H. T., LeBlanc, L. J., Schumm, T., Cieslak, B., Myrskog, S., Stummer, A., Aubin, S., and Thywissen, J. H. (2006). *Dual-Species Quantum Degeneracy of 40K and 87Rb on an Atom Chip*. In: *AIP Conf. Proc.*, Vol. 869, , pp. 241–249. AIP.
- Faber, A. (2011). *All optical formation of a Rubidium Bose-Einstein condensate for experiments on interacting Rydberg atoms*. Diploma thesis, University of Heidelberg.
- Fang, B., Dutta, I., Gillot, P., Savoie, D., Lautier, J., Cheng, B., Garrido Alzar, C. L., Geiger, R., Merlet, S., Pereira Dos Santos, F., and Landragin, A. (2016). *Metrology with Atom Interferometry: Inertial Sensors from Laboratory to Field Applications*. *J. Phys. Conf. Ser.*, **723**, 012049.
- Fattori, M., D’Errico, C., Roati, G., Zaccanti, M., Jona-Lasinio, M., Modugno, M., Inguscio, M., and Modugno, G. (2008). *Atom Interferometry with a Weakly Interacting Bose-Einstein Condensate*. *Phys. Rev. Lett.*, **100**, 080405.
- Fernholz, T., Stevenson, R., Hush, M. R., Lesanovsky, I. V., Bishop, T., Gentile, F., Jammi, S., Pyragius, T., Bason, M. G., Mas, H., Pandey, S., Vasilakis, G., Poullos, K., and von Klitzing, W. (2016). *Towards rotation sensing with a single atomic clock*. Vol. 9900, , p. 990007. International Society for Optics and Photonics.
- Ferreira Cao, M. (2017). *Control and characterisation of a Rydberg spin system to explore many-body physics*. PhD thesis, University of Heidelberg.
- Fetter, A. L. (2009). *Rotating trapped Bose-Einstein condensates*. *Rev. Mod. Phys.*, **81**, 647.
- Foot, C. J. (2005). *Atomic physics*. Oxford University Press.
- Garraway, B. and Perrin, H. (2015). *Recent developments in trapping and manipulation of atoms with adiabatic potentials*. *J. Phys. B At. Mol. Phys.*, **49**, 172001.
- Garrido Alzar, C. L., Perrin, H., Garraway, B. M., and Lorent, V. (2006). *Evaporative cooling in a radio-frequency trap*. *Phys. Rev. A*, **74**, 053413.
- Gaunt, A. L., Schmidutz, T. F., Gotlibovych, I., Smith, R. P., and Hadzibabic, Z. (2013). *Bose-einstein condensation of atoms in a uniform potential*. *Phys. Rev. Lett.*, **110**, 200406.

- Geiger, R., Ménotet, V., Stern, G., Zahzam, N., Cheinet, P., Battelier, B., Villing, A., Moron, F., Lours, M., Bidet, Y., Bresson, A., Landragin, A., and Bouyer, P. (2011). *Detecting inertial effects with airborne matter-wave interferometry*. Nat. Commun., **2**, 474.
- Gibble, K. (2009). *Decoherence and Collisional Frequency Shifts of Trapped Bosons and Fermions*. Phys. Rev. Lett., **103**, 113202.
- Gibble, K. and Chu, S. (1993). *Laser-cooled Cs frequency standard and a measurement of the frequency shift due to ultracold collisions*. Phys. Rev. Lett., **70**, 1771.
- Gildemeister, M. (2010). *Trapping ultracold atoms in time-averaged adiabatic potentials*. PhD thesis, University of Oxford.
- Gildemeister, M., Nugent, E., Sherlock, B. E., Kubasik, M., Sheard, B. T., and Foot, C. J. (2010). *Trapping ultracold atoms in a time-averaged adiabatic potential*. Phys. Rev. A, **81**, 031402.
- Gildemeister, M., Sherlock, B. E., and Foot, C. J. (2012). *Techniques to cool and rotate Bose-Einstein condensates in time-averaged adiabatic potentials*. Phys. Rev. A, **85**, 53401.
- Glenn, R., Limes, M. E., Pankovich, B., Saam, B., and Raikh, M. E. (2013). *Magnetic resonance in slowly modulated longitudinal field: Modified shape of the Rabi oscillations*. Phys. Rev. B, **87**, 155128.
- Gong, M., Zhou, Y., Lan, D., Fan, Y., Pan, J., Yu, H., Chen, J., Sun, G., Yu, Y., Han, S., and Wu, P. (2016). *Landau-Zener-Stückelberg-Majorana interference in a 3D transmon driven by a chirped microwave*. Appl. Phys. Lett., **108**, 112602.
- Gordon, J. P. and Ashkin, A. (1980). *Motion of atoms in a radiation trap*. Phys. Rev. A, **21**, 1606.
- Griffin, A., Snoke, D. W., and Stringari, S. (1995). *Bose-Einstein condensation*. Cambridge University Press.
- Grimm, R., Weidemüller, M., and Ovchinnikov, Y. B. (2000). *Optical dipole traps for neutral atoms*. Adv. At. Mol. Opt. Phys., **42**, 95.
- Gross, C. and Bloch, I. (2017). *Quantum simulations with ultracold atoms in optical lattices*. Science, **357**, 995.

- Hafele, J. C. and Keating, R. E. (1972). *Around-the-World Atomic Clocks: Predicted Relativistic Time Gains*. *Science*, **177**, 166.
- Hakala, T. K., Moilanen, A. J., Väkeväinen, A. I., Guo, R., Martikainen, J.-P., Daskalakis, K. S., Rekola, H. T., Julku, A., and Törmä, P. (2018). *Bose-Einstein condensation in a plasmonic lattice*. *Nat. Phys.*, **14**, 739.
- Hamilton, P., Jaffe, M., Haslinger, P., Simmons, Q., Müller, H., and Khoury, J. (2015). *Atom-interferometry constraints on dark energy*. *Science*, **349**, 849.
- Harber, D. M., Lewandowski, H. J., McGuirk, J. M., and Cornell, E. A. (2002). *Effect of cold collisions on spin coherence and resonance shifts in a magnetically trapped ultracold gas*. *Phys. Rev. A*, **66**, 053616.
- Haroche, S. and Cohen-Tannoudji, C. (1970). *Resonant Transfer of Coherence in Nonzero Magnetic Field Between Atomic Levels of Different g Factors*. *Phys. Rev. Lett.*, **24**, 974.
- Haroche, S., Cohen-Tannoudji, C., Audoin, C., and Schermann, J. P. (1970). *Modified Zeeman Hyperfine Spectra Observed in $H\ 1$ and $Rb\ 87$ Ground States Interacting with a Nonresonant rf Field*. *Phys. Rev. Lett.*, **24**, 861.
- Hirose, M., Aiello, C. D., and Cappellaro, P. (2012). *Continuous dynamical decoupling magnetometry*. *Phys. Rev. A*, **86**, 062320.
- Hodapp, T. W., Gerz, C., Furtlehner, C., Westbrook, C. I., Phillips, W. D., and Dalibard, J. (1995). *Three-dimensional spatial diffusion in optical molasses*. *Appl. Phys. B*, **60**, 135.
- Hodby, E., Hechenblaikner, G., Mara, O. M., Arlt, J., Hopkins, S., and Foot, C. J. (2000). *Bose-Einstein condensation in a stiff TOP trap with adjustable geometry*. *J. Phys. B At. Mol. Opt. Phys.*, **33**, 4087.
- Hofferberth, S., Fischer, B., Schumm, T., Schmiedmayer, J., and Lesanovsky, I. (2007). *Ultracold atoms in radio-frequency dressed potentials beyond the rotating-wave approximation*. *Phys. Rev. A*, **76**, 013401.
- Hofferberth, S., Lesanovsky, I., Fischer, B., Verdu, J., and Schmiedmayer, J. (2006). *Radio-frequency dressed state potentials for neutral atoms*. *Nat. Phys.*, **2**, 710.
- Horsley, A. and Treutlein, P. (2016a). *Frequency-tunable microwave field detection in an atomic vapor cell*. *Appl. Phys. Lett.*, **108**, 211102.

- Horsley, A. and Treutlein, P. (2016b). *Frequency-Tunable Microwave Field Detection in an Atomic Vapor Cell: Supplementary Information*. Appl. Phys. Lett., **108**.
- Huang, K. (1987). *Statistical mechanics*. Wiley.
- Kaplan, A., Andersen, M. F., and Davidson, N. (2003). *Suppression of inhomogeneous broadening in rf spectroscopy of optically trapped atoms*. In: *2003 Eur. Quantum Electron. Conf. EQEC 2003*.
- Kaplan, A., Andersen, M. F., Grünzweig, T., and Davidson, N. (2005). *Hyperfine spectroscopy of optically trapped atoms*. J. Phys. B, **7**, 103.
- Kasprzak, J., Richard, M., Kundermann, S., Baas, A., Jeambrun, P., Keeling, J. M. J., Marchetti, F. M., Szymańska, M. H., André, R., Staehli, J. L., Savona, V., Littlewood, P. B., Deveaud, B., and Dang, L. S. (2006). *Bose-Einstein condensation of exciton polaritons*. Nature, **443**, 409.
- Kastler, A. (1963). *Displacement of Energy Levels of Atoms by Light*. J. Opt. Soc. Am., **53**, 902.
- Kastler, A. (1973). *The Hanle effect and its use for the measurements of very small magnetic fields*. Nucl. Instruments Methods, **110**, 259.
- Kazakov, G. A. and Schumm, T. (2015). *Magic radio-frequency dressing for trapped atomic microwave clocks*. Phys. Rev. A, **91**, 023404.
- Ketterle, W. and Druten, N. V. (1996). *Evaporative Cooling of Trapped Atoms*. Adv. At. Mol. Opt. Phys., **37**, 181.
- Klaers, J., Schmitt, J., Vewinger, F., and Weitz, M. (2010). *Bose-Einstein condensation of photons in an optical microcavity*. Nature, **468**, 545.
- Kleppner, D. (1999). *A short history of atomic physics in the twentieth century*. Rev. Mod. Phys., **71**, S78.
- Kovachy, T., Asenbaum, P., Overstreet, C., Donnelly, C. A., Dickerson, S. M., Sugarbaker, A., Hogan, J. M., and Kasevich, M. A. (2015). *Quantum superposition at the half-metre scale*. Nature, **528**, 530.
- Kovachy, T., Asenbaum, P., Overstreet, C., Donnelly, C. A., Dickerson, S. M., Sugarbaker, A., Hogan, J. M., and Kasevich, M. A. (2016). *Kovachy et al. reply*. Nature, **537**, E2.

- Kuhn, C. C. N., McDonald, G. D., Hardman, K. S., Bennetts, S., Everitt, P. J., Altin, P. A., Debs, J. E., Close, J. D., and Robins, N. P. (2014). *A Bose-condensed, simultaneous dual-species Mach-Zehnder atom interferometer*. *New J. Phys.*, **16**, 073035.
- Kunitomo, M., Hatanaka, H., and Hashi, T. (1977). *Effects of Non-Resonant Oscillating Field on NMR in the Rotating Frame: Modification of Zeeman Energy and Related Phenomena*. *J. Phys. Soc. Japan*, **42**, 453.
- Lakshmi, P. A. and Agarwal, G. S. (1985). *Squeezing of radiation produced by the Hanle effect*. *Phys. Rev. A*, **32**, 1643.
- Lee, J. G. and Hill, W. T. (2014). *Spatial shaping for generating arbitrary optical dipole traps for ultracold degenerate gases*. *Rev. Sci. Instrum.*, **85**, 103106.
- Legget, A. J. (2000). *Topics in the theory of the ultracold dilute alkali gases*. In: *Bose-Einstein Condens.*, , pp. 1–42. World Scientific.
- Lenef, A., Hammond, T. D., Smith, E. T., Chapman, M. S., Rubenstein, R. A., and Pritchard, D. E. (1997). *Rotation Sensing with an Atom Interferometer*. *Phys. Rev. Lett.*, **78**, 760.
- Lesanovsky, I., Hofferberth, S., Schmiedmayer, J., and Schmelcher, P. (2006a). *Manipulation of ultracold atoms in dressed adiabatic radio-frequency potentials*. *Phys. Rev. A*, **74**, 033619.
- Lesanovsky, I., Schumm, T., Hofferberth, S., Andersson, L. M., Krüger, P., and Schmiedmayer, J. (2006b). *Adiabatic radio-frequency potentials for the coherent manipulation of matter waves*. *Phys. Rev. A*, **73**, 033619.
- Lesanovsky, I. and Von Klitzing, W. (2007). *Time-averaged adiabatic potentials: Versatile matter-wave guides and atom traps*. *Phys. Rev. Lett.*, **99**, 083001.
- Lett, P. D., Watts, R. N., Westbrook, C. I., Phillips, W. D., Gould, P. L., and Metcalf, H. J. (1988). *Observation of Atoms Laser Cooled below the Doppler Limit*. *Phys. Rev. Lett.*, **61**, 169.
- Lin, Y.-J., Jiménez-García, K., and Spielman, I. B. (2011). *Spin-orbit-coupled Bose-Einstein Condensates*. *Nature*, **470**, 83.

- Lin, Y.-J., Perry, A. R., Compton, R. L., Spielman, I. B., and Porto, J. V. (2009). *Rapid production of Rb87 Bose-Einstein condensates in a combined magnetic and optical potential*. Phys. Rev. A, **79**, 063631.
- Loudon, R. and Knight, P. L. (1987). *Squeezed light*. J. Mod. Opt., **34**, 9.
- Luiten, O. J., Reynolds, M. W., and Walraven, J. T. M. (1996). *Kinetic theory of the evaporative cooling of a trapped gas*. Phys. Rev. A, **53**, 381.
- Luo, C., Huang, J., Zhang, X., and Lee, C. (2017). *Heisenberg-limited Sagnac interferometer with multiparticle states*. Phys. Rev. A, **95**, 23608.
- Marti, G. E., Olf, R., and Stamper-Kurn, D. M. (2015). *Collective excitation interferometry with a toroidal Bose-Einstein condensate*. Phys. Rev. A, **91**, 013602.
- McDonald, G. D., Keal, H., Altin, P. A., Debs, J. E., Bennetts, S., Kuhn, C. C., Hardman, K. S., Johnsson, M. T., Close, J. D., and Robins, N. P. (2013). *Optically guided linear Mach-Zehnder atom interferometer*. Phys. Rev. A, **87**, 013632.
- Menchon-Enrich, R., Benseny, A., Ahufinger, V., Greentree, A. D., Busch, T., and Mompert, J. (2016). *Spatial adiabatic passage: a review of recent progress*. Reports Prog. Phys., **79**, 074401.
- Ménoret, V., Vermeulen, P., Le Moigne, N., Bonvalot, S., Bouyer, P., Landragin, A., and Desruelle, B. (2018). *Gravity measurements below 10^{-9} g with a transportable absolute quantum gravimeter*. Sci. Rep., **8**, 12300.
- Merkel, S. T., Brennen, G., Jessen, P. S., and Deutsch, I. H. (2009). *Constructing general unitary maps from state preparations*. Phys. Rev. A, **80**, 023424.
- Merkel, S. T., Jessen, P. S., and Deutsch, I. H. (2008). *Quantum control of the hyperfine-coupled electron and nuclear spins in alkali-metal atoms*. Phys. Rev. A, **78**, 023404.
- Merloti, K., Dubessy, R., Longchambon, L., Perrin, A., Pottie, P.-E., Lorent, V., and Perrin, H. (2013). *A two-dimensional quantum gas in a magnetic trap*. New J. Phys., **15**, 033007.
- Messiah, A. (1999). *Quantum mechanics*. Dover Publications.

- Metcalf, H. J. and van der Straten, P. (1999a). *Evaporative Cooling*. In: Berry, R. S., Birman, J. L., Lynn, J. W., Silverman, M. P., Stanley, H. E., and Voloshin, M. (Eds.), *Laser Cool. Trapp.*, chapter 12, , pp. 165–175. Springer-Verlag. New York.
- Metcalf, H. J. and van der Straten, P. (1999b). *General Properties Concerning Laser Cooling*. In: Berry, R. S., Birman, J. L., Lynn, J. W., Silverman, M. P., Stanley, H. E., and Voloshin, M. (Eds.), *Laser Cool. Trapp.*, chapter 5, , pp. 57–70. Springer-Verlag. New York.
- Metcalf, H. J. and van der Straten, P. (1999c). *Multilevel Atoms*. In: Berry, R. S., Birman, J. L., Lynn, J. W., Silverman, M. P., Stanley, H. E., and Voloshin, M. (Eds.), *Laser Cool. Trapp.*, chapter 4, , pp. 39–56. Springer-Verlag. New York, 1 edition.
- Mischuck, B. E., Merkel, S. T., and Deutsch, I. H. (2012). *Control of inhomogeneous atomic ensembles of hyperfine qubits*. *Phys. Rev. A*, **85**, 022302.
- Morizot, O., Garrido Alzar, C. L., Pottie, P.-E., Lorent, V., and Perrin, H. (2007). *Trapping and cooling of rf-dressed atoms in a quadrupole magnetic field*. *J. Phys. B At. Mol. Opt. Phys.*, **40**, 4013.
- Morizot, O., Longchambon, L., Kollengode Easwaran, R., Dubessy, R., Knyazchyan, E., Pottie, P.-E., Lorent, V., and Perrin, H. (2008). *Influence of the Radio-Frequency source properties on RF-based atom traps*. *Eur. Phys. J. D*, **47**, 209.
- Navez, P., Pandey, S., Mas, H., Poullos, K., Fernholz, T., and Klitzing, W. V. (2016). *Matter-wave interferometers using TAAP rings*. *New J. Phys.*, **18**, 075014.
- Oliver, W. D., Yu, Y., Lee, J. C., Berggren, K. K., Levitov, L. S., and Orlando, T. P. (2005). *Mach-Zehnder Interferometry in a Strongly Driven Superconducting Qubit*. *Science* (80-.), **310**, 1653.
- Owens, D. J. and Hutson, J. M. (2017). *Inelastic losses in radio-frequency-dressed traps for ultracold atoms*. *Phys. Rev. A*, **96**, 042707.
- Pandey, S. (2019). *Time Averaged Adiabatic Potentials for atom interferometry*. PhD thesis, University of Crete.

- Pandey, S., Mas, H., Drougakis, G., Mavrakakis, K. G., Mylonakis, M., Vasilakis, G., Bolpasi, V., and Von Klitzing, W. (2018). *Antireflection coated semiconductor laser amplifier for Bose-Einstein condensation experiments*. Cit. AIP Adv., **8**, 95020.
- Pandey, S., Mas, H., Drougakis, G., Thekkepatt, P., Bolpasi, V., Vasilakis, G., Poullos, K., and von Klitzing, W. (2019). *Hypersonic transport of Bose-Einstein Condensates in an accelerator ring*. Submitted.
- Pappa, M. (2011). *Imaging Bose-Einstein Condensates at Ultra-Low Atom-Numbers and Time Averaged Adiabatic Potentials*. PhD thesis, University of Crete.
- Pappa, M., Condylis, P. C., Konstantinidis, G. O., Bolpasi, V., Lazoudis, A., Morizot, O., Sahagun, D., Baker, M., and Von Klitzing, W. (2011). *Ultra-sensitive atom imaging for matter-wave optics*. New J. Phys., **13**, 115012.
- Parker, R. H., Yu, C., Zhong, W., Estey, B., and Müller, H. (2018). *Measurement of the fine-structure constant as a test of the Standard Model*. Science, **360**, 191.
- Pegg, D. T. (1973). *Semi-classical model of magnetic resonance in intense RF fields*. J. Phys. B At. Mol. Phys., **6**, 246.
- Peil, S. and Ekstrom, C. R. (2014). *Analysis of atom-interferometer clocks*. Phys. Rev. A, **89**, 014101.
- Pelegrí, G., Mompert, J., and Ahufinger, V. (2018). *Quantum sensing using imbalanced counter-rotating Bose-Einstein condensate modes*. New J. Phys., **20**, 103001.
- Perrin, H. and Garraway, B. M. (2017). *Trapping Atoms With Radio Frequency Adiabatic Potentials*. Adv. At. Mol. Opt. Phys., **66**, 181.
- Peters, A., Chung, K. Y., and Chu, S. (1999). *Measurement of gravitational acceleration by dropping atoms*. Nature, **400**, 849.
- Pethick, C. and Smith, H. (2008). *Bose-Einstein condensation in dilute gases*. Cambridge University Press.
- Petrich, W., Anderson, M. H., Ensher, J. R., and Cornell, E. A. (1995). *Stable, Tightly Confining Magnetic Trap for Evaporative Cooling of Neutral Atoms*. Phys. Rev. Lett., **74**, 3352.

- Phillips, W. D. (1998). *Laser cooling and trapping of neutral atoms*. Rev. Mod. Phys., **70**, 721.
- Phillips, W. D. and Metcalf, H. (1982). *Laser Deceleration of an Atomic Beam*. Phys. Rev. Lett., **48**, 596.
- Pitaevskii, L. P. and Stringari, S. (2003). *Bose-Einstein condensation*. Clarendon Press.
- Polo, J., Benseny, A., Busch, T., Ahufinger, V., and Mompert, J. (2016). *Transport of ultracold atoms between concentric traps via spatial adiabatic passage*. New J. Phys., **18**, 015010.
- Post, E. J. (1967). *Sagnac Effect*. Rev. Mod. Phys., **39**, 475.
- Randall, J., Weidt, S., Standing, E. D., Lake, K., Webster, S. C., Murgia, D. F., Navickas, T., Roth, K., and Hensinger, W. K. (2015). *Efficient preparation and detection of microwave dressed-state qubits and qutrits with trapped ions*. Phys. Rev. A, **91**, 012322.
- Reinhard, F. (2009). *Design and construction of an atomic clock on an atom chip*. PhD thesis, University Paris VI- Pierre et Marie Curie.
- Robert, A. (2011). *Encyclopedia of Medieval Philosophy*. In: Lagerlund, H. (Ed.), *Encycl. Mediev. Philosophy*, chapter Medieval A, , pp. 122–125. Springer. Dordrecht-Heidelberg- London-New York.
- Roncaglia, M., Rizzi, M., and Dalibard, J. (2011). *From rotating atomic rings to quantum Hall states*. Sci. Rep., **1**, 43.
- Rosenbusch, P. (2009). *Magnetically trapped atoms for compact atomic clocks*. Appl. Phys. B Lasers Opt., **95**, 227.
- Rosi, G., Sorrentino, F., Cacciapuoti, L., Prevedelli, M., and Tino, G. M. (2014). *Precision measurement of the Newtonian gravitational constant using cold atoms*. Nature, **510**, 518.
- Roura, A. (2018). *Gravitational redshift in quantum-clock interferometry*. <https://arxiv.org/pdf/1810.06744.pdf>.
- Rubbmark, J. R., Kash, M. M., Littman, M. G., and Kleppner, D. (1981). *Dynamical effects at avoided level crossings: A study of the Landau-Zener effect using Rydberg atoms*. Phys. Rev. A, **23**, 3107.

- Sagnac, G. (1913). *Sur la preuve de la réalité de l'éther lumineux par l'expérience de l'interférographe tournant*. C. R. Acad. Sci., **157**, 1410.
- Sahagun, D., Bolpasi, V., and von Klitzing, W. (2013). *A simple and highly reliable laser system with microwave generated repumping light for cold atom experiments*. Opt. Commun., **290**, 110.
- Saiko, A. P., Fedaruk, R., and Markevich, S. A. (2014). *Relaxation, decoherence, and steady-state population inversion in qubits doubly dressed by microwave and radiofrequency fields*. J. Phys. B At. Mol. Opt. Phys., **47**, 155502.
- Schkolnik, V., Hellmig, O., Wenzlawski, A., Grosse, J., Kohfeldt, A., Döringshoff, K., Wicht, A., Windpassinger, P., Sengstock, K., Braxmaier, C., Krutzik, M., and Peters, A. (2016). *A compact and robust diode laser system for atom interferometry on a sounding rocket*. Appl. Phys. B, **122**, 217.
- Schoser, J., Batär, A., Löw, R., Schweikhard, V., Grabowski, A., Ovchinnikov, Y. B., and Pfau, T. (2002). *Intense source of cold Rb atoms from a pure two-dimensional magneto-optical trap*. Phys. Rev. A, **66**, 023410.
- Schreiber, K. U., Gebauer, A., Igel, H., Wassermann, J., Hurst, R. B., and Wells, J.-P. R. (2014). *The centennial of the Sagnac experiment in the optical regime: From a tabletop experiment to the variation of the Earth's rotation*. Comptes Rendus Phys., **15**, 859.
- Shau-Yu, L., Pei-Chen, K., Estey, B., English, D., Brown, J. M., Hohensee, M. A., and Muller, H. (2013). *A Clock Directly Linking Time to a Particle's Mass*. Science, **339**, 554.
- Sherlock, B. (2011). *Ultracold quantum gases in time-averaged adiabatic potentials*. PhD thesis, University of Oxford.
- Sherlock, B. E., Gildemeister, M., Owen, E., Nugent, E., and Foot, C. J. (2011). *Time-averaged adiabatic ring potential for ultracold atoms*. Phys. Rev. A, **83**, 043408.
- Shvarchuck, I., Buggle, C., Petrov, D. S., Kemmann, M., Von Klitzing, W., Shlyapnikov, G. V., and Walraven, J. T. M. (2003). *Hydrodynamic behavior in expanding thermal clouds of 87Rb* . Phys. Rev. A, **68**, 063603.
- Silveri, M. P., Tuorila, J. A., Thuneberg, E. V., and Paraoanu, G. S. (2017). *Quantum systems under frequency modulation*. Reports Prog. Phys., **80**, 056002.

- Sinuco-Leon, G. and Garraway, B. (2012). *Radio-frequency dressed atoms beyond the linear Zeeman effect*. New J. Phys., **14**, 123008.
- Sinuco-Leon, G., Garraway, B. M., Mas, H., Pandey, S., Vasilakis, G., von Klitzing, W., Foxon, B., Jammi, S., Poullos, K., and Fernholz, T. (2019). *Microwave Spectroscopy of Radio-Frequency Dressed Rubidium 87*. Prep.
- Solaro, C., Bonnin, A., Combes, F., Lopez, M., Alauze, X., Fuchs, J.-N., Piéchon, F., Pereira, F., and Santos, D. (2016). *Competition between Spin Echo and Spin Self-Rephasing in a Trapped Atom Interferometer*. Phys. Rev. Lett., **117**, 163003.
- Stamper-Kurn, D. M., Marti, G. E., and Müller, H. (2016). *Verifying quantum superpositions at metre scales*. Nature, **537**, E1.
- Stark, A., Aharon, N., Huck, A., El-Ella, H. A. R., Retzker, A., Jelezko, F., and Andersen, U. L. (2018). *Clock transition by continuous dynamical decoupling of a three-level system*. Sci. Rep., **8**, 14807.
- Steane, A. M. and Foot, C. J. (1991). *Laser Cooling below the Doppler Limit in a Magneto-Optical Trap*. Europhys. Lett. Eur. Lett, **14**, 231.
- Steck, D. A. (2001). *Rubidium 87 D Line Data* (<http://steck.us/alkalidata>).
- Stevenson, R., Hush, M. R., Bishop, T., Lesanovsky, I., and Fernholz, T. (2015). *Sagnac Interferometry with a Single Atomic Clock*. Phys. Rev. Lett., **115**, 163001.
- Sugawa, S., Yamazaki, R., Taie, S., and Takahashi, Y. (2011). *Bose-Einstein condensate in gases of rare atomic species*. RAPID Commun. Phys. Rev. A, **84**, 11610.
- Szmuk, R., Dugrain, V., Maineult, W., Reichel, J., and Rosenbusch, P. (2015). *Stability of a trapped-atom clock on a chip*. Phys. Rev. A, **92**, 012106.
- Tarbutt, M. R. (2015). *Magneto-optical trapping forces for atoms and molecules with complex level structures*. New J. Phys., **17**, 015007.
- Townsend, C. G., Edwards, N. H., Cooper, C. J., Zetie, K. P., Foot, C. J., Steane, A. M., Szriftgiser, P., Perrin, H., and Dalibard, J. (1995). *Phase-space density in the magneto-optical trap*. Phys. Rev. A, **52**, 1423.

- Townsend, C. G., Edwards, N. H., Zetie, K. P., Cooper, C. J., Rink, J., and Foot, C. J. (1996). *High-density trapping of cesium atoms in a dark magneto-optical trap*. Phys. Rev. A, **53**, 1702.
- Treutlein, P. (2008). *Coherent manipulation of ultracold atoms on atom chips*. PhD thesis, Ludwig Maximilians Universität München.
- Trypogeorgos, D., Valdés-Curiel, A., Lundblad, N., and Spielman, I. B. (2018). *Synthetic clock transitions via continuous dynamical decoupling*. Phys. Rev. A, **97**, 013407.
- Turpin, A., Polo, J., Loiko, Y. V., Küber, J., Schmaltz, F., Kalkandjiev, T. K., Ahufinger, V., Birkl, G., and Mompert, J. (2015). *Blue-detuned optical ring trap for Bose-Einstein condensates based on conical refraction*. Opt. Express, **23**, 1638.
- Ungar, P. J., Weiss, D. S., Riis, E., and Chu, S. (1989). *Optical molasses and multilevel atoms: theory*. J. Opt. Soc. Am. B, **6**, 2058.
- Upadhyay, S., Dargyte, U., Prater, R. P., Dergachev, V. D., Varganov, S. A., Tscherbul, T. V., Patterson, D., and Weinstein, J. D. (2018). *Enhanced spin coherence of rubidium atoms in solid parahydrogen*. arXiv:1811.10535.
- van der Waerden, B. L. (2007). *Sources of quantum mechanics*. Dover Publications. New York.
- Viefers, S. (2008). *Quantum Hall physics in rotating Bose-Einstein condensates*. J. Phys. Condens. Matter, **20**, 123202.
- Walhout, M., Dalibard, J., Rolston, S. L., and Phillips, W. D. (1992). *$\sigma + \sigma$ -Optical molasses in a longitudinal magnetic field*. J. Opt. Soc. Am. B, **9**, 1997.
- Walraven, J. T. M. (2017). *Quantum Gases lectures University of Amsterdam*.
- Weiner, J., Bagnato, V. S., Zilio, S., and Julienne, P. S. (1999). *Experiments and theory in cold and ultracold collisions*. Rev. Mod. Phys., **71**, 1.
- Williams, J., Chiow, S.-w., Yu, N., and Müller, H. (2016). *Quantum test of the equivalence principle and space-time aboard the International Space Station*. New J. Phys., **18**, 025018.

- Xie, D., Wang, D., Gou, W., Bu, W., and Yan, B. (2018). *Fast production of rubidium Bose-Einstein condensate in a dimple trap*. J. Opt. Soc. Am. B, **35**, 500.
- Xin, M., Leong, W. S., Chen, Z., and Lan, S.-Y. (2018). *An atom interferometer inside a hollow-core photonic crystal fiber*. Sci. Adv., **4**, e1701723.
- Ye, Q., Huang, J., Zhuang, M., Zhong, H., and Lee, C. (2018). *Dressed state dynamics of two-component Bose-Einstein Condensates in state-dependent potentials*. Sci. Rep., **8**, 4484.
- Zanon-Willette, T., de Clercq, E., and Arimondo, E. (2012). *Magic Radio-Frequency Dressing of Nuclear Spins in High-Accuracy Optical Clocks*. Phys. Rev. Lett., **109**, 223003.
- Zobay, O. and Garraway, B. M. (2001). *Two-dimensional atom trapping in field-induced adiabatic potentials*. Phys. Rev. Lett., **86**, 1195.

